Validation and Statistical Downscaling of ERA-Interim Reanalysis Data for Integrated Applications

Dissertation der Fakultät für Geowissenschaften der

Ludwig–Maximilians–Universität München

zur Erlangung des akademischen Grades

"doctor rerum naturalium" (Dr. rer. nat.)

vorgelegt von

Lu Gao

aus Hubei, P.R.China

München, den 12.06.2013

Erstgutachter: Prof. Dr. Karsten Schulz

Zweitgutachter: Prof. Dr. Ralf Ludwig

Tag der mündlichen Prüfung: 07.08.2013

"The first requisite of success is the ability to apply your physical

and mental energies to one problem without growing weary."

- Thomas Edison

Acknowledgments

Summary

Climate change is attracting increasing attention due to its challenge effects on nature and the human environment. Global Climate Models (GCMs), the primary tool for climate impact studies, have been widely applied in the past decades. Although GCMs are adept at representing the past, present and future climate by simulating the general circulation, of the atmosphere and the oceans, their coarse spatial resolution is unable to provide reliable information at a finer scale. Regional Climate Models (RCMs) nested in GCMs represent better descriptions of local-scale characteristics, because of their finer spatial resolution of 10-50 km. This, however, still does not satisfy the requirements of hydrological and climatic impact models, which typically run on the scale of 0.1-1 km. Furthermore, in the mountain regions, the shortage of observations constrains the climate, hydrology, snow, glacial and permafrost researches. Reanalysis products are being increasingly applied for climate impact studies, due to its strength for estimating the closest state of real atmospheric and land surface characteristics. However, it still does not match the spatial resolution of climate and hydrology models.

To meet this major challenge, this dissertation attempts to evaluate a newly generated reanalysis database, the ERA-Interim, produced by the European Centre for Medium-Range Weather Forecasts (ECMWF), and to develop a robust temperature downscaling approach that is independent of observations in mountainous areas, as well as presenting a new machine learning method for precipitation downscaling. Furthermore, the validation and application of ERA-Interim data and downscaling methods for end users is also presented.

The large-scale error of ERA-Interim reanalysis data was evaluated by comparing it to gridded observations data (E-OBS) derived from the high density of measurements in the central Alps. It illustrated that the large-scale error of temperature on a daily scale is generally small, with an averaged bias of 0.6 °C. However, ERA-Interim is weak in capturing the extreme temperatures in complex terrains. Significant wet seasons (May to August) and dry seasons (November to February) were simulated by ERA-Interim. Although ERA-Interim has almost the same standard deviation as E-OBS for the inter-annual variability of daily precipitation (1.0 mm day^{-1}), the mean absolute error (MAE) was large and varied between 4.5 mm day^{-1} and 9.5 mm day^{-1} on wet days for the entire area. Therefore, the downscaling and correction is necessary for ERA-Interim application in alpine regions.

A novel temperature downscaling model was developed using the ERA-Interim internal lapse rate. Benchmark methods that use the conventional fixed lapse rate (Kunkel, 1989) and observed lapse rate derived from high and low stations were applied for model evaluation. The results demonstrated that the fixed lapse rate was not satisfactory and led to a large bias for high elevation measurements. The observed lapse rate worked best, but its application was limited, because not enough stations in high mountainous and high altitude regions are available to provide good lapse rates. The new method, based on the ERA-Interim modeled lapse rate, was derived from temperatures and geopotential heights at representative pressure levels and was independent of observations. This novel approach showed a convincing performance, especially for higher elevations.

A new machine learning method, Lasso, was introduced for the downscaling of ERA-Interim daily precipitation. The benchmark methods, Local downscaling (LOCI) and Quantile-Mapping (QM), as well as stepwise regression, were applied for model comparison in the mountainous regions. LOCI and QM demonstrated advantages in predicting precipitation occurrence, compared to the original ERA-Interim data. Stepwise regression yielded the worst predictions, although it applied the same set of local circulation variables as Lasso. The Lasso algorithm, combined with variable selection and a sparse model, generated slightly worse variations than LOCI and QM, but significantly reduced the relative errors (RMSE and MAE), for some stations in particular, only Lasso was effectual.

Flux tower sites from FLUXNET, which represented various vegetation and climate types in several topographic regions, were adopted for ERA-Interim validation. In general, ERA-Interim captured flux tower measurements with respect to temperature and precipitation well. Temperature downscaling methods were proven valid for micrometeorological stations. Large city observations over Europe were also applied for the validation of ERA-Interim in urban areas. Along with the rapidly expanding global markets, the world's largest motor vehicle manufacturer, Volkswagen Group and its subsidiary company AUDI AG have recognized that temperature distribution and extremes affect the automobiles' technical design. Therefore, under their urgent need, a visual framework for ERA-Interim application was developed, based on GIS for extreme temperature distributions.

In summary, the temperature downscaling method based on ERA-Interim modeled lapse rate was applicable for mountainous areas as well as for flux tower sites. In particular, the precipitation model was valid for high elevation stations for which the conventional benchmark methods did not work. Both downscaling methods are simple and can be easily implemented for

in future studies. The ERA-Interim reanalysis data is appropriate for various spatial resolution applications, from individual sites up to continental and global scales.

Contents

List of Figures

List of Tables

List of Symbols and Abbreviations

Symbols

a_p	The fraction of precipitation in the grid cell
$A(l)$, $A(a)$	Rate of change of cloud water/ice and cloud area due to transport through the boundaries of the grid volume.
c_{pdry}	Specific heat at constant pressure of dry air (J g^{-1} °C^{-1})
c_{pvap}	Specific heat at constant pressure of water vapor (J g^{-1} °C^{-1})
c_p	Specific heat at constant pressure of moist air (J g^{-1} °C^{-1})
CP	Convective Precipitation (mm)
E_{cld}	Rate of evaporation of cloud water/ice
FG_{10}	10 meter wind gust (m s^{-1})
G_{prec}	Rate of generation of precipitation from cloud water/ice
g	The acceleration of gravity (m s^{-2})
H_{850}, H_{700}, H_{500}	Geopotential height at 850 hpa, 700 hpa and 500 hpa (m)
$H(l)$	The ratio of cloudy in the grid area
LSP	Large scale precipitation (mm)
$MSLP$	Mean sea-level pressure (hPa)
P^{cld}	precipitation in cloudy situation (mm)
P^{clr}	precipitation in clear sky (mm)
P_{ERA}	ERA-Interim precipitation (mm)
P_{OBS}	Observed precipitation (mm)
q_l	Specific humidity at lowest model level (kg kg^{-1})
q_{surf}	Specific humidity at surface (kg kg^{-1})
RH_{850}, RH_{700}, RH_{500}	Relative humidity at 850 hpa, 700 hpa and 500 hpa (%)
rr	Daily total precipitation (mm)
SH_{850}, SH_{700}, SH_{500}	Specific humidity at 850 hpa, 700 hpa and 500 hpa (kg kg^{-1})
S_{conv}, δa_{conv}	Rate of formation of cloud water/ice and cloud area by convective processes

S_{strat}, δa_{strat}	Rate of formation of cloud water/ice and cloud area by stratiform condensation processes
s_l	Dry static energy at lowest model level (kJ kg^{-1})
s_{surf}	Dry static energy at surface (kJ kg^{-1})
T_{850}, T_{700}, T_{500}	Temperature at 850 hpa, 700 hpa and 500 hpa (°C)
T_{3h}	3-hourly air temperature (°C)
T_a	Near surface air temperature (°C)
T_d	Daily air temperature (°C)
TCW	Total column water (mm)
T_{ERA_2m}	ERA-Interim 2m temperature (°C)
T_{ERA_850}	ERA-Interim temperature at the 850hPa pressure level (°C)
T_g	Daily average temperature (°C)
T_n	Daily minimum temperature (°C)
T_{ref}	Reference temperature (°C)
T_x	Daily maximum temperature (°C)
U_{10}	10 meter U wind component (m s^{-1})
V_{10}	10 meter V wind component (m s^{-1})
WS_{10}	Wind speed at 10m (m s^{-1})
Γ	Lapse rate (°C km^{-1})
Γ_{700_850}	Lapse rate between 700hPa and 850hPa pressure level (°C km^{-1})
Γ_{700_925}	Lapse rate between 700hPa and 925hPa pressure level (°C km^{-1})
Γ_{850_925}	Lapse rate between 850hPa and 925hPa pressure level (°C km^{-1})
Γ_{E-OBS}	Lapse rate from E-OBS dataset (°C km^{-1})
Γ_{Kunkel}	Lapse rate from literature (°C km^{-1})
Δh	Elevation difference (m)
T^*	Surface temperature (°C)
Λ	Constant lapse rate -6.5 °C km^{-1}
T_l	Temperature at the lowest model level (°C)
p_{surf}	Surface pressure (hPa)
p_l	Lowest model level pressure (hPa)
T_x	290.5 K
T_y	255 K

z_2	Height of screen level observation (2 m)
z_l	Height of the lowest model level (m)
z_{0H}	Roughness length for heat (m)
z_{0HWMO}	Roughness length for heat at SYNOP station (m)
z_{0Q}	Roughness length for moisture (m)
z_{0QWMO}	Roughness length for moisture at SYNOP station (m)
ϕ_{surf}	Surface geopotential ($m^2 s^{-2}$)
δa_{evap}	Rate of decrease of cloud area due to evaporation
Ψ_M	The exchange coefficient for momentum at surface

Abbreviations

20CR	NOAA-CIRES 20th Century Reanalysis V2
4D-Var	Four-Dimensional Variational Assimilation
ASR	Arctic System Reanalysis
BPRC-PMG	Byrd Polar Research Center, Polar Meteorology Group
cdf	Cumulative distribution function
CFSR	NCEP Climate Forecast System Reanalysis
CHRM	An adaptation of HRM, Swiss Federal Institute of Technology (ETH)
COR	Weighted pattern correlation
CR	Corresponding Ratio
CRIEPI	The Central Research Institute of Electric Power Industry
CRU	Climate Research Unit
DD	Dynamical Downscaling
DKRZ	Deutsches Klimarechenzentrum
DWD	German Weather Service
ECA&D	European Climate Assessment and Dataset
ecdf	Empirical Cumulative distribution function
ECMWF	European Centre for Medium-Range Weather Forecasts
ENSEMBLES	Project from European Commission's 6th Framework Program
E-OBS	E-OBS gridded dataset from ECA&D
ERA-15	ECMWF Re-analysis 15 Project
ERA-40	ECMWF Re-analysis 40 Project
FLUXNET	Global Network of Micrometeorological Tower Sites

GCM	Global Climate Model or Global Circulation Model
GCOS	The Global Climate Observation System
GHCND	Global Historical Climatology Network
GISS	Goddard Institute for Space Studies at NASA
GKSS	Gesellschaft für Kommunikation, Schutz und Sicherheit
GLADS	Global Land Data Assimilation System
GMAO	Global Modeling and Assimilation Office
GPCC	Global Precipitation Climatology Centre
GSFC	Goddard Space Flight Center
GTS	Global Telecommunication System
HadGHCND	Gridded daily temperature dataset provided by Hadley centre.
HadRM3	Third generation RCM developed by the Hadley Centre
HIRHAM	Regional Atmospheric Climate model by Danish Meteorological Institute
ICTP	Abdus Salam International Centre for Theoretical Physics
IPCC	Intergovernmental Panel on Climate Change
JMA	The Japan Meteorological Agency
KNMI	Royal Netherlands Meteorological Institute
Lasso	Least absolute shrinkage and selection operator
LMDz4	Laboratoire de Meteorologie Dynamique zoom version 4
LOCI	Local Scaling
LWD	Bavarian Avalanche Warning Service
MAE	Mean absolute error
MAP	Mesoscale Alpine Program
MERRA	NASA Modern Era Reanalysis for Research and Applications
MM5	The fifth-Generation Penn State/NCAR Mesoscale Model
MOS	Model Output Statistic
MPIfM	Max Planck Institute for Meteorology
NASA	The National Aeronautics and Space Administration
NCAR	The National Center for Atmospheric Research
NCEP	The National Centers for Environmental Prediction
NSE	Nash-Sutcliffe efficiency coefficient
OLS	Ordinary least squares regression
OMR	Observation Minus Reanalysis
ORNL DAAC	The Oak Ridge National Laboratory Distributed Active Archive Center

PP	Prefect Prognosis
PWC	Physics of Weather and Climate Group
QM	Quantile-Mapping
RCA1	Rossby Centre regional Atmospheric model version I
RCM	Regional Climate Model
RegCM3	3-dimensional, sigma-coordinate, primitive equation regional climate model
REMO	Regional climate model developed by MPIfM, DKRZ, DWD and GKSS
RMSD	Normalized root-mean-square difference
RMSE	Root mean square error
RSS	Root of Sum of Squares
SD	Statistical Downscaling
SF	Scaling factor for LOCI
STD	Standard deviation
SYNOP	Surface synoptic observations
UKMO	U.K. Meteorological Office
WCRP	The World Climate Research Programme
WMO	World Meteorological Organization

Chapter 1

Introduction

1.1 Background and Motivation

1.1.1 Climate Change and Global Climate Models

Climate change is one of the most important long-term issues which the global community has to face over coming decades. Negative effects of climate change on nature and the human environment, such as temperature increasing and rising sea level have been observed (IPCC, 2007a; IPCC, 2007c). Therefore, accurate investigations and assessments of the impacts of climate change on natural and human systems are highly desired by decision makers and stakeholders (IPCC, 2007b).

Global Climate Models (or general circulation models, GCMs), the primary tool for weather forecasting, climate understanding, and projecting climate change for the future have been widely applied in the past decades (Gregory et al., 2001; Maraun et al., 2010; Schmidli et al., 2007; Snell et al., 2000; Wilby and Wigley, 2000; Xu, 1999). GCMs attempt to represent the past, present or future climate by simulating the general circulation of the atmosphere, and the oceans, as well as their interaction with powerful computer systems (IPCC, 2007c) (Figure 1.1). GCMs normally run on a 3-dimensional grid with a horizontal resolution of 250-600 km, 10 to 20 vertical layers in the atmosphere and approximately 30 layers in the oceans (e.g. Flato et al., 2000) (Figure 1.2).

However, the GCMs are currently unable to provide reliable information for decision makers and impact model developers, due to their coarse resolution (Dodson and Marks, 1997; Maurer et al., 2002; Minder et al., 2010). Specifically, for complex terrain, the GCMs only represent characteristics for a mean elevation of a grid box. In reality, the situations from high mountain crests to deep valleys differ considerably. Local processes, such as orographic precipitation formulation along mountain slopes, as well as snowpack accumulation and melting, are not represented by the coarse resolution. Although Regional Climate Models (RCMs) nested in GCMs represent better descriptions of local-scale characteristics, based on the finer spatial

resolution of 10-50 km, they still do not satisfy the requirements of hydrological and climatic impact models, which typically run on the scale of 0.1-1 km (Ahrens, 2003; Charles et al., 2004; Maraun et al., 2010; Mauser and Bach, 2009; Xu, 1999). Also, RCMs would require very expensive and bring complex computer calculations, making this approach unavailable for many potential users.
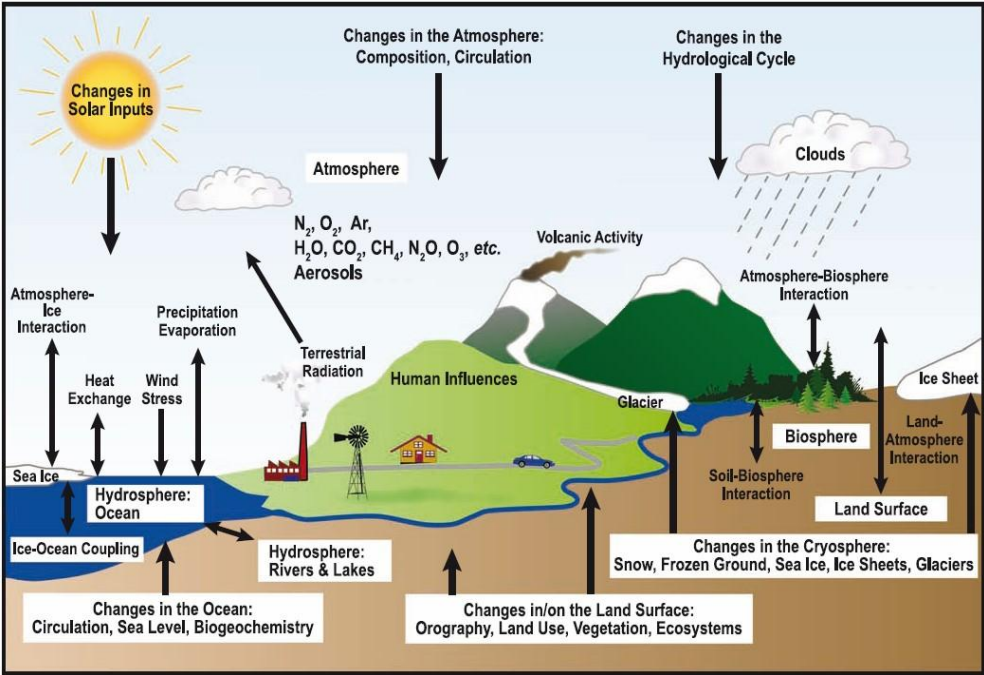
Figure 1.1: Schematic of physical processes in Global Climate Models (IPCC, 2007c).
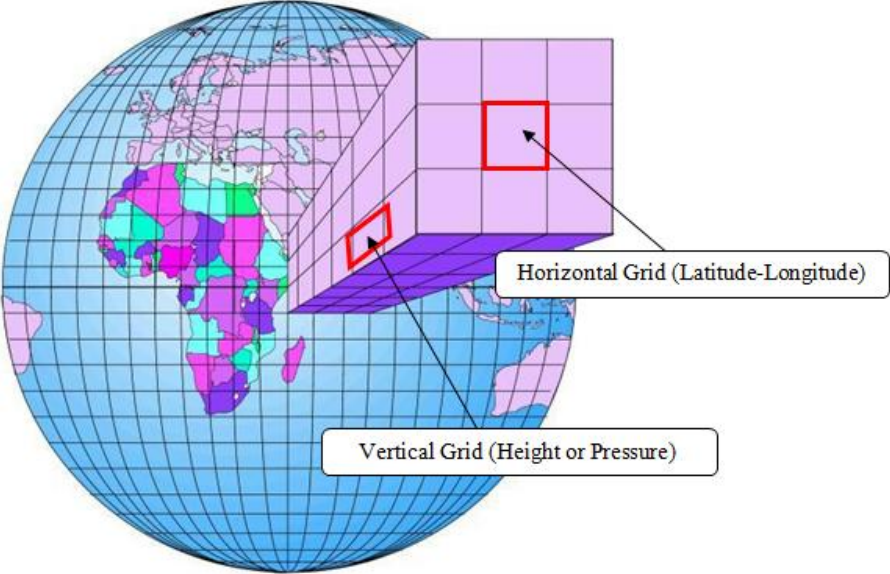
Figure 1.2: Schematic of Global Climate Models spatial resolutions.

Motivated by the requirements for finer spatial resolution in impact modeling, the scientific community has paid much attention to resolving the scale discrepancy between coarse model data and finer local requirements (Bardossy and Plate, 1992; Charlton et al., 2006; Guan et al., 2009; Hertig and Jacobeit, 2008; Spak et al., 2007). Downscaling procedures – the disaggregation of larger scale mean values to sub-grid smaller scale values – can be used to overcome the deficits of the coarse scale models and to generate meaningful information for areas without meteorological measurements (Maraun et al., 2010; Wilby and Wigley, 1997; Xu, 1999; Zorita and von Storch, 1999). Figure 1.3 schematically illustrates the theoretic scaling processes. Dynamic atmosphere and ocean processes, as well as hydrology, land use, topography and social systems, are considered within the scaling framework.
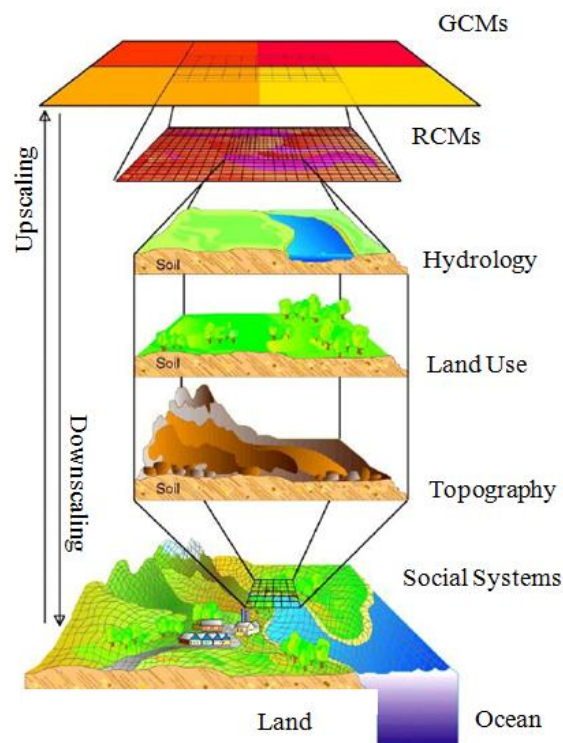
Figure 1.3: Schematic for a theoretic downscaling and upscaling framework, modified from Viner and Hulme (1997).

Downscaling techniques are classified into two main categories: dynamical downscaling (DD) and statistical downscaling (SD). In the past two decades, DD (e.g. Almazroui, 2012; Haensler et al., 2011) and SD (e.g. Hofer et al., 2010; Huth et al., 2008) have been widely implemented; however, an universal method for various variables and complex terrains is still lacking.

Reanalysis products, surrogates for large-scale observations, have been increasingly applied to assess climate impact in the last decade, because they most closely estimate the state of real

atmosphere and land surface characteristics (Decker et al., 2012; Simmons et al., 2010). However, they are still too coarse for use in the finer spatial resolution of climate and hydrology models (Ahrens, 2003).

In summary, accurate downscaling GCMs and reanalysis data in complex terrain is still a major challenge for alpine areas. To meet this challenge, this dissertation attempts to i) evaluate and validate a newly generated reanalysis dataset, the ERA-Interim produced by European Centre for Medium-Range Weather Forecasts (ECMWF), ii) develop a robust temperature downscaling approach which is independent of observations in mountainous areas, iii) introduce a precipitation downscaling method based on machine learning in complex terrain, iv) validate ERA-Interim in various regions, including large urban area and various vegetation covers, and v) illustrate an example of ERA-Interim application in a socio-economic context.

1.1.2 Downscaling Methods Overview

1.1.2.1 Dynamical Downscaling

Dynamical Downscaling (DD, i.e. RCMs) is one downscaling method that is driven by boundary conditions derived from a GCM at high-resolution for a limited area (Wilby and Wigley, 1997). Compared with GCMs, DD uses two approaches to achieve a better representation of orographic effects, land-sea contrast, and land surface characteristics, with the help of finer spatial resolution and reduced model time step (Giorgi, 2008; Rummukainen, 2010). One approach is straightforward and uses a high-resolution atmospheric global model (Christensen et al., 2007); the second approach uses a coarse global model with dense variable-resolution grids in limited-areas (Lal et al., 2008).

RCMs have some advantages that are absent in GCMs, such as more detailed local scale characteristics. However, large sets of simulations cannot be achieved. Additionally, some limitations constrain the model's accuracy. Firstly, the quality of DD relies on the accurate representation of boundary conditions, which include temperature, moisture, and wind speed, amongst others. Secondly, GCMs-driven RCMs inherit the systematic bias of boundary conditions from GCMs, because of the non-local physical process forcing (Maraun et al., 2010; Rummukainen, 2010). Reanalysis-driven RCMs reduce biases because observations are assimilated into the reanalysis system. Unfortunately, model evaluations are limited by the availability of independent observations. Even though RCMs run with a higher spatial resolution, they are still more homogenous in space, compared to actual observations (Rummukainen, 2010).

Thirdly, a quite important drawback of RCMs is their high computational demand (Wilby et al., 2004; Wilby and Wigley, 1997). Although RCMs yield better results by using finer temporal-spatial resolution, the computation requirements rise accordingly. Expensive computation adversely limits the number of grids, spatial resolution, and length of time period under investigation (Maraun et al., 2010; Rummukainen, 2010). At present, many RCMs are available that have been developed by various research institutes over the world. Table 1.1 shows a small selection of previous studies using RCMs.

Table 1.1: Literature review of dynamical downscaling studies.

RCMs	Predictand	Boundary forcing	Vertical/horizontal resolution	Region	Reference
REMO	2 m temperature Seasonal precipitation	ERA-40	20-level/18 and 50 km	South African	(Haensler et al., 2011)
HadRM3 and CHRM	Seasonal heavy precipitation	HadAM3 HRM	19-level/50 and 20-level/55 km	United Kingdom	(Haylock et al., 2006)
RCA1	Monthly Precipitation	HadCM2 ECHAM4	19-level/44 km	Sweden	(Hellstrom et al., 2001)
ECHAM4/ ECHAM5	Annual Rainfall	NCEP Reanalysis	19-level/T42 and 23-level/T63	Southern Morocco	(Huebener and Kerschgens, 2007)
CHRM, HadRM3 and HIRHAM	Daily precipitation	HRM, HadAM3 and HIRHAM4	20-level/0.5°, 19-level/0.44° and 19-level/0.44°	European Alps	(Schmidli et al., 2007)
MM5	Monthly Surface temperature	GISS-GCM	20-level /36 km	North America	(Spak et al., 2007)
LMDz4	Summer rainfall	ERA-40	19-level/stretched grid, 120 points in longitude and 91 points in latitude	Eastern China	(Zou et al., 2010)
UKMO Model	Monthly temperature precipitation	GCM	19-level/0.44° and 19-level/2.5°×3.75°	Europe	(Murphy, 1999)

1.1.2.2 Statistical Downscaling

Statistical Downscaling (SD) is another form of downscaling that is based on the statistical relationship between large-scale variables (e.g. surface pressure from GCMs) and local-scale variables (e.g. temperature at a particular site). The established relationship is then used to yield

the local variables from large-scale outputs (Wilby and Wigley, 1997). The main assumptions of SD methods include: predictors from large-scale data should be skillfully and adequately reproduced; the relationships between predictands and predictors remain valid for periods outside the fitting period, especially for future climate scenarios (Harpham and Wilby, 2005; Wilby et al., 2002; Wilby and Wigley, 1997). Compared to DD, SD methods have lower computational demands and they provide site-specific information in an easier way (Wilby et al., 2002; Wilby et al., 2004; Wilby and Wigley, 1997; Huth, 2004).

Table 1.2: A summary of the strengths and weaknesses of the main statistical downscaling methods, modified from Wilby et al. (2004).

Methods	Strengths	Weaknesses	Examples
Weather typing (e.g. analogue method, hybrid approaches, fuzzy classification, self organizing maps, Monte Carlo methods)	1. Yields physically interpretable linkages to surface climate 2. Versatile (e.g. can be applied to surface climate, air quality, flooding, erosion, etc.) 3. Compositing for analysis of extreme events	1. Requires additional task of weather classification 2. Circulation-based schemes can be insensitive to future climate forcing 3. May not capture intra-type variations in surface climate	(Alexander et al., 2009; Bardossy et al., 2005; Vrac et al., 2007; Yin et al., 2011;)
Weather generators (e.g. Markov chains, stochastic models, spell length methods)	1. Production of large ensembles for uncertainty analysis or long simulations for extremes 2. Spatial interpolation of model parameters using landscape 3. Can generate sub-daily information	1. Arbitrary adjustment of parameters for future climate 2. Unanticipated effects to secondary variables of changing precipitation parameters	(Charles et al., 2004; Greene et al., 2011; Mehrotra and Sharma, 2005)
Regression methods (e.g. linear/non-linear regression, neural networks, canonical correlation analysis, kriging)	1. Relatively straightforward to apply 2. Employs full range of available predictor variables 3. "Off-the-shelf" solutions and software available	1. Poor representation of observed variance 2. May assume linearity and/or normality of data 3. Poor representation of extreme events	(Harpham and Wilby, 2005; Huth et al., 2008; Schoof and Pryor, 2001; Stahl et al., 2006)

SD methods are classified according to several perspectives. Wilby and Wigley (1997) and Wilby et al. (2004) grouped SD methods into three categories: weather classification schemes, regression models, and weather generators. An alternative classification was presented by Rummukainen (1997) and based on the nature of predictors, namely, prefect prognosis (PP) and model output statistics (MOS). Wilby et al. (2004) have summarized the advantages and drawbacks of three SD methods (Table 1.2).

Regression methods are widely used because they are simple and easy to implement. Multiple regression (Murphy, 1999), canonical correlation analysis (Vonstorch et al., 1993), and artificial neural networks (Cannon, 2007; Crane and Hewitson, 1998) are most frequently applied. Support vector machines based on machine learning algorithms, are becoming popular (Anandhi et al., 2009; Chen et al., 2010; Kumar et al., 2008; Kumar et al., 2009). Based on their strengths, this study used regression methods for temperature and precipitation downscaling. To avoid repetition, the applied temperature and precipitation downscaling methods are described in Chapters 4 and 5, respectively.

1.1.3   Reanalysis Data – State of the Art

Reanalysis data is produced by a data assimilation project that incorporates observations into a computer model of the atmospheric, land surface, and ocean real system. Data assimilation is implemented by analysis cycles. In each analysis cycle, the current (or past) observations are combined with the results from a forecast model (e.g. numerical weather prediction model). The uncertainty and bias between observations and forecasts are balanced and optimized in this step, and then the advanced model yields new forecasts that are brought into next analysis cycle (Figure 1.4).
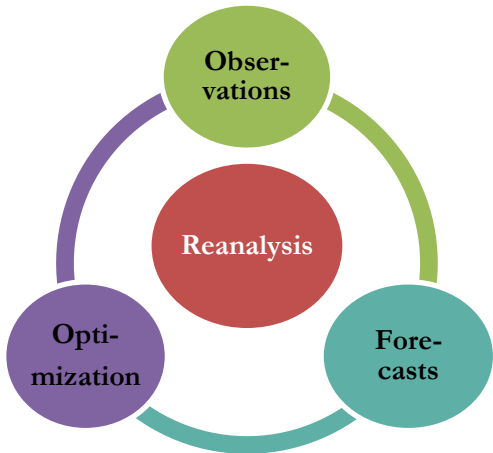
Figure 1.4: General view of the reanalysis process.

At present, reanalysis products are provided by four major centers: the National Centers for Environmental Prediction/National Center for Atmospheric Research (NCEP/NCAR), the European Centre for Medium-Range Weather Forecasts (ECMWF), the National Aeronautics and Space Administration (NASA) Goddard Space Flight Center (GSFC), and the Japan Meteorological Agency (JMA) & the Central Research Institute of Electric Power Industry (CRIEPI). Table 1.3 summarizes the main available reanalysis productions. More details including model descriptions can be found in the relevant references.

The key strengths that reanalysis products contain are: i) data is multivariate, spatially and temporally completed and gridded; ii) observations are assimilated; iii) data is physically and dynamically modeled. In the past two decades, reanalysis products have been increasingly applied in climate impact studies. Typically, they are adopted to provide boundary conditions for regional climate models. Although reanalysis products generally estimate the closest state of the real atmosphere and of land surface characteristics (Decker et al., 2012; Simmons et al., 2010), there are some uncertainties in the reanalysis data, such as observation changes and model misrepresentation. Therefore, the quantification of uncertainty and the evaluation of the quality of reanalysis data is still a great challenge (Bosilovich et al., 2008; Trenberth et al., 2008).

Table 1.3: Main available reanalysis products.

Production	Time Period	Producer	Reference
NCEP/DOE Reanalysis II	1979-present	NCEP/NCAR	(Kanamitsu et al., 2002)
NCEP/NCAR Reanalysis I	1948-present	NCEP/NCAR	(Kalnay et al., 1996)
ERA-15	1978-1994	ECMWF	(Gibson et al., 1996)
ERA-40	Sep. 1957- Aug.2002	ECMWF	(Uppala et al., 2005)
ERA-Interim	1979-present	ECMWF	(Dee et al., 2011; Simmons et al., 2006)
CFSR	1979-2011	NASA & GSFC	(Saha and Coauthors, 2010)
JRA-25	1979-2004	JMA & CRIEPI	(Onogi et al., 2007)
JCDAS	2005-present	JMA	
ASR	2000-2011	OSU & BPRC-PMG	(Bromwich et al., 2009; Hines and Bromwich, 2008)
MERRA	1979-present	NASA	(Rienecker et al., 2011)
20CR	1871-2010	NOAA & NCEP	(Compo et al., 2011)

ERA-Interim is the newest-generation reanalysis product from the ECMWF, with an improved atmospheric model and assimilation systems. ERA-Interim provides data from 1979 onwards, and continues in real time (Berrisford et al., 2009; Dee et al., 2011). The ERA-Interim project was launched in order to improve key aspects of ERA-40, such as the representation of the hydrological cycle, the quality of the stratospheric circulation, as well as the handling of biases and changes in the observing system (Dee and Uppala, 2009; Dee et al., 2011; Simmons et al., 2006; Uppala et al., 2008). This has been achieved by including many model improvements, such as the use of 4-dimensional variation (4D-Var) analysis, a revised humidity analysis, the use of bias correction for satellite data, and further improvements in data handling (Berrisford et al., 2009; Dee et al., 2011). Figure 1.5 shows the schematic of the revised 4D-Var solution algorithm implemented in CY25r4 (a version of ECMWF's Integrated Forecast System released in 2003). 4D-Var includes an inner loop and an outer loop, which perform at lower resolution by using tangent-linear forecast model (first T95, then T255 resolution) and at high resolution by using a non-linear model (T799 resolution), respectively (ECMWF, 2009a). The truncation operator is used to interpolate trajectory fields from high to low resolution. The cost function is used for measuring the distance between the model trajectory and background or observations in an assimilation window (ECMWF, 2009a).
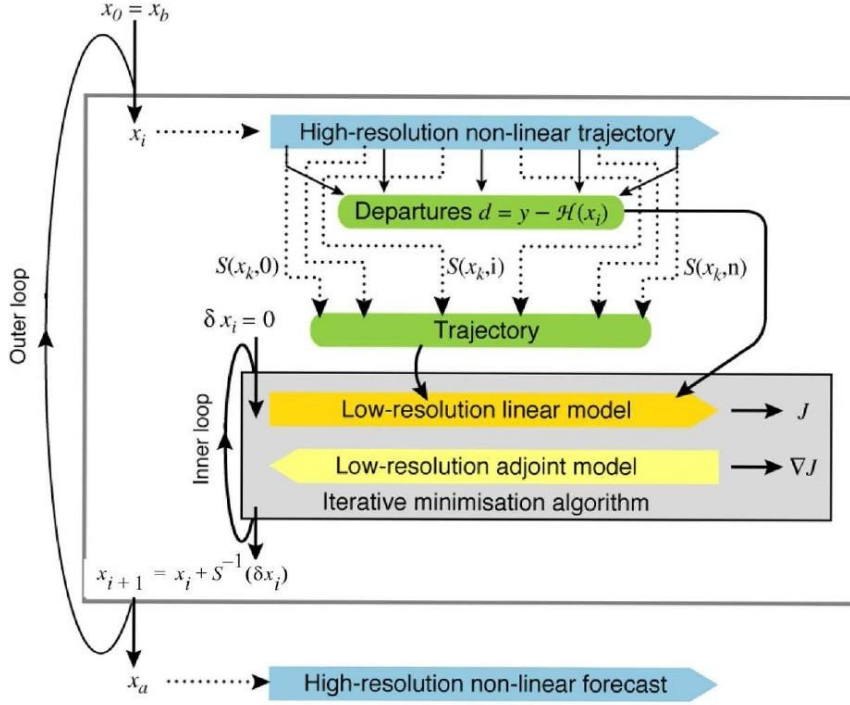
Figure 1.5: Schematic of the revised 4D-Var solution algorithm implemented in CY25r4. S denotes the truncation operator which takes the trajectory fields from high to low resolution, J the cost function and ∇J the gradient of J. x indicates the atmospheric state vector, i the time index and k the variable index. x_b is the initial input, and x_a is the result of the loop. δx_i is the analysis increment, and $S^{-1}(\delta x_i)$ is the minimum increment of δx_i. d is the innovation vector, and y is the observation vector. $H(x_i)$ indicates the observation operator with low-resolution in the vicinity of x_i (ECMWF, 2009a).

Figure 1.6 illustrates the schematic of the data assimilation cycling with the operational early-delivery configuration. In the delayed cut-off 12-hour 4D-Var computation, 0000 UTC and 1200 UTC analysis are implemented separately. Observations in the time window 2101-0900 UTC are used for 0000 UTC analysis, while observations in the window 0901-2100 UTC are used for 1200 UTC analysis. A separate surface analysis is run every 6 hours at 0000 UTC, 0600 UTC, 1200 UTC and 1800 UTC. 4D-Var computation and surface analysis are combined for the final analysis. The three-hour forecasts are obtained from 0000 UTC 12-hour 4D-Var analysis based on the previous day's 1800 UTC delayed cut-off analysis, and the forecasts from 1200 UTC analysis are obtained from the 0600 UTC. This propagates forwards day to day (ECMWF, 2009a). The early-delivery analysis is implemented every 6 hours. The observations in the time window 2101-0300 UTC and 0901-1500 UTC are possible maxima used for 0000 UTC and 1200 UTC 6-

hour 4D-Var analysis. The 3-hour 10 days forecasts are obtained from 6-hour 4D-Var analysis, combined with the separate surface analysis.
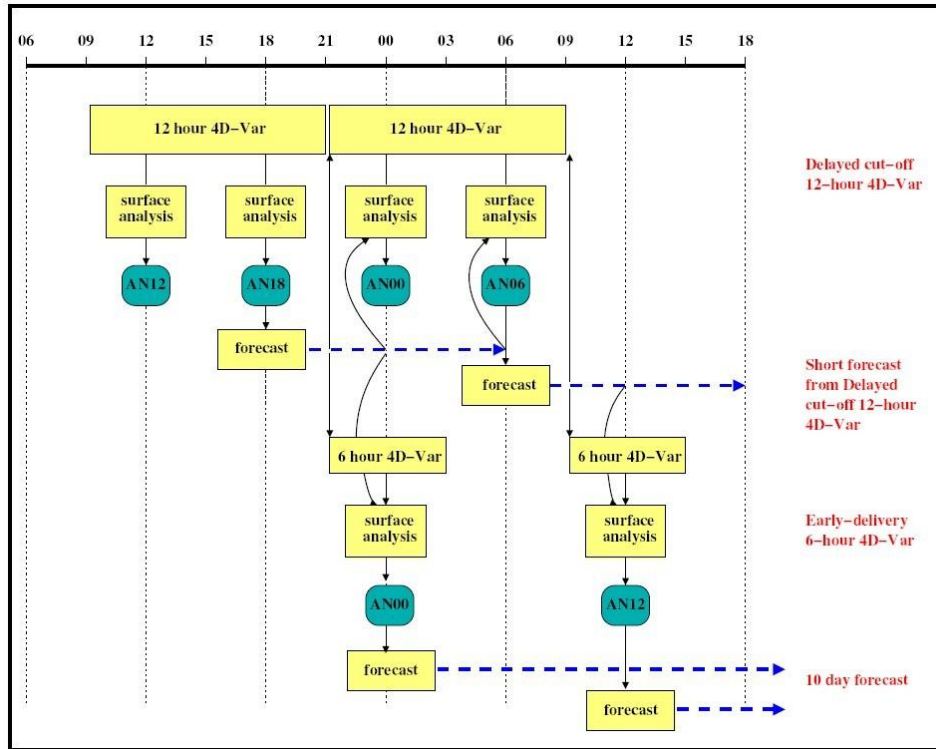
Figure 1.6: Schematic of data assimilation cycling with the operational early-delivery configuration (ECMWF, 2009a). Yellow means computation steps, and blue data sets.

1.2 Research Objectives

1.2.1 Outline

Air temperature and precipitation are the most relevant variables for hydrological modeling, and they are particularly important for mountainous climate, snow, glacial, and permafrost research (Maraun et al., 2010; Schmidli et al., 2007; Xu, 1999). Conventionally, temperature and precipitation are collected from meteorological networks. Nevertheless, due to sparse observations in complex terrains, particularly at high altitudes such as in mountains, these two variables are difficult to obtain, because of difficulties with the installation and maintenance of the stations (Clark and Slater, 2006; Guan et al., 2005; Kunkel, 1989; Pages and Miro, 2010; Rolland, 2003). This work attempts to downscale new reanalysis data (ERA-Interim) for air temperature and precipitation in high mountainous areas, i.e. in the central Alps. Meanwhile, the temperature downscaling method is validated for FLUXNET sites over Europe.

This thesis is structured into five main chapters. Firstly, the usage of ERA-Interim Reanalysis data is investigated in the mountainous areas in Chapter 3. Then, a robust statistical downscaling approach for temperature is presented in Chapter 4, followed by a new precipitation downscaling method in Chapter 5. Subsequently, the validation of the downscaling method using data from micrometeorology station and an application example related to socio-economic work is illustrated in Chapter 6 and 7, respectively. Finally, Chapter 8 gives an overall discussion and outlook for further research activities. The preceding Chapter 2 describes the data resources. A brief description of the core five chapters are presented in the following.

1.2.2 Evaluation of ERA-Interim Reanalysis Data

Generally, GCMs are the primary data resource for downscaling, especially for RCMs. Reanalysis data, currently used as the surrogate for large-scale observations, has been widely applied in downscaling methods such as ERA-40 and NCEP/NCAR reanalysis data (Maraun et al., 2010; Mooney et al., 2011; Poli et al., 2010). Reanalysis data was designed to estimate the closest state of real atmosphere and land surface characteristics with the assimilation of large numbers of observations, which cover complete global and temporal data series. Although reanalysis products are improving, previous studies showed that these products contain errors, due to a variety of reasons, e.g. observation errors and interpolation errors. Therefore, it is of major importance to evaluate reanalysis data against observations before applying them to climate and hydrological models (Berg et al., 2003; Decker et al., 2012; Trenberth and Guillemot, 1998). In Chapter 3, E-OBS, a new observed gridded dataset that interpolated a high density of observations over Europe with finer spatial resolution ($0.25° \times 0.25°$) is employed to compare with ERA-Interim 2 m temperature and daily total precipitation data. The bias, as well as the elevation dependence of temperature and precipitation is analyzed.

1.2.3 Temperature Downscaling

A novel method that uses ERA-Interim internal lapse rates for near-surface temperature downscaling in high mountain regions is developed in Chapter 4. This study distinguishes itself from the previous research by i) rejecting the use of the fixed lapse rate (e.g. -6.5 °C km^{-1}) and lapse rates from the literature (Kunkel, 1989), which are unable to capture the variability of temperature in high mountain regions; ii) allowing for data reproduction for remote alpine areas where no meteorological station exists; iii) making the method flexible and easy to implement with the help of the linear regression framework; and iv) allowing for the varied spatial resolution downscaling based on a variety of elevation data.

1.2.4   Precipitation Downscaling

Precipitation downscaling is much more difficult than temperature due to its higher spatial and temporal variability, especially in complex terrains (Barry, 2008; Guan et al., 2009). Although many downscaling methods have been tested, a universal best method does not exist. In Chapter 5, a new and powerful machine learning technique, "Lasso" (Least absolute shrinkage and selection operator), which has the advantage of dealing with large numbers of variables, is explored for downscaling daily total precipitation at 50 meteorological stations in the central Alps. In order to evaluate the performance of the Lasso algorithm, benchmark methods, such as local scaling (LOCI) and quantile-mapping (QM), which are the most frequently used methods for climate impact studies, are applied for model comparison. Additionally, stepwise regression, which uses the same variables, is applied to evaluate the ability of Lasso to deal with the selection of variables.

1.2.5   Validation of ERA-Interim for FLUXNET Data

In Chapter 6, 48 FLUXNET tower sites located in the expanses of land with varying topography and vegetation covers and climate regimes over Europe are applied to validate ERA-Interim data and temperature downscaling methods. FLUXNET is a global network that covers a collection of micrometeorological flux observation sites, measuring the exchanges of carbon dioxide, water vapor, and energy between the biosphere and atmosphere, using eddy covariance methods, but also standard climate data including temperature, relative humidity, precipitation, and radiation components (Baldocchi et al., 2001; Gu and Baldocchi, 2002). Besides temperature, 3-hourly ERA-Interim precipitation data is also validated by FLUXNET data.

1.2.6   ERA-Interim Application - A Case Study

The world's largest motor vehicle manufacturer, the "Volkswagen Group" and its subsidiary company "AUDI AG" recognized that temperature distribution and extremes affect the automobiles' technical design features, such as the engine cooling system and coolant additives. Besides, this information is urgently needed for their marketing planning. However, there are some difficulties in data collection for their imperative needs, in the global context. For example, weather stations are not widely available, especially in the developing countries, which correspond with the rapidly emerging markets. ERA-Interim forecast data with significantly strengths for the long-term (32 years) and with high temporal resolution (3-hourly) is highly desirable. Within a Matlab and GIS framework, the temperature distribution and extremes of ERA-Interim are analyzed and presented visually. As the main markets, the accuracy of ERA-

Interim data for large cities is much important. Therefore, nine large city temperature measurements over Europe are applied for validation of ERA-Interim temperature data. This validation provides the information on the reliability of ERA-Interim data in this socio-economic context.

Datasets

2.1 Overview

Throughout this thesis, data from six sources are applied: individual meteorological measurements provided by the German Weather Service (DWD), the Bavarian Avalanche Warning Service (LWD), the European Climate Assessment & Dataset (ECA&D), and the Swiss Federal Office of Meteorology and Climatology (MeteoSwiss); individual micrometeorological measurements provided by FLUXNET; gridded observations (E-OBS) provided by ECA&D, and the Global Precipitation Climatology Centre (GPCC) gridded data provided by DWD; reanalysis data (ERA-Interim) developed by the European Centre for Medium-Range Weather Forecasts (ECMWF). In this chapter, each dataset is briefly introduced and data processing methods are specifically explained in the corresponding chapters.

2.2 DWD and LWD Data

In this study, the observations from two meteorological stations (Zugspitze and Garmisch) operated by the German Weather Service (DWD), as well as one station (Zugspitzplatt) operated by the Bavarian Avalanche Warning Service (LWD) are used for downscaling tests. All three test sites are located in the southern part of Germany, at the Austrian border. The Garmisch site is located at the bottom of a valley (Garmisch-Partenkirchen 719m a.s.l.); the Zugspitze site is close the crest of the Zugspitze mountain (2964m a.s.l.) and the Zugspitzplatt site (2250m a.s.l.) is located on the side of the mountain (Figure 2.1). The DWD provides hourly data, while the LWD operates at 10-minute resolution. The data was aggregated to 3-hourly (T_{3h}) and daily (T_d) averages for comparison with the ERA-Interim data described in Chapter 4.
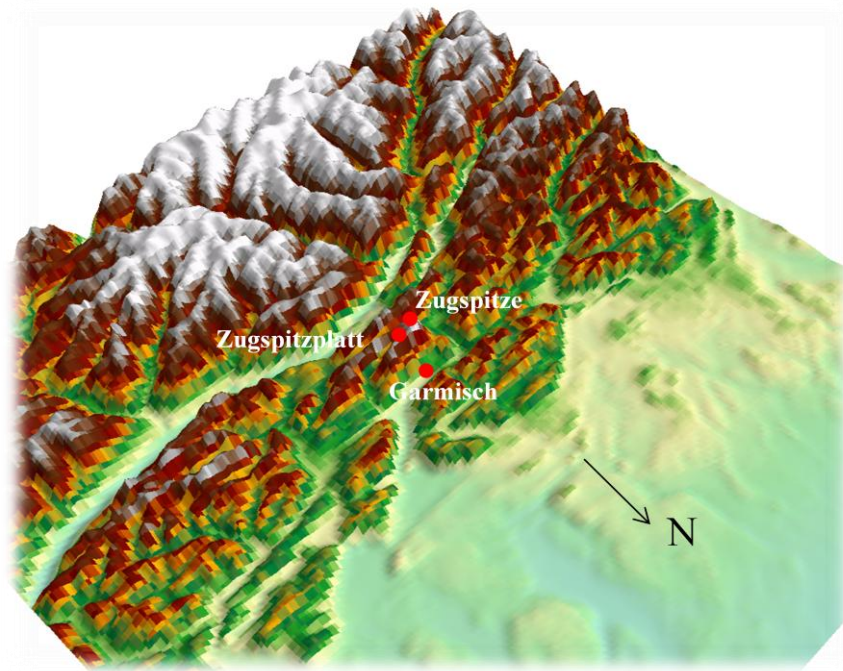
Figure 2.1: Locations of the DWD and LWD observation sites.

2.2 MeteoSwiss Data

MeteoSwiss (the Swiss Federal Office of Meteorology and Climatology) provides extensive archive data from its ground level monitoring networks. Registered users can directly access the archive through an interactive tool (IDAWEB). The observation data from the beginning of the monitoring activities until the preceding day can be obtained in two formats: CSV and Bulletin. The main available climatological and meteorological parameters include: cloud cover, lightning, ground temperature, vapor pressure, global radiation, atmospheric pressure, air humidity, air temperature, precipitation, snow, sunshine duration, wind force, and wind speed. Several temporal resolutions data can be freely downloaded, 10-minute, hourly, daily, monthly, annual. For hourly data, the measuring and observing time is HH = (HH-1): 41 - HH: 40, for example, 13 = observation period 12:41 to 13:40. MeteoSwiss also provides the calendar data by data interpolation and time shifting (MeteoSwiss, 2013). In this study, hourly air temperature and daily total precipitation is obtained and further processed for downscaling applications. The detailed process information and the stations used are given in Chapter 4 and 5.

2.3 ECA&D Data

The ECA&D (European Climate Assessment & Dataset) project focused on the changes in weather and climate extremes, as well as on the daily dataset needed to monitor and analyze these extremes. This project was initiated by the European Climate Support Network (ECSN) and supported by the Network of European Meteorological Services (EUMETNET). Currently, ECA&D provides a dataset containing 36959 series of observations for 12 elements at 7847 meteorological stations throughout Europe and the Mediterranean from 61 participants in 62 countries (ECA&D, 2013, Klein Tank et al., 2002). The 12 elements include maximum, minimum, mean temperature, sunshine, snow depth, precipitation amount, humidity, wind gusts, wind speed, wind direction and cloud cover. Nine large city sites used for validation of ERA-Interim are listed in Chapter 7. Detailed site information is given in Chapter 7.

2.4 FLUXNET Data

FLUXNET is a global collection of micrometeorological flux observation sites, measuring the exchanges of carbon dioxide, water vapor, and energy between the biosphere and atmosphere, using eddy covariance methods, but also standard climate data including temperature and precipitation (Baldocchi et al., 2001; Gu and Baldocchi, 2002). The FLUXNET database is maintained by the Oak Ridge National Laboratory Distributed Active Archive Center (ORNL DAAC).
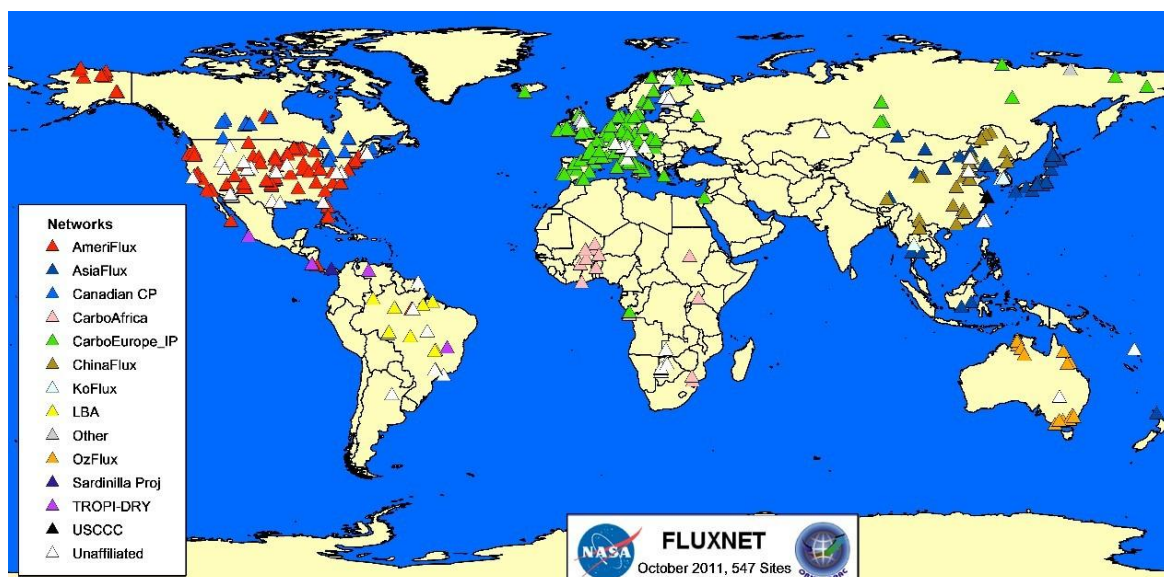
Figure 2.2: Locations of the FLUXNET site towers and their organizational affiliation (FLUXNET, 2013).

At present, more than 500 tower sites across five continents are operating on a long-term basis covering a large variety of climates and biomes (Figure 2.2). The LaThuile dataset is one of the FLUXNET synthesis data products, and currently includes data from approximately 250 sites, which is available under a "free fair-use" policy (Fluxdata, 2013). From this dataset, 48 sites located in Europe and having a continuous record of at least 2 years have been chosen for ERA-Interim validation. For more details see Chapter 6.

2.5 E-OBS Data

The European daily high-resolution gridded dataset of surface temperature (mean, minimum and maximum) and precipitation (E-OBS) was developed as part of the European Union Framework 6 ENSEMBLES project, with the objective of validating RCM models for climate change studies (Haylock et al., 2008). The E-OBS dataset was produced for representing the best estimates of grid box averages. Gridded 0.25° and 0.5° latitude/longitude data is available, as well as a 0.22° and 0.44° rotated pole grid with the North Pole at 39.25N, 162W (E-OBS, 2013). The available data covers a large area (all of Europe, without oceans) and a long time period (1950-present).

The E-OBS dataset was produced from large number of observations. Daily observations of maximum, mean and minimum temperature, and precipitation were collected since 1950 by the Royal Netherlands Meteorological Institute (KNMI), which also is in charge of European Climate Assessment and Dataset (ECA&D). The number of observation stations increased from 250 at the beginning to currently more than 2300 by incorporation with other datasets, such as GCOS (Global Climate Observing System), GHCND (Global Historical Climatology Network), and MAP (Mesoscale Alpine Program) (Haylock et al., 2008). The quality of the raw observations was controlled and suspicious records were eliminated, based on the criteria of, for example, less than zero and more than 300 mm for precipitation and temperatures higher than 60 °C (Haylock et al., 2008). The measured time at some stations was shifted forwards or backwards by one day between different countries. Maximum and minimum temperatures were calculated from 0000, 0600, 1200 and 1800 UTC. Precipitation was assumed to be measured at 0900 UTC and 0.5 mm threshold was defined for dry/wet day. The values of 0000 and 0600 UTC on the second day were added to 1200 and 1800 UTC values on the first day for the first day record (Haylock et al., 2008).

E-OBS has significant advantages including high spatial resolution, long-term period, uncertainty estimation incorporation and a novel interpolation method. The 0.25° grid of E-OBS is much

finer than that of HadGHCND (Caesar et al., 2006), which has global gridded daily data projected on a much coarser 2.5° latitude by 3.75° longitude grid as well as that of the MARS-STAT database, which is based on a 50 km grid. The E-OBS covers a long-term period from 1950 to the present, whilst HadGHCND data only spans the period of 1946-2000, and MARS-STAT only started in 1975. Although Alpine precipitation gridded data (Frei and Schar, 1998) was developed at a spatial resolution of 25km, it was only available for the period 1971-1990.

Given its strengths, this study applied the E-OBS dataset to evaluate ERA-Interim data. Daily maximum, mean and minimum temperature, and precipitation on a 0.25°×0.25° spatial resolution from E-OBS version 6.0, which was released in April 2012 and which covers the period from 1950-2011, was retrieved from E-OBS datasets. This evaluation is specifically illustrated in Chapter 3.

2.6 GPCC Data

The GPCC data is a contribution of the German Weather Service (DWD) to the World Climate Research Program (WCRP) and to the Global Climate Observation System (GCOS) (Schneider et al., 2011). GPCC represents long-term monthly land surface precipitation derived from rain-gauges built on the Global Telecommunication System (GTS) and from historic data for global and regional climate monitoring and research (Meyer-Christoffer et al., 2011). GPCC data is available on a regular latitude/longitude grid with a spatial resolution of 0.25°, 0.5°, 1.0°, and 2.5°. In this study, GPCC Climatology Version 2011, based on the 67,200 stations world-wide that have record durations of 10 years or longer for the target reference period January 1951 to December 2000 is applied for the evaluation of the ERA-Interim precipitation product. The data can be downloaded via: ftp://ftp.dwd.de/.

2.7 ERA-Interim Reanalysis Data

The European Centre for Medium-Range Weather Forecasts (ECMWF), located in Reading in the United Kingdom, is an intergovernmental organization that provides operational medium- and extended-range forecasts for 34 states (ECMWF, 2013). ECMWF not only provides the state-of-the-art super-computing facility for scientific research, but also collaborates with other agencies, such as satellite agencies and the European Commission, in scientific and technical matters. In the past, ECMWF has issued three major reanalysis data products: FGGE, ERA-15, and ERA-40. ERA-15 was generated from December 1978 to February 1994 at spectral T106

resolution with 31 vertical hybrid levels (ECMWF, 2013). The extended reanalysis data ERA-40 was generated from September 1957 to August 2002, and has been extensively utilized for atmospheric and oceanic processes. ERA-40 was assimilated at T159 spectral resolution (1.125 ° × 1.125 °) with 60 vertical hybrid levels. The results were projected on a reduced Gaussian grid (N80) with an almost uniform spacing of ~125km, the same as for ERA-15 (Uppala et al., 2005). As the second generation of reanalysis data, ERA-40 is superior to ERA-15, which has been well illustrated by Uppala et al. (2005).

Based on ERA-40, ERA-Interim represents a third generation reanalysis product with an improved atmospheric model and assimilation system. ERA-Interim provides data from 1979 onwards, and continues in real time (Berrisford et al., 2009; Dee et al., 2011). The ERA-Interim project was launched in order to improve key aspects of ERA-40, such as the representation of the hydrological cycle, the quality of the stratospheric circulation, as well as the handling of biases and changes in the observing system (Dee and Uppala, 2009; Dee et al., 2011; Simmons et al., 2006; Uppala et al., 2008). This has been achieved by including many model improvements, such as the use of 4-dimensional variation analysis, a revised humidity analysis, the use of variation bias correction for satellite data, and other improvements in data handling (Berrisford et al., 2009; Dee et al., 2011). Cycle 31r2 of ECMWF's Integrated Forecast System (IFS) was used for the ERA-Interim product. In this configuration, the model comprises 60 vertical levels, with the top level at 0.1 hPa; it uses the T255 spectral harmonic representation for the basic dynamical fields and a reduced Gaussian grid (N128, Figure 2.3, see section A.1) with an approximately uniform spacing of 79 km (Dee et al., 2011; Uppala et al., 2008). For more detailed model description, see the series report of ECMWF (ECMWF, 2013).

The atmospheric component is coupled to an ocean-wave model resolving 30 wave frequencies and 24 wave directions at the nodes of its reduced 1°×1° latitude/longitude grid. ERA-Interim assimilates four analyses per day at 00, 06, 12 and 18 UTC. Furthermore, two 10-day forecasts with a 3-hourly resolution are initialized on the basis of the 00 UTC and 12 UTC analyses. Observations from 15 UTC of the previous day to 03 UTC on the present day are used for the 00 UTC analyses, and observations from 03 UTC to 15 UTC are used for 12 UTC analyses (Dee et al., 2011; Uppala et al., 2008). ECMWF provides a variety of data in uniform lat/long grids (0.25°, 0.5°, 0.75°, 1°, 1.125°, 1.5°, 2°, 2.5° and 3°). The parameters (excepting vegetation, soil type fields, and wave 2D spectra) are interpolated from the original N128 reduced Gaussian grid using bilinear methods. Due to the limited scope of this dissertation, only the main research

targets - temperature and precipitation - are introduced briefly in the next two sections, based on an ECMWF technical series report (ECMWF, 2009b).
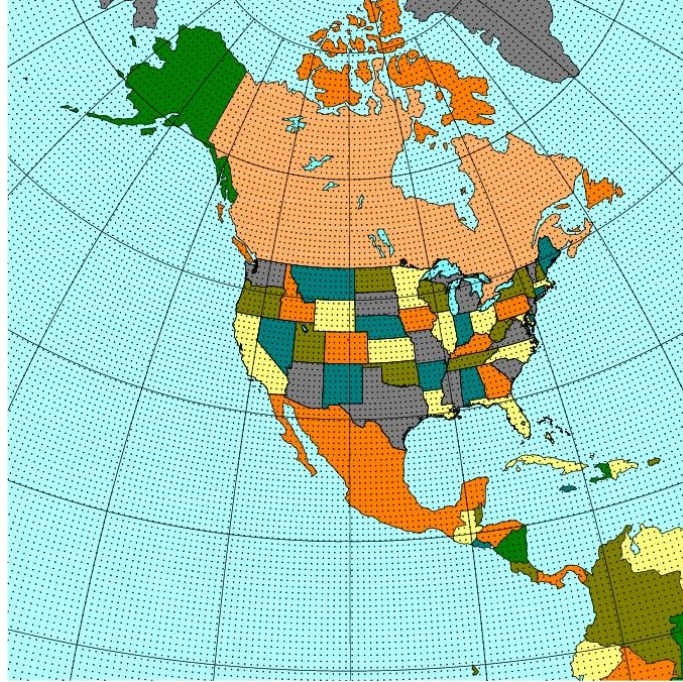
Figure 2.3: Reduced Gaussian Grid N128.

2.7.1   2 m Temperature

In the ERA-Interim model (IFS CY31r2), the 2 m temperature is interpolated between the lowest model level (about 10 m above the surface in the 60-level model) and the surface temperature by making use of the profile functions, which are similar for other surface fluxes. The 2 m temperature is derived from Eq. 2.1.

$$s = c_{pdry}(1 + \delta q)T + gz = c_p T + \phi \tag{2.1}$$

$$\text{with } \delta = \frac{c_{pvap}}{c_{pdry}} - 1 \tag{2.2}$$

where, s and q are the dry static energy and specific humidity, respectively. c_{pdry}, c_{pvap} and c_p are the specific heats at constant pressure of dry air, water vapor, and moist air, separately, and ϕ is the geopotential. g is the acceleration of gravity. s and q at 2 m level are calculated from Eq. 2.3 and 2.4.

$$s_2 = s_{surf} + (s_l - s_{surf}) \frac{\log\left(\frac{z_2 + z_{0MWMO}}{z_{0HWMO}}\right) - \Psi_M\left(\frac{z_2 + z_{0MWMO}}{L}\right) + \Psi_M\left(\frac{z_{0HWMO}}{L}\right)}{\log\left(\frac{z_l + z_{0MWMO}}{z_{0HWMO}}\right) - \Psi_M\left(\frac{z_l + z_{0MWMO}}{L}\right) + \Psi_M\left(\frac{z_{0HWMO}}{L}\right)} \tag{2.3}$$

$$q_2 = q_{surf} + (q_l - q_{surf}) \frac{\log\left(\frac{z_2 + z_{0MWMO}}{z_{0QWMO}}\right) - \Psi_M\left(\frac{z_2 + z_{0MWMO}}{L}\right) + \Psi_M\left(\frac{z_{0QWMO}}{L}\right)}{\log\left(\frac{z_l + z_{0MWMO}}{z_{0QWMO}}\right) - \Psi_M\left(\frac{z_l + z_{0MWMO}}{L}\right) + \Psi_M\left(\frac{z_{0QWMO}}{L}\right)} \tag{2.4}$$

where, s_{surf} and q_{surf} is the dry static energy and specific humidity at the surface, respectively. Similarly, s_l and q_l are at lowest model level. z_2 is 2 m, z_l is the height of the lowest model level and z_{0HWMO} and z_{0QWMO} are roughness lengths, which both equal to 0.003 when larger than 0.03, otherwise z_{0HWMO} equals to z_{0H} and z_{0QWMO} equals to z_{0Q}. L is the Obukhov length. Ψ_M represents the exchange coefficient for momentum at the surface. The subscript WMO means WMO reporting practice (ECMWF, 2009b).

2.7.2   Total Precipitation

Total precipitation is comprised of convective precipitation (CP) and large scale precipitation (LSP or stratiform precipitation) from various sources, pure ice clouds, pure water clouds and mixed phases. Because microphysical processes are different in clear and cloudy skies, the precipitation is assimilated in these two parts separately (ECMWF, 2009b). The precipitation (P) is summarized by:

$$P = P^{cld} + P^{clr} \tag{2.5}$$

where, P^{cld} is the precipitation in the cloudy situation, while P^{clr} is for clear sky. They are calculated separately, based on Eq. 2.6 and 2.7.

$$P^{cld} \equiv \frac{1}{A} \int P \cdot H(l) dA \tag{2.6}$$

$$P^{clr} \equiv \frac{1}{A} \int P \cdot (1 - H(l)) dA \tag{2.7}$$

where, $H(l)$ represents the ratio of cloudy in the grid area A with the specific humidity l. The fraction of precipitation a_p in the grid cell is obtained by:

$$a_p = a_p^{cld} + a_p^{clr} \tag{2.8}$$

$$a_p^{cld} \equiv \frac{1}{A} \int H(l) H(P) dA \tag{2.9}$$

$$a_p^{clr} \equiv \frac{1}{A} \int (1 - H(l)) H(P) dA \tag{2.10}$$

Here, only the basic equations for the time change of the grid-box averaged cloud water/ice content are given and the cloud fraction is obtained by:

$$\frac{\partial l}{\partial t} = A(l) + S_{conv} + S_{bl} + S_{strat} - E_{cld} - G_{prec}$$

(2.11)

$$\frac{\partial a}{\partial t} = A(a) + \delta a_{conv} + \delta a_{strat} - \delta a_{evap} \tag{2.12}$$

The variables and notations in Eq. 2.11 and 2.12 represent the following processes:

$A(l),\ A(a)$	Rate of change of cloud water/ice and cloud area due to transport through the boundaries of the grid volume.
$S_{conv},\ \delta a_{conv}$	Rate of formation of cloud water/ice and cloud area by convective processes
$S_{strat},\ \delta a_{strat}$	Rate of formation of cloud water/ice and cloud area by stratiform condensation processes
E_{cld}	Rate of evaporation of cloud water/ice
G_{prec}	Rate of generation of precipitation from cloud water/ice
δa_{evap}	Rate of decrease of cloud area due to evaporation

The formulas for precipitation generation, fallout, evaporation, melting, and freezing processes are given specifically in ECMWF (2009b).

Chapter 3

Evaluation of ERA-Interim Reanalysis Data

3.1 Introduction

Reanalysis products are widely applied in climate impact studies. Typically they are adopted to provide boundary conditions for regional climate models. Reanalysis products contain the following key strengths: i) data is multivariate, spatially and temporally completed, and gridded; ii) observation are assimilated; iii) data is physically and dynamically modeled. Generally, reanalysis products estimate the closest state of real atmosphere and land surface characteristics (Decker et al., 2012; Simmons et al., 2010). However, there are some uncertainties related to reanalysis data such as observation errors and model misrepresentation. The quantification of uncertainty in reanalysis data is a serious challenge. At present, reanalysis products are provided by four major centers: NCEP/NCAR Reanalysis from the National Centers for Environmental Prediction/National Center for Atmospheric Research (NCEP/NCAR), ERA-15, ERA-40 and ERA-Interim from the European Centre for Medium-Range Weather Forecasts (ECMWF), the Climate Forecast System Reanalysis (CFSR) from the National Aeronautics and Space Administration (NASA) Goddard Space Flight Center (GSFC), and JAR-15 from the Japan Meteorological Agency (JMA) and the Central Research Institute of Electric Power Industry (CRIEPI) (Table 1.3).

A number of studies were carried out to evaluate the quality of reanalysis products, from global-to-continental-to-basin-to-single site. Simmons et al. (2004) compared the monthly air temperature trends derived from ERA-40 and NCEP/NCAR against Climate Research Unit (CRU) CRUTEM2v datasets at 5°×5° grids globally and continentally. They found a good agreement in surface air temperature anomalies between ERA-40 and CRUTEM2v (Simmons et al., 2004). The variations in surface atmospheric humidity, temperature (5°×5° grid) and precipitation (2.5°×2.5° grid) from ERA-40 and ERA-Interim against CRUTEM3 temperature, HadCRUH humidity, and GPCC precipitation datasets were also diagnosed by Simmons et al.

(2010), respectively. They found a high temporal correlation (r = 0.997) between CRUTEM3 and ERA-Interim temperature for the period from 1989 to 2001 with respect to Europe. It was shown that the accordance of ERA-Interim and CRUTEM3 is generally good with respect to large-scale patterns and magnitudes (Simmons et al., 2010). For precipitation, ERA-Interim and GPCC have the best agreement for all six continents (Europe, Asia, North America, Africa, Australia and South America). Their diagnosis also indicated that ERA-Interim has sufficient accuracy in continental-scale precipitation for monthly anomalies (Simmons et al., 2010). NCEP/NCAR reanalysis data showed significant bias in moisture fields, especially in the tropics (Trenberth and Guillemot, 1998).

Betts et al. (2009) evaluated the performance of ERA-40 and ERA-Interim temperature, precipitation and shortwave radiation data against observations from three large river basins (Amazon, Mississippi and Mackenzie). The seasonal cycle between two reanalysis data and observation are different for diverse variables and basins. For instance, ERA-40 and ERA-Interim have higher 2 m temperature than observations in the Mississippi basin, whereas ERA-Interim increases the precipitation and ERA-40 drifts the annual precipitation over the Amazon (Betts et al., 2009). ERA-Interim has some improvements over ERA-40, which results in a different bias against observations. Belo-Pereira et al. (2011) found ERA-Interim outperformed ERA-40 over the Iberian Peninsula in precipitation. However, the total precipitation was strongly underestimated, due to the mountainous topography.

Decker et al. (2012) evaluated air temperature, wind speed, precipitation, downward shortwave radiation, net surface radiation, and latent and sensible fluxes from GSFC, NCEP, and ECMWF reanalysis datasets, using 33 FLUXNET flux towers. The results showed that ERA-Interim performed best in terms of variability for 6-hourly air temperature, and ERA-40 had the lowest bias in latent flux and precipitation. The variability of 6-hourly precipitation was best assimilated by GLDAS and ERA-Interim datasets (Decker et al., 2012).

Although reanalysis products are improving, previous studies have shown that these products contain errors, due to various reasons. The application of reanalysis data for climate and hydrological studies should be done carefully and bias correction strategies are necessary for model initiation (Berg et al., 2003; Decker et al., 2012; Trenberth and Guillemot, 1998). Furthermore, those atmospheric fields that are crucial for snowpack, permafrost, glacier masses balance, or a variety of other geomorphic and ecological considerations in mountain regions, e.g. temperature and precipitation, should be evaluated.

This study adopts the high spatial resolution (0.25°×0.25°) gridded observation data E-OBS in the central Alps to evaluate daily minimum temperature, mean temperature, maximum temperature, and daily total precipitation in ERA-Interim products. E-OBS has significant advantages, including high spatial resolution, long-term period, uncertainty estimation incorporation and a novel interpolation method. This critical evaluation not only provides the guidelines for reanalysis product application in climate and hydrological studies, but also for reanalysis product downscaling and correction in complex terrain.

3.2 Datasets

3.2.1 ERA-Interim Data

3-hourly ERA-Interim forecast data (03, 06, 09, 12, 15, 18, 21 and 24 UTC), initialized at 00 UTC from 1979-2010 and projected on a grid of 0.25°×0.25°, are applied. The 00 UTC data were chosen, because the differences between 00 UTC and 12 UTC data are minor and not relevant for the results. The used output variables are 2 m temperature, total precipitation, as well as surface geopotential. Daily minimum, average, and maximum temperature were calculated from 3-hourly values, respectively. The geopotential height was calculated by normalizing of the geopotential over the gravity. 3-hourly forecast precipitation was cumulated to daily totally precipitation.

3.2.2 E-OBS Data

Daily minimum temperature (T_n), daily mean temperature (T_g), daily maximum temperature (T_x) and daily total precipitation (rr) are retrieved with a 0.25°×0.25° spatial resolution from E-OBS version 6.0 which was released in April 2012 and which covers the period from 1950-2011. The time period from 1979-2010 was extracted for a comparison with the 0.25°×0.25° ERA-Interim products. ERA-Interim and E-OBS data are shifted in latitudinal and longitudinal directions by 0.125°. The center point of the E-OBS grid is located at the cross junction of four ERA-Interim grid elements (Figure 3.1). The study area is located in the central Alps within 45.5-48°N, 6.25-11.5°E. The heights of the E-OBS grids are also retrieved from the datasets.
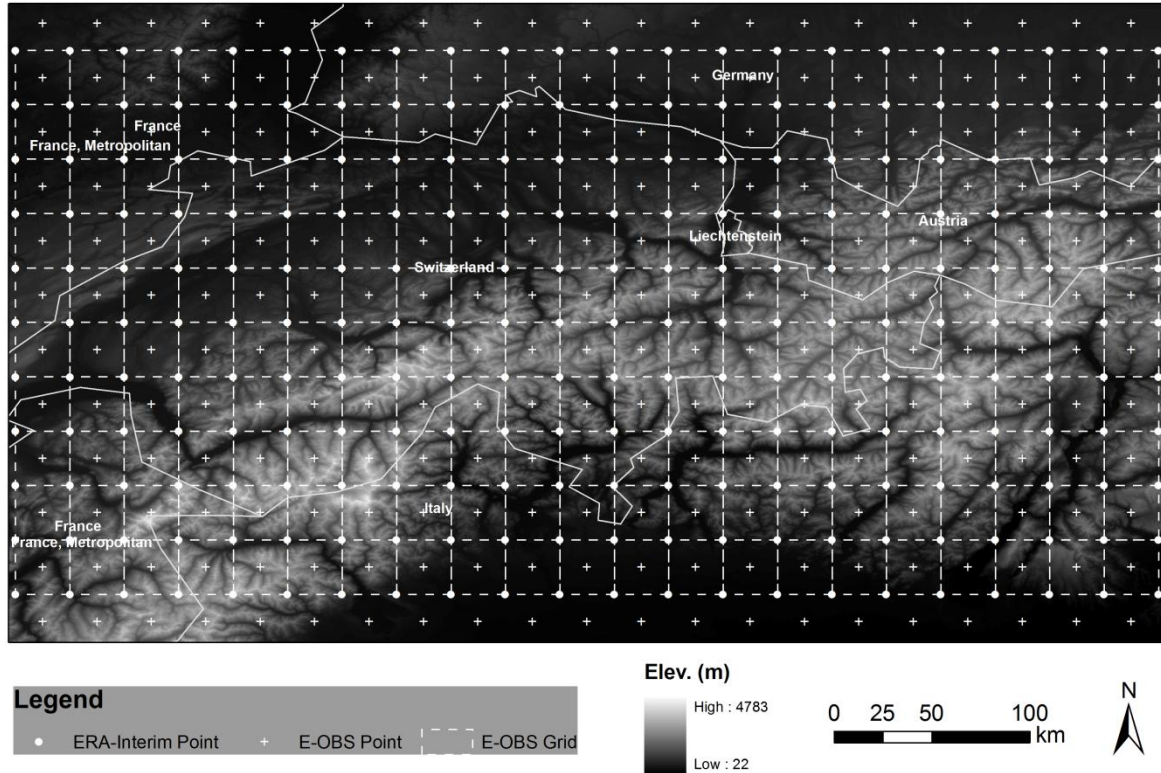
Figure 3.1: Location of ERA-Interim and E-OBS grids. The dots are the center points of ERA-Interim grids, the crosses are the center points of E-OBS grids, and the dashed lines are E-OBS grids (in total 210 grids in the study area).

3.2.3 GPCC Data

The GPCC data is available on a regular latitude/longitude grid with a spatial resolution of 0.25°, 0.5°, 1.0°, and 2.5°. In this study, the GPCC Climatology Version 2011 with a spatial resolution of 0.25° in 1950-2000 is applied for the evaluation of the ERA-Interim precipitation product (Meyer-Christoffer et al., 2011). Note that GPCC only provide the averaged monthly precipitation data from 1951-2000, rather than continuous records for one grid.

3.3 Methods

3.3.1 2 m Temperature

To compare the ERA-Interim temperature with the E-OBS dataset at different grid heights, ERA-Interim data first have to be interpolated at the heights of the E-OBS grids. The interpolation scheme is implemented in four steps. Because ERA-Interim and E-OBS data are shifted in latitude and longitude direction by 0.125°, the pair-wise high correlations were first

analyzed for every four ERA-Interim points, and then the average values of the four surrounding ERA-Interim points were equal-weighted averaged for the corresponding E-OBS value. Secondly, the averaged ERA-Interim data is interpolated based on lapse rates (Γ). The lapse rate (Γ) that describes the decrease of temperature with elevation is used for interpolation according to Eq. 3.1.

$$T_t = T_{ref} + \Gamma \times \Delta h \qquad (3.1)$$

T_{ref} is the reference temperature, which is defined by the ERA-Interim 2 m temperature (T_{ERA_2m}). Δh is the elevation difference between ERA-Interim and E-OBS grid height. This study used the specific monthly lapse rate, which is calculated from the monthly mean maximum and minimum temperature derived from station data published by Kunkel (1989) and Liston and Elder (2006) (Table 3.1). These values are widely applied in earth surface modeling and their temporal resolution of one month can be seen as a standard with respect to generalized lapse rates (Bernhardt and Schulz, 2010; Liston et al., 2008; Mernild et al., 2009).

Table 3.1: Fixed monthly lapse rates (°C km^{-1}) extracted from Kunkel (1989) and Liston and Elder (2006).

	Jan	Feb	Mar	Apr	May	Jun	Jul	Aug	Sep	Oct	Nov	Dec
Γ	-4.4	-5.9	-7.1	-7.8	-8.1	-8.2	-8.1	-8.1	-7.7	-6.8	-5.5	-4.7

Subsequently, daily minimum, average and maximum temperatures, as well as quantiles (1 %, 5 %, 50 %, 95 %, and 99 %) and mean values are calculated from 3-hourly records. The "observation minus reanalysis" (OMR) method is used to evaluate the anomaly between observation and reanalysis data, which has previously been demonstrated to be a simple and effective method (Kalnay and Cai, 2003; Kalnay et al., 2006; Lim et al., 2008). The root mean square error (RMSE) and mean absolute error (MAE) are used for an assessment of the differences between ERA-Interim and E-OBS (Eq. 3.2 and 3.3).

$$RMSE = \sqrt{\frac{1}{N} \sum_{t=1}^{N} \left(T_{EOBS}^t - T_{ERA}^t \right)^2} \qquad (3.2)$$

$$MAE = \frac{1}{N} \sum_{t=1}^{N} \left| T_{EOBS}^t - T_{ERA}^t \right| \qquad (3.3)$$

with T_{ERA}^t = ERA-Interim temperature at time t, T_{EOBS}^t = E-OBS temperature at time t, and N = number of records.

3.3.2 Daily Total Precipitation

Like temperature, ERA-Interim daily total precipitation is simply first averaged, using the four surrounding ERA-Interim grids (Figure 3.1). Occurrence and amount as the most important precipitation characteristics are analyzed. In term of occurrence, this study used several threshold values (0.5, 1, 5, 10 and 20 mm) to define wet/dry days. 10 mm and 20 mm thresholds represent the heavy events. The Correspondence Ratio (CR) is introduced for occurrence assessment (Eq. 3.4), which represents the ratio of dry and wet days that occurred on the same day in both ERA-Interim and E-OBS (Belo-Pereira et al., 2011). The RMSE and MAE are also adopted for daily precipitation amount evaluation. In addition, the annual cycle of precipitation is diagnosed with respect to daily and monthly total precipitation.

$$CR = \frac{n_{dry} + n_{wet}}{N} \tag{3.4}$$

where n_{dry} and n_{wet} are the dry and wet days that occurred simultaneously in ERA-Interim and E-OBS, respectively, N is the number of days in the entire period from 1979-2010. The value of occurrence is 1 on wet days and 0 on dry days above/below various threshold values.

3.4 Results

3.4.1 2 m Temperature

The correlations of the four ERA-Interim grid elements are first analyzed pair-wisely to check whether there are some large errors (or outliers). The four surrounding ERA-Interim points are sequentially numbered 1 to 4 from northwest corner to southeast corner. Thus, there are six pairs. Figure 3.2 shows the histograms of the pair-wise correlations of four ERA-Interim points for each E-OBS grid (entire 210 grids in the study area). High correlations (close to 1) are found for temperature and precipitation, especially in three temperature fields (Figure 3.2). The grids in the same latitude (e.g. 1 & 2 and 3 & 4) are most agreeable. The two points on the diagonal (1 & 4) are correlated worst. Here, the average value of the four surrounding ERA-Interim points is applied for the corresponding E-OBS grid.
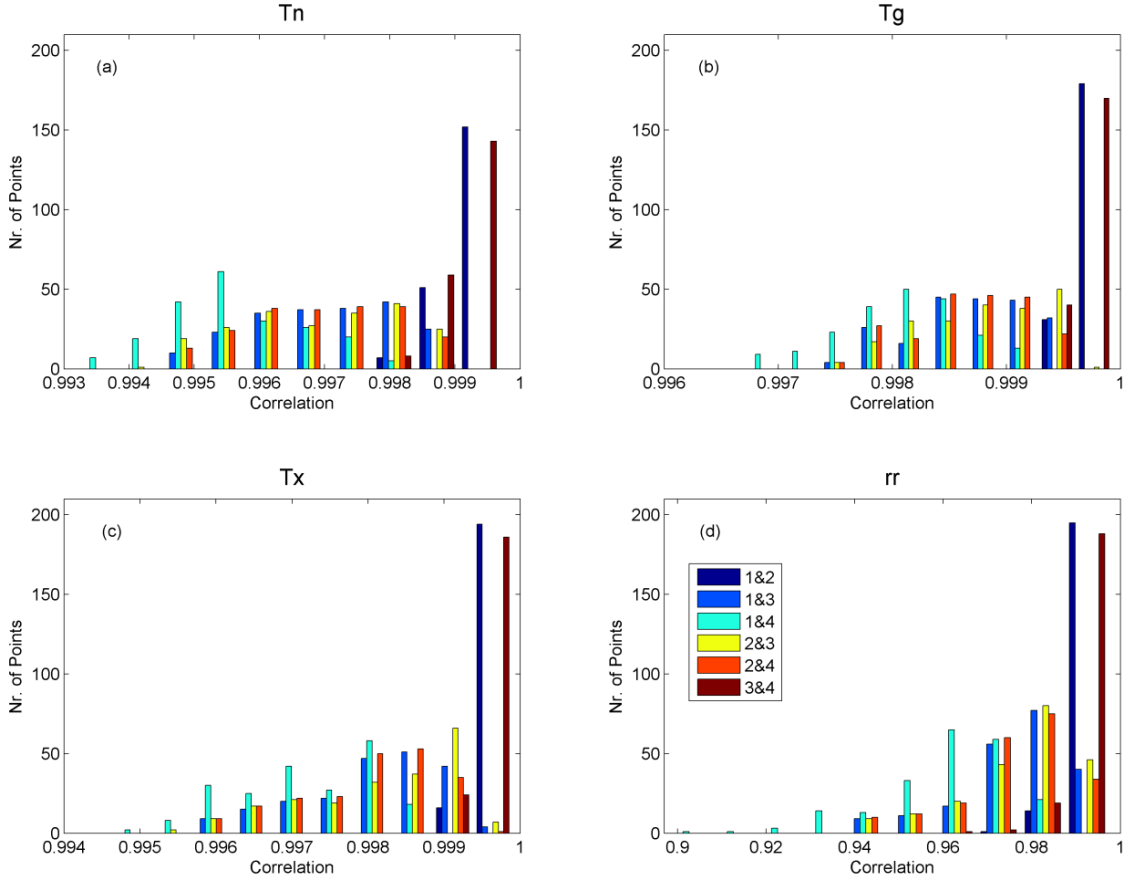
Figure 3.2: Histogram of the pair-wise correlations of four ERA-Interim points for each E-OBS grid. (a) is for T_n, (b) is for T_g, (c) is for T_x and (d) is for rr.

Figure 3.3 shows the correlations and mean anomalies in daily minimum temperature between ERA-Interim and E-OBS with a spatial resolution of 0.25°×0.25° over 1979-2010. The mean anomaly was calculated by the OMR method. The correlations between two datasets change from 0.94 to 0.98 and the mean anomalies vary between -1.4 and 3.4 °C. Generally, ERA-Interim overestimates in low altitudes and underestimates in high elevation areas. The lower correlations and positive anomalies are distributed along the mountain crest, while higher correlation and negative anomaly occur in the lower elevation areas in the northeast of mountain ridge. The high mountain barrier effect possibly leads to the positive anomaly in the southeast of the mountains. A similar situation is found for T_g in Figure 3.4. The correlations fall within a range 0.96 to 1 and the mean anomalies range from -0.8 to 2.4 °C. The average anomaly of whole area is 0.6 °C for both T_n and T_g, which indicates the good agreement between ERA-Interim and E-OBS dataset. The correlations and mean anomalies for T_x are shown in Figure 3.5. It is interesting that the lower correlations not only occur in the mountain crest, but also distribute parallel to the mountain ridge from southwest to northeast. The correlations vary from 0.95 to 0.99 and the

anomalies change between -0.4 and 2.1 °C. However, ERA-Interim underestimates T_x over the majority of grids (around 95 %), with an average of 0.9 °C for the whole area. This comparison demonstrates that the ERA-Interim product generally agrees well with E-OBS dataset, with the average anomalies of 0.6 °C both for T_n and T_g, and 0.9 °C for T_x. However, T_n and T_g are overestimated by ERA-Interim at the low altitude and are underestimated in the high mountain crest. Around 95 % of the study area is underestimated for T_x. It is worth noting that the interpolation based on monthly fixed lapse rate also contributes to the anomalies.
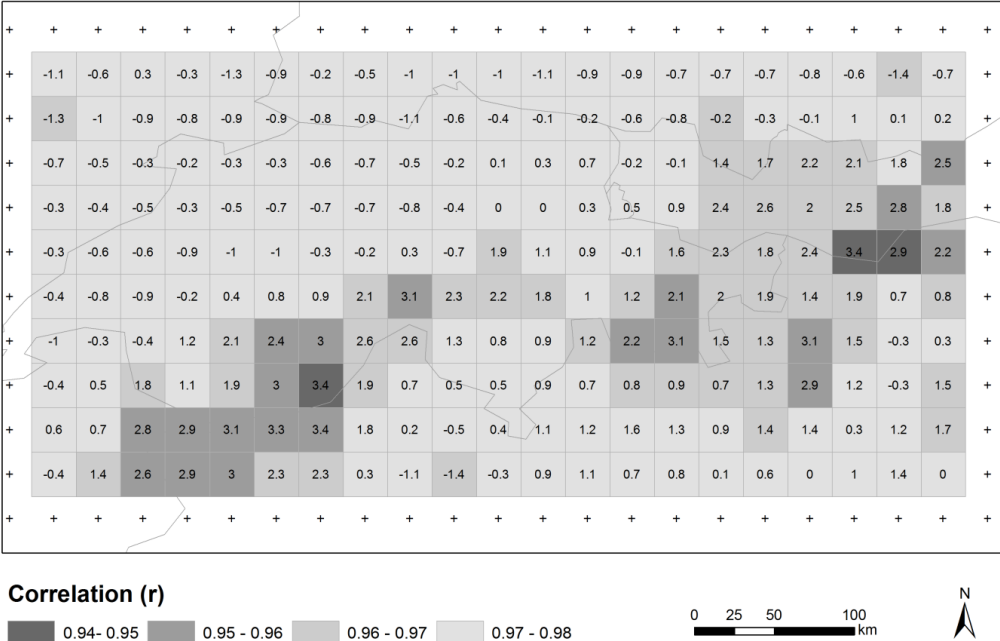
Figure 3.3: Correlations and anomalies of daily minimum temperature between ERA-Interim and E-OBS dataset from 1979-2010. The mean anomalies are labeled in the grids.
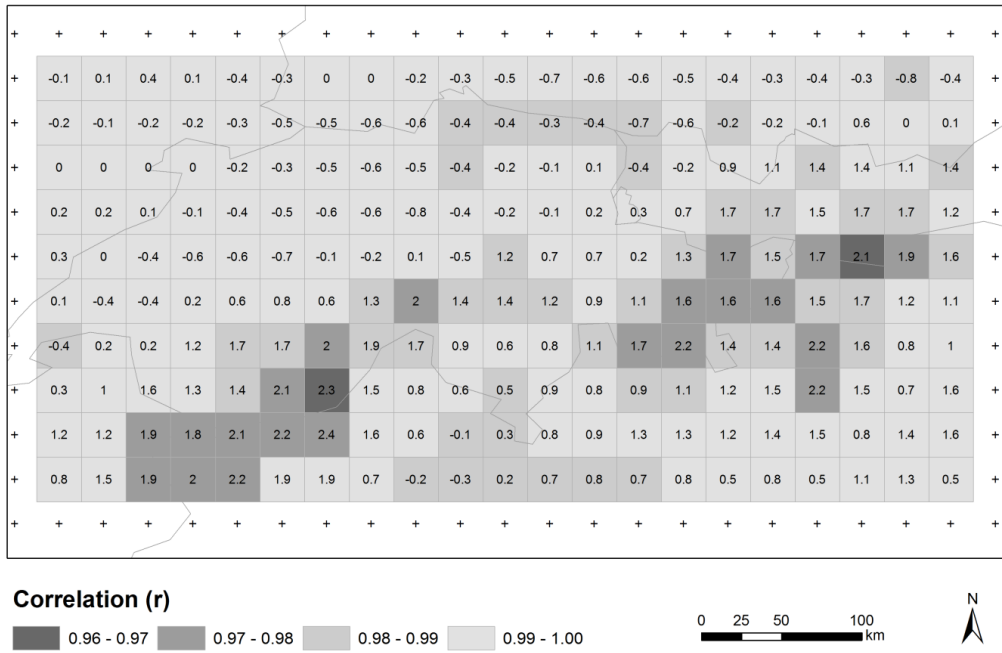
Figure 3.4: Correlations and anomalies of daily average temperature between ERA-Interim and E-OBS dataset from 1979-2010. The mean anomalies are labeled in the grids.
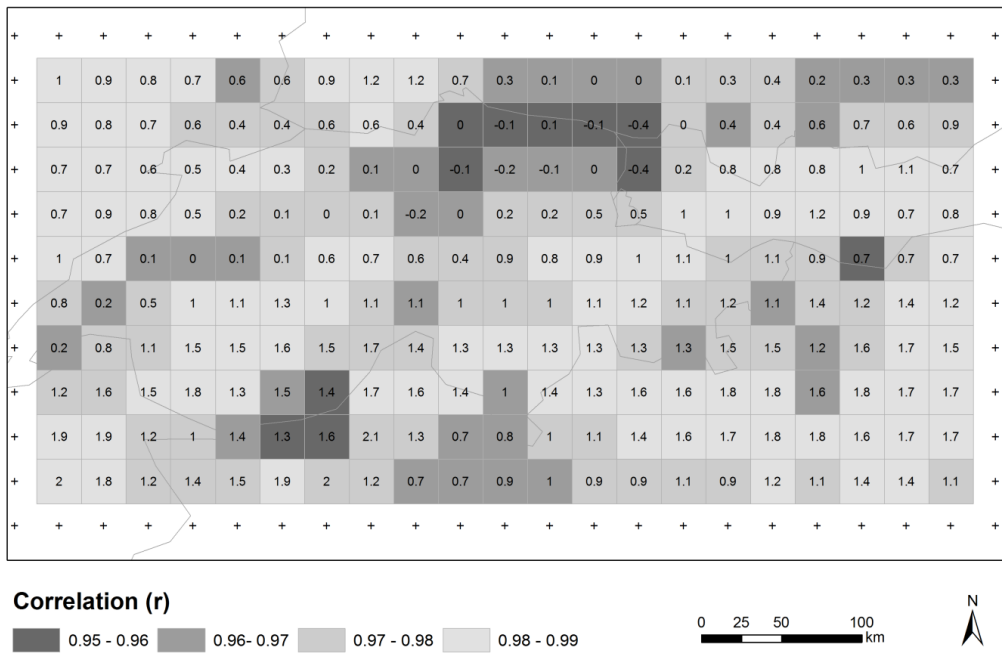
Figure 3.5: Correlations and anomalies of daily maximum temperature between ERA-Interim and E-OBS dataset from 1979-2010. The mean anomalies are labeled in the grids.

Figure 3.6 shows the anomalies of five quantiles (1 %, 5 %, 50 %, 95 %, and 99 %) between ERA-Interim and E-OBS dataset for T_n, T_g and T_x for the whole study area. In general, the

anomalies vary in a similar range from -6 to 4 °C, especially for 25 % to 75 % range within -2 to 2 °C. T_x has more outliers than T_n and T_g. The extreme quantiles 1 % and 99 % as well as 95 % have much higher deviations than the median values. This again illustrates that ERA-Interim is less able to capture extreme temperature in complex terrains.
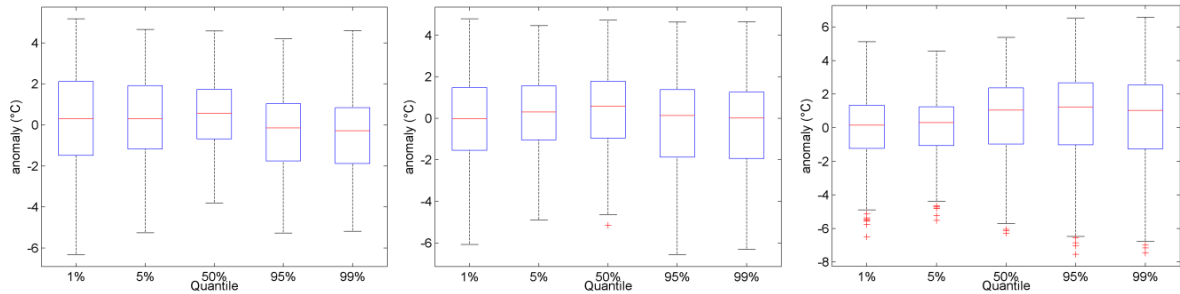
Figure 3.6: Boxplots of the anomalies of five quantiles (1 %, 5 %, 50 %, 95 %, and 99 %) for T_n (left), T_g (middle), and T_x (right) from 1979-2010 for the whole area. Thick horizontal lines in the boxes represent the median values. Boxes indicate the inner-quantile range (25 % to 75 %) and the red crosses show the outliers.

Figure 3.7 presents the monthly anomalies and 12 month running mean anomalies for T_n, T_g and T_x over the entire area. The monthly anomaly is defined with respect to the monthly average anomaly and is also standardized from 1979-2010. After this adjustment, the inter-annual variability and long-term shifts are easy to compare. Figure 3.7 illustrates that ERA-Interim and E-OBS identify generally similar inter-annual variations over the long-term period. The anomalies are generally small and show a slight drift over time. For three temperature fields, the negative anomalies occurred from 1979-1985, and then turned to positive beginning in 1986 and ending around 1991. From 1986-1991, the trends, in particular for T_g, are significantly changed for ERA-Interim. However, the underlying reason for this trend mutation cannot yet be explained; it is possibly related to ERA-Interim data assimilation system. In addition, T_n has a much longer positive anomalies in the middle of the 1990s, and a longer negative anomalies in late 2000s. ERA-Interim underestimated T_x in the last ten years.
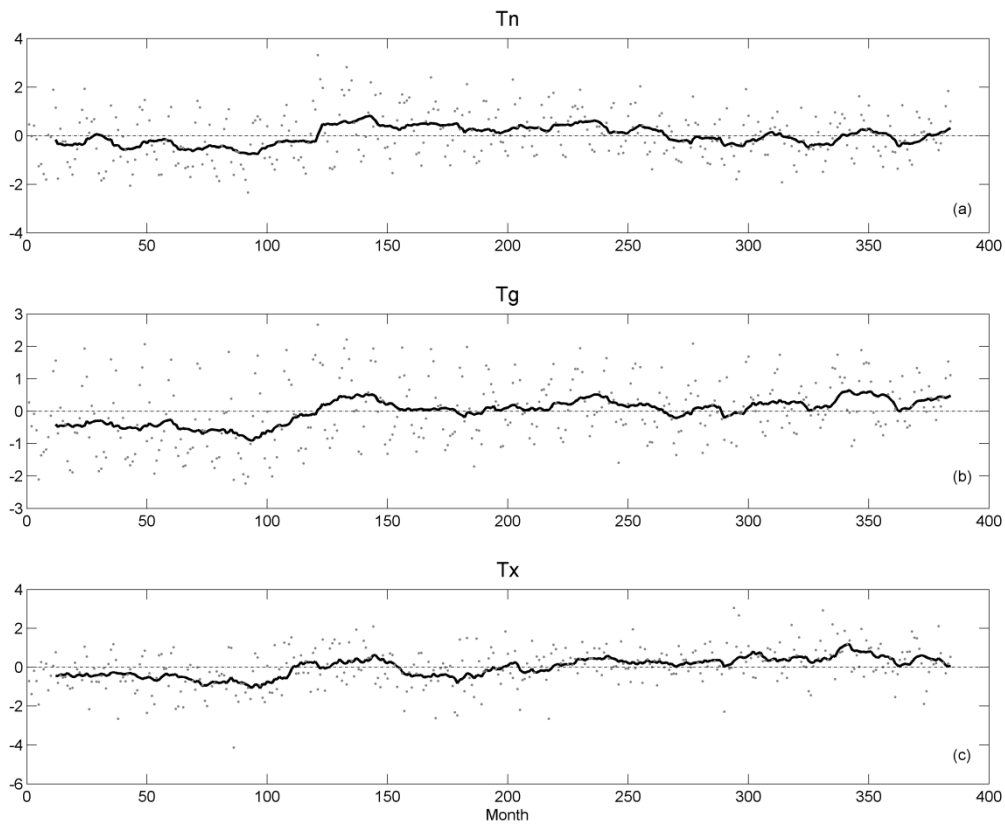
Figure 3.7: Monthly anomalies (grey dots) and twelve-month running averages (black solid line) over entire area from 1979-2010. The monthly anomaly is defined with respect to the monthly average anomaly and is also standardized from 1979-2010. a) is for T_n, b) is for T_g and c) is for T_x.

3.4.2   Daily Total Precipitation

3.4.2.1   Annual Cycle for the Entire Area

Figure 3.8 presents the mean annual cycle of daily total precipitation for the whole area for the period 1979-2010. The black line is for E-OBS while the blue line is for ERA-Interim, both from 1979-2010. ERA-Interim has almost the same standard deviation of the inter-annual variability of daily precipitation as E-OBS, 1.0 mm day^{-1}. Generally, ERA-Interim has wet biases throughout the warm season and dry biases in the cold season. The largest biases occur during May to August with a range of 0.6-0.8 mm day^{-1}. The same results are found for monthly total precipitation.
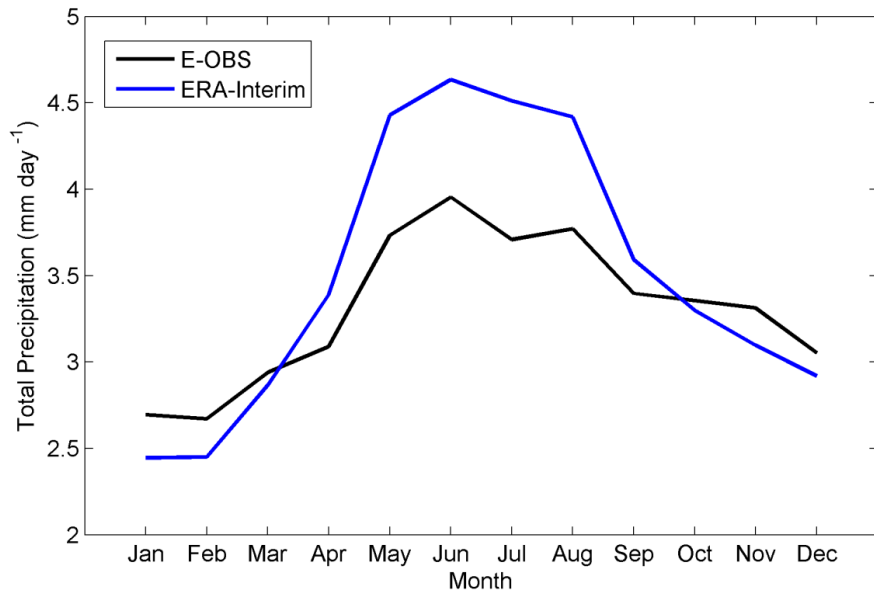
Figure 3.8: Mean annual cycle of daily total precipitation for the whole area from 1979-2010.

Overall, the standard deviation of the inter-annual variability of monthly precipitation from 1979-2010 is similar for both ERA-Interim and E-OBS, 32.5 mm month^{-1} and 31.1 mm month^{-1}, respectively. Figure 3.9 shows the comparison of mean annual cycle of monthly total precipitation for the whole area. ERA-Interim underestimates the total precipitation compared to E-OBS in the cold season (November to February) and overestimates in the warm season (April to September). ERA-Interim has a significant wet bias, particularly from May to August, with approximately 19.3 % more precipitation than E-OBS. March and October have the lowest dry bias between ERA-Interim and E-OBS, 1.5 % and 0.8 % respectively. The GPCC monthly precipitation (Version 2011) (Meyer-Christoffer et al., 2011), as the reference data, is presented in Figure 3.9 as well. The GPCC represents long-term (1951-2000) monthly land surface precipitation derived from rain gauges built on GTS (The Global Telecommunications System) and the historic data (Meyer-Christoffer et al., 2011). Although the time series differs from ERA-Interim, it has little effect on the annual variability. ERA-Interim has also a wet bias (12.2 %) against GPCC from May to August. ERA-Interim underestimates in November, January, and February, and overestimates for the other months. January has the lowest bias, whilst July has the greatest. The annual cycle comparison provides a basic confidence in the ability of ERA-Interim to capture precipitation variability in the cold season, which is of special interest for snowpack and glacial studies. However, some biases corrections depend on the period of years are still necessary.
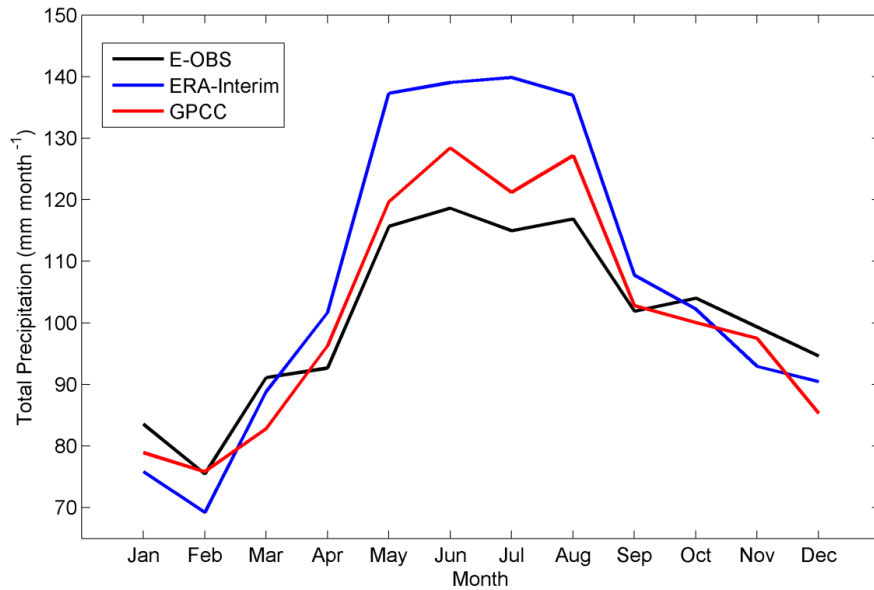
Figure 3.9: Mean annual cycle of monthly total precipitation for the whole area. The time period of ERA-Interim and E-OBS dataset is from 1979-2010, and GPCC's time period is from 1951-2000.

3.4.2.2   Precipitation Spatial Variability

Figure 3.10 shows the E-OBS annual precipitation distribution from 1979-2010. The annual precipitation varies from 600 to 2000 mm, with higher precipitation distributed along the higher elevation mountain area. ERA-Interim precipitation did not capture the variability of E-OBS well with respect to the same period (Figure 3.11). The link between elevation and precipitation is weakly reflected by ERA-Interim. Figure 3.12 illustrates the annual precipitation difference between E-OBS and ERA-Interim. ERA-Interim underestimates the annual precipitation in the high mountainous area and clearly overestimates in the lower elevation areas. The largest bias is -120 % in the southeast of the study area in Figure 3.12. The ERA-Interim data should be corrected for further hydrological application, because of the annual bias has been demonstrated in the Figure 3.12.
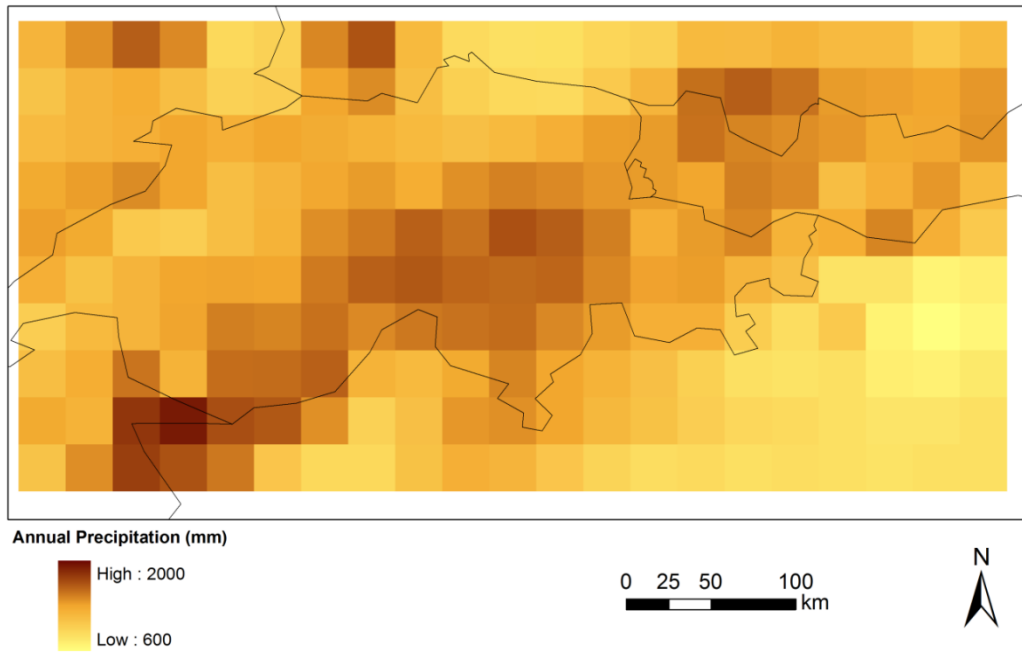
Figure 3.10: Annual precipitation of E-OBS data from 1979-2010.
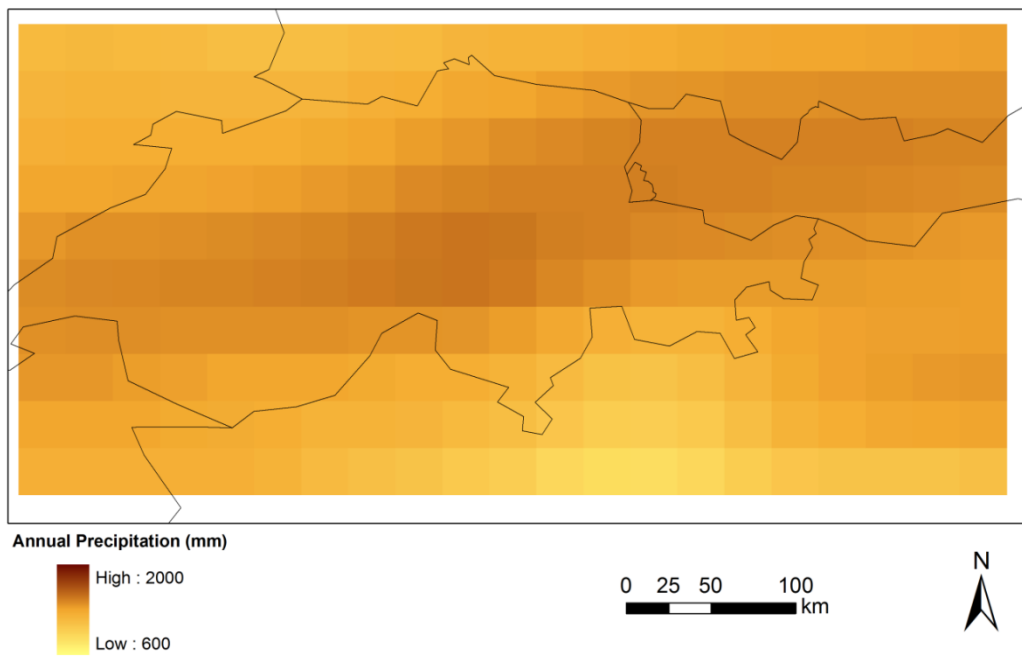
Figure 3.11: Annual precipitation of ERA-Interim data from 1979-2010.

E-OBS minus ERA-Interim (mm)

High : 650

Low : -750

0 25 50   100
km

N
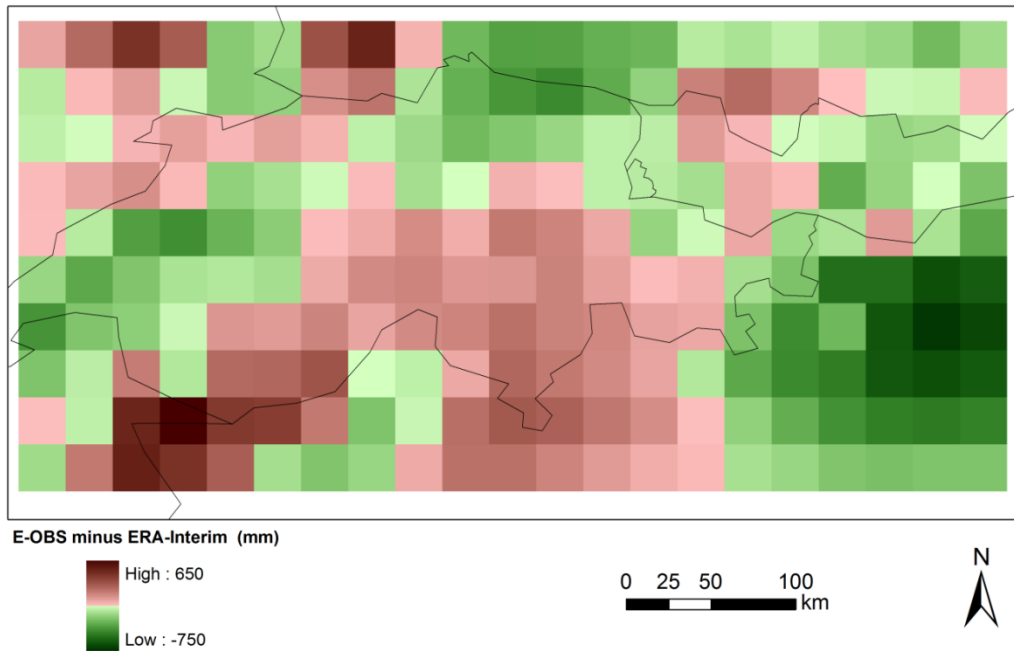
Figure 3.12: Annual precipitation bias between E-OBS and ERA-Interim from 1979-2010.

Figure 3.13 displays the monthly mean anomaly of daily total precipitation between E-OBS and ERA-Interim from 1979-2010. Here, based on monthly mean daily total precipitation, it is easy to investigate the variability of the seasons, which is of great interesting for hydrologists. In general, ERA-Interim remarkably underestimates the daily total precipitation in the winter season from November to March in the high elevation areas (Southeast of Switzerland), with a range of 2.5-3.4 mm day^{-1} and significantly overestimates in the summer season from April to August in the lower elevations, with a range of 2.1-3.3 mm day^{-1}. September and October have relative small biases within the range of -1.7-1.9 mm day^{-1}. The potential cause of these biases is that snow accumulation in the winter and melting in summer modeled inaccurately in the ERA-Interim forecast model.
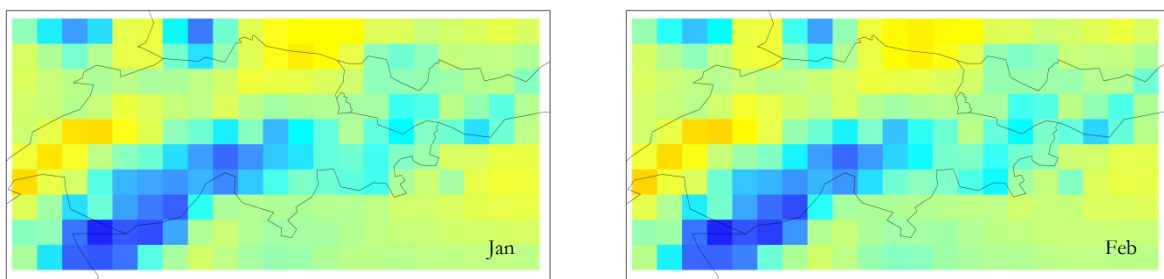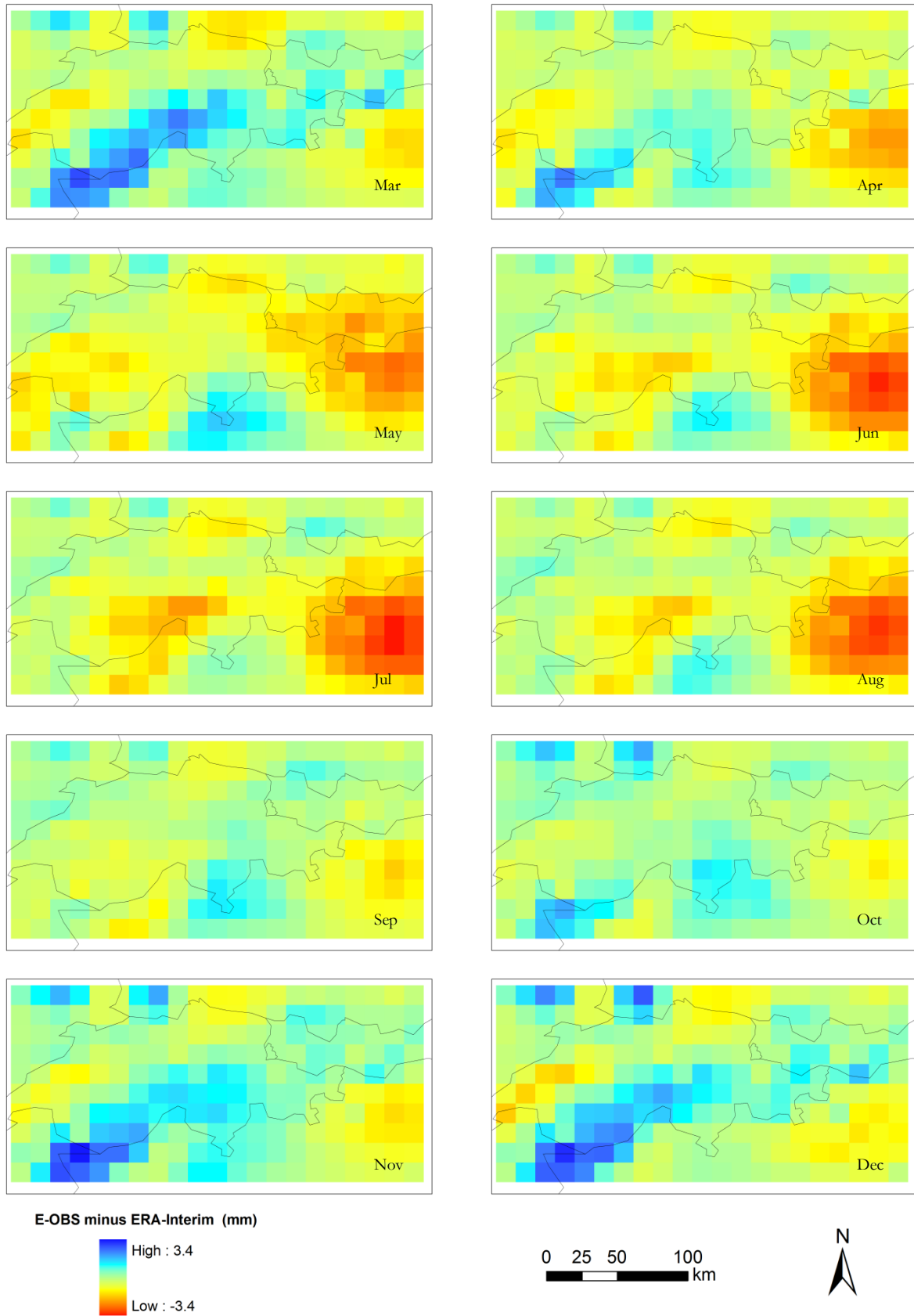
Figure 3.13: Monthly mean anomaly of daily total precipitation between E-OBS and ERA-Interim from 1979-2010.

3.4.2.3   Precipitation Occurrence and Amount

Figure 3.14 shows the correspondence ratio (CR) for various precipitation threshold values: 0.5, 1, 5, 10 and 20 mm. The grids are sequentially numbered 1 to 210 from northwest corner to southeast corner. The CR increases with higher thresholds over the whole study area. 0.5 mm and 1 mm threshold have similar occurrences in ERA-Interim and E-OBS, particularly the same fluctuation in low elevation grids. These fluctuations become indistinguishable for 10 mm and 20 mm, which illustrate that ERA-Interim capture the occurrence of heavy amount well, compared to E-OBS. The CRs vary between 0.93 and 0.99 for 20 mm threshold. Figure 3.15 illustrates the CRs distribution for the 0.5 mm threshold. The low CRs occurred in the same places where the large anomalies were found in the summer season, from May to August. These two figures imply that ERA-Interim has some bias for summer precipitation assimilation, both in occurrence and amount. In contrast, MAE and RMSE show significant fluctuations for higher thresholds (Figure 3.16 and 3.17). The grids have larger MAE and RMSE are consistent with the grids that have shown larger monthly mean daily total precipitation anomalies in Figure 3.13. Figure 3.18 shows the mean absolute error (MAE) for 0.5 mm threshold values for all grids.
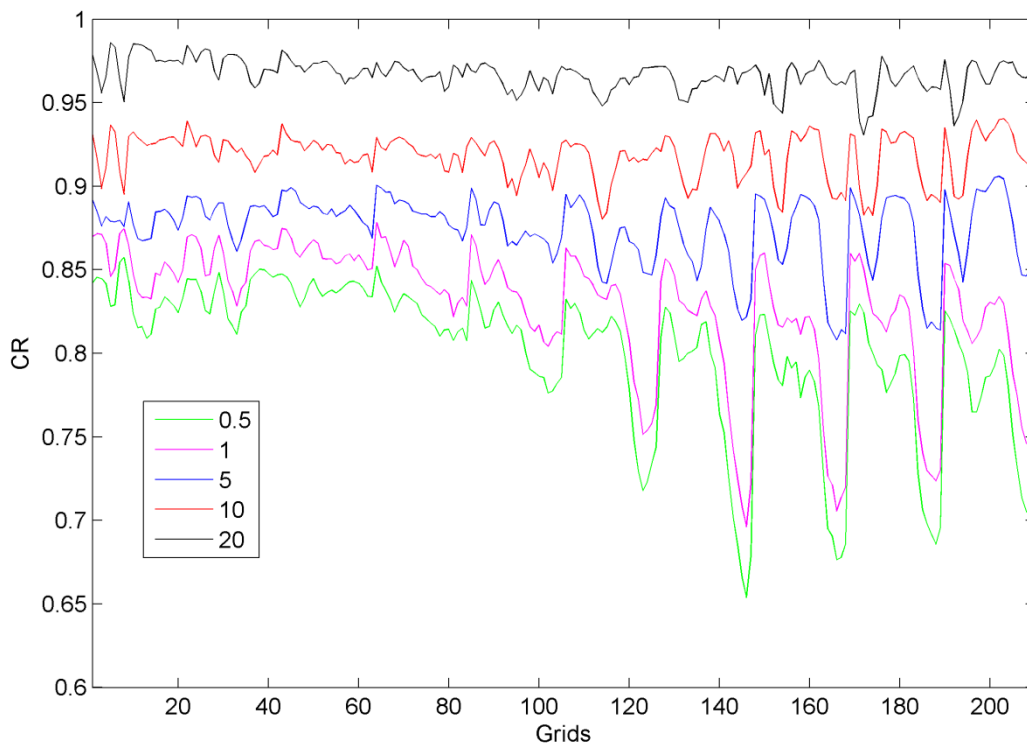
Figure 3.14: Correspondence ratio (CR) for various threshold values for all grids. The grids are sequentially numbered 1 to 210 from northwest corner to southeast corner.
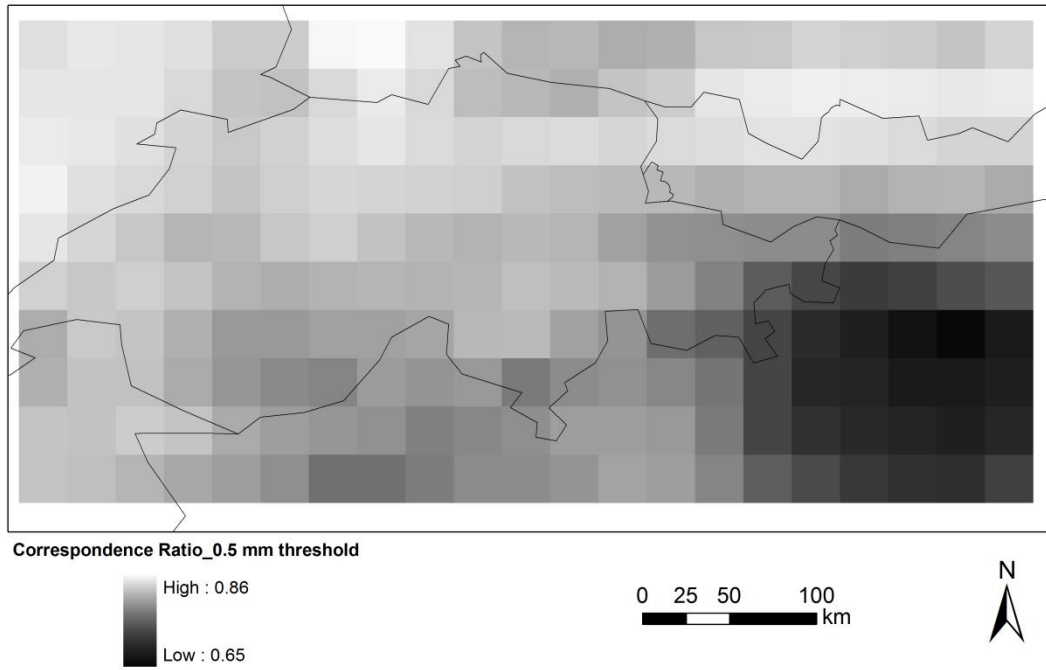
Figure 3.15: Correspondence ratio (CR) for 0.5 mm threshold values for all grids.
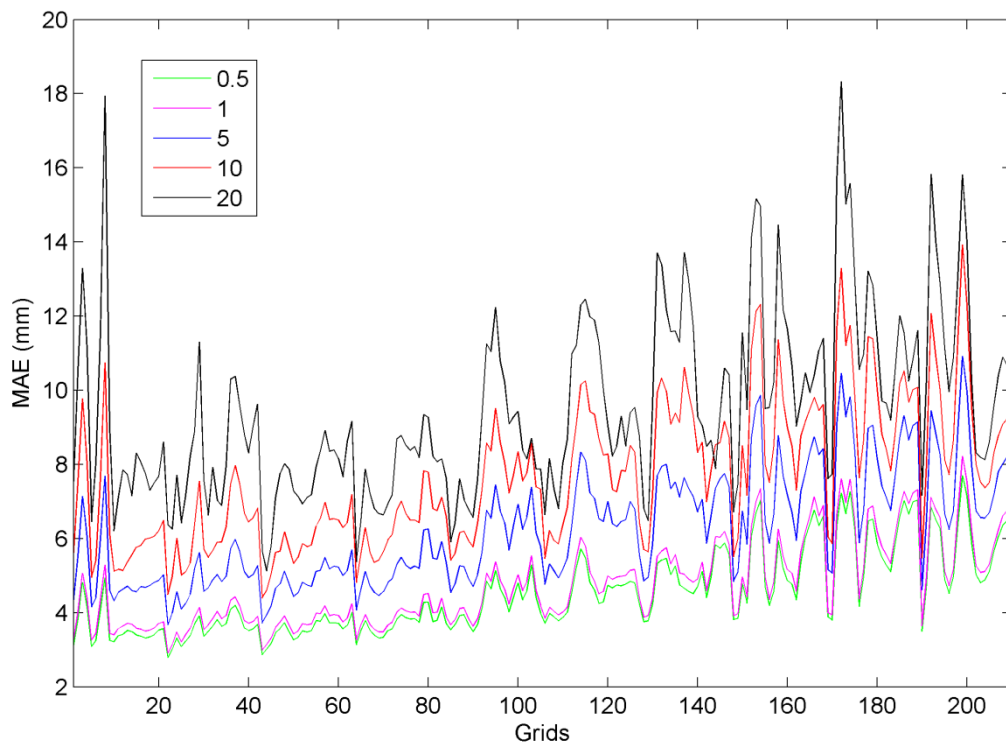
Figure 3.16: Mean absolute error (MAE) for various threshold values for all grids. The grids are sequentially numbered 1 to 210 from northwest corner to southeast corner.
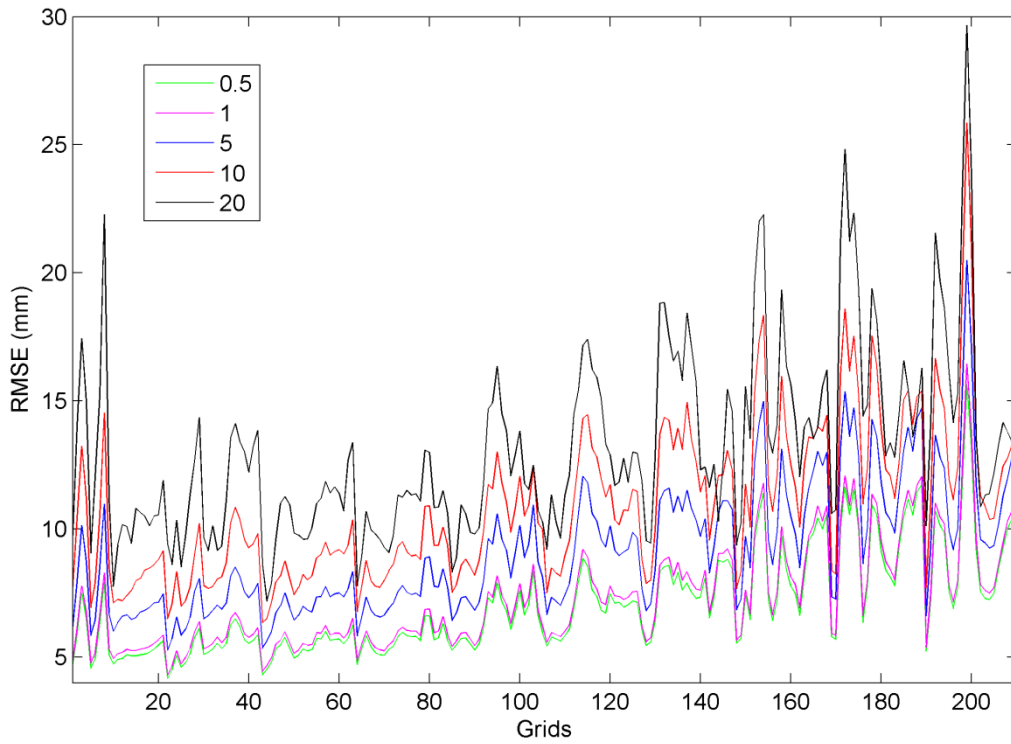
Figure 3.17: Root mean square error (RMSE) for various threshold values for all grids. The grids are sequentially numbered 1 to 210 from northwest corner to southeast corner.
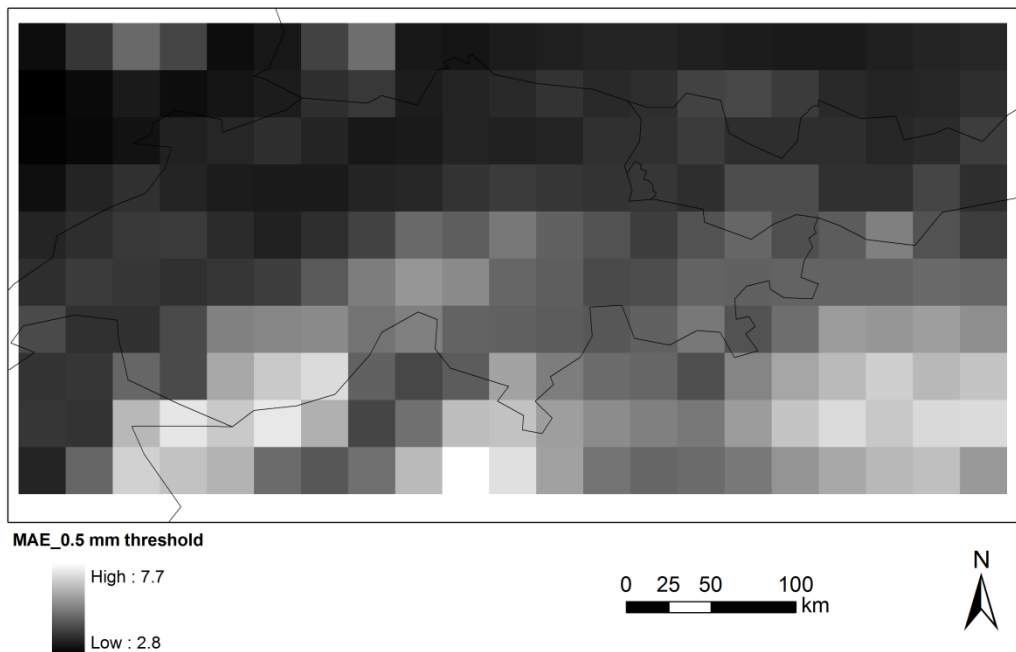
Figure 3.18: Mean absolute error (MAE) for 0.5 mm threshold values for all grids.

3.4.3 Elevation Dependence of Temperature and Precipitation

The empirical relationship between elevation and temperature and precipitation is always applied prior to interpolation and disaggregation (e.g. Im et al., 2009). Figure 3.19-3.21 show the linear regression between elevation and T_n, T_g and T_x for 5 quantiles and the mean value from E-OBS dataset, respectively. Note that each quantile is calculated from the distribution over 1979-2010 for each grid. The slopes in figures reflect the gradient of temperature decrease. Overall, the relationship between elevation and temperature is strong (R^2 varied from 0.78 to 0.94), in other words, elevation is the key factor that affects temperature changes. T_x has a higher gradient than T_n on average. Low quantiles have more scatter grids than high quantiles for all three temperature fields (1 % quantile have lowest R^2 for three temperature fields). This illustrates that ERA-Interim is relatively poor in capturing the variation in lower temperatures. Meanwhile, these slopes confirmed that proved a fixed lapse rate (-6.5 °C km^{-1}) for the whole period is inappropriate.
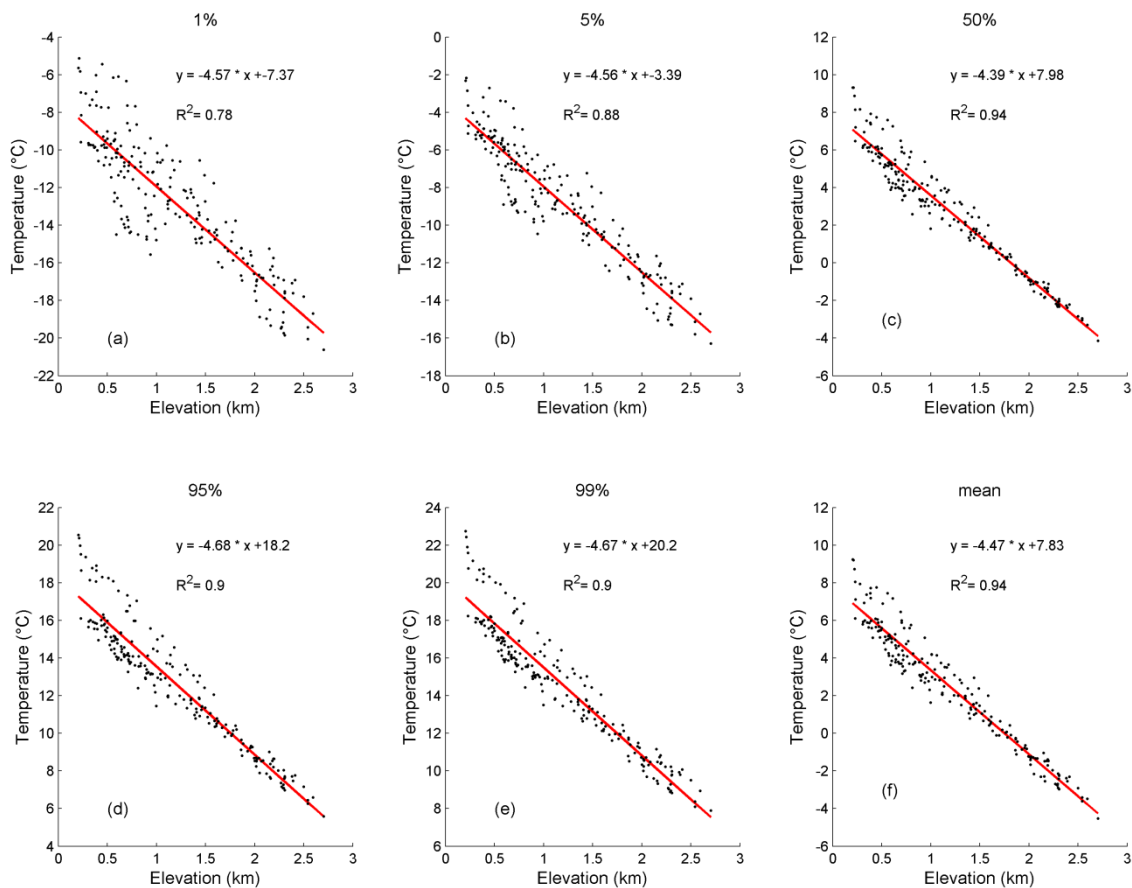
Figure 3.19: Linear regression between elevation and T_n for 5 quantiles and mean value for all grids from 1979-2010.

For T_n, the slope ranges from -4.68 to -4.39 °C km^{-1}. 1 % and 5 % quantiles show the larger dispersive feature in the lower elevations (lower R^2). In contrast, 95 % and 99 % quantiles are converged in the higher areas. The points above the fitting line represents the grids in the southeast of mountain and the below points represents the grids in the northwest of the mountain. In term of T_g, the slope ranges from -5.70 to -4.66 °C km^{-1}. The 5 % quantile of T_g shows the lowest gradient, whereas 99% demonstrates the highest gradient. Generally, as for T_n, the low quantiles (1 % and 5 %) distributed with more scatter in the lower locations than in higher elevation areas. For T_x, the slope ranges from -6.89 to -4.66 °C km^{-1}. The lowest and highest gradients occur in the 5 % and 99 % quantile, like T_g, respectively. There are significant differences between high quantile and low quantile for T_x. Again, the linear regressions show that elevation is the key factor that determines the temperate variation. However, the fixed lapse rate is not inappropriate in the complex terrain.
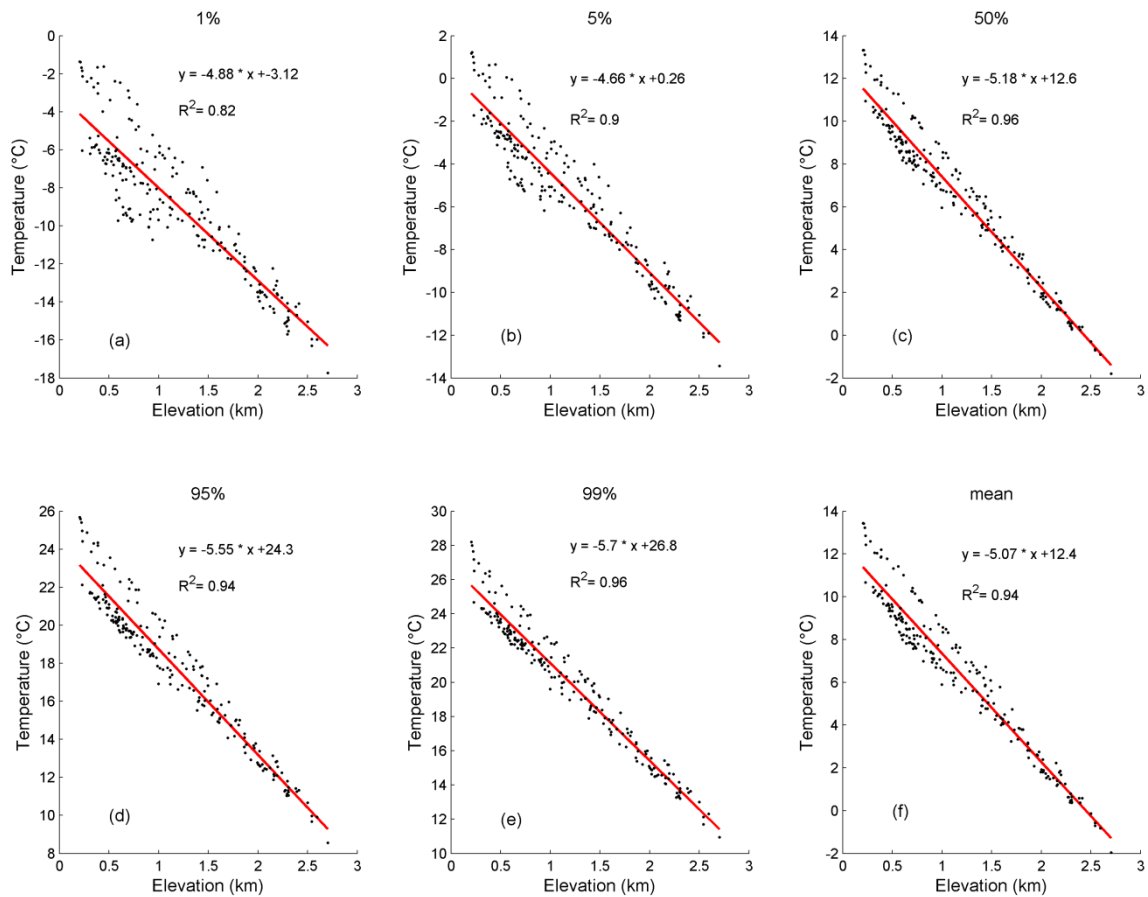
Figure 3.20: Linear regression between elevation and T_g for 5 quantiles and mean value for all grids from 1979-2010.

Figure 3.22 illustrates the seasonal dynamic of E-OBS ($\Gamma_{E\text{-}OBS}$) and Kunkel lapse rates (Γ_{Kunkel}, Table 3.1) for T_n, T_g and T_x for the whole area from 1979-2010, respectively. The Γ_{Kunkel} do not

show any inter-monthly variability since they are defined by a single value for each month. Generally, $\Gamma_{E\text{-}OBS}$ in winter (October-February) are smaller but with higher variability. Lapse rates in warm months varied in lower inter-monthly variability, especially from May to August. For T_n and T_g, in most of 12 months, Γ_{Kunkel} is larger than $\Gamma_{E\text{-}OBS}$, in particular in summer. In the contrast, Γ_{Kunkel} is closest to $\Gamma_{E\text{-}OBS}$ for T_x. The lapse rate comparison between Γ_{Kunkel} and $\Gamma_{E\text{-}OBS}$ implied that using a fixed monthly lapse rate to downscale ERA-Interim is problematic. The temperature bias between ERA-Interim and E-OBS also results from the applied lapse rate during interpolation. Therefore, an appropriate lapse rate determines the downscaling accuracy. This issue will be discussed in the Chapter 4, in which, a new robust approach based on ERA-Interim lapse rate is developed.
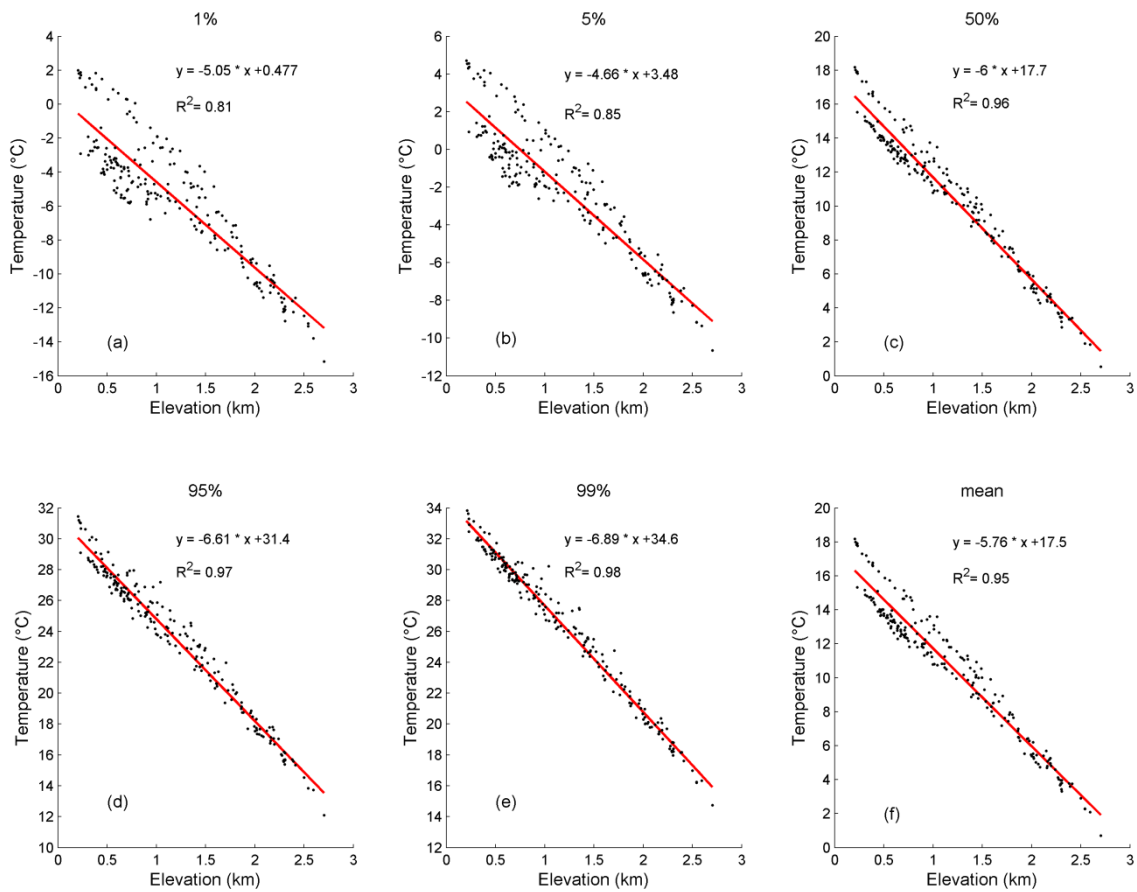
Figure 3.21: Linear regression between elevation and T_x for 5 quantiles and mean value for all grids from 1979-2010.
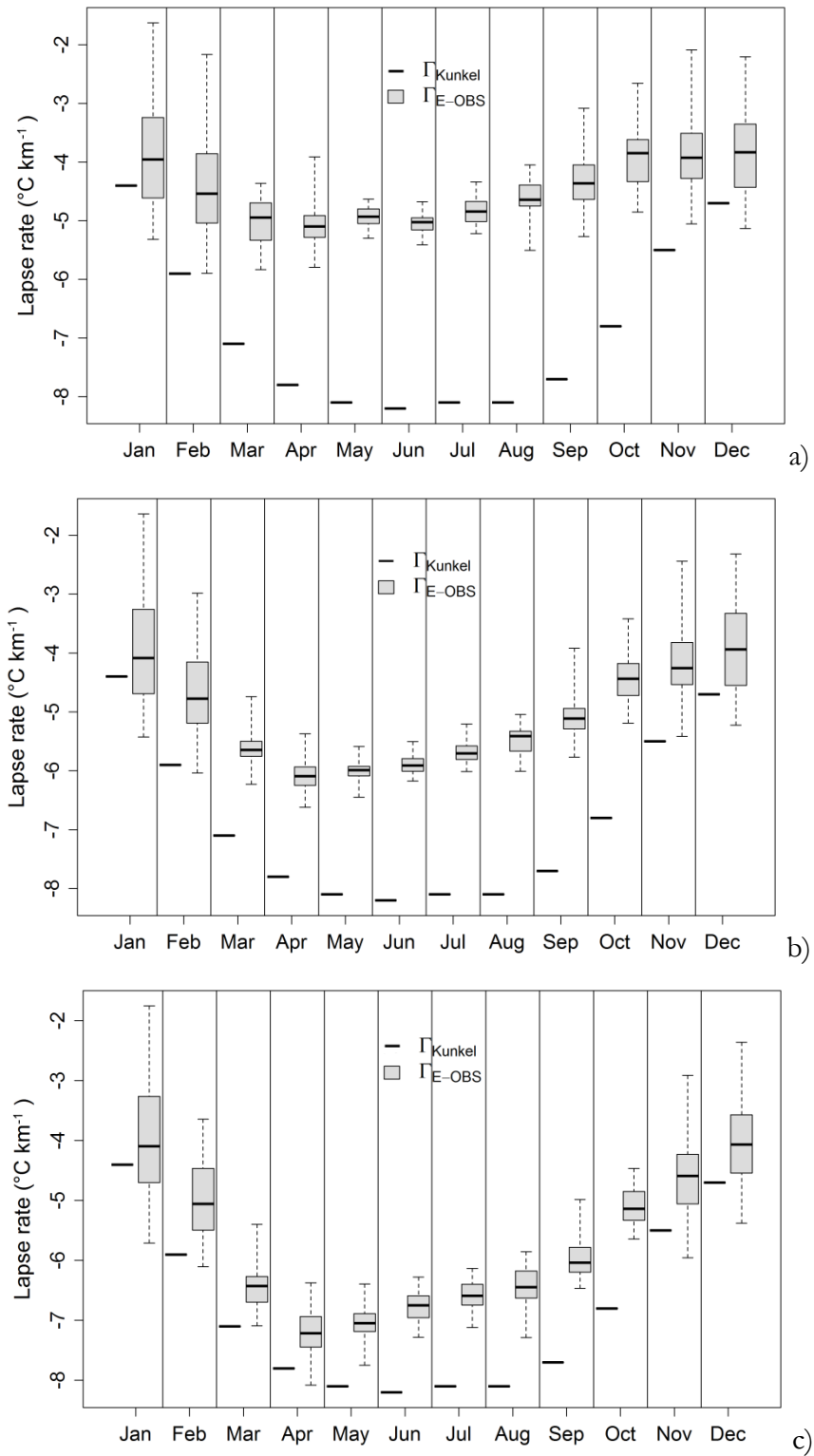
Figure 3.22: Boxplots of monthly lapse rates. a) for T_n, b) for T_g, and c) for T_x. Thick horizontal lines in the boxes represent the median values from 1979-2010. Boxes indicate the inner-quantile range (25 % to 75 %) and the whiskers show the full range of the values.

Figure 3.23 shows the correlation between elevation and annual precipitation. The linear link is weak between these two variables, with an R^2 of only 0.14. This relationship does not work in this complex terrain. This again confirms the results that have been presented by Barry (2008), that it is difficult to find a general relationship between precipitation and elevation, due to the great variability in the interaction between atmosphere circulation and complex topographical characteristics. Therefore, in precipitation downscaling, variables representing atmosphere circulation should be considered, such as humidity.
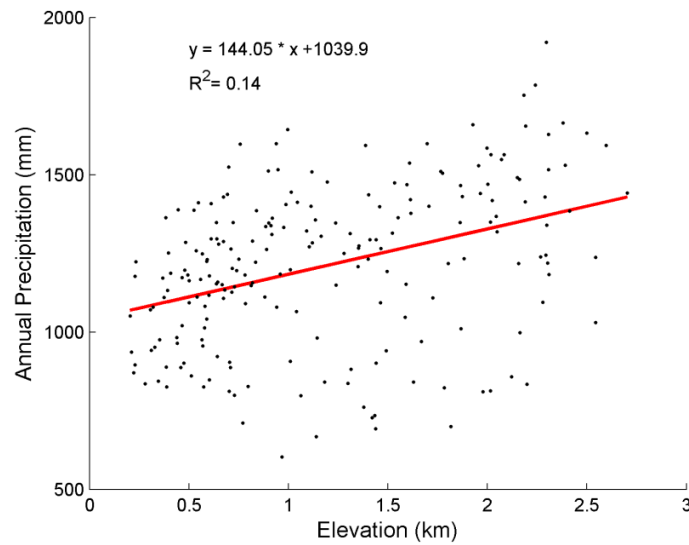
Figure 3.23: Linear regression between elevation and annual precipitation.

3.5 Discussion and Conclusion

This study evaluated the daily temperature and precipitation data from ERA-Interim, which is the latest reanalysis product developed by ECMWF. ERA-Interim daily total precipitation is compared with a high resolution gridded observation dataset (E-OBS) at 0.25°×0.25° grids for the period 1979-2010, over the central Alps (45.5-48°N, 6.25-11.5°E). The differences of temperature and precipitation within these two datasets are small in general. The correlations fall with a range of 0.96 to 1 and the mean anomaly ranges from -0.8 to 2.4 °C for T_g. The average anomaly of the whole area is 0.6 °C for both T_n and T_g, and 0.9 °C for T_x. T_n and T_g are overestimated by ERA-Interim at low altitudes and are underestimated on high mountain crests. The quantile analysis showed that, in general, the ERA-Interim data product generally agrees well with E-OBS observations, but ERA-Interim is less able to capture extreme temperature in complex terrains.

The linear regression between elevation and temperature showed that elevation effects between ERA-Interim geopotential heights and E-OBS grid heights could explain the main bias. Nevertheless, elevation is not the only factor. The fixed lapse rate may results in the bias. In addition, the ERA-Interim data has the large-scale errors, such as observation errors, model background errors, operator errors, and errors resulting from the interpolation from the original N128-reduced Gaussian grid to lat/long grids (Dee, 2005). In addition, although the best interpolation method has been tested and applied for E-OBS, the bias is difficult to eliminate, due to the limited observations and inconsistent time periods (Caesar et al., 2006; Hofstra et al., 2009; Kysely and Plavcova, 2010).

For precipitation, the effect of elevation is certainly not the main factor (with a low R^2 of 0.14). Dry/wet days are defined using several threshold values (0.5 mm, 1 mm, 5 mm, 10 mm and 20 mm). The result shows that ERA-Interim captures precipitation occurrence well, with a range of CR from 0.65 to 0.99 for 0.5 mm to 20 mm thresholds. However, the bias for the precipitation amount increases with increasing thresholds. The mean absolute error (MAE) varies between 4.5 mm day^{-1} and 9.5 mm day^{-1} on wet days for the entire area. In terms of mean annual cycle, ERA-Interim has almost the same standard deviation of the inter-annual variability of daily precipitation as E-OBS, 1.0 mm day^{-1}. Significant wet biases occurred in ERA-Interim throughout the warm season (May to August) and dry biases in the cold season (November to February).

The spatial distribution of mean annual daily precipitation shows that ERA-Interim significantly underestimates precipitation amount in high mountains and on the northern flank of the Alpine chain from November to March, whilst pronounced overestimation occurs for in the southern flank of the Alps. The poor representation of topographical characteristic such as grid height of the ERA-Interim model is possibly responsible for the bias (Decker et al., 2012). The comparison demonstrates that ERA-Interim precipitation amount needs bias correction for further alpine climate studies, although it reasonably captures precipitation occurrence. This critical evaluation not only diagnosed the data quality of ERA-Interim, but also provided evidence for effective reanalysis product downscaling and bias correction in complex terrains.

Chapter 4

Downscaling Temperature Based on Modeled Lapse Rate

4.1 Introduction

The near surface air temperature (T_a) is an important control for a large variety of environmental processes and influences the local as well as the global water, energy and matter cycle (Bolstad et al., 1998; Prihodko and Goward, 1997; Prince et al., 1998). Changes in T_a have a distinct influence on biogeochemical processes, the turbulent exchange between surface and atmosphere as well as on plant growth and many other components at the interface between earth surface and atmosphere (Bolstad et al., 1998; Nieto et al., 2011; Regniere, 1996; Stahl et al., 2006). Therefore, historic, current and future temperature time series are needed for analyzing possible changes and impacts on the environment (Barry, 1992; Pepin and Seidel, 2005). They can also provide reliable data for decision-makers (e.g. tourism planning) and model developers (Dodson and Marks, 1997; Maurer et al., 2002; Minder et al., 2010; Mooney et al., 2011).

The most common sources for T_a time series are meteorological stations. However, meteorological networks are sparse in complex terrains, in particular at high altitudes, such as in mountains. This is mainly due to difficulties with the installation and maintenance of the stations (Kunkel, 1989; Rolland, 2003). Hence, information about T_a has to be calculated on the basis of surrounding stations, which are usually far away from the point of interest. The T_a can also be calculated with the help of climate models, which usually have a limited spatial resolution

(Dodson and Marks, 1997; Ishida and Kawashima, 1993; Vicente-Serrano et al., 2003). Both methods tend to work well in homogeneous terrains, but tend to fail in heterogeneous terrains, where changes in the surface temperature can occur over short distances. Reasons for failure are the misrepresentations of key relationships between T_a and elevation (DeGaetano and Belcher, 2007) and the limitations of climate models to consider small-scale variations of the land surface.

Hence, lapse rates (Γ), which display the empirical relationship between T_a and altitude, are often used to interpolate measurements or to scale model results of T_a with respect to elevation as well as for generating the required small-scale information of T_a (e.g. Wörlen et al., 1999). One has to distinguish between near surface temperature and free air lapse rates in general. The first one is influenced by the surface energy balance and adiabatic effects while the second one is dependent on the adiabatic effect and the current stratification of the atmosphere (Cullen and Marshall, 2011; Marshall et al., 2007). Both kinds of lapse rates are used in this study and investigate their performance with respect to a correction of ERA-Interim model results. The most common methods typically assume lapse rates in the range of -6.0 °C km^{-1} (e.g. Dodson and Marks, 1997) to -6.5 °C km^{-1} (e.g. Lundquist and Cayan, 2007; Maurer et al., 2002; Stahl et al., 2006), consider some similarity to the theoretical pseudo adiabatic lapse rate (Hamlet and Lettenmaier, 2005) or to the monthly variability of the temperature gradient within the atmosphere (Kunkel, 1989; Liston and Elder, 2006). However, many studies have proven that a fixed lapse rate may be problematic since the values of the lapse rate can vary significantly within short time periods of less than a month (Lundquist and Cayan, 2007; Minder et al., 2010; Rolland, 2003). The reason for these variations can be traced back to topographical characteristics of an area (Cullen and Marshall, 2011; Mahrt, 2006), the synoptic circulation (Blandford et al., 2008; Cullen and Marshall, 2011; Marshall et al., 2007; Pages and Miro, 2010), the activity of the vegetation (Laughlin, 1982), seasonal variations with respect to the incoming radiation (Blandford et al., 2008; Rolland, 2003) and diurnal variations, e.g. due to a changing cloud cover (Minder et al., 2010). This lapse rate variability can only be monitored by dense meteorological station networks or by using alternative strategies that are able to cover the temporal and spatial variability of air temperature.

One of such strategies is using global or regional scale climate model temperature outputs (e.g. reanalysis data) for different pressure levels that can also be used for a characterization of lapse rates and a subsequent downscaling of modeled temperatures without a direct use of observations (Maraun et al., 2010). Mokhov and Akperov (2006) used NCEP/NCAR reanalysis temperature profiles to investigate the relationship of tropospheric lapse rates and global averages of monthly surface temperatures. However, they focused on large scale patterns rather than

testing this approach against local site data. In a similar way, Gruber (2012) applied the lowest seven pressure levels of NCEP data for the calculation of corrected surface temperatures. However, a detailed analysis of the quality of the method was not a focus.

This chapter presents and tests a newly developed elevation correction approach that is based on the European Centre for Medium Range Weather Forecast (ECMWF) reanalysis product ERA-Interim (Berrisford et al., 2011; Dee et al., 2011) with a focus on often critical Alpine environments. The method accounts for the temporal variability of lapse rates by using model internal temperature profiles. It allows for a scaling of 0.25°, 3-hourly ERA-Interim data to the point scale, and is tested and validated against two different, standard correction methods (one based on station measurements, and another one that uses fixed data from literature) at twelve meteorological stations located in mountainous environments in the German and the Swiss Alps.

4.2 Data and Methods

4.2.1 ERA-Interim data

ERA-Interim provides a variety of data in uniform latitude/longitude grids (0.25°, 0.5°, 0.75°, 1°, 1.125°, 1.5°, 2°, 2.5° and 3°). The parameters (except vegetation, soil type fields and wave 2D spectra) are interpolated from the original N128 reduced Gaussian grid using bilinear methods. The elevation dependency of the 2m temperature is not considered within the interpolation scheme. 3-hourly forecast data (03, 06, 09, 12, 15, 18, 21 and 24 UTC) initialized at 00 UTC from 1979-2010 which are projected on a grid of 0.25°×0.25° is applied. The used output variables are 2m temperature, surface geopotential, as well as temperature and geopotential height at 925 hPa, 850 hPa and 700 hPa levels. The geopotential height is calculated by the normalization of the geopotential over the gravity.

4.2.2 Test sites

The data from twelve test sites, all located in the German and Swiss Alps, have been used in the analysis. The stations are located within four different ERA-Interim grid elements. The stations can be seen as four clusters of three stations (one at the valley bottom, one at the crest region and a station in between). A detailed description of the measurements and of the location of the different stations is given in Figure 4.1 and Table 4.1. All measurements were aggregated to 3-hourly (T_{3h}) and daily (T_d) data for a later comparison with ERA-Interim data (Table 4.1). Days with missing values were excluded and were not used for any further analysis.
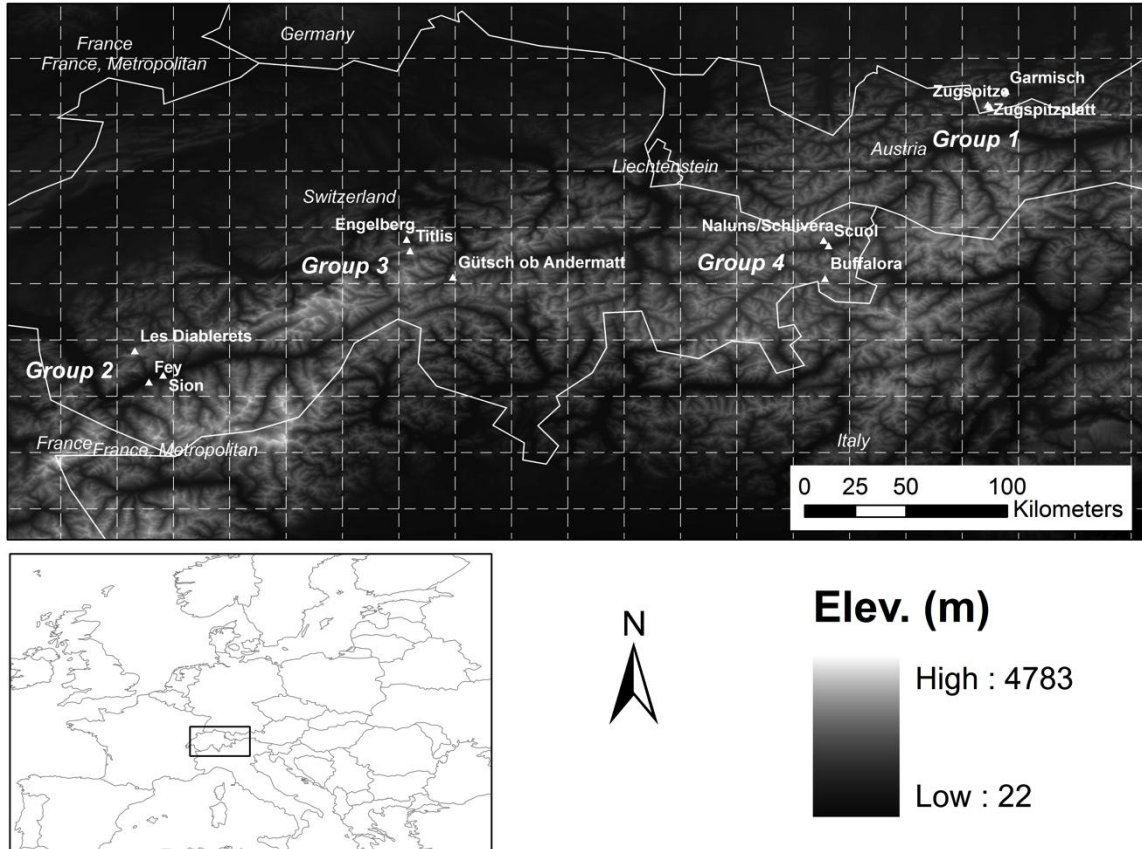
Figure 4.1: Location of the twelve meteorological stations (triangles), and ERA-Interim 0.25°×0.25° grids (dashed line). Twelve stations were clustered into four groups according to the different ERA-Interim grids. The elevation ranges from 22 to 4783 m a.s.l., with a DEM resolution of 90 m.

One important but difficult to answer question is, whether individual stations might be used by ERA-Interim for assimilation purposes. If assimilated, the ERA-interim predictions are not fully independent from the observed data which are subsequently used for calibration and validation of the suggested downscaling methods. However, even a direct contact with the ECMWF personnel could not give a clear answer to this question (Pappenberger, 2012). It is probable that the data of the stations Zugspitze, Garmisch and Sion are used for assimilation, given their status as WMO SYNOP stations (Dee et al., 2011; Simmons et al., 2010). According to the information of the ECMWF it can be assumed that at least the majority of the stations at Zugspitzplatt, Fey, Les Diablerets, Engelberg, Gütsch ob Andermatt, Titlis, Scuol, Buffalora and Naluns/Schlivera are not used by ERA-Interim and therefore represent fully independent dataset.

Table 4.1: Test sites information (ERA_height is the ERA-Interim model elevation).

	Site	latitude	longitude	Altitude (m a.s.l)	ERA_ height (m a.s.l)	Time Series
Group 1	Garmisch	47.48	11.07	719	1287	1979-2010
	Zugspitzplatt	47.41	11.00	2250		1999-2010
	Zugspitze	47.42	10.99	2964		1979-2010
Group 2	Sion	46.22	7.33	482	1408	2002-2004
	Fey	46.19	7.27	737		
	Les Diablerets	46.33	7.20	2966		
Group 3	Engelberg	46.82	8.41	1036	1432	1994-2010
	Gütsch ob Andermatt	46.65	8.62	2287		
	Titlis	46.77	8.43	3040		
Group 4	Scuol	46.79	10.28	1304	1818	1999-2010
	Buffalora	46.65	10.27	1968		
	Naluns/Schlivera	46.82	10.26	2400		

4.2.3 Downscaling Methods

Lapse rates (Γ) describe the decrease of T_a with elevation. Equation 3.1 is used for all of the four presented correction methods, but the calculation of T_{ref} and Γ varied. In this chapter, T_{ref} is the reference temperature, which was either defined by the ERA-Interim 2 m temperature (T_{ERA_2m}) or the ERA-Interim temperature at the 850 hPa pressure level (T_{ERA_850}).

This test used four different methods for calculating Γ, Method I) specific monthly lapse rates ($Γ_S$) extracted from the literature, Method II) measured lapse rates ($Γ_M$), which were calculated on the basis of two meteorological stations covering the maximum elevation range of the area, and Method III) and IV) ERA-Interim lapse rates ($Γ_{700\_925}$ and $Γ_{850\_925}/Γ_{700\_850}$) which were calculated on the basis of ERA-Interim temperatures at different pressure levels. Method I made use of monthly values of $Γ_S$, which are calculated from the monthly mean maximum and minimum temperature derived from stations published by Kunkel (1989) and Liston and Elder (2006) (Table 3.1).

Method II used measured data from two meteorological stations for calculating 3-horly and daily lapse rates. The highest and lowest elevated stations per group for this calculation are used (Table 4.1). The lower elevated station represents the conditions at the valley bottom while the higher elevated station is representative for the crest region. Method II was used as a benchmark to compare to all other methods. Since stations at high elevation that are able to properly represent the meteorology are rare, other correction methods that are independent of surface measurements have to be developed (Blandford et al., 2008; Pages and Miro, 2010; Rolland, 2003).

In the following, two methods are introduced based on ERA-Interim internal temperature gradients for addressing this need. Temperatures as well as the geopotential heights of the 700 hPa, 850 hPa and 925 hPa levels were used for calculating Γ_{700_925}, Γ_{850_925} and Γ_{700_850}. This was done by calculating temperature differences between the 700 hPa and 850 hPa (Γ_{700_850}), 700 hPa and 925 hPa (Γ_{700_925}), as well as 850 hPa and 925 hPa (Γ_{850_925}) level (Figure 4.2) and by dividing through the differences in the corresponding geopotential heights.
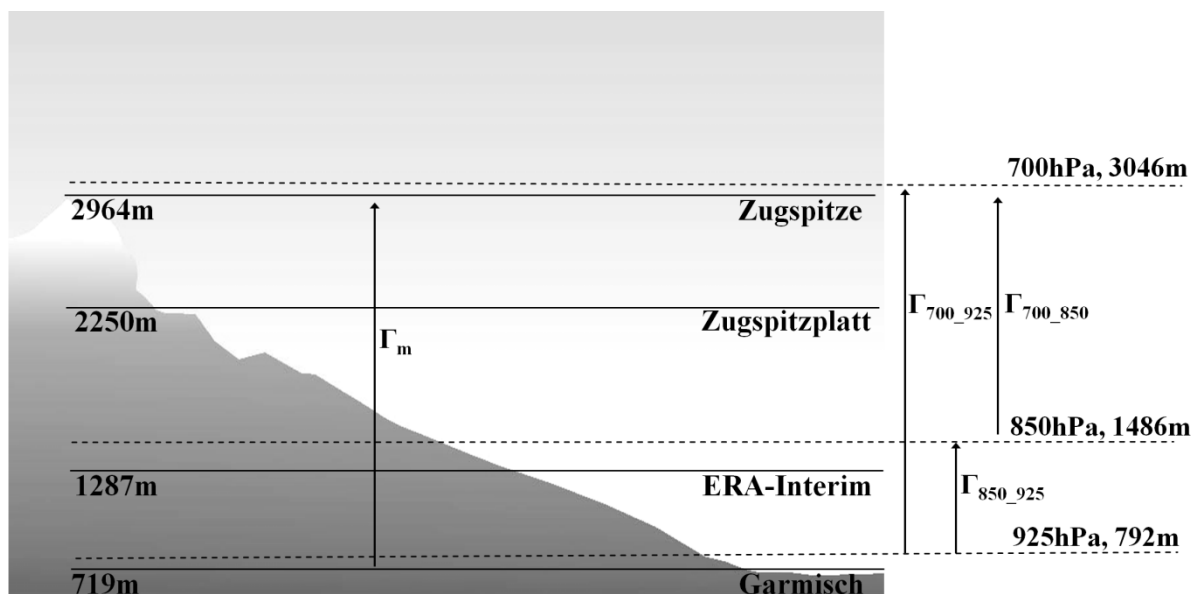
Figure 4.2: Schematic illustration of measured lapse rate and ERA-Interim derived lapse rates for Group 1. Γ_m was calculated based on the two largest-elevation-difference stations (e.g. Garmisch and Zugspitze station). Temperatures as well as the geopotential heights of the 700 hPa, 850 hPa and 925 hPa levels were used for calculating Γ_{700_925}, Γ_{850_925} and Γ_{700_850}. The dashed line represents the mean geopotential height of the corresponding pressure level (for the period 1979-2010).

A differentiation into Γ_{850_925} and Γ_{700_850} was introduced to accommodate for different atmospheric conditions and therefore dominant controls on surface temperature. While low

altitudes are often influenced by local circulation patterns (represented by Γ_{850_925}), temperature conditions at higher elevations (represented by Γ_{700_850}) are more representative to free air flow conditions (Mahrt et al., 2001; Pepin and Seidel, 2005). Tabony (1985) noted that the transition from local circulation dominated to free air-dominated temperatures could be found at approximately 1400 m a.s.l. within the Austrian Alps. This estimate is used for splitting up the temperature gradient into a lower, local flow dominated and a higher, free air flow dominated, gradient. For test sites, the 850 hPa level varying around 1500 m a.s.l., was used as a transition level dividing the local circulation dominated zone, from the free air flow dominated zone. This study used T_{ERA_850} instead of T_{ERA_2m} as a basis for the calculation of the elevation correction for locations higher than 1500 m. Figure 4.2 illustrates (for stations in group 1 as an example) the different parameters used in Eq. 3.1. Method III uses T_{ERA_2m} and Γ_{700_925} for the calculation of the temperature (T_a) at Garmisch station and T_{ERA_850} and Γ_{700_925} for Zugspitze and Zugspitzplatt stations. In Method IV, T_{ERA_2m} and Γ_{850_925} are the basis for the calculation of T_a at Garmisch station and T_{ERA_850} as well as Γ_{700_850} for Zugspitze and Zugspitzplatt stations (Table 4.2).

Table 4.2: Applied lapse rate (Γ) and reference temperature (T_{ref}) of four correction methods for twelve test stations.

Method	Γ	T_{ref}	Station
Method I	Γ_S	T_{ERA_2m}	All
Method II	Γ_m	T_{ERA_2m}	All
Method III	Γ_{700_925}	T_{ERA_2m}	< 1500 m a.s.l.
	Γ_{700_925}	T_{ERA_850}	> 1500 m a.s.l.
Method IV	Γ_{850_925}	T_{ERA_2m}	< 1500 m a.s.l.
	Γ_{700_850}	T_{ERA_850}	> 1500 m a.s.l.

4.3 Results

4.3.1 Validation of the original ERA-Interim temperature data

In a first step, the quality of the uncorrected ERA-Interim data was analysed. A very good agreement between ERA-Interim and E-OBS data with high correlation values was found in Chapter 3. The mean average error (MAE) between the two datasets becomes larger in the Alpine parts of the test area and can be connected to elevation differences between ERA-Interim

model elevations and E-OBS grid elevations. The elevation-dependent analysis shows that the existing errors can be well connected to elevation effects and that the large scale error of ERA-Interim is small in general. A comparison of ERA-Interim results with the available meteorological stations underlines these results (Figure 4.3). It can be seen that the 0.25° ERA-Interim results show large deviations with respect to point measurements. This is especially true in case the elevation of the stations differ significantly from mean elevation of the corresponding ERA-Interim grid elements. The largest biases for the higher elevated stations are found, while the stations located at the valley bottom show the highest accordance to the model (Table 4.3).
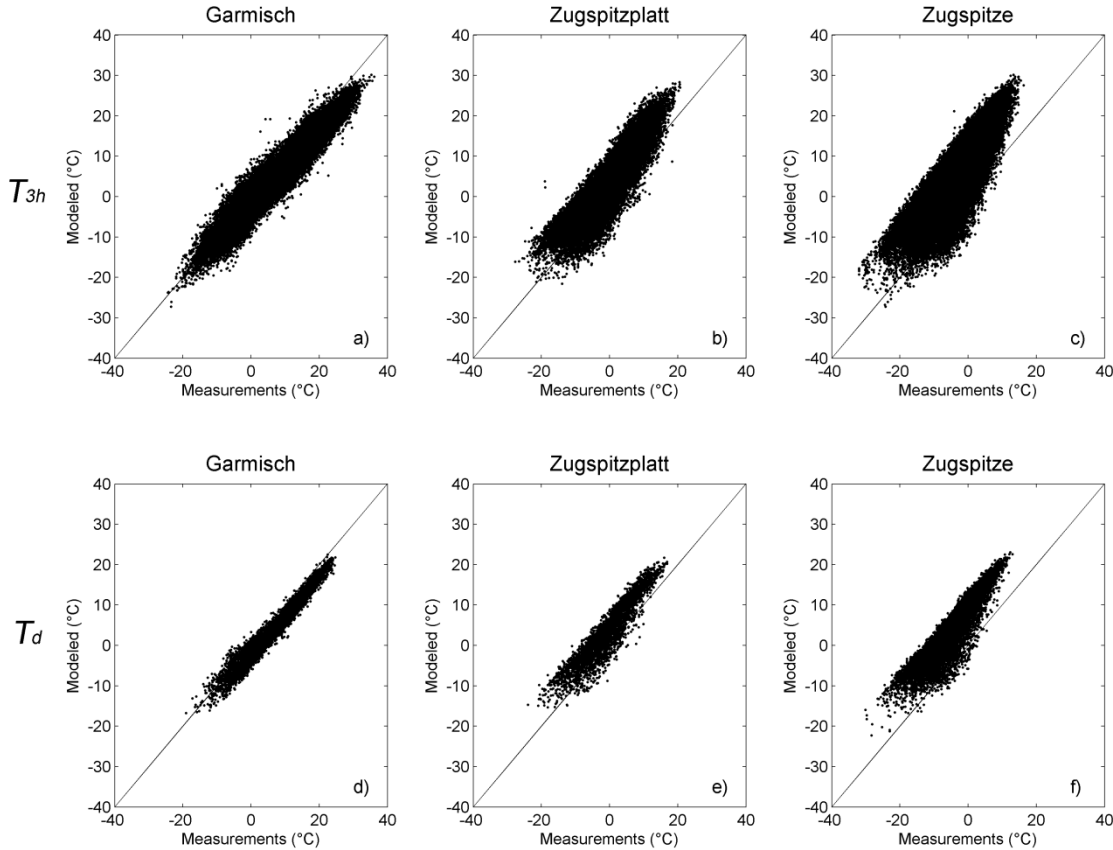
Figure 4.3: The scatter plots show the comparison of 3-hourly ERA-Interim 2 m temperature and meteorological stations for Group 1, (a) Garmisch station (1979-2010), (b) Zugspitzplatt station (1999-2010) and (c) Zugspitze station (1979-2010). All the related accuracy measures can be found in Table 4.3.

Table 4.3: Comparison of ERA-Interim 2 m temperature with 3-hourly and daily data of twelve meteorological stations. The NSE, as well as the RMSE and MAE in °C are also listed, and the elevations (m) are labeled in brackets.

Group 1	Garmisch (719 m)			Zugspitzplatt (2250 m)			Zugspitze (2964 m)		
	NSE	RMSE	MAE	NSE	RMSE	MAE	NSE	RMSE	MAE
T_{3h}	0.85	3.45	2.93	0.45	5.55	4.84	-1.00	9.92	9.22
T_d	0.85	3.03	2.76	0.51	4.95	4.47	-0.93	9.52	9.09
Group 2	Sion (482 m)			Fey (737 m)			Les Diablerets (2966 m)		
	NSE	RMSE	MAE	NSE	RMSE	MAE	NSE	RMSE	MAE
T_{3h}	0.50	6.20	5.76	0.48	5.77	5.32	-0.79	8.61	7.78
T_d	0.43	6.00	5.74	0.47	5.51	5.30	-0.74	8.20	7.59
Group 3	Engelberg (1036 m)			Gütsch ob Andermatt (2287 m)			Titlis (3040 m)		
	NSE	RMSE	MAE	NSE	RMSE	MAE	NSE	RMSE	MAE
T_{3h}	0.84	3.15	2.53	0.50	4.96	4.40	-0.93	9.41	8.65
T_d	0.87	2.69	2.22	0.57	4.49	4.14	-0.88	9.00	8.51
Group 4	Scuol (1304 m)			Buffalora (1968 m)			Naluns/Schlivera (2400 m)		
	NSE	RMSE	MAE	NSE	RMSE	MAE	NSE	RMSE	MAE
T_{3h}	0.78	4.15	3.60	0.87	3.44	2.49	0.80	3.35	2.78
T_d	0.78	3.77	3.49	0.91	2.52	1.83	0.86	2.73	2.39

4.3.2 Temporal variability of the lapse rates

The different lapse rates (Γ_S, Γ_M, Γ_{700_925} and $\Gamma_{850\_925}/\Gamma_{700\_850}$) show a different annual variability. Figure 4.4 illustrates the seasonal dynamics of measured and modeled lapse rates as well as those obtained from the literature. The latter ones do not show any inter-monthly variability as they are defined by a single value per month. It can be seen that the lapse rates are generally smaller in winter but showed a higher variability during these colder months (October to February). Warmer months are characterized by lapse rates in the range of -6 °C km^{-1} to -7 °C km^{-1} and by a low inter-monthly variability (April-August). March and September represent transition months, where the regime changed from winter to summer or from summer to winter conditions. The between-group-variability of the derived lapse rates also varies significantly. Group 2 shows the

lowest variability, due to the very short time period of data availability. Γ_S generally represents the largest temperature gradient and is significantly different from the measurements, especially during the summer months. Γ_{700_925} and $\Gamma_{850\_925}/\Gamma_{700\_850}$ show larger variations during winter time and dynamics which are closer to the measurements (Γ_M). Only the temporal dynamics of Group 4 are not well covered by the ERA-Interim lapse rates. This group is located in the central Alps were the respective ERA-Interim grid elements do also show a large deviation to the E-OBS data. The overall difference between measured and modeled lapse rates is in general small in summertime (June-August) and shows stronger deviations in winter time (November-February), possibly due to frequent local inversion events during winter months that cannot be reproduced by the ERA-Interim model.
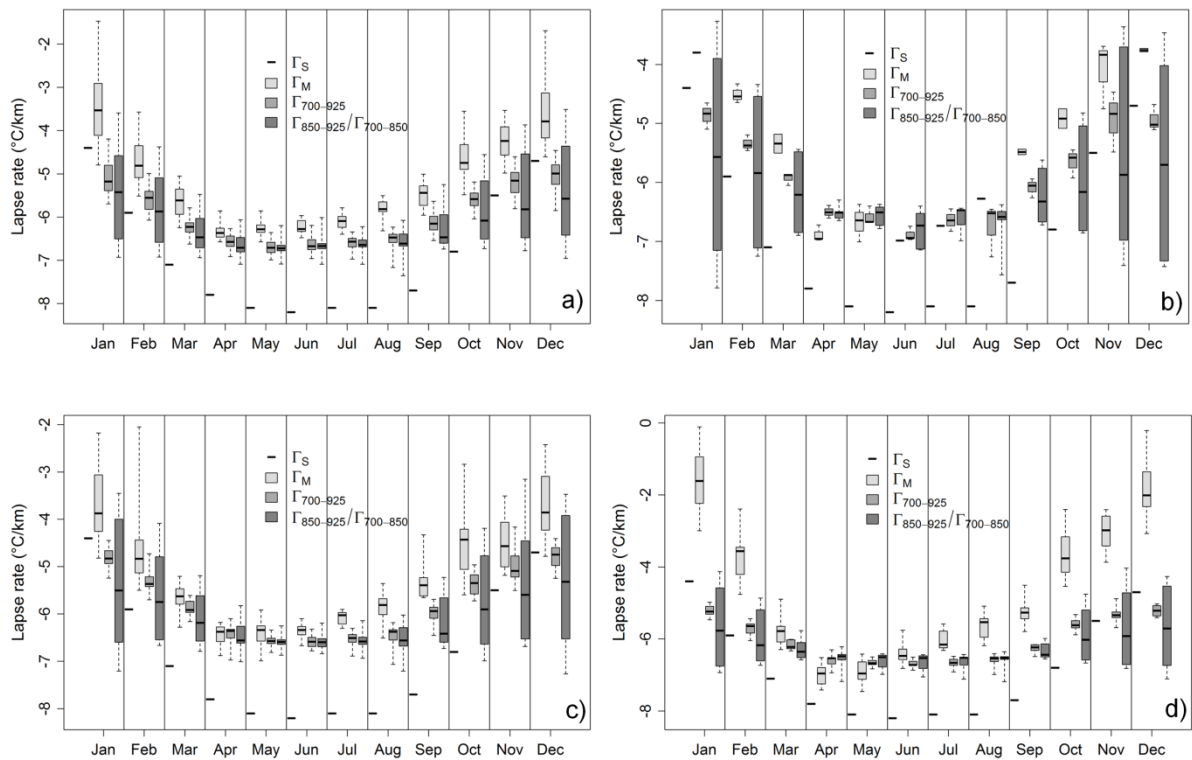
Figure 4.4. Boxplots of monthly lapse rates for (a) Group 1(1979-2010), (b) Group 2 (2002-2004), (c) Group 3 (1994-2010) and (d) Group 4 (1999-2010). Γ_S (short horizontal line), Γ_M (light gray), Γ_{700_925} (medium gray) and $\Gamma_{850\_925}/\Gamma_{700\_850}$ (dark gray). Thick horizontal lines in boxes show the median values. Boxes indicate the inner-quantile range (25 % to 75 %) and the whiskers show the full range of the values.

4.3.3 Evaluation of downscaling methods

In order to evaluate the presented correction methods, three statistical accuracy measures were used. The root mean square error (RMSE) and mean absolute error (MAE) are used for an assessment of the bias between downscaled temperature and observation (Eq. 3.2 and 3.3). The Nash-Sutcliffe efficiency coefficient (NSE) evaluates the performance of the correction methods using Eq. 4.1, which ranges from 1 (perfect fit) to minus infinity. A negative value of the NSE indicates that the model is a worse estimator than the mean of the observed data (Nash and Sutcliffe, 1970).

$$
NSE = 1 - \frac{\sum_{t=1}^{N}\left(T_o^t - T_d^t\right)^2}{\sum_{t=1}^{N}\left(T_o^t - \overline{T_o^t}\right)^2}
\tag{4.1}
$$

with T_o^t = observed temperature at time t, T_d^t = downscaled temperature at time t, and N = number of records.

In term of overall performance, 4 methods are compared by averaging NSE, RMSE and MAE statistics for all 12 test sites (Table 4.4). Method III and IV outperformed Method II moderately regardless of T_{3h} and T_d and Method I work worst. The specific performance of the four correction methods with respect to 3-hourly temperature data is summarized in Table 4.5. Figure 4.5 shows the results by taking Group 1 as the example. Method I work well for stations located in the valley bottom, show only moderate improvements for the average altitude stations and even failed for the higher elevated stations (Table 4.5 and Figure 4.5). Station Fey is an exception here showing the second best results when method I is applied. Method II delivered the best results for the valley stations, but showed also acceptable results for the average altitude and high altitude stations. However, Method III and IV outperformed Method II for seven out of eight average and high altitude stations. The reduction of the MAE for the valley stations was between 34.0 % (Engelberg) and 73.6 % (Sion), when using Method II. The MAE could be also improved for the average altitude stations (improvement between 53.8 % and 59.7 %) with the exception of Buffalora were less accurate than the original ERA-Interim results (2.49°C, method I; 2.67°C, Method II). The MAE at the high altitude stations was reduced between 1.2°C (Naluns/Schlivera) and 7.8°C (Zugspitze). Methods III and IV performed almost as well as our benchmark Method II, with particular good results for average and high altitude stations. Another interesting result can be found at the high altitude station Titlis. Method II provided lapse rates without any outliers while the other methods show significant outliers for the period from to December 4

1995 to February 28 1996. The measurements show frequent and rapid changes with respect to temperature. The temperatures are reaching high values around 30 °C and fall back to normal values afterwards while the surrounding station does not show any anomalies. Therefore, a measurement error at station Titlis has to be expected. Method II which is based on the measurements is consequently forcing the model results into the direction of the nonconforming measurements. The other methods which are independent of the station measurements do not reproduce this error. This is another example why methods which are independent of surface data of value in high alpine areas were error-prone measurements are common. Furthermore, Methods III and IV performed very well in case the gap between measurement and model became bigger. The MAE at the average altitude stations could be reduced by 57.9 % to 74.7 % and by 59.4 % to 87.9 % for the high altitude stations. Nevertheless, the differences between methods III and IV are negligible and an application of the simpler Method III seems to be sufficient, at least for the stations used in here.

Table 4.4: Comparison of measurements with downscaled 3-hourly and daily data for 4 methods by averaging NSE, RMSE and MAE statistics for all 12 test sites.

	T_{3h}			T_d		
Method	NSE	RMSE	MAE	NSE	RMSE	MAE
I	0.78	3.37	2.60	0.85	2.59	2.09
II	0.91	2.31	1.77	0.95	1.63	1.25
III	0.92	2.21	1.64	0.95	1.57	1.15
IV	0.92	2.21	1.65	0.95	1.56	1.14

Table 4.5: Comparison of measurements with downscaled 3-hourly and daily data for group 1-4. The NSE as well as the RMSE and MAE in °C are also listed.

Group 1		Garmisch			Zugspitzplatt			Zugspitze		
	Method	NSE	RMSE	MAE	NSE	RMSE	MAE	NSE	RMSE	MAE
T_{3h}	I	0.91	2.70	2.13	0.71	4.07	3.11	0.59	4.47	3.46
	II	0.96	1.84	1.40	0.88	2.56	1.95	0.93	1.84	1.40
	III	0.92	2.44	1.87	0.91	2.31	1.74	0.96	1.45	1.12
	IV	0.91	2.62	1.99	0.91	2.29	1.73	0.94	1.73	1.33
T_d	I	0.94	2.00	1.64	0.79	3.22	2.61	0.74	3.47	2.89
	II	0.98	1.07	0.82	0.94	1.76	1.37	0.98	1.07	0.82
	III	0.95	1.69	1.29	0.96	1.36	1.07	0.98	1.00	0.78
	IV	0.94	1.91	1.43	0.97	1.31	1.03	0.96	1.32	1.00
Group 2		Sion			Fey			Les Diablerets		
	Method	NSE	RMSE	MAE	NSE	RMSE	MAE	NSE	RMSE	MAE
T_{3h}	I	0.92	2.47	1.98	0.90	2.60	2.00	0.46	4.74	3.68
	II	0.94	2.03	1.52	0.83	3.21	2.46	0.90	2.03	1.52
	III	0.92	2.45	1.89	0.87	2.88	2.24	0.89	2.13	1.31
	IV	0.93	2.32	1.81	0.90	2.55	1.99	0.90	2.04	1.25
T_d	I	0.94	1.92	1.54	0.93	1.94	1.47	0.60	3.91	3.26
	II	0.96	1.56	1.15	0.89	2.46	1.90	0.94	1.56	1.15
	III	0.94	1.90	1.46	0.92	2.18	1.64	0.92	1.79	1.02
	IV	0.95	1.74	1.35	0.94	1.83	1.40	0.93	1.62	0.86

Table 4.5: continued

Group 3		Engelberg			Gütsch ob Andermatt			Titlis		
	Method	NSE	RMSE	MAE	NSE	RMSE	MAE	NSE	RMSE	MAE
T_{3h}	I	0.89	2.60	2.01	0.78	3.33	2.52	0.56	4.50	3.44
	II	0.92	2.19	1.67	0.89	2.35	1.78	0.89	2.19	1.67
	III	0.90	2.51	1.89	0.95	1.54	1.18	0.92	1.92	1.18
	IV	0.90	2.48	1.86	0.95	1.50	1.16	0.92	1.94	1.24
T_d	I	0.93	2.02	1.61	0.86	2.57	2.05	0.70	3.57	2.89
	II	0.96	1.53	1.18	0.95	1.59	1.19	0.95	1.53	1.18
	III	0.94	1.82	1.38	0.98	1.01	0.77	0.95	1.48	0.88
	IV	0.94	1.85	1.41	0.98	0.96	0.74	0.95	1.51	0.97
Group 4		Scuol			Buffalora			Naluns/Schlivera		
	Method	NSE	RMSE	MAE	NSE	RMSE	MAE	NSE	RMSE	MAE
T_{3h}	I	0.94	2.26	1.80	0.89	3.21	2.46	0.79	3.45	2.66
	II	0.95	2.00	1.57	0.86	3.51	2.67	0.93	2.00	1.57
	III	0.94	2.23	1.75	0.89	3.22	2.46	0.96	1.47	1.10
	IV	0.93	2.38	1.87	0.89	3.16	2.42	0.96	1.51	1.13
T_d	I	0.97	1.43	1.14	0.93	2.21	1.59	0.85	2.85	2.34
	II	0.97	1.51	1.23	0.92	2.43	1.72	0.96	1.51	1.23
	III	0.97	1.49	1.18	0.93	2.18	1.57	0.98	0.99	0.78
	IV	0.96	1.58	1.23	0.94	2.14	1.55	0.98	0.95	0.75

Figure 4.6 illustrates the performance of all 4 methods with respect to daily average temperatures also by taking Group 1 as the example. While the accuracy of the correction results was similar when compared to the use of 3-hourly data, some additional interesting aspects can be analyzed for the aggregated data. For example, daily averages as well as daily minima and maxima temperature data are often used for characterizing local sites given current or predicted future climate conditions. Figure 4.6 clearly shows that the results at the lower end of the temperature spectrum were overestimated while warmer temperatures were underestimated. The extrapolation of the original ERA-Interim data or of data downscaled using Method I would therefore lead to a

systematic misinterpretation of minimum and maximum values. This effect could only be eliminated when site specific lapse rates are used. This again is a strong argument against a general application of lapse rates, which are only oriented on stationary temperature gradient, but which do not factor in the local characteristics of a specific site.
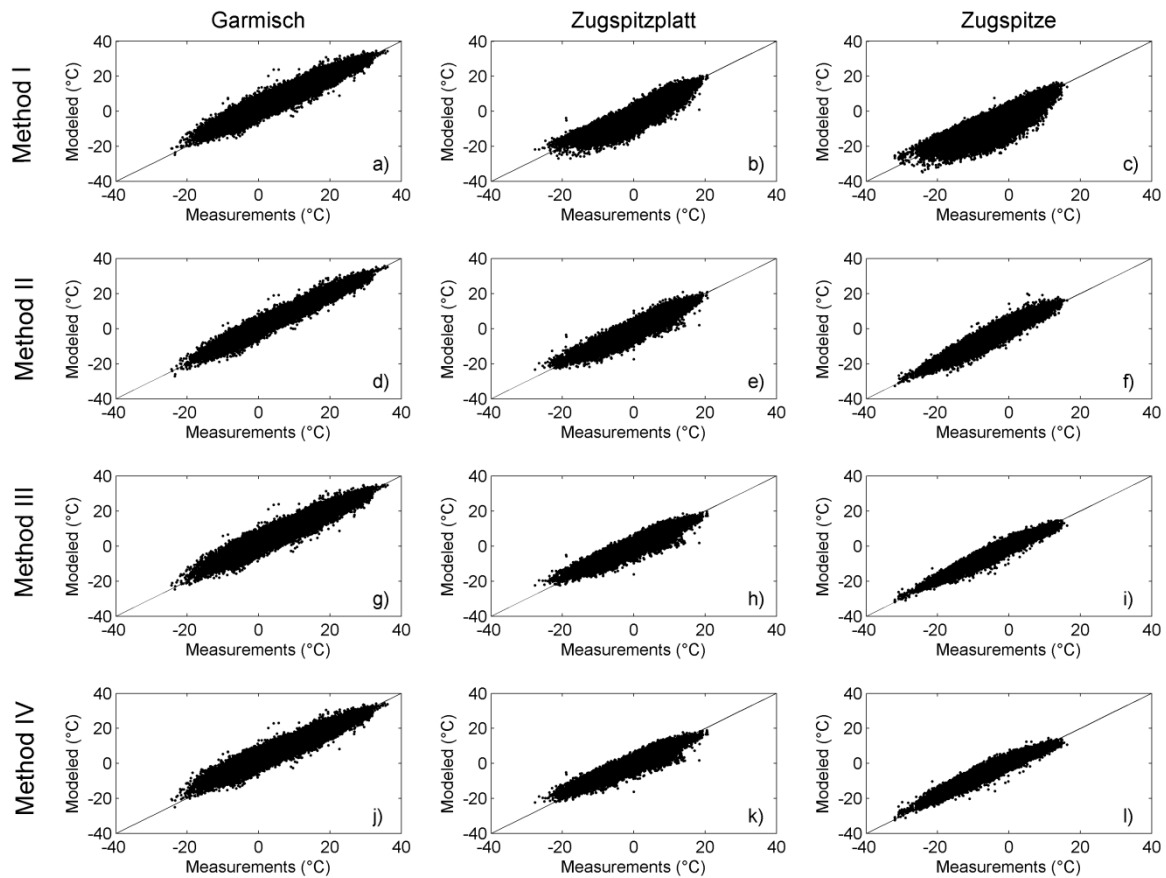
Figure 4.5: The scatter plots show the comparison of measured and modeled 3-hourly temperatures for Group 1. (a) shows the results of Method I for Garmisch from 1979-2010, (b) shows the results of Method I for Zugspitzplatt from 1999-2010 and (c) shows the results of Method I for Zugspitze from 1979-2010. (d)-(f) show the results for Method II, (g)-(i) for Method III and (j)-(l) those for Method IV. All the related accuracy measures can be found in Table 4.5.
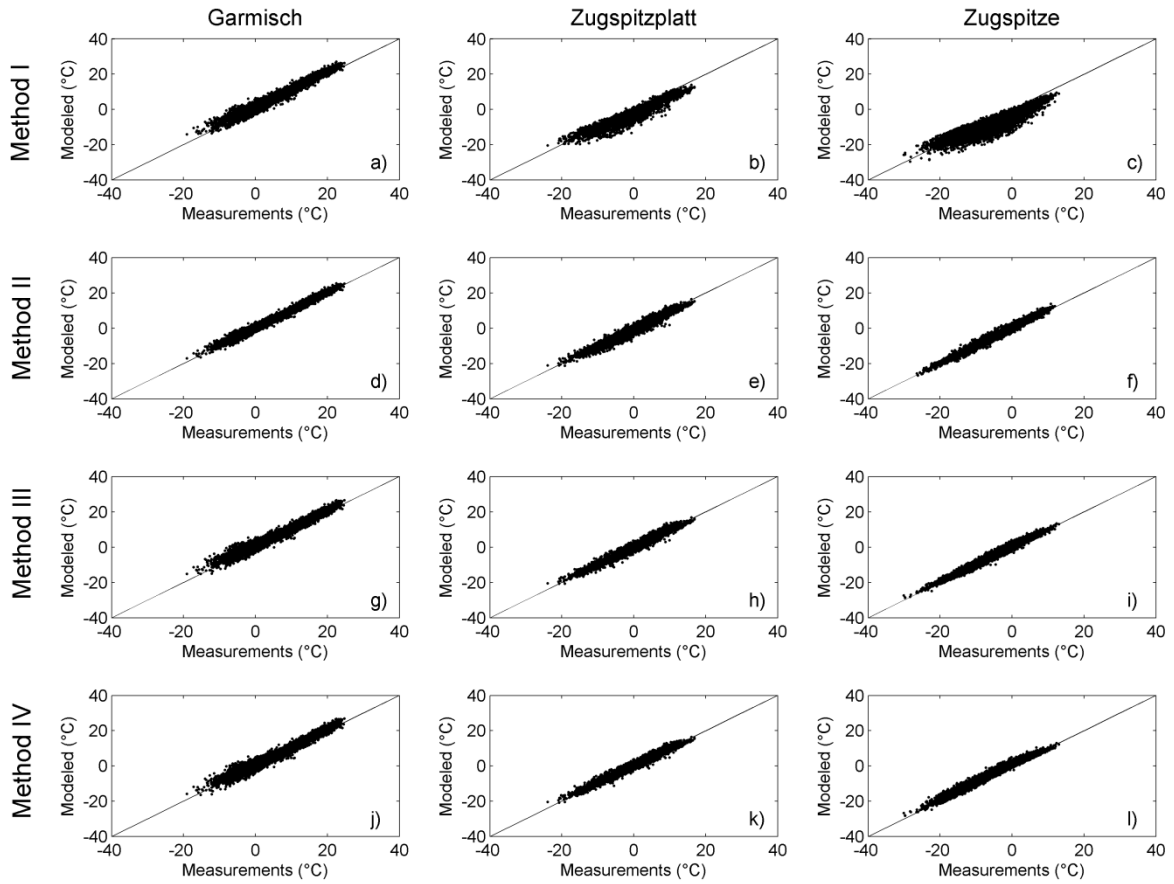
Figure 4.6: The scatter plots show the comparison of measured and modeled daily temperatures for Group 1. (a) shows the results of Method I for Garmisch from 1979-2010, (b) shows the results of Method I for Zugspitzplatt from 1999-2010 and (c) shows the results of Method I for Zugspitze from 1979-2010. (d)- (f) show the results for Method II, (g)-(i) for Method III and (j)-(l) those for Method IV. All the related accuracy measures can be found in Table 4.5.

Figure 4.7 shows downscaled ERA-Interim temperatures in unobserved area using Method III based on DEM (90 m) at January 1 1979 12 UTC. Taking Group 1 as the example, the gridded ERA-Interim temperature is -11.5 °C, which significantly overestimated for Zugspitze (-21 °C) and underestimated for Garmisch (-9 °C). Using Method III, ERA-Interim temperature was downscaled into 90 m grid (DEM resolution). The downscaled temperature for Zugspitze was -23.9 °C while for Garmisch was -7.7 °C. The biases are both improved by downscaling model, especially for Zugspitze station. Zugspitzplatt station, which has no record at January 1 1979 12 UTC, but the downscaled temperature was obtained by the model, -19.6 °C. This again illustrated that the downscaling model based on ERA-Interim internal lapse rate is independent of observations.
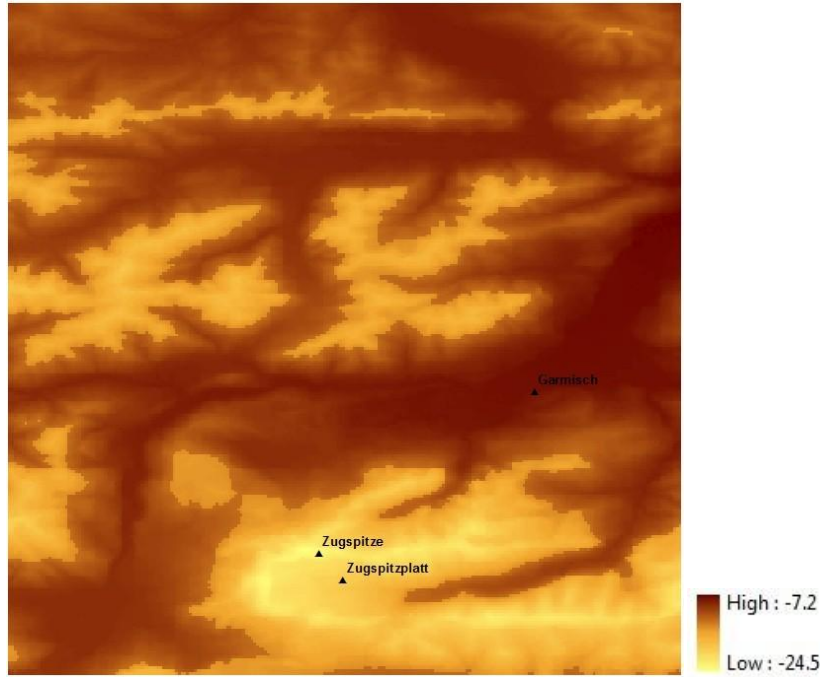
Figure 4.7: Downscaling ERA-Interim temperature at 90 m grid using Method III. Data time: January 1 1979 12 UTC, ERA-Interim gridded mean temperature: -11.5 °C, Zugspitze temperature: -21 °C, Garmisch temperature: -9 °C, and no records for Zugspitzplatt.

4.4 Conclusion

In the previous sections correction methods for ERA-Interim temperature data on the basis of lapse rates have been described and analyzed. Certainly, the total error between a station measurement and an ERA-Interim prediction is not only due to the elevation difference between the ERA-Interim grid average and the individual site. Other factors like large scale biases of ERA-Interim, observation errors, model background errors, operator errors, errors resulting from the interpolation from original N128 reduced Gaussian grid to latitude/longitude grids and others can affect the observed difference between model and measurements (Dee, 2005; Dee et al., 2011).

The results demonstrates that the large scale biases of ERA-Interim for temperature are very small except for regions were the elevation differences between model grid and real world are high, as for example in the central Alps. Also, the total integral error between model and measurement was strongly reduced by using lapse rate approaches for elevation correction. In that context ERA-Interim internal lapse rate showed a better performance than observed lapse rate and reduced the RMSE and MAE for high altitudes. However, it has to be noted that still for

some periods and locations significant differences between modeled and observed lapse rates could be observed.

The comparison between ERA-Interim 2 m temperature and E-OBS gridded data for the period from 1979 to 2010 indicates that elevation is the driving force for the observed error which should be therefore correctable via elevation based approaches like lapse rates. Subsequently, 0.25°×0.25° 3-hourly and daily ERA-Interim 2 m temperature data were compared with local measurements at twelve stations within the German and Swiss Alps. The comparison has illustrated that there is a need for a correction of ERA-Interim data if it should be used at a given point in the mountains. The results in Table 4.3 make clear that a correction is heavily needed for accounting for elevation driven temperature variations in heterogeneous mountain terrain, which cannot be represented by the original ERA-Interim grid.

Four different methods were used to derive the needed lapse rates Γ: a fixed monthly lapse rate (Γ_S) extracted from the literature (Method I); a measured lapse rate (Γ_M) (Method II); and ERA-Interim model internal lapse rates (Γ_{700_925} and $\Gamma_{850\_925}/\Gamma_{700\_850}$) derived from predictions at different pressure levels (Method III and IV).

Observed changes of lapse rates with elevation and with time, demonstrated that the use of fixed lapse rates (Γ_S) were not satisfactory and led to large biases between corrected and locally measured temperature values, especially for high elevation stations. Method II represented an almost ideal situation where the complete vertical elevation/temperature gradient is covered by two stations providing continuously measured lapse rates. While this approach provided the best results, it would be interesting to analyze how far these measured lapse rates could be extrapolated in a spatial context. A major disadvantage of Method II is its dependency on the availability of meteorological stations; only very few places in mountainous and high altitude regions worldwide can offer such a station setup. Furthermore, the usage of measured lapse rates can lead to the fact that the model is forced into the direction of implausible temperatures if one of the stations which are used for calculating the lapse rate delivers incorrect measurements.

Method III and IV represent alternatives for deriving temperature lapse rates by using (global climate) model (here ERA-Interim) internal lapse rates from representative pressure levels. Both methods showed a convincing performance when compared to measured data of the twelve stations, again especially for those in higher elevations. The ERA-Interim internal lapse rate is a useful tool for correcting the original output data to the station scale, even if they underestimating the observed lapse rates for the whole season with all of the occurring variations.

The additional implementation of an internal baseline at approximately 1500 m and the calculation of separate lapse rates above and below (Method IV), allowed a vertical differentiation and the consideration of local circulation effects (below) and the dominance of free air conditions (above) on the temperature distribution (Blandford et al., 2008; Mahrt et al., 2001; Rolland, 2003) . However, results only showed minimal differences between Method III and IV for the used test sites. Further validation is carried out with help of FLUXNET tower observations in Chapter 6.

Chapter 5

Downscaling Precipitation Using Lasso Algorithm

5.1 Introduction

Precipitation is one of the most sensitive variables for a large variety of environmental processes and it influences the local as well as the global water, energy and matter cycle (Beuchat et al., 2011; Chandler and Wheater, 2002; Guan et al., 2009). Precipitation variations in spatial distribution and amount directly influence the water resources on the local, the regional and the global scale, which adversely affect the socio-economic-ecological aspects (Benestad et al., 2007; Bray et al., 2011; Lamptey, 2008). Precipitation is also an essential input parameter for land surface models in fields such as in hydrology, ecology and climatology (Daly et al., 2008; Fealy and Sweeney, 2007; Ferraris et al., 2003). Traditionally, precipitation is measured by rain gauge stations. However, most of them are located in homogeneous terrains. In complex terrains, few gauge stations exist due to difficulties with snow depth measuring and maintenance of stations which result in lack of long-term and high spatial resolution records (Anders et al., 2007). In order to meet this challenge, in the past decades, GCMs have been widely applied to meet the specific needs of environmental impact models by providing time series of precipitation and plausible scenarios of change (Fealy and Sweeney, 2007).

However, a defect related to coarse spatial resolution (~300 km) in GCMs limits their provision of reliable information for decision makers and impact model developers (Dodson and Marks, 1997; Maurer et al., 2002; Minder et al., 2010). Specifically, the GCMs only represent characteristics on a mean elevation of a grid box, which runs counter to the reality. Local processes, such as orographic precipitation formulation along mountain slopes, as well as snowpack accumulation and melting, are not represented in the coarse grids. Although RCMs nested in GCMs represent better descriptions of local scale characteristics, based on the finer spatial resolution of 10-50 km, they still do not satisfy the requirement of hydrological and

climatic impact models, which typically run on the scale of 0.1-1 km (Ahrens, 2003; Charles et al., 2004; Maraun et al., 2010; Xu, 1999).

Thus, the methods that attempt to bridge the scale discrepancy between coarse model data and finer local requirements are receiving much attention (Charlton et al., 2006; Guan et al., 2009; Hertig and Jacobeit, 2008; Spak et al., 2007). Dynamical downscaling and statistical downscaling are the two main approaches. The former is also called regional climate model (RCM). Chapter 1 gives a literature review for dynamical downscaling methods (Table 1.1). The latter approach establishes the statistical connections between large-scale circulation variables (predictors) and local observed variables (predictands) (Wilby and Wigley, 1997; Zorita and von Storch, 1999). Wilby and Wigley (1997) and Wilby et al. (2004) grouped SD methods into three categories: weather classification schemes, regression models and weather generators. Wilby et al. (2004) summarized the advantages and drawbacks of three SD methods (Chapter 1, Table 1.2).

Unlike temperature, it is difficult to find a general relationship between precipitation and elevation, due to the great variability in the interaction between atmosphere circulation and complex topographical characteristics (Barry, 2008). Maraun et al. (2010) reviewed precipitation downscaling methods comprehensively from the point of view of end users. For example, local scaling (LOCI) and quantile-mapping (QM) are the representative methods that directly correct GCMs or RCMs for local observations (Maraun et al., 2010), although some drawbacks are contained in LOCI and QM. Specifically, LOCI weakens the variation of future data because it adjusts the mean and variance of future precipitation time series while QM is less able to derive new extremes from observed distributions (Maraun et al., 2010). Other methods (not directly correction methods) have focused on investigating the relationship between local precipitation and large-scale atmosphere circulation, using variables that varied from simple linear regression to complicated non-linear models. Table 5.1 lists a small selection of previous studies on precipitation downscaling based on a variety of model datasets and methods.

Table 5.1: Literature review of precipitation downscaling methods.

Method	Predictor	Predictand	Region	Reference
Extended non-homogeneous hidden Markov Model (extended-NHMM)	gradient of sea level pressure, dew-point temperature depression at 850 hPa from NCEP-NCAR reanalysis	Daily precipitation	Southwest Australia	(Charles et al., 2004)
Auto-searched orographic and Atmospheric	Precipitation-elevation, aspect, and spatial gradient of atmospheric moisture	Monthly precipitation	Northern New Mexico	(Guan et al., 2005)

Effects Detrended Kriging (ASOADek)				
CCA and multiple regression	1000 hPa/500 hPa geopotential heights, and 1000 hPa specific humidity from NCEP-NCAR reanalysis	Monthly precipitation	Mediterranean	(Hertig and Jacobeit, 2008)
ANN to an analog model	mean sea-level pressure, 700 hPa relative humidity, 700 hPa horizontal wind components, and 500 hPa geopotential height data precipitation from the NCEP-NCAR Reanalysis	Daily precipitation	British of Canada	(Cannon, 2007)
Regression adding Inflation model	500 hPa geopotential height, 850 hPa temperature and 700 hPa specific humidity	Daily precipitation	Germany	(Burger and Chen, 2005; Yang et al., 2010)
Artificial Neural Network	Potential temperature, vertical component of the wind, specific humidity, air temperature, precipitable water, relative vorticity and moisture divergence flux	Daily rainfall	Paulo State, Brazil	(Ramirez et al., 2005)
CCA, and multivariate linear regression with ICA and PCA	500 hPa and 700 hPa geopotential heights, sea-level pressures, 500 hPa vertical pressure velcocities and 500-1000hPa geopentential thicknesses	Monthly precipitation	Turkey	(Tatli et al., 2004)
Censored quantile regression	Daily means of relative vorticity and vertical velocity, both at the 850 hPa pressure level and precipitable water from NCEP-NCAR Reanalysis	Extreme precipitation	Germany	(Friederichs and Hense, 2007)
ANN (RBF and MLP), SDSM	Vorticity at the surface and 850 hPa, specific humidity at 500 hPa,	Heavy daily precipitation occurrence and amounts	England	(Harpham and Wilby, 2005)
Statistical Downscaling model (SDSM)	Specific humidity at 500 hPa for both two regions. Near-surface relative humidity and near-surface southerly wind and near-surface vorticity	Daily precipitation	Eastern England and the Scottish Borders	(Wilby et al., 2003)
Regression model and ANNs	500 and 700 hPa height, 850 hPa temperature, sea level pressure, column relative humidity	Total daily and monthly precipitation	Indianapolis, USA	(Schoof and Pryor, 2001)

Geostatistical methods and regression model	Latitude, distance to Cantabrian sea, Maximum elevation in northward direction with a radius of 5 km, mean elevation with radius of 25km	Annual precipitation	Ebro Valley, Spain	(Vicente-Serrano et al., 2003)
Support Vector Machine (SVM)	Mean sea level pressure, pressure temperature, vorticity, divergence, wind direction, geopotential height, specific humidity, relative humidity etc.	Daily/Monthly precipitation	Taiwan, India	(Chen et al., 2010; Ghosh and Mujumdar, 2008; Kumar et al., 2008)
Stepwise linear regression	Mean sea level pressure, max and min temperature, dry and wet bulb temperature, relative humidity, vapor pressure etc.	Daily rainfall	Karnataka in India	(Agnihotri and Mohapatra, 2012; Benestad et al., 2007)
Generalized linear model	Mean temperature, Mean sea level pressure, geopotential height, relative humidity etc.	Daily precipitation	Ireland, Mediterranean	(Fealy and Sweeney, 2007; Hertig and Jacobeit, 2013)

Although numerous studies were carried out for different temporal precipitation and for varied locations, a general precipitation downscaling method still does not exist, especially in complex terrains. A separate predictor selection process (e.g. principal components analysis, empirical orthogonal functions and cluster analysis) was usually implemented before downscaling, in order to search for the most sensitive variables in precipitation regimes (Ghosh and Mujumdar, 2006; Harpham and Wilby, 2005; Hessami et al., 2008; Lundquist and Cayan, 2007; Schmidli et al., 2001; Schoof and Pryor, 2001; Wilby and Wigley, 2000). These procedures reduced the dimensionality of models by removing less relevant variables while some potential variables were excluded, due to their nonlinear interactions.

Here, a new machine learning method, the Lasso algorithm (Least absolute shrinkage and selection operator), is introduced for downscaling ERA-Interim precipitation data. Compared to the normal downscaling approach, Lasso is well-suited for sparse and possibly under-determined linear regression problems, as well as for joint estimation and continuous variable selection. Lasso allows for a scaling of 0.25°, daily ERA-Interim data to the point scale, and was tested and validated against three different methods, -LOCI, QM and stepwise regression- at 50 meteorological stations located in the high mountainous region of the central Alps.

5.2 Datasets

5.2.1 ERA-Interim

3-hourly forecast data (03, 06, 09, 12, 15, 18, 21 and 24 UTC) initialized at 00 UTC from 1983-2010, which are projected on a grid of 0.25°×0.25°, is applied here. 3-hourly forecasts data are aggregated into daily temporal scales according to observation measuring time. The 20 used output variables used are listed in Table 5.2.

Table 5.2: Used predictors from ERA-Interim dataset.

Abbreviation	Predictors
Surface variables	
P_{ERA}	ERA-Interim precipitation (mm)
MSLP	Mean sea-level pressure (hPa)
TCW	Total column water (mm)
U_{10}	10 meter U wind component (m s^{-1})
V_{10}	10 meter V wind component (m s^{-1})
WS_{10}	Wind speed derived from $WS_{10} = \sqrt{U_{10}^2 + V_{10}^2}$ (m s^{-1})
FG_{10}	10 meter wind gust (m s^{-1})
LSP	Large scale precipitation (mm)
Upper-atmosphere variables	
$H_{850}, H_{700}, H_{500}$	Geopotential height at 850 hpa, 700 hpa and 500 hpa (m)
$T_{850}, T_{700}, T_{500}$	Temperature at 850 hpa, 700 hpa and 500 hpa (°C)
$RH_{850}, RH_{700}, RH_{500}$	Relative humidity at 850 hpa, 700 hpa and 500 hpa (%)
$SH_{850}, SH_{700}, SH_{500}$	Specific humidity at 850 hpa, 700 hpa and 500 hpa (g kg^{-1})

5.2.2 Test sites

Daily total precipitation in the period 1983-2010 at 50 meteorological stations were downloaded through the interactive tools of IDAWEB, which is designed by MeteoSwiss (the Swiss Federal Office of Meteorology and Climatology) providing freely available and extensive archive data of ground level monitoring networks. Table 5.3 lists the information about stations and Figure 5.1 shows the locations of test sites. The observations and ERA-Interim data are processed for the time shift. The time period is partitioned into 1983-1994 for calibration and 1999-2010 for validation. The dry/wet day is defined using a 1 mm threshold. ERA-Interim grid data in which

test sites are located in are extracted from the datasets according to the coordinates of the sites. It is necessary to note that the data of the stations GUE, PAY and GVE are used for precipitation assimilation, given their status as WMO SYNOP stations (Dee et al., 2011; Simmons et al., 2010). According to the information of the ECMWF it can be assumed that the majority of the stations (47 of 50 sites) are not used by ERA-Interim and therefore represent a fully independent dataset.

Table 5.3: Test sites information. ERA-Interim grid height is also listed.

ID	Sites	Latitude	Longitude	Elevation (m)	Grid height (m)
COV	Piz Corvatsch	46.42	9.82	3305	1618
WFJ	Weissfluhjoch	46.83	9.81	2690	1722
SAE	Säntis	47.25	9.34	2502	1154
GSB	Col du Grand St-Bernard	45.87	7.17	2472	1493
GUE	Gütsch ob Andermatt	46.65	8.62	2287	1432
PIL	Pilatus	46.98	8.25	2106	1154
MLS	Le Moléson	46.55	7.02	1974	1193
SAM	Samedan	46.53	9.88	1709	1661
DOL	La Dôle	46.42	6.10	1670	699
CIM	Cimetta	46.20	8.79	1661	1281
SBE	S. Bernardino	46.46	9.18	1639	1532
ZER	Zermatt	46.03	7.75	1638	1552
CHA	Chasseral	47.13	7.05	1599	669
DAV	Davos	46.81	9.84	1594	1722
MVE	Montana	46.30	7.47	1427	1470
NAP	Napf	47.00	7.93	1403	1115
ULR	Ulrichen	46.50	8.30	1345	1435
SCU	Scuol	46.80	10.28	1303	1818
FRE	Bullet / La Frétaz	46.83	6.58	1205	818
DIS	Disentis / Sedrun	46.70	8.85	1197	1479
ROB	Poschiavo / Robbia	46.35	10.07	1078	1394
ENG	Engelberg	46.82	8.42	1035	1432
CDF	La Chaux-de-Fonds	47.08	6.80	1018	770
PIO	Piotta	46.52	8.68	990	1447
STG	St. Gallen	47.43	9.40	775	1027
VIS	Visp	46.30	7.85	639	1498
RUE	Rünenberg	47.43	7.88	611	701
FAH	Fahy	47.42	6.93	596	554
INT	Interlaken	46.67	7.87	577	1325
CHU	Chur	46.87	9.53	556	1668
SMA	Zürich / Fluntern	47.38	8.57	555	780
BER	Bern / Zollikofen	46.98	7.47	552	1008
TAE	Aadorf / Tänikon	47.48	8.90	539	897
GLA	Glarus	47.03	9.07	516	1312
PAY	Payerne	46.82	6.95	490	1030

WAE	Wädenswil	47.22	8.68	485	1011
NEU	Neuchâtel	47.00	6.95	485	849
SIO	Sion	46.22	7.33	482	1408
VAD	Vaduz	47.13	9.52	457	1226
PUY	Pully	46.52	6.67	455	1100
CGI	Nyon / Changins	46.40	6.23	455	835
LUZ	Luzern	47.03	8.30	454	1154
REH	Zürich / Affoltern	47.43	8.52	443	780
GUT	Güttingen	47.60	9.28	440	962
SHA	Schaffhausen	47.68	8.62	438	662
ALT	Altdorf	46.88	8.62	438	1193
KLO	Zürich / Kloten	47.48	8.53	426	780
WYN	Wynau	47.25	7.78	422	827
GVE	Genève-Cointrin	46.25	6.13	420	973
AIG	Aigle	46.33	6.92	381	1346
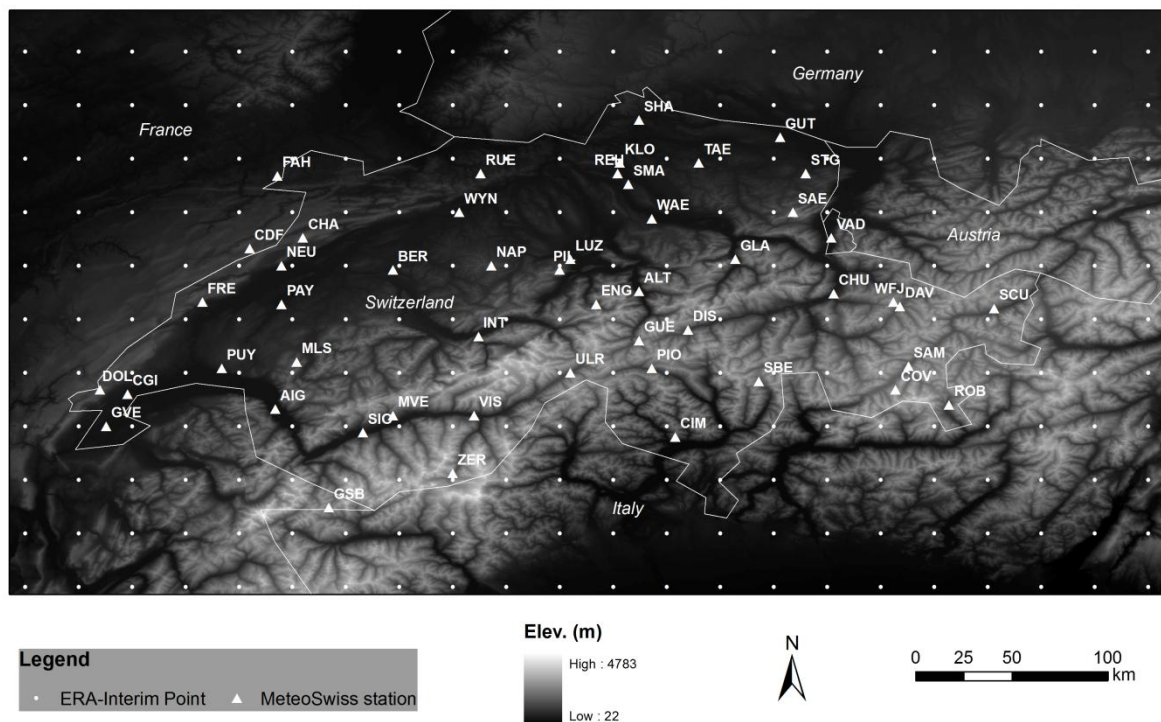
Figure 5.1: Location of the MeteoSwiss sites (triangles), and ERA-Interim 0.25°×0.25° points (dots). The elevation ranges from 22 to 4783 m a.s.l., with a DEM resolution of 90 m.

5.3 Methods

5.3.1 Local Scaling

Local Scaling is a robust method to directly correct GCM or RCM outputs for local observations. Although GCMs or RCMs are partly unrealistic due to their coarse resolution, they contain valuable information about the actual precipitation (Maraun et al., 2010). The assumption is realized by a so-called scaling factor, calculated from observation and climate model data of a reference period, which then is expanded to scenarios data. Here, LOCI is applied as the benchmark method for comparison with Lasso. LOCI was developed by Widmann and Bretherton (2000). Widmann et al. (2003) used it for scenario precipitation corrections. Not only GCMs, but also RCMs were corrected using the LOCI approach (Engen-Skaugen, 2007; Graham et al., 2007; Leander et al., 2008). Schmidli et al. (2006) further modified LOCI for precipitation occurrence and amount correction, separately. In this study, LOCI is implemented based on a monthly scaling factor which is calculated in three steps as follows:

$$Fre\left(P_{ERA} \geq P_{ERA}^{thres}\right) = Fre\left(P_{obs} \geq P_{obs}^{thres}\right) \tag{5.1}$$

$$SF = \frac{\overline{\left(P_{obs} \geq P_{obs}^{thres}\right)} - P_{obs}^{thres}}{\overline{\left(P_{ERA} \geq P_{ERA}^{thres}\right)} - P_{ERA}^{thres}} \tag{5.2}$$

$$P_t = \max\left(P_{obs}^{thres} + SF\left(P_{ERA}^{Val} - P_{ERA}^{thres}\right), 0\right) \tag{5.3}$$

where P_t is the target station precipitation, P_{ERA}^{Val} is the undownscaled ERA-Interim data for validation, P_{ERA}^{thres} ERA-Interim precipitation threshold, P_{obs}^{thres} the observation threshold, and the brackets present the frequency condition judgment function. Here, 1 mm is used to define wet/dry days and *SF* is the scaling factor. In the first step, an adjusted threshold for ERA-Interim data is found that matches the occurrence of wet/dry days, based on the 1 mm threshold of observation. In a second step, the scaling factor is obtained and then, finally, the target station precipitation is calculated.

5.3.2 Quantile-Mapping

Quantile-Mapping (QM) introduced by Panofsky and Brier (1968), is a popular statistical transformations approach to correct GCM and RCM outputs straightforwardly (Boe et al., 2007; Dobler et al., 2012; Gudmundsson et al., 2012; Hashino et al., 2007; Piani et al., 2010; Themeßl et

al., 2012; Themeßl et al., 2011; Wood et al., 2004). The distribution function (e.g. cumulative distribution function, cdf) of model precipitation is first adjusted to match the distribution of observations. Subsequently, this matched distribution is used for unbiased model (or future scenario) data. On this assumption, new extremes in the distribution are limited (Boe et al., 2007). The mapping is usually implemented based on empirical quantiles or quantiles of gamma distributions (Maraun et al., 2010; Themeßl et al., 2011). In this study, the corrected ERA-Interim can be obtained via

$$P_t = P_{ERA}^{Val} + \Delta f \tag{5.4}$$

$$\Delta f = f_{obs,cal}^{-1}(p) - f_{ERA,cal}^{-1}(p) \tag{5.5}$$

$$p = f_{ERA,cal}(P_{ERA}^{Val}) \tag{5.6}$$

where, $f_{obs,cal}^{-1}$ and $f_{ERA,cal}^{-1}$ is the inverse cdf (quantile function) of observations and ERA-Interim for calibration, respectively, $f_{ERA,cal}$ is the cdf (quantile function) of P_{ERA}^{Val}.

5.3.3 Stepwise Regression

Stepwise Regression (Stepwise hereafter) is an automatic procedure that combines a normal regression (Eq. 5.7) with predictor variable selection. Three main approaches are used in Stepwise according to the relevant selection sequence: forward selection, backward elimination or bidirectional elimination. Usually, forward selection starts without any variable and adds the most statistically significant variables until all resting variables are tested. The statistical criteria can be F-tests or other tests such as t-tests and R-square. In contrast, backward elimination starts with all variables and then removes the least significant (t-tests or R-square) variable until the end. Bidirectional elimination is a combination of these two methods. The advantage of stepwise regression is easily explained and implemented, even though it involves some risks. For example, test criticism (e.g. F-tests) and the initial model affect the variable selection. Several previous studies have used stepwise regression for different purposes. For example, Harpham and Wilby (2005), Hessami et al. (2008) and Huth (2002) adopted Stepwise for predictor selection; Agnihotri and Mohapatra (2012) applied it to occurrence estimation of daily summer monsoon precipitation. In this study, stepwise regression is adopted to test Lasso performance. Stepwise regression is implemented using the forward selection method (with an exit tolerance value 0.1) in MATLAB[®]

$$y_i = x_{ij}\beta_j + \varepsilon \tag{5.7}$$

where y is the $i \times 1$ response (dependent) vector, x is the $i \times j$ variable (independent) vector, β is the $j \times 1$ parameter vector and ε the random errors. Note that the set of 20 variables used for stepwise regression and Lasso remains the same, for the comparison.

5.3.4 Lasso

Least absolute shrinkage and selection operator (Lasso) is an alternative regularized version of least squares, which is useful for feature selection and to avoid over-fitting problems. Lasso shrinks the estimates of the regression coefficients towards zero to prevent over-fitting problem and to reduce variables by using a penalty parameter. To simplify understanding, the history of Lasso is introduced briefly. Equation 5.7 presents the ordinary least squares regression (OLS) that tries to minimize the error RSS (Root of Sum of Squares), which is calculated from Eq. 5.8.

$$RSS = \arg\min_{\beta} \left\{ \sum_{i=1}^{N} \left(y_i - \beta_0 - \sum_{j=1}^{p} x_{ij}\beta_j \right)^2 \right\} \tag{5.8}$$

OLS is not always satisfactory for minimizing the RSS, especially when x contains a large number of variables, although it is simply implemented. Hoerl and Kennard (1970a) and Hoerl and Kennard (1970b) introduced ridge regression to yield better prediction with the help of a constraint (Eq. 5.9).

$$\hat{\beta}_{rdg} = \arg\min_{\beta} \left\{ \sum_{i=1}^{N} \left(y_i - \beta_0 - \sum_{j=1}^{p} x_{ij}\beta_j \right)^2 \right\} \quad \text{subject to} \quad \sum_{j=1}^{p} \beta_j^2 \leq t \tag{5.9}$$

where p is the number of variables and t is a specified constraint. The Lagrangian form of Eq. 5.9 is

$$\hat{\beta}_{rdg} = \arg\min_{\beta} \left\{ \sum_{i=1}^{N} \left(y_i - \beta_0 - \sum_{j=1}^{p} x_{ij}\beta_j \right)^2 + \lambda \sum_{j=1}^{p} \beta_j^2 \right\} \tag{5.10}$$

Based on ridge regression, Frank and Friedman (1993) developed bridge regression using a revised constraint $\sum_{j=1}^{p} \beta_j^\gamma \leq t$ with $\gamma \geq 0$.

$$\hat{\beta}_{brdg} = \arg\min_{\beta}\left\{\sum_{i=1}^{N}\left(y_i - \beta_0 - \sum_{j=1}^{p} x_{ij}\beta_j\right)^2\right\} \quad \text{subject to } \sum_{j=1}^{p}\beta_j^{\gamma} \leq t \qquad (5.11)$$

If $\gamma = 2$, bridge regression equals ridge regression. The values of γ determine the constrained area in parameter space. However, Frank and Friedman (1993) did not discuss all the possibilities of γ. Tibshirani (1996) developed the Lasso framework defining $\gamma = 1$ (Eq. 5.12 and 5.13).

$$\hat{\beta}_{lasso} = \arg\min_{\beta}\left\{\sum_{i=1}^{N}\left(y_i - \beta_0 - \sum_{j=1}^{p} x_{ij}\beta_j\right)^2\right\} \quad \text{subject to } \sum_{j=1}^{p}\beta_j \leq t \qquad (5.12)$$

Lagrangian form:

$$\hat{\beta}_{lasso} = \arg\min_{\beta}\left\{\sum_{i=1}^{N}\left(y_i - \beta_0 - \sum_{j=1}^{p} x_{ij}\beta_j\right)^2 + \lambda\sum_{j=1}^{p}\beta_j\right\} \qquad (5.13)$$

An efficient algorithm for solving Lasso is given as follows (Fu, 1998):

1. Start with $\hat{\beta}_0 = \hat{\beta}_{ols}$

2. Let $S_0 = -2x_j^T y + \sum_{i \neq j} 2x_j^T x_i \beta_i$, update β_j as :

$$\hat{\beta}_j = \begin{cases} \dfrac{\lambda - S_0}{2x_j^T x_j}, S_0 > \lambda \\[2mm] \dfrac{-\lambda - S_0}{2x_j^T x_j}, S_0 < -\lambda \\[4mm] 0, otherwise \end{cases}$$

3. Repeat until convergence

Compared to bridge regression, Lasso performs not only shrinkage, but also performs variable selection. Figure 5.2 shows how Lasso works. If only 2 predictors (β_1 and β_2) are input into the model, the center point $\hat{\beta}$ in the ellipse contours, which means that the residual sum of squares is minimized. The residual sum of squares will increase when the points move away from the center point $\hat{\beta}$. Although the residual sum of squares increases, the RSS are the same for the points on the same elliptical contour. The cyan square represents the set of vectors that satisfy

the constraint $\sum_{j=1}^{p} \beta_j \leq t$ (Weisberg, 2012). The Lasso estimator points are in this cyan square, with the smallest residual sum of squares for a tolerant t. In the Lasso solution, the first point is the intersection point of the rotated square and elliptical contour. Sometimes, the estimator points occur on the corner, in which case the vector is set exactly to zero and others are non-zero (Tibshirani, 1996; Weisberg, 2012).
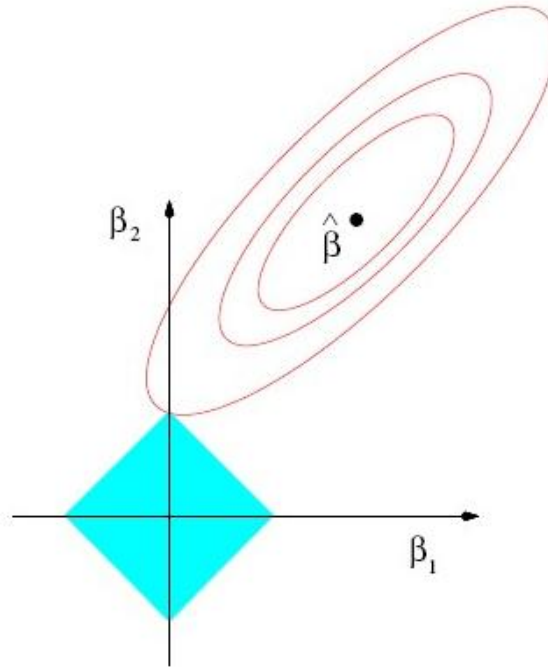
Figure 5.2: Estimation graphic for Lasso theory (Tibshirani, 1996; Weisberg, 2012).

Lasso imposes intentionally that many of the coefficients to be zero, thus achieving a sparse model. This sparse model is therefore easy to interpret. The penalty parameter (regularizer) λ controls the level of sparsity of the resulting model. A larger λ can produce a model that is sparser. In this study, the Lasso framework is implemented in MATLAB® software (Pendse, 2011, codes can be found in A.2).

5.4 Results

5.4.1 Validation of the original ERA-Interim precipitation data

The root mean square error (RMSE) and mean absolute error (MAE) are used for an assessment of the precipitation amount and CR is applied for the evaluation of occurrence (for equations see Eq. 3.2-3.4). In Chapter 3, original 0.25° ×0.25° ERA-Interim precipitation data was analyzed by

comparing it with observed gridded datasets, E-OBS and GPCC. ERA-Interim has the same standard deviation of the inter-annual variability of daily precipitation as E-OBS for the mean annual cycle. Significant wet biases occurred in ERA-Interim throughout the warm season (May to August) and dry biases in the cold season (November to February). ERA-Interim significantly underestimates precipitation amount in high mountains and on the northern flank of the Alpine chain from November to March and overestimates on the southern flank of the Alps.

Table 5.4: Comparison of ERA-Interim daily precipitation with observations at 50 meteorological stations from 1983-2010. The CR, as well as the RMSE and MAE in mm day^{-1} are listed. Because the elevations of sites are different with ERA-Interim grid heights, the altitude differences (Δh, elevation minus ERA-Interim grid height) are also labeled.

ID	Sites	CR	RMSE	MAE	Δh
COV	Piz Corvatsch	0.76	4.69	2.35	1687
WFJ	Weissfluhjoch	0.79	5.86	2.92	968
SAE	Säntis	0.84	11.15	5.18	1348
GSB	Col du Grand St-Bernard	0.83	10.88	4.58	979
GUE	Gütsch ob Andermatt	0.79	6.98	3.29	855
PIL	Pilatus	0.82	9.20	3.95	952
MLS	Le Moléson	0.79	5.44	2.72	781
SAM	Samedan	0.68	4.88	2.59	48
DOL	La Dôle	0.86	6.06	2.74	971
CIM	Cimetta	0.76	8.99	3.43	380
SBE	S. Bernardino	0.74	9.18	3.89	107
ZER	Zermatt	0.74	5.37	2.61	86
CHA	Chasseral	0.80	5.26	2.55	930
DAV	Davos	0.76	5.14	2.67	-128
MVE	Montana	0.75	5.54	2.72	-43
NAP	Napf	0.82	5.72	2.76	288
ULR	Ulrichen	0.75	6.36	3.11	-90
SCU	Scuol	0.69	5.03	2.71	-515
FRE	Bullet / La Frétaz	0.82	5.11	2.44	387
DIS	Disentis / Sedrun	0.75	6.16	3.03	-282
ROB	Poschiavo / Robbia	0.77	5.48	2.48	-316
ENG	Engelberg	0.81	5.93	2.99	-397
CDF	La Chaux-de-Fonds	0.84	4.89	2.31	248
PIO	Piotta	0.72	8.20	3.54	-457
STG	St. Gallen	0.81	5.51	2.72	-252
VIS	Visp	0.68	5.69	2.94	-859
RUE	Rünenberg	0.79	4.66	2.35	-90
FAH	Fahy	0.81	4.44	2.19	42
INT	Interlaken	0.79	5.27	2.67	-748
CHU	Chur	0.72	5.22	2.78	-1112

SMA	Zürich / Fluntern	0.80	4.88	2.41	-225
BER	Bern / Zollikofen	0.78	5.10	2.56	-456
TAE	Aadorf / Tänikon	0.80	4.94	2.53	-358
GLA	Glarus	0.80	5.57	2.84	-796
PAY	Payerne	0.77	5.48	2.82	-540
WAE	Wädenswil	0.81	5.57	2.69	-526
NEU	Neuchâtel	0.77	5.11	2.56	-364
SIO	Sion	0.69	5.22	2.77	-926
VAD	Vaduz	0.76	5.14	2.67	-769
PUY	Pully	0.80	5.79	2.76	-645
CGI	Nyon / Changins	0.79	5.02	2.53	-380
LUZ	Luzern	0.78	5.49	2.77	-700
REH	Zürich / Affoltern	0.79	4.77	2.40	-337
GUT	Güttingen	0.77	5.04	2.64	-522
SHA	Schaffhausen	0.78	4.51	2.30	-224
ALT	Altdorf	0.77	5.35	2.71	-755
KLO	Zürich / Kloten	0.78	4.86	2.47	-354
WYN	Wynau	0.79	4.74	2.34	-405
GVE	Genève-Cointrin	0.78	5.16	2.58	-553
AIG	Aigle	0.79	4.85	2.41	-965

Table 5.4 shows the comparison of ERA-Interim daily precipitation with observations at 50 meteorological stations from 1983-2010. The CR, as well as the RMSE and MAE in mm day^{-1} are listed. CR varies from 0.68 to 0.86 and RMSE changes in the range of 4.69-11.15 mm day^{-1}, while MAE ranges of 2.31 to 5.18 mm day^{-1}. The altitude differences change sharply in a large interval. The COV station is 1687 m higher than ERA-Interim grid height while SCU is 515 m lower than grid height. ERA-Interim results show good agreement with occurrence observations (0.68 to 0.86), but large deviations with respect to precipitation amount, in general. However, unlike temperature, the altitude difference is unable to explain the bias. For example, The DOL site has the highest CR with the value of 0.86, but with a large elevation difference of 971 m. The ZER has a CR of 0.74 but its elevation matches the grid height very well with an altitude gap of only 86 m. Thus, this again proves that the general relationship between precipitation and elevation is not easy to obtain, due to the great variability in the interaction between atmosphere circulation and complex topographical characteristics (Barry, 2008).

Figure 5.3 illustrates the percentage of annual precipitation bias between ERA-Interim and stations from 1983-2010. Positive values indicate that annual precipitations were overestimated by ERA-Interim and vice versa. In general, ERA-Interim data overestimated observed annual precipitation for the majority of test sites, and 7 of 50 sites were underestimated. Among them,

GSB has the largest negative bias with a value of -44.2 %. 5 of 50 sites showed overestimation of more than 100 %. WFJ and DAV are located in the same ERA-Interim grid. However, ERA-Interim overestimated for WFJ with 7.5 % and, significantly, for DAV with a value of 45.6 %. Besides, PIL and LUZ are also in the same ERA-Interim grid. ERA-Interim underestimated for PIL with 25.2 %. In the contrast, ERA-Interim overestimated for LUZ with a value of 28.6 %. This distinct difference implied again that the small-scale topographic features, such as slope and aspect, as well as the local circulations affect the precipitation formation and distribution. Obviously, the original ERA-Interim precipitation data possibly cause the uncertainties for hydrological modeling and magnify or reduce the risk of flood. The most lower stations located in the front of the Alps are underestimated by ERA-Interim, which indicate that ERA-Interim underestimate precipitation in the region affected by the air circulation in Atlantic.
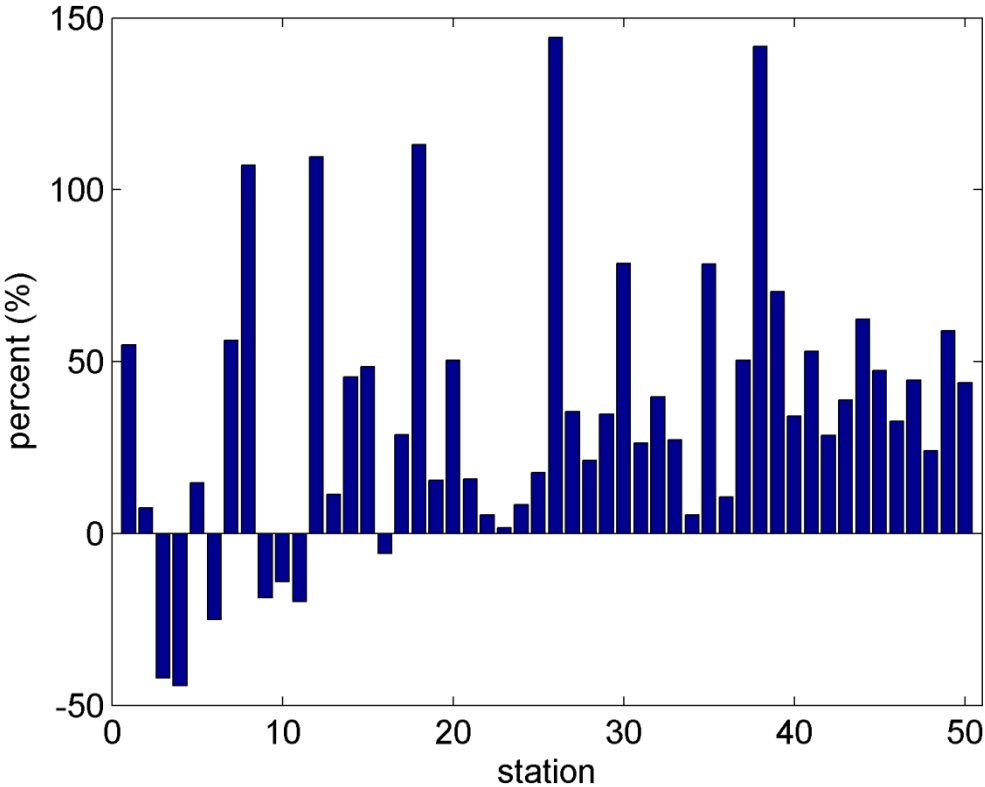
Figure 5.3: Percentage of annual precipitation bias between ERA-Interim and MeteoSwiss stations in the period 1983-2010. Positive values indicate the annual precipitations were overestimated by ERA-Interim and vice versa.

5.4.2 Evaluation of downscaling methods

Besides the criteria, CR, RMSE, and MAE, Taylor diagrams that provide a visual framework for modeling results to observations were applied for evaluating four downscaling models. The

weighted pattern correlation (COR), the normalized root-mean-square differences (RMSD), and the amplitude of variations (standard deviations, STD) are quantified in the diagram (Taylor, 2001). The COR represents the weighted correlation between modeled results and observations. Different with RMSE, RMSD characterizes the differences of root-mean-square. These three criteria do not provide the overall biases, but solely characterize the centered pattern error between modeled data and observations. The COR, RMSD and STD are computed as:

$$COR = \frac{\sum_{t=1}^{N}\left(\left(P_o - \overline{P_o}\right) \times \left(P_m - \overline{P_m}\right)\right)}{N \times STD(P_o) \times STD(P_m)} \tag{5.14}$$

$$RMSD = \sqrt{\frac{1}{N}\sum_{t=1}^{N}\left(\left(P_o - \overline{P_o}\right) - \left(P_m - \overline{P_m}\right)\right)^2} \tag{5.15}$$

$$STD(P_o) = \sqrt{\frac{1}{N}\sum_{t=1}^{N}\left(P_o - \overline{P_o}\right)^2} \tag{5.16}$$

where P_o and P_m is observed and modeled precipitation at time t, respectively. N = number of records in the validation period.

The overall performance of four downscaling methods, as well as the ERA-Interim original data in the validation period 1999-2010 is summarized in Table 5.5. Generally, the straightforward methods, LOCI and QM, captured the occurrence best. Lasso performs than the original ERA-Interim. Lasso performed best compared to other methods on the reduction of error; 12.2 % of RMSE and 17.2 % of MAE, respectively. Whereas QM and Stepwise were the worst methods, especially Stepwise had a larger MAE than LOCI, QM and Lasso methods (Table 5.5).

The specific performance of four downscaling methods is summarized in Table 5.6. LOCI and QM outperformed for occurrence (CR) for all test sites. CR for LOCI ranged from 0.81 to 0.88 and for QM varied from 0.82 to 0.88. Both methods did not consider the local circulation characteristics but only the historical records (calibration data). Stepwise generated the worst CR, with a range of 0.47-0.85. The sites, MVE, ULR, and VIS have the smallest CRs: lower than 0.5. Lasso modeled the CR from 0.70 to 0.84, and half of 50 sites better than original ERA-Interim but worse than the LOCI and QM benchmarks. In summary, LOCI and QM had the advantages on occurrence modeling and Lasso captured the occurrence in general. In terms of RMSE, Lasso yielded the best results for almost all test sites, with a RMSE of 3.11 to 9.77 mm day^{-1}, except MLS, CHA, LUZ and KLO. For MLS, Lasso showed approximately the same performance as

Stepwise. But for CHA, the original ERA-Interim was the best and none other downscaling methods worked efficiently. Stepwise yielded the best results for LUZ and KLO. Lasso was a little worse than Stepwise for these two sites. For WFJ, CIM, ROB, ENG, and GLA sites, only Lasso reduced the errors significantly, in contrast to increasing RMSE by LOCI, QM and Stepwise. For 50 % of all sites, QM produced the worst results, with increasing RMSE compared to the original ERA-Interim data, while Stepwise had similar RMSE results for 6 sites. Lasso had the lowest RMSE for 46 sites. For MAE, Lasso reduced the errors most with an average 17.2 % of MAE, following by LOCI with 15.8 %. Stepwise performed worst (1.1 %). The original ERA-Interim was better than downscaling methods for DOL on RMSE and for CHA on MAE.

Table 5.5: Comparison of observations with downscaled daily precipitation for four downscaling methods, as well as the original ERA-Interim data in the validation period 1999-2010 by averaging CR, RMSE and MAE in mm day^{-1} of all 50 test sites.

	CR	RMSE	MAE
ERA	0.77	5.86	2.85
LOCI	0.85	5.65	2.40
QM	0.85	5.81	2.44
Stepwise	0.72	5.67	2.82
Lasso	0.78	5.14	2.36
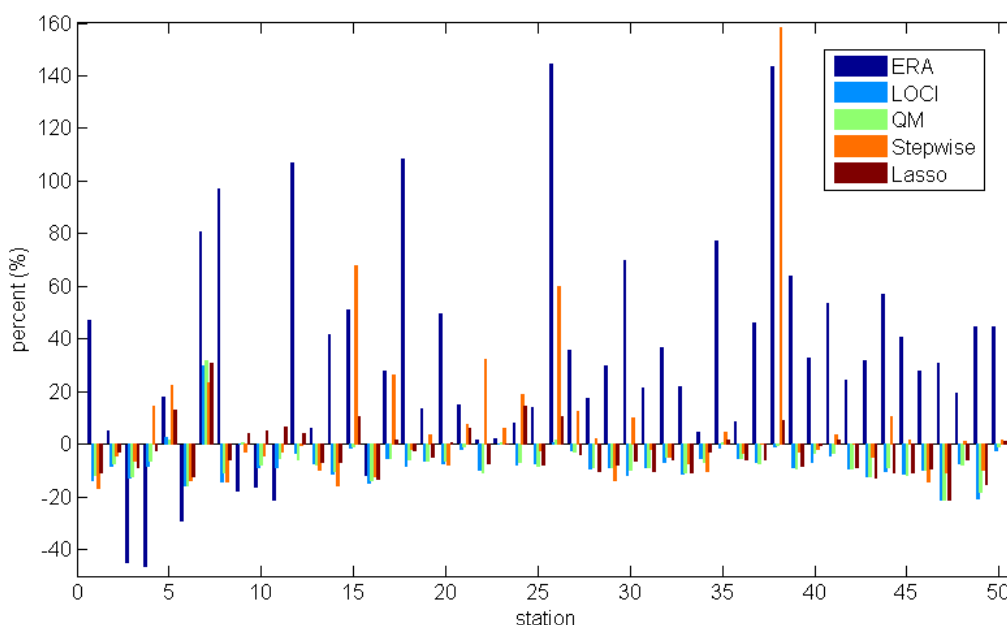
Figure 5.4: Percentage of annual precipitation bias between observations and four downscaled, as well as the original ERA-Interim data in the validation period 1999-2010.

Figure 5.4 illustrates the comparison of observations with downscaled annual precipitation for the four methods, as well as the original ERA-Interim data in the validation period 1999-2010. Lasso predicted the annual precipitation best, with percentage bias values of -21 % to 30.8 %. In general, LOCI and QM modeled drier and Stepwise modeled wetter results. 34 out of 50 sites were underestimated by Lasso with the range from -21 % (KLO) to -0.1 % (CDF) while 16 sites were overestimated by 0.7 % (DIS) to 30.8 % (MLS). The majority of sites were underestimated by LOCI (46 out of 50 sites) and QM (44 out of 50 sites) while 27 of 50 sites were underestimated by Stepwise. Stepwise performed unstable for different sites and had large amplitude of error. In particular, for SIO station, Stepwise had the largest error with value of 158 %.

Table 5.6: Comparison of observations with downscaled daily precipitation for four downscaling methods, as well as the original ERA-Interim data in the validation period 1999-2010. The CR, RMSE and MAE statistics of all 50 test sites are listed.

ID	Site	CR					RMSE					MAE				
		ERA	LOCI	QM	Stepwise	Lasso	ERA	LOCI	QM	Stepwise	Lasso	ERA	LOCI	QM	Stepwise	Lasso
COV	Piz Corvatsch	0.76	0.85	0.84	0.77	0.80	4.56	4.16	4.34	4.02	3.89	2.32	1.74	1.80	1.79	1.74
WFJ	Weissfluhjoch	0.78	0.82	0.82	0.55	0.76	6.14	6.31	6.48	6.47	5.48	3.02	2.88	2.93	3.56	2.67
SAE	Säntis	0.83	0.84	0.84	0.73	0.77	11.90	11.10	11.29	10.76	9.77	5.55	5.48	5.58	5.81	5.01
GSB	Col du Grand St-Bernard	0.83	0.83	0.82	0.53	0.74	11.21	10.61	10.67	11.77	9.20	4.60	4.71	4.79	7.40	4.48
GUE	Gütsch ob Andermatt	0.78	0.81	0.82	0.63	0.72	6.53	6.41	6.82	6.73	5.88	3.15	2.84	2.90	3.71	2.93
PIL	Pilatus	0.81	0.84	0.84	0.66	0.74	10.44	10.05	9.92	9.97	9.58	4.29	4.20	4.17	4.48	4.19
MLS	Le Moléson	0.76	0.83	0.83	0.77	0.77	5.89	5.31	5.69	4.69	4.70	3.01	2.41	2.49	2.26	2.31
SAM	Samedan	0.68	0.86	0.85	0.78	0.80	4.77	3.92	4.08	3.84	3.62	2.56	1.43	1.49	1.53	1.47
DOL	La Dôle	0.86	0.88	0.88	0.84	0.81	5.72	5.94	6.04	5.54	5.41	2.60	2.63	2.69	2.63	2.67
CIM	Cimetta	0.77	0.85	0.84	0.72	0.72	8.81	9.47	9.58	8.81	8.11	3.46	3.45	3.48	3.64	3.50
SBE	S. Bernardino	0.74	0.83	0.82	0.63	0.73	9.29	9.10	9.94	9.01	7.52	3.95	3.75	3.95	4.26	3.50
ZER	Zermatt	0.74	0.84	0.84	0.55	0.76	5.14	4.19	4.53	4.07	3.67	2.51	1.59	1.62	2.00	1.56
CHA	Chasseral	0.80	0.85	0.85	0.77	0.78	5.52	5.63	5.80	5.60	5.54	2.60	2.45	2.50	2.53	2.55
DAV	Davos	0.75	0.84	0.84	0.64	0.78	5.22	4.84	4.92	4.87	4.47	2.71	2.09	2.12	2.35	2.03
MVE	Montana	0.74	0.83	0.83	0.47	0.73	5.35	4.89	5.01	6.62	4.24	2.69	2.07	2.08	4.47	2.10
NAP	Napf	0.81	0.85	0.85	0.82	0.79	6.17	6.49	6.52	6.16	6.12	2.95	2.97	2.98	2.93	2.91
ULR	Ulrichen	0.75	0.84	0.83	0.48	0.73	6.25	5.94	6.24	7.23	5.73	3.08	2.51	2.58	4.43	2.66
SCU	Scuol	0.69	0.86	0.86	0.67	0.80	4.97	3.74	4.01	3.81	3.58	2.69	1.44	1.49	1.75	1.48
FRE	Bullet / La Frétaz	0.82	0.87	0.87	0.81	0.84	5.18	5.45	5.59	5.17	4.93	2.44	2.29	2.33	2.41	2.20
DIS	Disentis / Sedrun	0.75	0.84	0.84	0.72	0.74	6.00	5.34	5.52	5.59	5.31	2.98	2.16	2.17	3.33	2.32
ROB	Poschiavo / Robbia	0.76	0.84	0.83	0.56	0.75	5.74	6.16	6.26	5.96	5.10	2.64	2.39	2.44	3.04	2.32
ENG	Engelberg	0.80	0.82	0.82	0.68	0.76	6.18	6.66	6.44	8.33	5.82	3.11	3.16	3.09	4.98	2.88
CDF	La Chaux-de-Fonds	0.84	0.86	0.87	0.75	0.82	5.04	5.47	5.47	4.98	4.90	2.32	2.36	2.39	2.49	2.28

PIO	Piotta	0.71	0.84	0.83	0.51	0.70	7.91	7.74	8.01	8.93	6.78	3.50	2.99	3.05	4.82	3.14
STG	St. Gallen	0.81	0.85	0.84	0.83	0.80	5.70	5.83	5.95	5.60	5.55	2.74	2.54	2.58	2.56	2.52
VIS	Visp	0.68	0.85	0.85	0.48	0.75	5.53	4.15	4.55	4.72	3.77	2.88	1.51	1.55	2.72	1.55
RUE	Rünenberg	0.78	0.85	0.84	0.81	0.80	4.66	4.59	4.72	4.39	4.17	2.38	1.98	2.02	2.11	1.91
FAH	Fahy	0.81	0.86	0.86	0.72	0.83	4.70	4.71	4.81	4.63	4.47	2.25	1.98	2.02	2.33	1.96
INT	Interlaken	0.79	0.85	0.85	0.79	0.78	5.24	5.33	5.37	4.94	4.83	2.68	2.33	2.34	2.28	2.27
CHU	Chur	0.71	0.84	0.83	0.68	0.79	5.23	4.50	4.84	4.56	4.23	2.78	1.87	1.93	2.29	1.86
SMA	Zürich / Fluntern	0.80	0.86	0.86	0.84	0.83	4.89	4.97	5.16	4.75	4.74	2.42	2.17	2.21	2.16	2.11
BER	Bern / Zollikofen	0.77	0.86	0.86	0.75	0.80	5.17	5.18	5.27	4.79	4.70	2.61	2.14	2.18	2.20	2.10
TAE	Aadorf / Tänikon	0.80	0.86	0.86	0.83	0.80	4.77	4.82	5.00	4.57	4.53	2.52	2.23	2.28	2.23	2.22
GLA	Glarus	0.79	0.84	0.84	0.77	0.78	5.63	6.04	6.08	5.64	5.31	2.85	2.80	2.81	2.75	2.61
PAY	Payerne	0.76	0.86	0.85	0.82	0.79	5.33	4.54	4.63	4.13	3.99	2.81	1.86	1.89	1.85	1.81
WAE	Wädenswil	0.81	0.85	0.85	0.83	0.79	5.53	5.98	6.07	5.47	5.42	2.71	2.67	2.70	2.60	2.59
NEU	Neuchâtel	0.77	0.87	0.86	0.82	0.81	5.03	4.87	4.93	4.48	4.36	2.57	1.94	1.97	1.96	1.89
SIO	Sion	0.69	0.87	0.87	0.54	0.77	5.02	3.54	3.68	6.49	3.11	2.71	1.36	1.37	4.01	1.40
VAD	Vaduz	0.76	0.86	0.85	0.80	0.83	5.29	4.63	4.85	4.42	4.40	2.70	1.86	1.91	1.92	1.85
PUY	Pully	0.79	0.87	0.86	0.80	0.76	5.61	5.59	5.79	5.16	5.08	2.73	2.28	2.34	2.33	2.37
CGI	Nyon / Changins	0.78	0.88	0.88	0.83	0.83	4.99	4.52	4.72	4.30	4.17	2.52	1.82	1.87	1.89	1.79
LUZ	Luzern	0.77	0.84	0.84	0.80	0.77	5.43	5.51	5.55	5.20	5.23	2.79	2.45	2.47	2.50	2.47
REH	Zürich / Affoltern	0.79	0.85	0.85	0.83	0.82	4.95	4.85	4.91	4.59	4.57	2.44	2.04	2.05	2.04	1.98
GUT	Güttingen	0.78	0.84	0.84	0.76	0.81	4.87	4.37	4.59	4.31	3.99	2.57	1.91	1.97	2.18	1.84
SHA	Schaffhausen	0.78	0.85	0.85	0.83	0.82	4.39	4.27	4.37	3.97	3.93	2.28	1.84	1.86	1.84	1.75
ALT	Altdorf	0.77	0.84	0.84	0.71	0.79	5.50	5.49	5.59	5.42	5.25	2.77	2.39	2.41	2.46	2.32
KLO	Zürich / Kloten	0.79	0.85	0.85	0.85	0.83	4.94	4.85	5.00	4.60	4.65	2.49	2.06	2.09	2.04	2.01
WYN	Wynau	0.79	0.86	0.86	0.82	0.80	4.91	5.25	5.35	4.75	4.63	2.42	2.20	2.22	2.20	2.14
GVE	Genève-Cointrin	0.78	0.88	0.87	0.84	0.82	5.16	4.74	4.93	4.63	4.55	2.57	1.85	1.92	1.93	1.87
AIG	Aigle	0.78	0.86	0.86	0.79	0.78	4.71	4.57	4.68	4.13	4.04	2.40	1.91	1.94	1.97	1.92

Table 5.7: Selected variables in Stepwise and Lasso model. "+" indicates in-model variable and "-" for out-model variable.

ID		P_{ERA}	H_{850}	H_{700}	H_{500}	T_{850}	T_{700}	T_{500}	RH_{850}	RH_{700}	RH_{500}	SH_{850}	SH_{700}	SH_{500}	TCW	U_{10}	V_{10}	FG_{10}	WG_{10}	$MSLP$	LSP
COV	Stepwise	+	-	-	-	-	-	-	+	-	-	-	-	-	-	+	+	+	+	-	-
	Lasso	+	+	+	+	+	+	+	+	+	+	+	-	-	-	+	+	+	+	+	+
WFJ	Stepwise	+	-	+	-	+	-	-	+	-	-	+	-	-	+	+	-	+	+	-	+
	Lasso	+	+	+	+	+	+	+	+	+	+	+	+	-	+	+	+	+	+	+	+
SAE	Stepwise	+	+	+	+	-	-	+	+	+	+	+	+	-	-	+	-	-	+	+	+
	Lasso	+	+	+	+	+	+	+	+	+	+	+	+	-	-	+	+	+	+	+	+
GSB	Stepwise	+	-	-	-	+	-	-	+	+	+	+	+	-	+	+	+	+	+	-	+
	Lasso	+	+	+	+	+	+	+	+	+	+	+	+	-	+	+	+	+	+	+	+
GUE	Stepwise	+	+	+	+	-	+	+	+	-	-	+	-	-	-	+	+	+	+	+	+
	Lasso	+	+	+	+	+	+	+	+	+	+	+	+	+	+	+	+	+	+	+	+
PIL	Stepwise	+	-	-	-	+	+	-	+	-	-	+	-	-	-	+	+	+	+	-	+
	Lasso	+	+	+	+	+	+	+	+	+	+	+	+	+	+	+	+	+	+	+	+
MLS	Stepwise	+	-	-	-	-	-	-	-	-	-	-	+	-	-	-	-	+	+	-	+
	Lasso	+	+	+	+	+	+	+	+	+	+	+	+	+	+	+	+	+	+	+	+
SAM	Stepwise	+	-	-	-	-	-	-	+	+	-	-	-	+	-	+	+	+	+	+	+
	Lasso	+	+	+	+	+	+	+	+	+	+	+	-	+	+	+	+	+	+	+	+
DOL	Stepwise	+	+	-	-	-	-	-	+	-	-	-	-	-	-	+	+	-	+	-	+
	Lasso	+	+	+	+	+	+	+	+	+	+	+	-	-	-	+	+	+	+	+	+
CIM	Stepwise	+	-	-	-	+	-	-	+	-	-	+	-	-	-	+	+	+	+	-	+
	Lasso	+	+	+	+	+	+	+	+	+	+	+	+	+	+	+	+	+	+	+	+
SBE	Stepwise	+	-	-	-	+	+	+	+	+	-	+	+	-	-	+	+	+	-	-	+
	Lasso	+	+	+	+	+	+	+	+	+	+	+	+	+	+	+	+	+	+	+	+
ZER	Stepwise	+	-	-	-	+	-	-	+	+	-	+	-	-	+	+	-	+	+	-	+

	Method																			
CHA	Lasso	+	+	+	+	+	+	+	+	+	+	+	+	+	+	+	+	+	+	+
	Stepwise	+	−	−	−	−	−	−	−	−	−	−	−	−	−	−	−	+	−	+
DAV	Lasso	+	+	+	+	+	+	+	+	+	+	+	+	+	+	+	+	+	+	+
	Stepwise	+	−	−	−	−	−	−	−	−	+	−	−	−	−	+	−	+	+	−
MVE	Lasso	+	+	+	+	+	+	+	+	+	+	+	+	+	+	+	+	+	+	+
	Stepwise	+	−	−	−	+	+	+	−	+	+	−	−	−	+	+	−	+	−	−
NAP	Lasso	+	+	+	+	+	+	+	+	+	+	+	+	+	+	+	+	+	+	+
	Stepwise	+	−	−	−	−	−	−	−	−	−	−	−	+	+	+	−	+	+	+
ULR	Lasso	+	+	+	+	+	+	+	+	+	+	+	+	+	+	+	−	+	+	−
	Stepwise	+	−	−	−	+	+	+	+	−	−	−	−	−	+	+	+	+	+	+
SCU	Lasso	+	+	+	+	+	+	+	+	+	+	+	+	+	+	+	+	+	+	+
	Stepwise	+	−	−	−	+	+	+	+	−	−	−	−	−	+	+	−	+	+	−
FRE	Lasso	+	+	+	+	+	+	+	+	+	+	+	+	+	+	+	−	+	+	+
	Stepwise	+	−	−	−	−	−	−	−	−	+	+	−	−	−	−	−	+	+	+
DIS	Lasso	+	+	+	+	+	+	+	+	+	+	+	+	+	+	+	+	+	+	+
	Stepwise	+	−	−	−	−	−	−	+	−	+	+	+	−	−	−	−	+	−	+
ROB	Lasso	+	−	−	−	+	+	+	+	+	+	+	+	+	+	+	+	−	+	+
	Stepwise	+	+	+	+	+	+	+	+	+	+	+	+	+	+	+	+	+	+	+
ENG	Lasso	+	−	−	−	−	+	+	−	+	+	+	+	+	+	+	−	+	+	+
	Stepwise	+	+	+	+	+	+	+	+	+	+	+	+	+	+	+	+	−	+	+
CDF	Stepwise	+	−	−	−	−	−	−	−	−	−	−	+	+	−	+	−	+	+	+
	Lasso	+	+	+	+	+	+	+	+	+	+	+	+	+	+	+	+	+	+	+
PIO	Stepwise	+	−	−	−	+	+	+	−	−	−	−	+	+	−	+	−	+	+	+
	Lasso	+	+	+	+	+	+	+	+	+	+	+	+	+	+	+	+	+	+	+
STG	Lasso	+	+	+	+	+	+	+	+	+	+	+	+	+	+	+	+	+	+	+
	Stepwise	+	−	−	−	+	−	−	−	−	−	−	+	+	−	+	−	+	+	−
VIS	Lasso	+	−	−	−	−	−	−	−	−	−	−	+	+	−	+	−	+	+	+
	Stepwise	+	+	+	+	+	+	+	+	+	+	+	−	−	+	−	+	+	+	+

RUE	Lasso	+	+	+	+	+	+	+	+	+	+	+	+	+	+	+	+	+
	Stepwise	+	-	-	-	-	-	-	-	-	+	-	-	-	-	+	+	-	+
FAH	Lasso	+	+	+	+	+	+	+	+	+	+	+	+	+	+	+	+	+
	Stepwise	+	-	+	-	+	-	-	-	-	+	+	-	-	-	-	+	+	+
INT	Lasso	+	+	+	+	+	+	+	+	+	+	+	+	+	+	+	+	+
	Stepwise	+	+	-	-	-	-	-	-	-	-	-	-	-	-	-	-	-	-
CHU	Lasso	+	+	+	+	+	+	+	+	+	+	+	+	+	+	+	+	+
	Stepwise	+	+	+	-	+	+	-	-	+	+	+	-	-	+	+	+	+	+
SMA	Lasso	+	+	+	+	+	+	+	+	+	+	+	+	+	+	+	+	+
	Stepwise	+	-	-	-	+	-	+	-	-	-	-	+	-	-	-	-	+	+
BER	Lasso	+	+	+	+	+	+	+	+	+	+	+	+	+	+	+	+	+
	Stepwise	+	-	-	-	+	+	+	+	+	+	-	+	-	+	+	+	+	+
TAE	Lasso	+	+	+	+	+	+	+	+	+	+	+	+	+	+	+	+	+
	Stepwise	+	-	-	-	+	-	-	-	-	-	-	-	-	+	+	-	-	-
GIA	Lasso	+	+	+	+	+	+	+	+	+	+	+	+	+	+	+	+	+
	Stepwise	+	-	-	-	+	-	-	-	+	+	+	-	-	+	+	-	+	+
PAY	Lasso	+	+	+	+	+	+	+	+	+	+	+	+	+	+	+	+	+
	Stepwise	+	-	-	-	+	-	+	-	+	-	-	-	-	+	+	-	+	+
WAF	Lasso	+	+	+	+	+	+	+	+	+	+	+	+	+	+	+	+	+
	Stepwise	+	-	-	-	+	-	+	-	-	-	-	-	-	+	+	-	-	-
NEU	Lasso	+	+	+	+	+	+	+	+	+	+	+	+	+	+	+	+	+
	Stepwise	+	+	-	-	+	-	-	-	+	-	-	-	-	+	+	-	-	-
SIO	Lasso	+	+	+	+	+	+	+	+	+	+	+	+	+	+	+	+	+
	Stepwise	+	+	+	-	+	+	+	+	+	+	+	+	+	+	+	+	+	+
VAD	Lasso	+	+	+	+	+	+	+	+	+	+	+	+	+	+	+	+	+
	Stepwise	+	-	-	-	+	-	+	-	+	-	-	-	-	+	+	-	+	+
PUY	Lasso	+	+	+	+	+	+	+	+	+	+	+	+	+	+	+	+	+
	Stepwise	+	-	-	-	+	-	-	-	-	-	-	-	-	+	+	-	-	-

Group	Method																	
CGI	Lasso	+	+	+	+	+	+	+	+	+	+	+	+	+	+	+	+	+	+
	Stepwise	+	-	-	-	-	-	-	+	+	-	-	-	-	+	-	-	-	+
LUZ	Lasso	+	+	+	+	+	+	+	+	+	+	+	+	+	+	+	+	+	+
	Stepwise	+	-	-	-	-	-	-	-	-	-	-	-	+	-	-	-	-	+
REH	Lasso	+	+	+	+	+	+	+	+	+	+	+	+	+	+	+	+	+	+
	Stepwise	+	-	-	-	-	-	-	-	-	-	-	-	+	-	-	-	-	+
GUT	Lasso	+	+	+	+	+	+	+	+	+	+	+	+	+	+	+	+	+	+
	Stepwise	+	-	-	-	+	+	+	-	-	-	-	+	+	+	-	-	+	+
SHA	Lasso	+	+	-	-	-	-	-	+	+	-	-	-	-	-	-	-	+	+
	Stepwise	+	+	+	+	+	+	+	+	+	+	+	+	+	+	+	+	+	+
ALT	Lasso	+	-	-	-	-	-	+	-	+	+	-	-	+	+	-	-	-	+
	Stepwise	+	+	+	+	+	+	+	+	+	+	+	+	+	+	+	+	+	+
KLO	Lasso	+	-	-	-	-	-	+	+	-	-	-	-	-	-	-	+	+	+
	Stepwise	+	+	+	+	+	+	+	+	+	+	+	+	+	+	+	+	+	+
WYN	Lasso	+	-	-	-	-	-	-	-	-	-	-	-	+	-	-	-	-	+
	Stepwise	+	+	+	+	+	+	+	+	+	+	+	+	+	+	+	+	+	+
GVE	Lasso	+	-	-	-	-	-	+	+	-	-	-	-	-	-	-	+	-	+
	Stepwise	+	+	+	+	+	+	+	+	+	+	+	+	+	+	+	+	+	+
AIG	Lasso	+	-	-	-	-	-	+	-	-	-	-	-	+	-	-	-	-	+
	Stepwise	+	+	+	+	+	+	+	+	+	+	+	+	+	+	+	+	+	+
	Lasso	+	+	+	+	+	+	+	+	+	+	+	+	+	+	+	+	+	+

Figure 5.5 shows the Taylor diagrams of observations with downscaled daily precipitation for four methods as well as the original ERA-Interim data in the validation period 1999-2010 by taking the four highest stations as examples. The Taylor diagrams for all 50 sites can be found in A.3. Three statistics (COR, RMSD and STD) were computed for four methods as well as for the original ERA-Interim data, and a letter was assigned to each method considered. The location of each method in the diagram depicts how well the downscaled precipitation matches observations. For example, for the WFJ site, F (Lasso) has the highest pattern correlation with observations, about 0.75, while other methods ranged between 0.6-0.7. The normalized root-mean-square difference (RMSD) is proportional to the distance to the point A, which represents observations. The green contours indicate the RMSD values. It can be seen that F (Lasso) has RMSD of around 5.5 mm day^{-1}. Larger RMSD (around 6 mm day^{-1}) results for the other methods are found. The standard deviation of the modeled pattern is proportional to the radial distance from the point of origin. All methods had lower standard deviations than the observations, which are indicated by the gray arc at the observed value of 8.1 mm day^{-1}. In general, the methods that lie nearest to observations (point A) have relatively high correlations and low RMSD errors. The models lying closer to the arc in which observations are located in have relatively correct standard deviations, which indicate that the methods have smaller amplitude of pattern variations.

In Figure 5.5 and A.3, it can be seen that Lasso outperformed the other methods for most test sites. Stepwise seems to be the worst method having lower pattern correlation and larger RMSD errors. As benchmarks, LOCI and QM performed better on the amplitude of variations, because they inherited the variations from the calibration periods. Lasso smoothed the variation when it performed shrinkage function (regularized with λ parameter). The ERA-Interim local circulation variables also contributed to the variation error (deviation difference with observations). Heavy events, for example, are not represented by ERA-Interim data.

Table 5.7 shows the used variables in Stepwise and Lasso. Lasso selected more variables than Stepwise regression, and the latter method eliminated more variables. For the Lasso, geopotential height, temperature, and wind speed variables are the most frequently (all test sites) used variables. Specific humidity fields are least frequently (23 out of 50 sites) applied by Lasso. For Stepwise, in contrast, P_{ERA} is the only variable for all test sites; pressure level variables, such as H_{500} (only 12 % of the sites), T_{700} (16 % of the sites), RH_{500} (16 % of the sites) and SH_{500} (20 % of the sites) are rarely used. Four test sites (DOL, FRE, RUE, and FAH) have the smallest number of variables (16 variables) in the Lasso method. Stepwise method applied most variables (16 out of 20 variables) only for PIO site, and only 3 variables for INT and ALT sites. 32 out of 50 sites

selected fewer than 10 variables in Stepwise method. This demonstrates that Stepwise trends to exclude much more variables due to its test criteria.
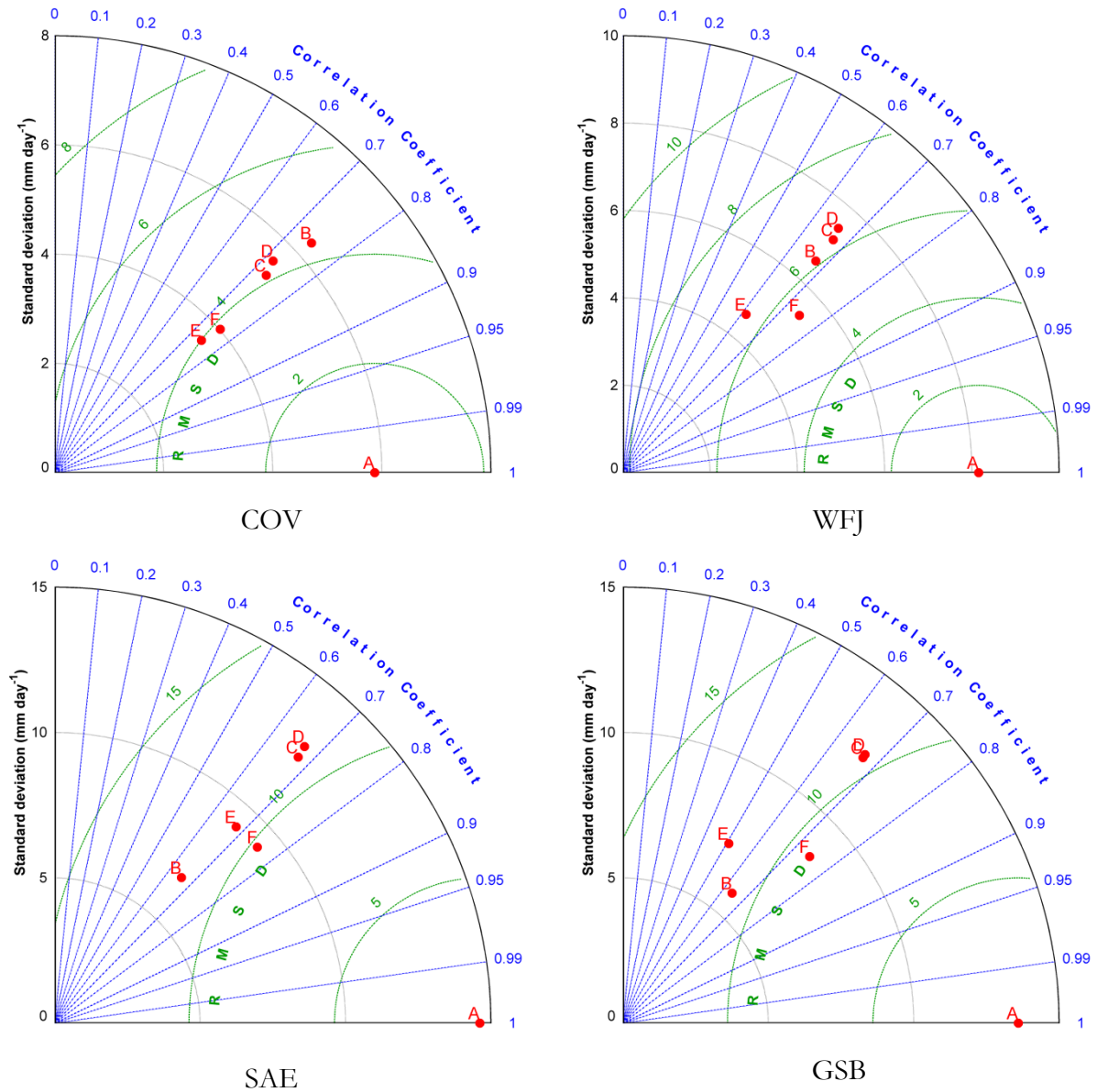

Figure 5.5: Taylor diagram of observations with downscaled daily precipitation for four downscaling methods, as well as the original ERA-Interim data for COV, WFJ, SAE and GSB stations in the validation period 1999-2010. A= observation, B= original ERA-Interim, C= LOCI, D= QM, E= Stepwise and F= Lasso.

5.5 Discussion and Conclusion

The comparison between ERA-Interim and observations showed that ERA-Interim has a large error (MAE ranges of 2.31 to 5.18 mm day^{-1}) in the central Alps (Table 5.4). Thus, there is a great

need for the correction and downscaling of ERA-Interim data. This study compared four downscaling methods, LOCI, QM, Stepwise and Lasso, for downscaling of ERA-Interim daily precipitation data in the central Alps.

As a frequent input variable for hydrological models, daily precipitation is always corrected or downscaled due to the limits of rain gauges. In the previous studies (e.g. Themeßl et al., 2012 and Schmidli et al., 2006), LOCI and QM methods have been widely used for the bias correction with the advantages of maintaining the variation and distribution of historical data. Table 5.6 and Figure 5.5 illustrated that LOCI and QM methods captured the best estimation of daily precipitation occurrence and variation. However, the reduction of error is not significant by these two methods, and even worse than the original ERA-Interim data for 19 out of 50 sites (Table 5.6, Figure 5.5). It demonstrates that straightforward methods are not always suitable for downscaling observations in complex terrain.

Stepwise regression took local circulations such as wind components and pressures into account by selecting variables automatically. However, Stepwise trends to exclude some relevant variables. Lasso selected more variables than Stepwise regression during coefficients shrinkage procedure (Table 5.7). For example, geopotential height, temperature, and wind speed variables are applied in the algorithm for all test sites. Specific humidity fields are least frequently (22 out of 50 sites) applied by Lasso. In contrast, only for PIO site, most variables (16 out of 20 variables) applied by Stepwise method. As many as 32 sites selected fewer than 10 variables in Stepwise, and P_{ERA} is the only variable for all test sites. Fewer variables considered in Stepwise resulted in the worst downscaling on daily precipitation occurrence and amount, as well as annual precipitation amount.

Although the Lasso algorithm did not simulate the occurrence of daily precipitation as well as LOCI and QM, it captured the occurrence for all test sites generally. Compared to the other three downscaling methods, it reduced the amount error most, to 12.2 % of RMSE and 17.2 % of MAE. Furthermore, only Lasso could reduce the error for certain sites, e.g. WFJ, CIM, ROB, ENG, and GLA sites. In Taylor diagrams, the outperformance of Lasso could be directly and visually demonstrated, with relatively high correlation with observations and lower RMSDs, in the comparison of four downscaling methods. The performance on the variation was relatively weak for Lasso, compared to LOCI and QM, both of which had the same distribution as the calibration data.

Although the Lasso algorithm has been developed for more than 15 years by statistician, the application in geosciences is still at the early-stage (e.g. Ebtehaj et al., 2012). A main practical challenge in applying Lasso for precipitation downscaling is that precipitation in heterogeneous terrain is such a complex process which tends to use more variables and to overestimate. To avoid the over-fitting problem, the penalty (or regularization) parameter λ plays a key role. A large λ can reduce the dimension of regression problem and produce a sparse model by estimating the coefficients to be zero. The cross-validation and hundreds of runs are necessary to find an appropriate penalty parameter. Therefore, Lasso is a little bit time-consuming compared to LOCI, QM and Stepwise methods.

So far, the work presented herein has been limited to the central Alps with 50 meteorological stations providing calibration/validation data sets for testing the Lasso algorithm. It would be necessary to extend the Lasso method to other high mountainous areas around the world. A limited number of variables (20 variables in this study) derived from ERA-Interim data were applied for Lasso; however, it should also be investigated whether other potential variables such as cloud cover can be used in the presented approach. This study focused on the daily total precipitation. Certainly, higher temporal resolution data, such as 3-hourly, would be of great interest in further investigations. Besides, using Lasso method to downscale heavy event features like intensity and frequency is of special interest to hydrologists. Although dynamic downscaling methods always demand more computations, it is worth comparing them to the Lasso method.

Chapter 6

Downscaling and Validation of ERA-Interim Data Using FLUXNET Sites

6.1 Motivation

Reanalysis data evaluation and validation is becoming more and more important due to its increasing applications in many fields. In Chapter 3 to Chapter 5, ERA-Interim data has been evaluated with E-OBS gridded observation data and local individual meteorological stations in Germany and Switzerland. However, these evaluations are carried out in similarly complex terrains and climate regimes. Observations near the land surface in dissimilar topographic regions experiencing a variety of climate regimes are deficient for validating reanalysis data. Thus, data from FLUXNET, a global network of micrometeorological flux observation sites, measuring the exchanges of carbon dioxide, water vapor and energy between the biosphere and atmosphere has been adopted for the validation of ERA-Interim data. Flux towers in FLUXNET are located in a broad range of climate regimes and vegetation zones, which is particularly favorable for the validation. This chapter tries to meet the challenges of validation of ERA-Interim temperature and precipitation data in different topographic regions. Also, the temperature downscaling approach is extended to flux towers.

6.2 Data and Method

6.2.1 ERA-Interim Data

ERA-Interim 2 m temperature and precipitation 3-hourly forecast data (03, 06, 09, 12, 15, 18, 21 and 24 UTC), initialized at 00 UTC from 1979-2010 and projected on a grid of 0.25°×0.25°, are applied here (details see Chapter 2). The surface geopotential height is also retrieved for grid height calculation. Temperature, as well as geopotential height at 950 hPa, 850 hPa and 700 hPa, is derived from the ERA-Interim dataset. The corresponding ERA-Interim grid is retrieved

according to the coordinates of the flux tower. The time period and temporal resolution are kept consistent with observations.

6.2.2 FLUXNET sites

48 flux tower sites located in Europe have been selected. There are three criteria for site selection: i) a continuous record of at least 2 years; ii) no gap in the records and iii) both temperature and precipitation have been recorded. Air temperature, precipitation, and elevation values are extracted from selected sites. The flux site locations are shown in Figure 6.1 and the basic information is listed in Table 6.1. More information about the tower sites such as vegetation and climate type can be found in the A.4. Temperature and precipitation data averaged at 30-minute intervals are converted to a 3-hourly temporal resolution. Daily precipitation also was compared to ERA-Interim precipitation data. Note that the heights of temperature and precipitation equipments range from 2 m to 10 m, which are ignored in this study. For temperature, correlation and NSE are used for model evaluation, whilst RMSE and MAE are used for error comparison. In terms of precipitation, a ratio criterion (Correspondence ratio, CR) is applied for occurrence and RMSE and MAE for amount of error validation (see Chapter 5), respectively.
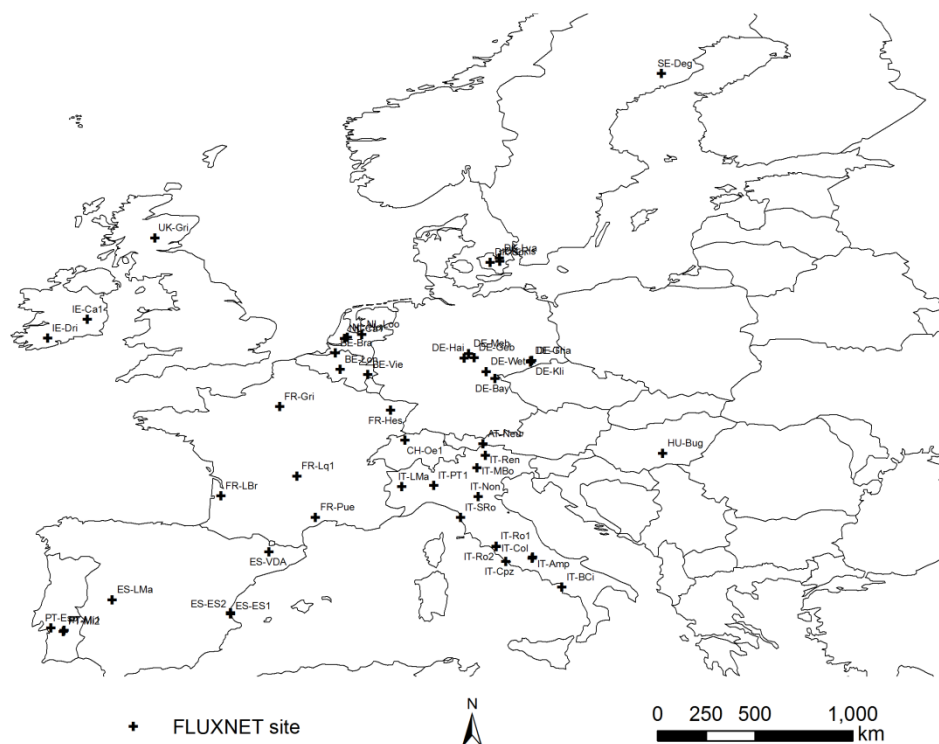

Figure 6.1: Location of FLUNXET site.

Table 6.1: Flux tower site information (the ERA-Interim grid heights are also listed, * indicates sites with different time period from precipitation. The precipitation period is labeled in brackets). The sites in bold type are selected for further temperature downscaling method validation.

ID	Name	Latitude	Longitude	Elevation	Grid height	Time period
AT-Neu	Neustift	47.12	11.32	970	1608	2002-2006* (2002-2005)
BE-Bra	Brasschaat	51.31	4.52	16	40	2000-2002
BE-Lon	Lonzee	50.55	4.74	167	166	2005-2006
BE-Vie	Vielsalm	50.31	6.00	450	327	1997-2006
CH-Oe1	Oensingen1	47.29	7.73	450	827	2002-2006
DE-Bay	Bayreuth	50.14	11.87	775	464	1997-1999
DE-Geb	Gebesee	51.10	10.91	162	337	2004-2006
DE-Gri	Grillenburg	50.95	13.51	385	299	2005-2006
DE-Hai	Hainich	51.08	10.45	430	338	2000-2006
DE-Kli	Klingenberg	50.89	13.52	480	299	2005-2006
DE-Meh	Mehrstedt1	51.28	10.66	286	301	2004-2006
DE-Tha	Anchor Station	50.96	13.57	380	299	1996-2006* (1998-2006)
DE-Wet	Wetzstein	50.45	11.46	785	408	2002-2006
DK-Lva	Lille Valby	55.68	12.08	15	12	2005-2006
DK-Ris	Risbyholm	55.53	12.10	10	12	2004-2005
DK-Sor	Soroe-LilleBogeskov	55.49	11.65	40	10	1997-2006
ES-ES1	El Saler	39.35	-0.32	10	203	1999-2006
ES-ES2	El Saler_Sueca	39.28	-0.32	10	203	2005-2006
ES-LMa	Las Majadas	39.94	-5.77	260	654	2004-2006
ES-VDA	Vall d'Alinya	42.15	1.45	1770	997	2004-2006* (2004-20065
FR-Gri	Grignon	48.84	1.95	125	138	2005-2006
FR-Hes	Hesse Forest	48.67	7.06	300	318	2001-2006
FR-LBr	Le Bray	44.72	-0.77	61	20	2003-2006
FR-Lq1	Laqueuille	45.64	2.74	1040	634	2004-2006
FR-Pue	Puechabon	43.74	3.60	270	399	2000-2006
HU-Bug	Bugacpuszta	46.69	19.60	140	107	2003-2006
IE-Ca1	Carlow1	52.86	-6.92	50	108	2004-2006
IE-Dri	Dripsey	51.99	-8.75	187	91	2003-2005
IT-Amp	Amplero	41.90	13.61	884	621	2003-2006
IT-BCi	Borgo Cioffi	40.52	14.96	20	362	2005-2006
IT-Col	Collelongo	41.85	13.59	1550	601	1997-2003* (1998-1999)
IT-Cpz	Castelporziano	41.71	12.38	68	254	2001-2006
IT-LMa	La Mandria	45.15	7.58	350	1261	2003-2004* (2003-2006)
IT-MBo	Monte Bondone	46.02	11.05	1550	1088	2003-2006

IT-Non	Nonantola	44.69	11.09	25	203	2001-2003* (2001-2002)
IT-PT1	Zerbolo	45.20	9.06	60	309	2003-2004
IT-Ren	Renon/Ritten	46.59	11.43	1730	1515	1999-2006* (2000-2002)
IT-Ro1	Roccarespampani1	42.41	11.93	235	320	2001-2006* (2002-2006)
IT-Ro2	Roccarespampani2	42.39	11.92	224	320	2002-2006
IT-SRo	San Rossore	43.73	10.28	4	163	1999-2006* (2003-2006)
NL-Ca1	Cabauw	51.97	4.93	1	2	2003-2006
NL-Hor	Horstermeer	52.03	5.07	-2	2	2005-2006
NL-Loo	Loobos	52.17	5.74	25	10	1997-2006
PT-Esp	Espirra	38.64	-8.60	95	131	2002-2004
PT-Mi1	Mitra (Evora)	38.54	-8.00	250	180	2003-2006
PT-Mi2	Mitra IV Tojal	38.48	-8.02	190	180	2005-2006
SE-Deg	Degero	64.18	19.55	270	215	2001-2005
UK-Gri	Griffin-Aberfeldy	56.61	-3.80	340	275	2005-2006

Due to the effect of elevation on temperature, the lapse rate, based on altitude difference, is the most frequently applied for temperature correction and interpolation (see section 4.1). Here, an adjusted method based on ERA-Interim internal lapse rate (Method III and IV in Chapter 4) is adopted for ten FLUXNET towers (see Table 6.1). The selected ten flux sites are located higher than 500 m a. s. l (approximately the geopotential height at 950 hPa) except Station IT-LMa. These ten towers also represent different topographic features. In the Alps, a transition level from local circulation-dominated to free air-dominated temperatures was defined at approximately 1400 m a.s.l. according to Tabony (1985). In this validation, the mean geopotential height at 850 hPa (H_{850}) is again used to judge the lapse rate and reference temperature. Note that here the lowest pressure level 950 hPa is used due to the geopotential height close to lowest site.

Table 6.2. Applied lapse rate (Γ) and reference temperature (T_{ref}) for ten test stations.

Method	Γ	T_{ref}	Station
Method III	Γ_{700_950}	T_{ERA_2m}	< mean H_{850}
	Γ_{700_950}	T_{ERA_850}	> mean H_{850}
Method IV	Γ_{850_950}	T_{ERA_2m}	< mean H_{850}
	Γ_{700_850}	T_{ERA_850}	> mean H_{850}

6.3 Results

6.3.1 2 m Temperature

The performance of ERA-Interim data against 48 flux sites with respect to 3-hourly temperature is summarized in Table 6.3. The correlation with values ranges from 0.88 to 0.98. An average value of 0.96 for all sites suggests that ERA-Interim agrees in general, with flux observations. The NSE ranges from 0.2 to 0.97 and the average value is 0.86 for all flux sites. Only 3 sites (ES-VDA, IT-Col and IT-LMa) have NSEs lower than 0.7. 41 of 48 sites have an NSE greater than 0.8, which indicates a good performance of the model. In terms of error, RMSE and MAE vary from 1.33-7.97 °C and 0.99-7.47 °C, respectively. 18 sites have RMSE larger than the average value of 2.68 °C, while 17 sites have a MAE larger than 2.15 °C.

Table 6.3: Comparison of ERA-Interim 2 m temperature with 3-hourly data of 48 FLUXNET sites. The correlation, NSE, as well as the RMSE and MAE in °C are also listed.

| ID	Correlation	NSE	RMSE	MAE	ID	Correlation	NSE	RMSE	MAE
AT-Neu	0.96	0.78	4.41	3.79	FR-Pue	0.97	0.92	2.09	1.68
BE-Bra	0.97	0.94	1.48	1.12	HU-Bug	0.95	0.89	3.42	2.57
BE-Lon	0.98	0.95	1.68	1.24	IE-Ca1	0.95	0.91	1.64	1.19
BE-Vie	0.97	0.92	2.07	1.59	IE-Dri	0.96	0.84	1.71	1.37
CH-Oe1	0.96	0.91	2.59	2.11	IT-Amp	0.91	0.75	4.91	3.68
DE-Bay	0.96	0.86	2.93	2.47	IT-BCi	0.96	0.77	3.41	2.91
DE-Geb	0.98	0.94	1.99	1.60	IT-Col	0.93	0.48	5.50	4.95
DE-Gri	0.97	0.93	2.29	1.68	IT-Cpz	0.95	0.88	2.40	1.84
DE-Hai	0.97	0.93	2.14	1.65	IT-LMa	0.95	0.20	7.97	7.47
DE-Kli	0.98	0.92	2.36	1.92	IT-MBo	0.96	0.84	3.15	2.66
DE-Meh	0.98	0.97	1.45	1.11	IT-Non	0.96	0.91	2.89	2.21
DE-Tha	0.97	0.94	2.04	1.54	IT-PT1	0.97	0.90	2.91	2.34
DE-Wet	0.96	0.84	3.30	2.87	IT-Ren	0.95	0.87	2.69	1.92
DK-Lva	0.98	0.96	1.47	1.11	IT-Ro1	0.97	0.88	2.60	2.06
DK-Ris	0.96	0.88	2.38	1.83	IT-Ro2	0.96	0.87	2.54	1.95
DK-Sor	0.96	0.88	2.38	1.83	IT-SRo	0.94	0.88	2.48	1.98
ES-ES1	0.96	0.89	2.05	1.64	NL-Ca1	0.98	0.96	1.33	0.99
ES-ES2	0.91	0.81	2.89	2.34	NL-Hor	0.95	0.91	2.20	1.59
ES-LMa	0.98	0.91	2.81	2.40	NL-Loo	0.98	0.95	1.56	1.10
ES-VDA	0.88	0.58	4.89	4.15	PT-Esp	0.95	0.90	2.12	1.59
FR-Gri	0.98	0.96	1.57	1.15	PT-Mi1	0.98	0.94	1.79	1.39
FR-Hes	0.98	0.95	1.75	1.30	PT-Mi2	0.97	0.88	2.93	2.36
FR-LBr	0.98	0.95	1.75	1.30	SE-Deg	0.92	0.84	4.29	2.93
FR-Lq1	0.93	0.78	3.61	3.11	UK-Gri	0.94	0.87	1.94	1.47
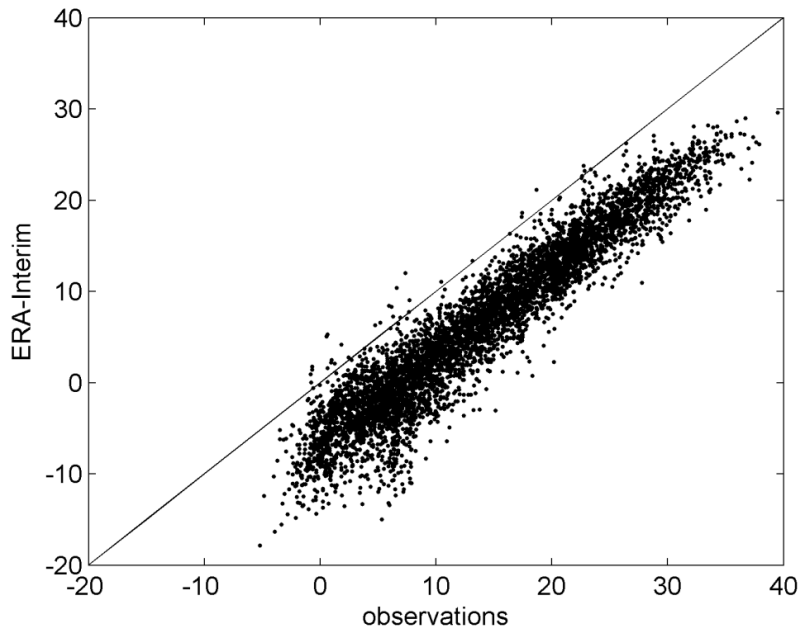
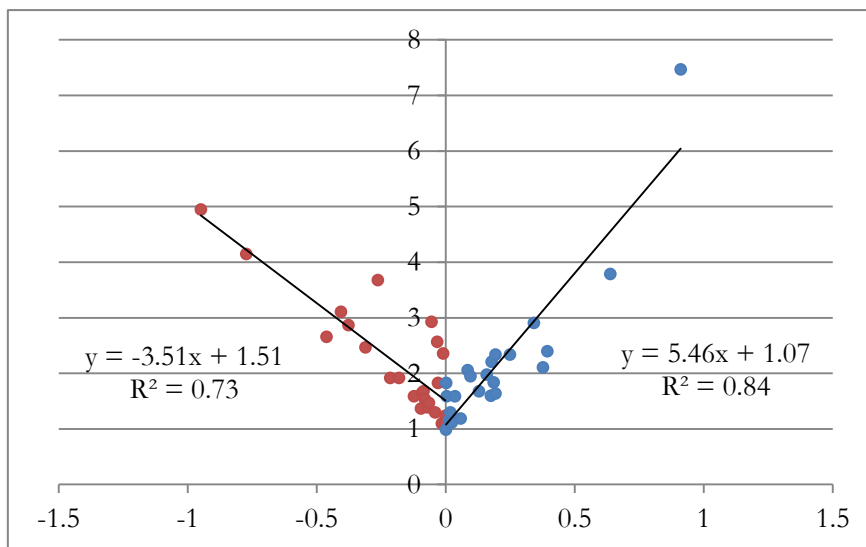Figure 6.2: The scatter plots show a comparison of flux sites and ERA-Interim 3-hourly temperatures for IT-LMa from 2002-2006.

Figure 6.3: Correlation of MAEs and elevation differences (grid height minus site elevation) for 3-hourly temperature. The y-axis is MAE (°C) and the x-axis is elevation difference (km). Red dots are the flux sites higher than ERA-Interim grid heights and blue dots are the sites lower than grid heights.

IT-LMa has the largest RMSE and MAE and lowest NSE. However, the correlation of the two datasets is 0.95, which means ERA-Interim captures the fluctuation of the observatons very well with observations. Figure 6.2 shows that ERA-Interim significantly underestimates observations, in particular for lower temperatures. The most likely reason for the error is that the grid height

modeled in ERA-Interim (1261 m) is much higher than its elevation of only 350 m (Table 6.1). The grid height of ERA-Interim modeled is determined by the modeled geopotential and surface pressure.

Figure 6.3 illustrates the trend with which MAE increases with increasing elevation differences. The y-axis is MAE (°C) and the x-axis is elevation difference (km). 48 sites are divided into two groups according to their elevation with respect to grid heights. 24 flux sites (red dots) higher than ERA-Interim grid heights showed less dependence (R^2=0.73) of elevation than the ones lower than grid heights (R^2=0.84). A possible reason is that the temperature at higher elevations is modeled according to free air-dominated circulation. In the ERA-Interim model, the 2 m temperature is interpolated from the lowest model level to higher pressure level (see Chapter 2). Therefore, the model level that is higher than the grid height is more related to free air-dominated circulations.

Table 6.4 summarizes the performance of two downscaling methods for 10 flux sites. In general, the two downscaling methods outperformed the original ERA-Interim data, with greater NSEs. The downscaling ability of Method III and IV is approximately the same for all flux sites. Although some sites have higher NSEs with lower correlations, the errors are reduced. Method III and IV reduced MAE of 29.2 % and 27.5 % for all test sites, respectively. For all high elevation sites, the downscaling methods worked very well. For example, IT-Col has the most significant improvement. The reduction of the RMSE and MAE is 36.9 % and 45.1 % using Method III, and 37.2 % and 45.5 % for Method IV, respectively. IT-Amp and IT-LMa show the least improvement, especially the latter. Only 6.5 % of RMSE and 7.4 % of MAE are reduced by Method III for the IT-LMa site. IT-LMa is located at the foot of a high mountainous region in the northwest of Italy. The result demonstrates that the downscaling methods have excellent transferability and worked well in high mountainous areas as well as at single flux site in various locations, which is very useful for climate impact models.

Table 6.4: Comparison of measurements with the original ERA-Interim 3-hourly 2 m temperatures and downscaled results for 10 flux sites. The correlation, NSE, as well as the RMSE and MAE in °C are also listed.

	AT-Neu (970 m)				DE-Bay (775 m)			
Method	Correlation	NSE	RMSE	MAE	Correlation	NSE	RMSE	MAE
Original	0.96	0.78	4.41	3.79	0.96	0.86	2.93	2.47
III	0.96	0.91	2.77	2.07	0.96	0.91	2.29	1.64
IV	0.95	0.89	3.10	2.33	0.96	0.92	2.26	1.59

	DE-Wet (785 m)				ES-VDA (1770 m)			
	Correlation	NSE	RMSE	MAE	Correlation	NSE	RMSE	MAE
Original	0.96	0.84	3.30	2.87	0.88	0.58	4.89	4.15
III	0.96	0.91	2.44	1.80	0.83	0.67	4.31	3.30
IV	0.96	0.91	2.44	1.77	0.83	0.68	4.26	3.26

	FR-Lq1(1040 m)				IT-Amp (884 m)			
	Correlation	NSE	RMSE	MAE	Correlation	NSE	RMSE	MAE
Original	0.93	0.78	3.61	3.11	0.91	0.75	4.91	3.68
III	0.94	0.88	2.68	2.02	0.91	0.80	4.37	3.43
IV	0.96	0.92	2.21	1.64	0.90	0.79	4.54	3.60

	IT-Col (1550 m)				IT-LMa (350 m)			
	Correlation	NSE	RMSE	MAE	Correlation	NSE	RMSE	MAE
Original	0.93	0.48	5.50	4.95	0.95	0.20	7.97	7.47
III	0.89	0.80	3.47	2.72	0.95	0.30	7.45	6.92
IV	0.89	0.80	3.45	2.70	0.95	0.31	7.42	6.89

	IT-MBo (1550 m)				IT-Ren (1730 m)			
	Correlation	NSE	RMSE	MAE	Correlation	NSE	RMSE	MAE
Original	0.96	0.84	3.15	2.66	0.95	0.87	2.69	1.92
III	0.95	0.89	2.63	2.11	0.96	0.92	2.07	1.57
IV	0.95	0.89	2.63	2.10	0.96	0.92	2.08	1.59

6.3.2 Precipitation

A threshold value of 1 mm 3-hourly^{-1} was applied to define dry/wet days. The comparison of ERA-Interim precipitation with 3-hourly and daily data of 48 flux sites is summarized in Table 6.5. For 3-hourly precipitation, ERA-Interim captures the occurrence very well, with a CR that ranged from 0.85 to 0.96. The averaged CR is 0.92 for all flux sites. ERA-Interim accurately estimated the dry/wet situation in 33 out of 48 sites for 90 % of the time period. ES-ES1 and ES-ES2 are two close sites located in the same ERA-Interim grid and they have the same CR with respect to different time periods. PT-Mi1 and PT-Mi2 are in a similar situation. IT-Ren, located in a high mountainous region (elevation 1730 m), has the worst CR performance. For error, RMSE ranges from 0.73 to 2.64 mm 3-hourly^{-1} while MAE varies from 0.15 to 0.54 mm 3-hourly^{-1}. The worst RMSE occurred at the IT-BCi site, with a value of 2.64 mm 3-hourly^{-1}, and the best RMSE occurred in FR-Gri, with a value of 0.73 mm 3-hourly^{-1}. MAE performs differently than RMSE. The highest MAE (0.54 mm 3-hourly^{-1}) appeared in IT-BCi, which is located close to the ocean and the lowest MAE (0.15 mm 3-hourly^{-1}) occurred in PT-Mi1, which is located in a homogenous plain.

Table 6.5: Comparison of ERA-Interim precipitation with 3-hourly and daily data of 48 flux sites. The CR as well as the RMSE and MAE in mm 3-hourly^{-1} are also listed.

ID	3-hourly			Daily		
	CR	RMSE	MAE	CR	RMSE	MAE
AT-Neu	0.87	1.94	0.52	0.70	7.46	3.49
BE-Bra	0.91	1.53	0.29	0.83	5.65	1.71
BE-Lon	0.91	0.98	0.24	0.79	3.08	1.51
BE-Vie	0.89	0.97	0.29	0.77	3.91	1.89
CH-Oe1	0.89	1.49	0.41	0.81	5.79	2.55
DE-Bay	0.90	1.33	0.32	0.81	4.40	2.04
DE-Geb	0.93	0.96	0.19	0.78	3.29	1.39
DE-Gri	0.92	1.16	0.24	0.83	3.83	1.50
DE-Hai	0.92	0.99	0.24	0.83	3.18	1.44
DE-Kli	0.92	1.06	0.21	0.79	3.39	1.43
DE-Meh	0.94	0.82	0.17	0.80	2.55	1.21
DE-Tha	0.91	1.11	0.26	0.82	4.23	1.61
DE-Wet	0.91	1.66	0.32	0.81	7.60	2.25
DK-Lva	0.91	1.41	0.33	0.80	4.71	2.09
DK-Ris	0.93	0.99	0.21	0.77	3.54	1.50
DK-Sor	0.92	1.35	0.29	0.81	4.94	1.88
ES-ES1	0.96	1.81	0.19	0.90	7.20	1.32
ES-ES2	0.96	1.60	0.21	0.88	5.99	1.56

ES-LMa	0.95	1.43	0.23	0.90	6.14	1.54
ES-VDA	0.91	1.80	0.36	0.75	7.34	2.72
FR-Gri	0.93	0.73	0.19	0.84	2.41	1.14
FR-Hes	0.90	1.16	0.30	0.83	4.00	1.75
FR-LBr	0.92	1.34	0.29	0.84	4.47	1.73
FR-Lq1	0.90	1.38	0.35	0.81	5.09	2.03
FR-Pue	0.94	1.76	0.31	0.86	6.46	1.87
HU-Bug	0.93	1.00	0.21	0.81	3.84	1.49
IE-Ca1	0.91	1.10	0.25	0.81	4.24	1.72
IE-Dri	0.91	1.00	0.30	0.84	3.71	1.74
IT-Amp	0.90	1.35	0.35	0.77	6.19	2.39
IT-BCi	0.90	2.64	0.54	0.82	10.42	3.42
IT-Col	0.88	1.87	0.45	0.77	8.03	2.98
IT-Cpz	0.92	1.60	0.32	0.81	5.15	1.90
IT-LMa	0.90	1.49	0.35	0.73	6.69	2.47
IT-MBo	0.86	1.53	0.44	0.70	6.71	3.15
IT-Non	0.90	1.92	0.44	0.82	6.51	2.45
IT-PT1	0.94	1.10	0.22	0.85	4.32	1.46
IT-Ren	0.85	1.18	0.41	0.74	5.31	2.76
IT-Ro1	0.92	1.64	0.31	0.82	5.82	1.95
IT-Ro2	0.92	1.64	0.32	0.82	5.83	1.95
IT-SRo	0.94	1.59	0.26	0.85	5.70	1.76
NL-Ca1	0.92	1.14	0.23	0.84	3.47	1.37
NL-Hor	0.90	1.36	0.33	0.85	4.63	1.73
NL-Loo	0.91	1.05	0.28	0.85	3.29	1.58
PT-Esp	0.94	0.90	0.19	0.93	2.75	0.94
PT-Mi1	0.96	0.86	0.15	0.94	2.72	0.76
PT-Mi2	0.96	1.23	0.20	0.94	3.51	1.04
SE-Deg	0.92	0.85	0.21	0.75	3.34	1.54
UK-Gri	0.89	1.43	0.29	0.65	5.35	2.42

Figure 6.4 gives a more detailed visualization of the 3-hourly precipitation at the ES-ES1 and ES-ES2 sites, as well as ERA-Interim in 2006. ES-ES1 and ES-ES2 are located close to the Mediterranean Sea and are only separated by about 8 km. ERA-Interim significantly overestimates precipitation over two flux sites in the winter time (December, January and February), in particular for the ES-ES2 site. From March to June, ERA-Interim underestimates for two sites. ERA-Interim did not capture the heavy events, especially for ES-ES1. ES-ES1 was affected more by the ocean circulation which could not be represented by the ERA-Interim model. From August to November, ES-ES2 has much more precipitation than ES-ES1, and this was captured well by ERA-Interim, generally. Figure 6.4 shows the comparison of 3-hourly precipitation between ES-ES1 and ES-ES2 sites and ERA-Interim data. The local circulations,

including the distance to the ocean affect the precipitation occurrence and amount. The fractional land cover (land or ocean is defined by a threshold of 0.5) is another potential factor that produces error in the ERA-Interim model (ECMWF, 2009b).
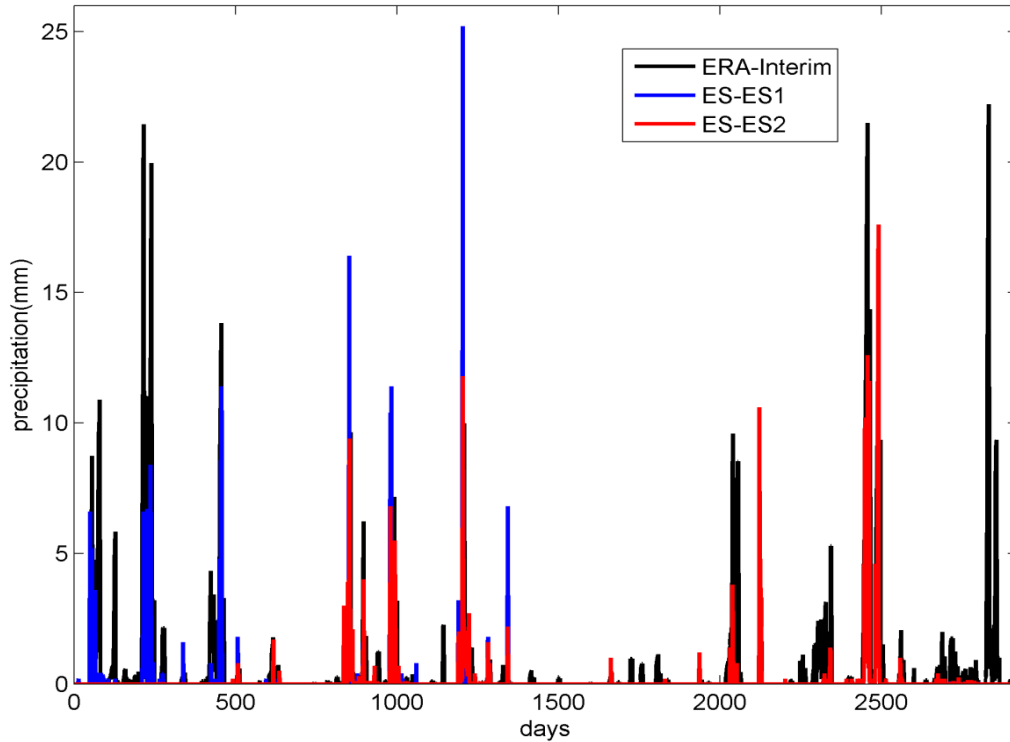
Figure 6.4: Plot of 3-hourly precipitation at the ES-ES1 and ES-ES2 sites as well as ERA-Interim data in 2006.

Daily precipitation has a different performance, because it reduces the variability by summing of eight 3-hourly precipitation events. CR ranges from 0.65 to 0.94 and has a lower average value of 0.81. PT-Mi1 and PT-Mi2 still have the high CRs. UK-Gri has the worst occurrence estimation. The highest RMSE for daily precipitation occurred at IT-BCi and the lowest at FR-Gri with values of 2.41 and 10.42 mm day^{-1}, respectively. PT-Mi1 has the smallest MAE of 0.76 and AT-Neu has the largest MAE of 3.49 mm day^{-1}.

Compared to 3-hourly precipitation, RMSE and MAE increased for daily precipitation because of the amount accumulation. It is difficult to judge which site has the best performance, due to the different time periods. However, the variation of the errors could be analyzed by RMSE and MAE. The larger difference between RMSE and MAE means larger variation in the magnitude of the errors and significant bias. IT-BCi has the largest difference between RMSE and MAE while FR-Gri has the lowest with respect to 3-hourly and daily precipitation.

A more detailed visualization of the daily precipitation is given in Figure 6.5. The large bias between ERA-Interim and IT-BCi is very clear. Although ERA-Interim captured the heavy event of March 11 at IT-BCi, it missed most of the heavy precipitation from September to December. On October 21, the heaviest precipitation occurred, with 124.2 mm, but only 4.3 mm was yielded in ERA-Interim. Apart from this heavy event, four other days experienced intense rainfall in excess of 40 mm, and these are recorded on September 17 and 25, November 12 and December 18. For FR-Gri, in general, the magnitude of the bias is more moderate than for IT-BCi. ERA-Interim underestimated 9.9 mm for the heavy event on June 25 and overestimated 11.2 mm on November 24. The reason for the differences in performance lies in the climate regime.

Unlike temperature, the correlation between MAE and elevation differences is not significant (Figure 6.6). 24 Flux sites (red dots) higher than ERA-Interim grid heights showed less dependence (R^2=0.50) of elevation than those lower than grid heights (R^2=0.25). This demonstrates that elevation differences only explain a small part of the errors. Therefore, more local effects should be taken into account. In particular, for the flux sites near the ocean or in the valleys of high mountains, the local circulations, such as wind and land-sea breezes, always play important roles in condensation of atmospheric water vapor and occur on a short time scale.
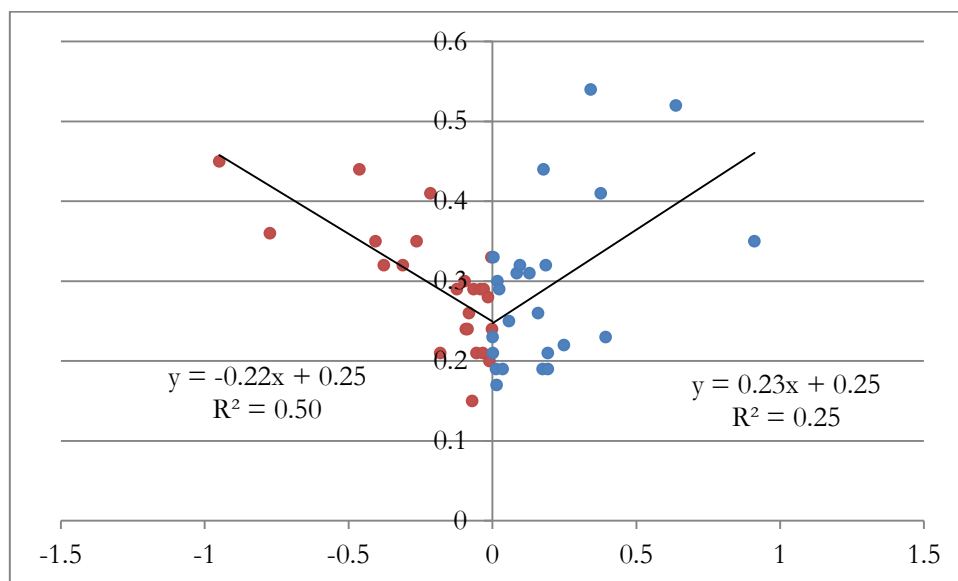
Figure 6.5: Correlation of MAEs and elevation differences (grid height minus site elevation) for 3-hourly precipitation. The y-axis is MAE (mm) while the x-axis is the elevation difference (km). Red dots are the flux sites higher than ERA-Interim grid heights and blue dots are the sites lower than grid heights.
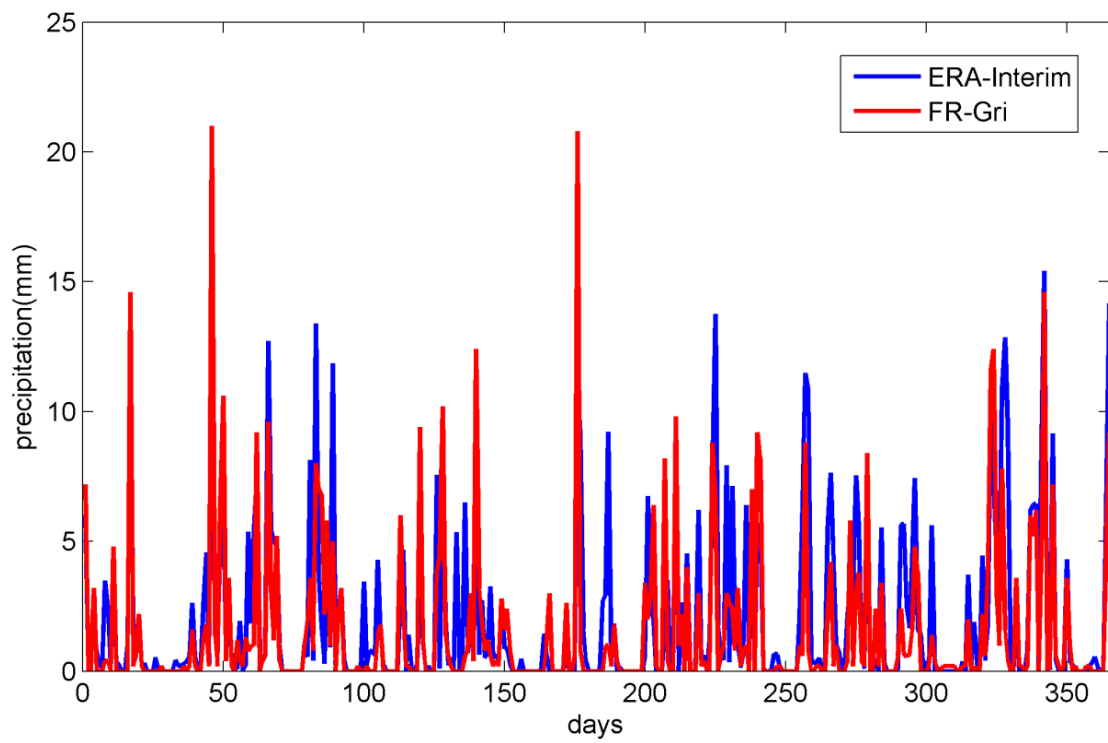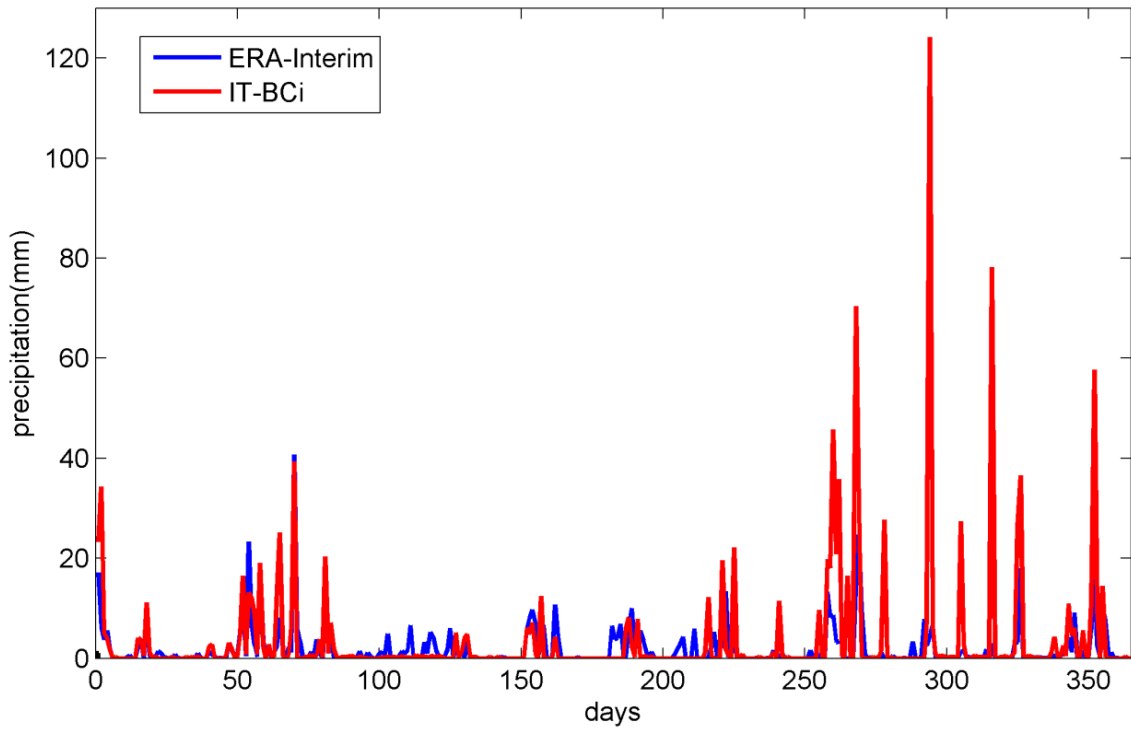
Figure 6.6: Plot of daily precipitation at the IT-BCi (upper) and FR-Gri (lower) sites, as well as ERA-Interim in 2006.

6.4 Discussion and Conclusion

It is important and necessary to investigate the performance of reanalysis data against the observations from different topographic regions experiencing various climate regimes and with different land use characteristics. In this study, temperature and precipitation of 48 flux tower sites from FLUXNET were adopted to evaluate the ERA-Interim data and to validate the performance of temperature downscaling approach.

For temperature, high temporal correlations, with values from 0.88 to 0.98 and an averaged value of 0.96 for all sites were found between ERA-Interim and flux observations. ERA-Interim performs well for 85 % of the sites, with the NSE greater than 0.8. The errors were assessed by RMSE and MAE, and varied from 1.33-7.97 °C and 0.99-7.47 °C, respectively. Although the errors are not only affected by the elevation differences between ERA-Interim grid heights and flux towers, the downscaling methods based on the ERA-Interim internal lapse rate (Method III and IV in chapter 4) reduced errors for the selected 10 flux sites (averaged 28.3 % MAE). The results illustrate that the downscaling methods worked well in high mountainous areas as well as for individual flux sites. For certain sites (e.g. IT-LMa), ERA-Interim did not perform well, due to its much higher grid height.

For precipitation, ERA-Interim captures the occurrence very well in general, with high CRs ranging from 0.85 to 0.96 for 3-hourly and from 0.65 to 0.94 for daily precipitation, based on the 1 mm 3-hourly^{-1} threshold. The topography features (e.g. in the valley of mountainous and near the ocean) determined the errors. Unlike temperature, the elevation effects only explain a small part of the precipitation errors. Even two flux sites located close to each other in the same ERA-Interim grid had different occurrence and amount of total precipitation (Figure 6.4). The distance to the ocean was a major factor affecting the precipitation. For example, IT-BCi flux sites experiences the typical Mediterranean climate (Csa) with little precipitation in the summer and heavy rains in the winter. This characteristic was not captured by ERA-Interim, especially the high amount in October. Other variables representing the local circulations, such as wind speed and direction, humidity, pressure, amongst others, should be incorporated into the precipitation correction and downscaling.

Chapter 7

ERA-Interim Data Application

7.1 Background

Along with the rapidly expanding global markets, the world's largest motor vehicle manufacturer, Volkswagen Group (hereafter VW) and its subsidiary company AUDI AG (hereafter AUDI) have recognized that temperature distribution and extremes affect the automobiles' technical design, for example, the engine cooling system or coolant additives. Therefore, VW and AUDI urgently need knowledge about temperature distributions and extremes for their emerging markets.

Normally, long-term time series of data are provided by local meteorological stations or by national meteorological services (e.g. DWD in Germany). However, there are some difficulties in data collection in the global context. Firstly, weather stations are not widely available, especially in the developing countries, where rapidly emerging markets for VW and AUDI are located. Secondly, weather stations are distributed unevenly and some regions have only a low station density. Thirdly, records are not consistent, for example, the measuring equipment and measured heights differ. Finally, acquiring long-term and high temporal resolution data is very time-consuming and costly. For these reasons, ERA-Interim data has significant strengths that can meet these challenges. Within a Matlab and GIS framework, the temperature distribution and extremes of ERA-Interim are analyzed and presented visually. These global and regional thematic maps help VW and AUDI with their fast marketing planning.

However, the accuracy of ERA-Interim data for large cities, which are the main car markets, should be tested. In order to validate the ERA-Interim temperature data, nine large city measurements, from ECA&D are adopted. This validation provides the information on the reliability of ERA-Interim data in this socio-economic application. This chapter is partitioned into two parts: temperature distribution maps based on ERA-Interim data for the globe and regions and comparison of ERA-Interim data with measurements of large cities.

7.2 Thematic Map Making

7.2.1 ERA-Interim Data

3-hourly forecast temperature data (03, 06, 09, 12, 15, 18, 21 and 24 UTC) initialized at 00 UTC from 01.10.1989 to 31.12.2009 which are projected on a reduced Gaussian grid (N128) with an approximately uniform 79 km spacing for the surface is applied here. The extreme temperatures are represented by quantiles: 0.1 %, 0.5 %, 1 % and 5 % quantiles for lower temperatures and 95 %, 99 %, 99.5 % and 99.9 % quantiles for higher temperatures, respectively. According to the time period and record steps, the individual quantiles correspond to time periods per year the quantile values are exceeded or fallen short of (Table 7.1). For example, 0.1 % quantile temperature represents temperatures lower than 0.1 % quantile temperature is less than 9 hours per year. In contrast, higher 99.9 % quantile temperatures last less than 9 hours per year (Table 7.1).

Table 7.1: Duration per year the quantile values exceeded or fallen short of for each quantile according to the time period and record steps.

	0.1 %	0.5 %	1 %	5 %	95 %	99 %	99.5 %	99.9 %
Duration (h)	9	45	90	450	450	90	45	9

7.2.2 Map Making Method

ArcMap, the main component of Esri's ArcGIS$^{®}$ suite of geospatial processing programs, is applied for thematic map making. First, the quantile data and region boundaries are entered into ArcMap, and then the Data Management Tools are used to adjust all data to the same projection. Second, the Spatial Analyst Tools are applied to interpolate quantile data and extract the regional interpolation data from globe dataset. Finally, the appropriate classification and layout functions adding scale bar, legend, and titles are used to export the maps in different formats. Figure 7.1 shows the technical flow of map-making in ArcMap Version 9.3. The thematic maps provide a clear and rapid review process regarding the classification of regions according to the temperature extremes.
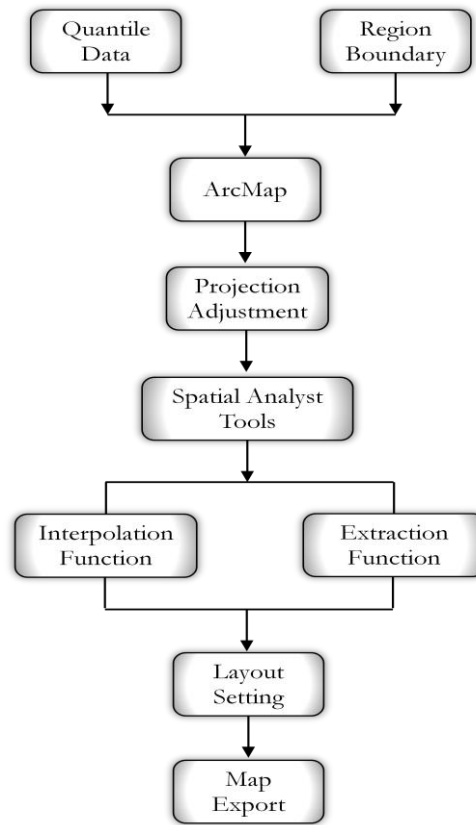
Figure 7.1: Technical flow of map production.

7.2.3 Global and Regional Maps

This comparison illustrates that calculating ERA-Interim data in different quantiles with 3-hourly temporal resolution and over the long term period 1989-2009, as well as interpolating quantile data from the original N128 grid to defined areas, and finally, creating thematic maps for each area and each quantile global and local areas (Australia, China, Germany, Japan, India, southern North America and southern Europe). Here, only the global and southern Europe thematic maps are shown as the examples (see A.4). Figure 7.2 displays the global temperature distribution for the 0.1 % and 99.9 % quantile on an interpolated grid of 100×100 km^2. The individual quantiles correspond to time periods per year the quantile values are exceeded or fallen short of according to the time period and record steps. Generally, high latitude countries, such as Russia and Canada have extremely low temperatures, and Equatorial countries experience the extremely high temperatures. Figure 7.3 shows the southern European temperature distribution for 0.1 % and 99.9 % quantiles on 25 km grids. Note that all final thematic maps are derived from the original N128 grid (about 79 km) and that ArcMap software constrains the grid number (i.e. spatial resolution) that can be processed.
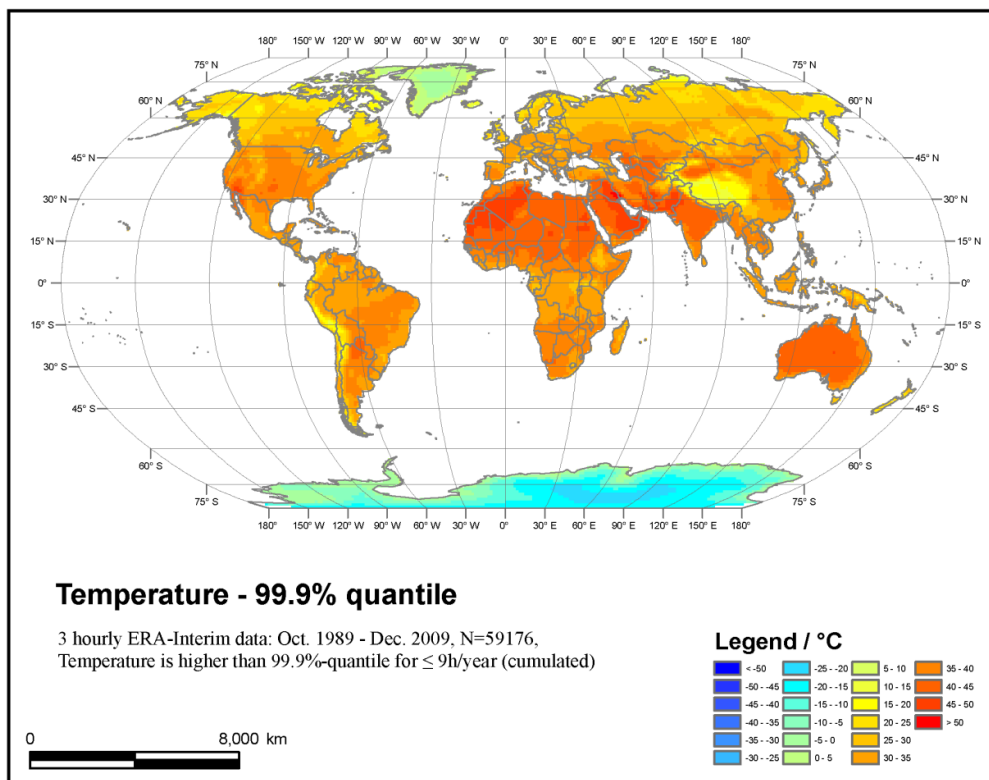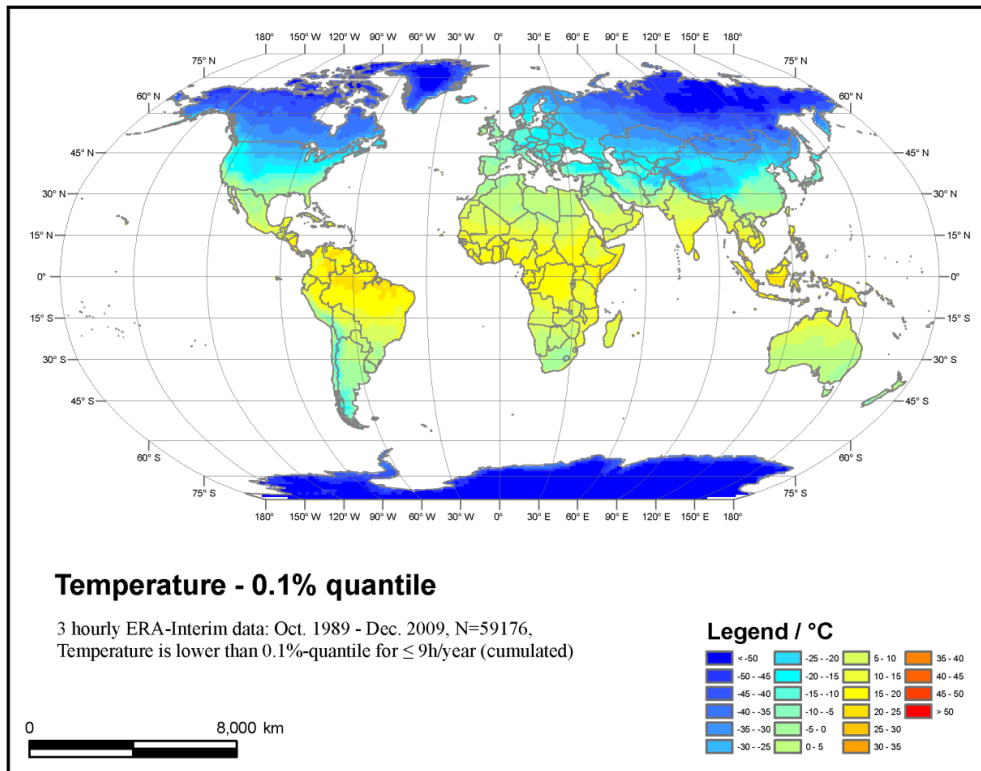
Figure 7.2: Global temperature distribution for 0.1 % and 99.9 % quantiles (Geographical Coordinate System: WGS 1984, Projection System: World Robinson, spatial resolution: 100 km, original ERA-Interim spatial resolution: ~79 km).

Temperature - 0.1% quantile

3 hourly ERA-Interim data: Oct. 1989 - Dec. 2009, N=59176,
Temperature is lower than 0.1%-quantile for ≤ 9h/year (cumulated)

Legend /°C

Temperature - 99.9% quantile

3 hourly ERA-Interim data: Oct. 1989 - Dec. 2009, N=59176,
Temperature is higher than 99.9%-quantile for ≤ 9h/year (cumulated)

Legend /°C
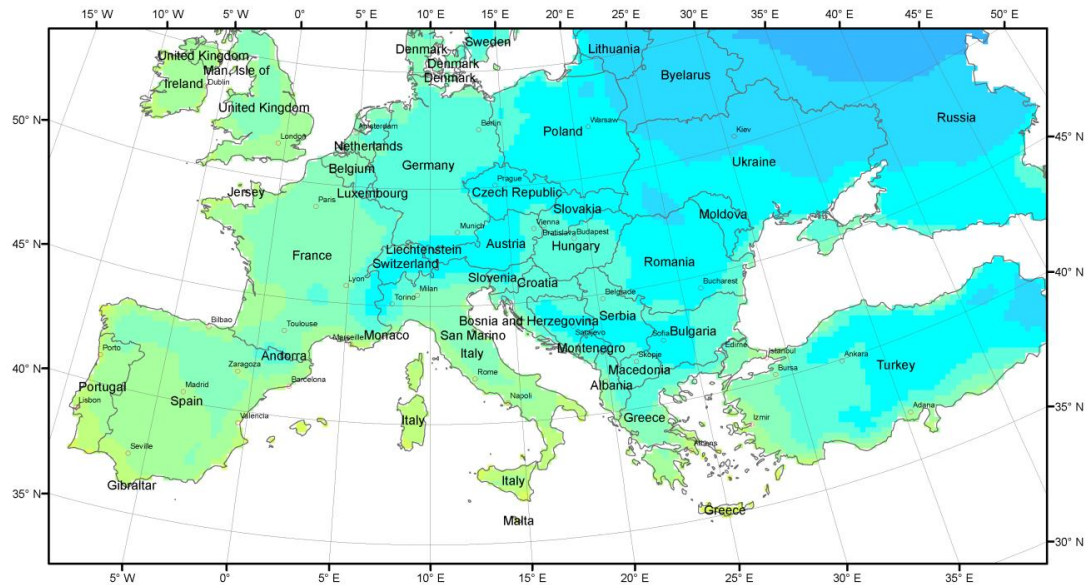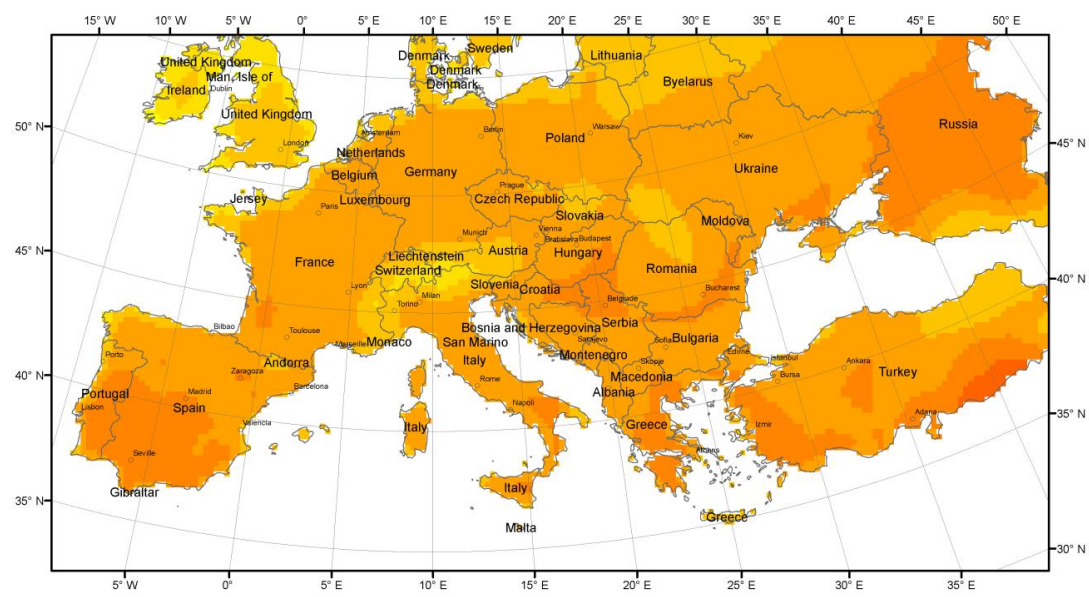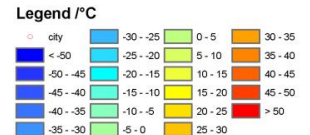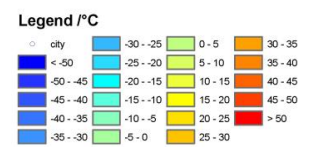
Figure 7.3: Southern European temperature distribution for 0.1 % and 99.9 % quantiles (Geographical Coordinate System: European 1950, Projection System: Lambert Conformal Conic, spatial resolution: 25 km, original ERA-Interim spatial resolution: ~79 km).

7.3 Validation of the ERA-Interim Temperature for Large Cities

7.3.1 ECA&D Data

Nine large representative cites (Berlin, Dublin, Istanbul, Kiev, Madrid, Moscow, Munich, Paris, and Vienna) located over a wide range of longitude in Europe, have been chosen from the ECA&D dataset and compared for daily minimum, maximum and mean temperature with the nearest ERA-Interim grid data from October 1 1989- December 31 2009. The altitude difference between ERA-Interim grid height and the elevations of the cities ranges from -36 to 164 m (Table 7.2). Munich has the largest altitude difference, due to its location close to the Alps. Generally, these differences are small and the effect on temperature resulting from the altitude gap could be ignored in the comparison. NSE, RMSE, and MAE are again adopted for data evaluation.

Table 7.2: City information (the corresponding nearest ERA-Interim grid heights also are listed).

Sites	Latitude	Longitude	Elevation (m)	Grid height (m)
Berlin	52.50	13.38	34	57
Dublin	53.35	-6.25	9	82
Istanbul	41.01	28.95	28	73
Kiev	50.45	30.52	169	133
Madrid	40.38	-3.72	667	811
Moscow	55.75	37.62	151	179
Munich	48.13	11.57	519	683
Paris	48.85	2.35	35	138
Vienna	48.21	16.37	346	323

7.3.2 Validation Results

The comparison of ERA-Interim 2 m temperature with daily data of nine meteorological stations is summarized in Table 7.3. ERA-Interim data agree well with observations with respect to daily minimum, mean and maximum temperature. The Berlin station has the smallest bias (MAE) with the values of 1.03, 0.75 and 1.26 °C for minimum, mean and maximum temperature, respectively. The Kiev and Moscow stations have the same performances for NSE and similar RMSEs and MAEs. Dublin has the worst NSE for minimum temperature while Istanbul has the worst NSE and MAE for maximum temperature. In terms of MAE, Paris has the largest bias (2.09 °C) with regard to minimum temperature. For mean temperature, ERA-Interim performs well for all cities,

and the NSE ranges from 0.90 to 0.98. Figure 7.4 and 7.5 give a more detailed visualization of the results for Berlin and Istanbul, separately.
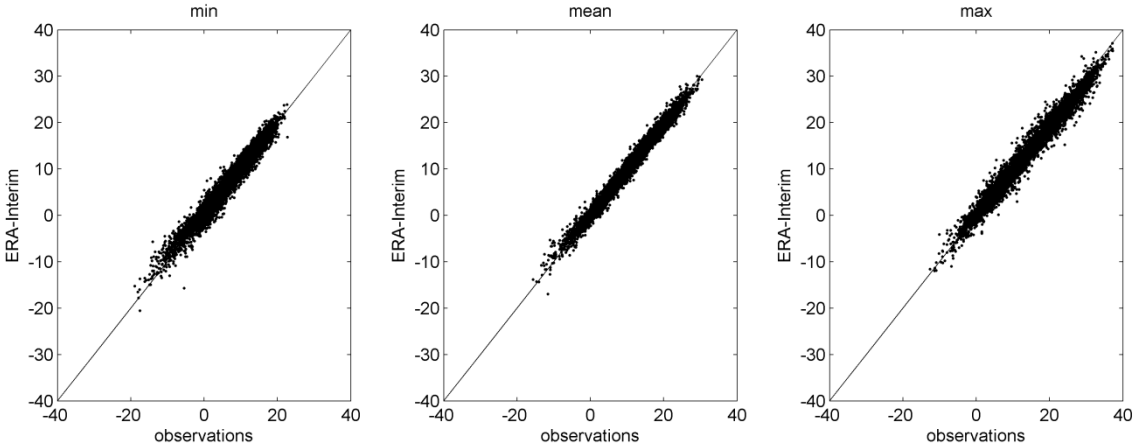

Figure 7.4: The scatter plots show the comparison of daily ERA-Interim 2 m temperatures and measurements for Berlin, minimum temperature (left), mean (middle) and maximum (right).
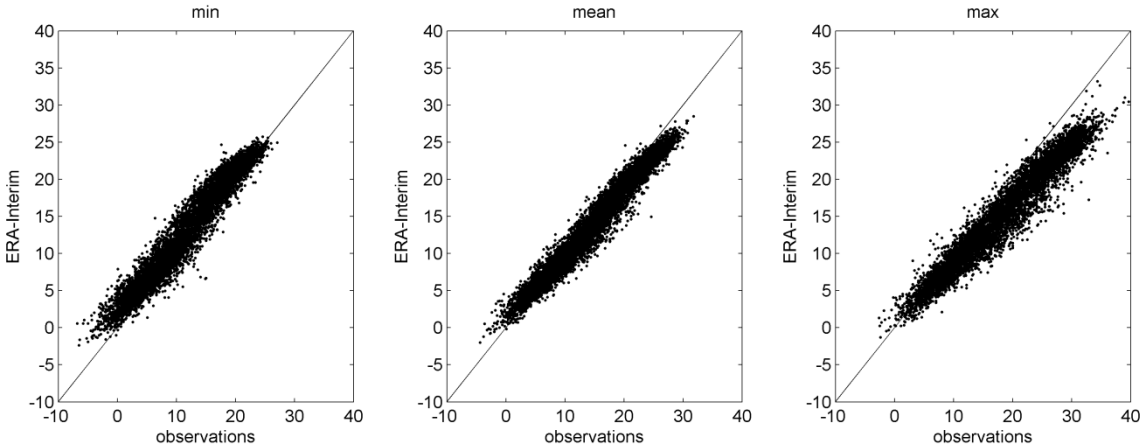

Figure 7.5: The scatter plots show the comparison of daily ERA-Interim 2 m temperatures and measurements for Istanbul, minimum temperature (left), mean (middle) and maximum (right).

Table 7.3: Comparison of ERA-Interim 2 m temperature with daily data of nine meteorological stations. The NSE, as well as the RMSE and MAE in °C, are also listed.

Site	NSE			RMSE			MAE		
	min	mean	max	min	mean	max	min	mean	max
Berlin	0.96	0.98	0.97	1.35	0.97	1.59	1.03	0.75	1.26
Dublin	0.77	0.92	0.85	2.21	1.26	1.93	1.73	1.01	1.60
Istanbul	0.91	0.94	0.79	2.09	1.78	3.84	1.65	1.42	3.21
Kiev	0.96	0.98	0.97	1.66	1.30	1.80	1.25	1.00	1.37
Madrid	0.87	0.91	0.93	2.28	2.23	2.36	1.92	1.95	1.98
Moscow	0.96	0.98	0.97	2.00	1.37	2.03	1.50	1.05	1.55
Munich	0.92	0.94	0.90	1.95	1.80	2.80	1.45	1.47	2.30
Paris	0.81	0.90	0.92	2.49	2.07	2.15	2.09	1.82	1.85
Vienna	0.87	0.91	0.93	2.58	2.49	2.56	2.06	1.89	2.15

7.4 Conclusion

Based on ERA-Interim data, Matlab and a GIS framework, the thematic maps of temperature distribution and temperature extremes (represented by quantiles) were produced for globe and regions. These direct viewing maps could help users to rapidly judge the temperature distribution and extremes. The application of VW and AUDI is a good example of ERA-Interim data application to socio-economic context.

It is necessary to validate the ERA-Interim data for large cities, which are the main markets for automobiles. Nine large city measurements have been compared to ERA-Interim with respect to daily minimum, mean and maximum temperatures. In general, ignoring the elevation difference effects (only 23-164 m altitude differences), ERA-Interim agrees well with observations in nine large cities (Table 7.3). The average MAEs is 1.03, 0.75 and 1.26 °C for minimum, mean and maximum temperature, respectively. However, there is bias for individual large city, for large-scale analysis, the original ERA-Interim data projected on the reduced Gaussian grid of N128 is appropriate and sufficient with respect to its long-term period and 3-hourly temporal resolution.

Chapter 8

Conclusions and Outlook

8.1 Conclusions

The aim of this thesis was to resolve the spatial resolution discrepancy between reanalysis data (ERA-Interim) and local measurements, using simple and novel statistical downscaling approaches with respect to temperature and precipitation, which are the most important input variables for hydrological and climate models.

Firstly, the large-scale error of ERA-Interim reanalysis data was evaluated for the central Alps by comparing it to gridded observations data (E-OBS) derived from the high density of measurements on a 0.25° grid from 1979-2010. It can be pointed out that the large-scale error of temperature is generally small, which agreed with previous studies (e.g. Simmons et al., 2010). The average anomaly of the entire area is 0.6 °C for both T_n and T_g, and 0.9 °C for T_x. However, the quantile analysis showed that ERA-Interim is weak in capturing the extreme temperature in complex terrains. The analysis of elevation dependence has shown that the error could be reduced significantly by using an appropriate lapse rate. This is also the theoretical principle of the temperature downscaling model (Chapter 4). ERA-Interim has significant bias in the wet season (May to August) and the dry season (November to February), compared to observations. Although ERA-Interim has almost the same standard deviation as the inter-annual variability of daily precipitation with E-OBS: 1.0 mm day^{-1}, the mean absolute error (MAE) was large and varied between 4.5 mm day^{-1} and 9.5 mm day^{-1} in wet days for the entire area. Precipitation is more complex than temperature in the high mountainous regions, which implies that the elevation is not the only factor to be considered for downscaling. Other variables such as wind components and humidity fields also play significant roles in the precipitation process.

A new and novel temperature downscaling approach was presented, based on the ERA-Interim internal lapse rate. The method's performance has been compared to benchmark methods that use the conventional fixed lapse rate (Kunkel, 1989) and the observed lapse rate derived from high and low stations. The results demonstrated that using a fixed lapse rate was not satisfactory and led to a large bias for high elevations. The observed lapse rates worked best but its

acquisition is generally limited, because only a small number of stations in high mountainous regions and in high altitude regions exist and thus cannot provide an appropriate lapse rate. Furthermore, the usage of measured lapse rates can lead to the fact that the model is forced into the direction of implausible temperatures if one of the stations which are used for calculating the lapse rate delivers incorrect measurements. The new method, based on ERA-Interim modeled lapse rate, which is derived from temperatures and geopotential heights at representative pressure levels (925 hPa, 850 hPa, and 700 hPa), was independent of observations. This novel approach showed a convincing performance, especially for higher elevations. The ERA-Interim internal lapse rate is a useful tool for correcting the original output data to the station scale, even if they underestimating the observed lapse rates for the whole season with all of the occurring variations (see Chapter 4). An extended test was carried out for flux tower sites, which again proved that the ERA-Interim internal lapse rate is a useful tool for correcting the original output data to the station scale (see Chapter 6).

A new machine learning method, Lasso, was introduced for downscaling ERA-Interim daily precipitation. It is useful for variable selection and prevention of the over-fitting. These advantages were implemented by adding a penalty parameter into the ordinary least-squares regression model. Benchmark methods, LOCI and QM, as well as Stepwise regression, were applied for method comparison in a high mountainous region, the central Alps. LOCI and QM showed advantages in predicting precipitation occurrence but led to a large error, compared to the original ERA-Interim data. Nevertheless, even though Stepwise considered the same set of local circulation variables as Lasso, it yielded the worst predictions, due to its flaws in variable selection and regression shrinkage. The Lasso algorithm generated a slightly worse variation when compared with LOCI and QM but a precipitation occurrence similar to the original ERA-Interim. The error that was reduced by Lasso was significant (12.2 % RMSE and 17.2 % of MAE), especially for some stations for which only Lasso was effectual (see Chapter 5). In summary, Lasso is well-suited for sparse and possibly under-determined linear regression problems, as well as for joint estimation and continuous variable selection.

Information from FLUXNET tower sites, which represented various vegetation and climate types in different topographic regions, were adopted for ERA-Interim validation. The analysis illustrated that ERA-Interim captures temperature and precipitation well for micrometeorological stations, in general. However, errors still existed, due to complex reasons, such as ERA-Interim grid height errors. The novel temperature downscaling methods were validated for ten flux tower sites, which illustrated that they have a good transferability. MAE was reduced 28.3 % by the

downscaling methods. Consequently, ERA-Interim temperature data is suitable for large-scale application, which was also furthermore demonstrated by a socio-economic example. The temperature quantile maps for the globe and regions provide the visual information for VW and AUDI's marketing planning. As the main markets, nine large cities were applied for validation of ERA-Interim data. The average MAEs for minimum, mean and maximum temperatures are 1.03, 0.75 and 1.26 °C, respectively. However, there is bias for individual large city, for large-scale analysis, the original ERA-Interim data projected on the reduced Gaussian grid of N128 is appropriate and sufficient with respect to its long-term period and 3-hourly temporal resolution.

In sum, the temperature downscaling method based on ERA-Interim modeled lapse rate was applicable for mountainous areas as well as other areas. The precipitation model was valid for high elevation stations, for which, in particular, the conventional benchmark method did not work. Both downscaling methods are simple and easily implemented for further studies. ERA-Interim reanalysis data is appropriate for various spatial resolution applications, from individual site to continental and global scales.

8.2 Outlook

Although novel and efficient downscaling methods for temperature and precipitation have been provided, several considerations for model extensions or improvements can be foreseen. First of all, even though this thesis focused on ERA-Interim reanalysis data, there are other mature reanalysis products provided by different institutions in the world, such as NCEP/NCAR data (Table 1.3). It is of great interest and valuable to investigate other reanalysis products that represent different land surface regimes. Different assimilation models could result in various results in complex terrains. Besides, this study used only 0.25° grid data, and other spatial resolutions also are worth testing, which could help users to investigate the errors arising from grid interpolation.

Secondly, for temperature downscaling methods, a transition dividing local circulation and free-air dominant circulation was used in the central Alps. How this transition level changes with respect to various topographies should be further tested. Furthermore, temperature and geopotential heights at 925 hPa, 850 hPa and 700 hPa were applied for computing the internal lapse rate. Do other pressure levels work equally well? It would also be worthwhile to investigate this interesting question. Additionally, the characteristics of vertical lapse rates from ERA-Interim are also important for downscaling model extensions.

Thirdly, for the Lasso algorithm, due to its fewer applications in precipitation downscaling, many more validation tests should be implemented in the future. More relevant variables (e.g. variables used in previous studies) and higher temporal resolution (sub-daily) tests would be helpful for model improvement. More input data means more computation demands. Thus, the computing time and efficiency also are worth evaluating. Numerous methods for precipitation have been employed in the previous studies. This thesis selected only three representative approaches for comparison. The evaluation of other methods, in particular non-linear models, such as support vector machine (SVM), is of great interest to end users.

Last but not least, apart from temperature and precipitation, other variables, including wind components, soil moisture, and snow depth, also must be downscaled for model application. The performance of hydrological models in certain catchments, especially for high elevation watersheds driven by downscaled input variables, should be tested. This is the ultimate aim for the further development of downscaling methods.

Bibliography

Agnihotri, G., Mohapatra, M., 2012. Prediction of occurrence of daily summer monsoon precipitation over Karnataka. Meteorol Appl, 19(2): 130-139.

Ahrens, B., 2003. Rainfall downscaling in an alpine watershed applying a multiresolution approach. J Geophys Res-Atmos, 108(D8).

Alexander, L.V., Uotila, P., Nicholls, N., 2009. Influence of sea surface temperature variability on global temperature and precipitation extremes. J Geophys Res-Atmos, 114.

Almazroui, M., 2012. Dynamical downscaling of rainfall and temperature over the Arabian Peninsula using RegCM4. Climate Res, 52: 49-62.

Anandhi, A., Srinivas, V.V., Kumar, D.N., Nanjundiah, R.S., 2009. Role of predictors in downscaling surface temperature to river basin in India for IPCC SRES scenarios using support vector machine. Int J Climatol, 29(4): 583-603.

Anders, A.M., Roe, G.H., Durran, D.R., Minder, J.R., 2007. Small-Scale Spatial Gradients in Climatological Precipitation on the Olympic Peninsula. J. Hydrometeorol., 8(5):1068-1081.

Baldocchi, D. et al., 2001. FLUXNET: A new tool to study the temporal and spatial variability of ecosystem-scale carbon dioxide, water vapor, and energy flux densities. B Am Meteorol Soc, 82(11): 2415-2434.

Bardossy, A., Bogardi, I., Matyasovszky, I., 2005. Fuzzy rule-based downscaling of precipitation. Theor Appl Climatol, 82(1-2): 119-129.

Bardossy, A., Plate, E.J., 1992. Space-time model for daily rainfall using atmospheric circulation patterns. Water Resour Res, 28(5): 1247-1259.

Barry, R., 2008. Mountain Weather and Climate. Cambridge University Press: pp:19-70.

Barry, R.G., 1992. Mountain Climatology and Past and Potential Future Climatic Changes in Mountain Regions - a Review. Mt Res Dev, 12(1): 71-86.

Belo-Pereira, M., Dutra, E., Viterbo, P., 2011. Evaluation of global precipitation data sets over the Iberian Peninsula. J Geophys Res-Atmos, 116.

Benestad, R.E., Hanssen-Bauer, I., Forland, E.J., 2007. An evaluation of statistical models for downscaling precipitation and their ability to capture long-term trends. Int J Climatol, 27(5): 649-665.

Berg, A.A., Famiglietti, J.S., Walker, J.P., Houser, P.R., 2003. Impact of bias correction to reanalysis products on simulations of North American soil moisture and hydrological fluxes. J Geophys Res-Atmos, 108(D16).

Bernhardt, M., Schulz, K., 2010. SnowSlide: A simple routine for calculating gravitational snow transport. Geophys Res Lett, 37.

Berrisford, P. et al., 2009. The ERA-Interim archive (version 1.0). ERA Report Series:European Centre for Medium Range Weather Forecasts.

Berrisford, P. et al., 2011. Atmospheric conservation properties in ERA-Interim. Q J Roy Meteor Soc, 137(659): 1381-1399.

Betts, A.K., Kohler, M., Zhang, Y.C., 2009. Comparison of river basin hydrometeorology in ERA-Interim and ERA-40 reanalyses with observations. J Geophys Res-Atmos, 114.

Beuchat, X., Schaefli, B., Soutter, M., Mermoud, A., 2011. Toward a robust method for subdaily rainfall downscaling from daily data. Water Resour Res, 47.

Blandford, T.R. et al., 2008. Seasonal and synoptic variations in near-surface air temperature lapse rates in a mountainous basin. J Appl Meteorol Clim, 47(1): 249-261.

Boe, J., Terray, L., Habets, F., Martin, E., 2007. Statistical and dynamical downscaling of the Seine basin climate for hydro-meteorological studies. Int J Climatol, 27(12): 1643-1655.

Bolstad, P.V., Swift, L., Collins, F., Regniere, J., 1998. Measured and predicted air temperatures at basin to regional scales in the southern Appalachian mountains. Agr Forest Meteorol, 91(3-4): 161-176.

Bosilovich, M.G., Chen, J., Robertson, F.R., Adler, R.F., 2008. Evaluation of Global Precipitation in Reanalyses. J Appl Meteorol Clim, 47(9): 2279-2299.

Bray, M., Han, D.W., Xuan, Y.Q., Bates, P., Williams, M., 2011. Rainfall uncertainty for extreme events in NWP downscaling model. Hydrol Process, 25(9): 1397-1406.

Bromwich, D.H., Hines, K.M., Bai, L.-S., 2009. Development and testing of Polar Weather Research and Forecasting model: 2. Arctic Ocean. Journal of Geophysical Research: Atmospheres, 114(D8): D08122.

Burger, G., Chen, Y., 2005. Regression-based downscaling of spatial variability for hydrologic applications. J Hydrol, 311(1-4): 299-317.

Caesar, J., Alexander, L., Vose, R., 2006. Large-scale changes in observed daily maximum and minimum temperatures: Creation and analysis of a new gridded data set. J Geophys Res-Atmos, 111(D5).

Cannon, A.J., 2007. Nonlinear analog predictor analysis: A coupled neural network/analog model for climate downscaling. Neural Networks, 20(4): 444-453.

Chandler, R.E., Wheater, H.S., 2002. Analysis of rainfall variability using generalized linear models: A case study from the west of Ireland. Water Resour Res, 38(10): 1192.

Charles, S.P., Bates, B.C., Smith, I.N., Hughes, J.P., 2004. Statistical downscaling of daily precipitation from observed and modelled atmospheric fields. Hydrol Process, 18(8): 1373-1394.

Charlton, R., Fealy, R., Moore, S., Sweeney, J., Murphy, C., 2006. Assessing the impact of climate change on water supply and flood hazard in Ireland using statistical downscaling and hydrological modelling techniques. Climatic Change, 74(4): 475-491.

Chen, S.T., Yu, P.S., Tang, Y.H., 2010. Statistical downscaling of daily precipitation using support vector machines and multivariate analysis. J Hydrol, 385(1-4): 13-22.

Christensen, J.H., Hewitson, B., Busuioc, A., Chen, A., Gao, X., 2007. Regional climate projections. In: Solomon S, Qin D, Manning M, Chen Z, Marquis M, et al. eds. Climate Change 2007: The Physical Science Basis. Contribution of Working Group I to the Fourth Assessment Report of the Intergovernmental Panel on Climate Change. Cambridge and New York: Cambridge University Press.

Clark, M.P., Slater, A.G., 2006. Probabilistic quantitative precipitation estimation in complex terrain. J. Hydrometeorol., 7(1): 3-22.

Compo, G.P. et al., 2011. The Twentieth Century Reanalysis Project. Q J Roy Meteor Soc, 137(654): 1-28.

Crane, R.G., Hewitson, B.C., 1998. Doubled CO2 precipitation changes for the susquehanna basin: Down-scaling from the genesis general circulation model. Int J Climatol, 18(1): 65-76.

Cullen, R.M., Marshall, S.J., 2011. Mesoscale Temperature Patterns in the Rocky Mountains and Foothills Region of Southern Alberta. Atmos Ocean, 49(3): 189-205.

Daly, C. et al., 2008. Physiographically sensitive mapping of climatological temperature and precipitation across the conterminous United States. Int J Climatol, 28(15): 2031-2064.

Decker, M. et al., 2012. Evaluation of the Reanalysis Products from GSFC, NCEP, and ECMWF Using Flux Tower Observations. J Climate, 25(6): 1916-1944.

Dee, D.P., 2005. Bias and data assimilation. Q J Roy Meteor Soc, 131(613): 3323-3343.

Dee, D.P., Uppala, S., 2009. Variational bias correction of satellite radiance data in the ERA-Interim reanalysis. Q J Roy Meteor Soc, 135(644): 1830-1841.

Dee, D.P. et al., 2011. The ERA-Interim reanalysis: configuration and performance of the data assimilation system. Q J Roy Meteor Soc, 137(656): 553-597.

DeGaetano, A.T., Belcher, B.N., 2007. Spatial interpolation of daily maximum and minimum air temperature based on meteorological model analyses and independent observations. J Appl Meteorol Clim, 46(11): 1981-1992.

Dobler, C., Hagemann, S., Wilby, R.L., Stötter, J., 2012. Quantifying different sources of uncertainty in hydrological projections in an Alpine watershed. Hydrol Earth Syst Sc, 16(11): 4343-4360.

Dodson, R., Marks, D., 1997. Daily air temperature interpolated at high spatial resolution over a large mountainous region. Climate Res, 8(1): 1-20.

Ebtehaj, A.M., Foufoula-Georgiou, E., Lerman, G., 2012. Sparse regularization for precipitation downscaling. Journal of Geophysical Research: Atmospheres, 117(D8): D08107.

ECA&D, 2013. URL http://eca.knmi.nl.

ECMWF, 2009a. IFS Documentation-Cy33r1 Part II: Data Assimilation.

ECMWF, 2009b. IFS Documentation-Cy33r1 Part IV: Physical Processes.

ECMWF, 2013. URL http://www.ecmwf.int/.

Engen-Skaugen, T., 2007. Refinement of dynamically downscaled precipitation and temperature scenarios. Climate Change, 84(3): 365-382.

E-OBS, 2013. URL http://www.ecad.eu/.

Fealy, R., Sweeney, J., 2007. Statistical downscaling of precipitation for a selection of sites in Ireland employing a generalised linear modelling approach. Int J Climatol, 27(15): 2083-2094.

Ferraris, L., Gabellani, S., Rebora, N., Provenzale, A., 2003. A comparison of stochastic models for spatial rainfall downscaling. Water Resour Res, 39(12).

Flato, G.M. et al., 2000. The Canadian Centre for Climate Modelling and Analysis global coupled model and its climate. Clim Dynam, 16(6): 451-467.

Fluxdata, 2013. URL http://www.fluxdata.org/DataInfo/default.aspx.

FLUXNET, 2013. URL http://fluxnet.ornl.gov/introduction.

Frank, I.E., Friedman, J.H., 1993. A Statistical View of Some Chemometrics Regression Tools. Technometrics, 35: 109-148.

Frei, C., Schar, C., 1998. A precipitation climatology of the Alps from high-resolution rain-gauge observations. Int J Climatol, 18(8): 873-900.

Friederichs, P., Hense, A., 2007. Statistical downscaling of extreme precipitation events using censored quantile regression. Mon Weather Rev, 135(6): 2365-2378.

Fu, W.J., 1998. Penalized Regressions: The Bridge versus the Lasso. Journal of Computational and Graphical Statistics, 7(3): 397-416.

Ghosh, S., Mujumdar, P.P., 2006. Future rainfall scenario over Orissa with GCM projections by statistical downscaling. Curr Sci India, 90(3): 396-404.

Ghosh, S., Mujumdar, P.P., 2008. Statistical downscaling of GCM simulations to streamflow using relevance vector machine. Adv Water Resour, 31(1): 132-146.

Gibson, R., Kallberg, P., Uppala, S., 1996. The ECMWF Re-Analysis (ERA) Project. ECMWF Newsletter, 73: 7-17.

Giorgi, F., 2008. Regionalization of climate change information for impact assessment and adaptation. WMO Bulletin, 57(2): 86-92.

Graham, L.P., Andréasson, J., Carlsson, B., 2007. Assessing climate change impacts on hydrology from an ensemble of regional climate models, model scales and linking methods: A case study on the Lule River basin. Climate Change, 81: 293-307.

Greene, A.M., Robertson, A.W., Smyth, P., Triglia, S., 2011. Downscaling projections of Indian monsoon rainfall using a non-homogeneous hidden Markov model. Q J Roy Meteor Soc, 137(655): 347-359.

Gregory, J.M. et al., 2001. Comparison of results from several AOGCMs for global and regional sea-level change 1900-2100. Clim Dynam, 18(3-4): 225-240.

Gruber, S., 2012. Derivation and analysis of a high-resolution estimate of global permafrost zonation. The Cryosphere, 6: 221-233.

Gu, L.H., Baldocchi, D., 2002. Fluxnet 2000 synthesis - Foreword. Agr Forest Meteorol, 113: 1-2.

Guan, H., Wilson, J.L., Makhnin, O., 2005. Geostatistical mapping of mountain precipitation incorporating autosearched effects of terrain and climatic characteristics. J. Hydrometeorol., 6(6): 1018-1031.

Guan, H., Wilson, J.L., Xie, H.J., 2009. A cluster-optimizing regression-based approach for precipitation spatial downscaling in mountainous terrain. J Hydrol, 375(3-4): 578-588.

Gudmundsson, L., Bremnes, J.B., Haugen, J.E., Engen-Skaugen, T., 2012. Technical Note: Downscaling RCM precipitation to the station scale using statistical transformations – a comparison of methods. Hydrol Earth Syst Sc, 16(9): 3383-3390.

Haensler, A., Hagemann, S., Jacob, D., 2011. Dynamical downscaling of ERA40 reanalysis data over southern Africa: added value in the simulation of the seasonal rainfall characteristics. Int J Climatol, 31(15): 2338-2349.

Hamlet, A.F., Lettenmaier, D.P., 2005. Production of temporally consistent gridded precipitation and temperature fields for the continental United States. J. Hydrometeorol., 6(3): 330-336.

Harpham, C., Wilby, R.L., 2005. Multi-site downscaling of heavy daily precipitation occurrence and amounts. J Hydrol, 312(1-4): 235-255.

Hashino, T., Bradley, A.A., Schwartz, S.S., 2007. Evaluation of bias-correction methods for ensemble streamflow volume forecasts. Hydrol Earth Syst Sc, 11: 939-950.

Haylock, M.R., Cawley, G.C., Harpham, C., Wilby, R.L., Goodess, C.M., 2006. Downscaling heavy precipitation over the United Kingdom: A comparison of dynamical and statistical methods and their future scenarios. Int J Climatol, 26(10): 1397-1415.

Haylock, M.R. et al., 2008. A European daily high-resolution gridded data set of surface temperature and precipitation for 1950-2006. J Geophys Res-Atmos, 113(D20).

Hellstrom, C., Chen, D.L., Achberger, C., Raisanen, J., 2001. Comparison of climate change scenarios for Sweden based on statistical and dynamical downscaling of monthly precipitation. Climate Res, 19(1): 45-55.

Hertig, E., Jacobeit, J., 2008. Assessments of Mediterranean precipitation changes for the 21st century using statistical downscaling techniques. Int J Climatol, 28(8): 1025-1045.

Hertig, E., Jacobeit, J., 2013. A novel approach to statistical downscaling considering nonstationarities: application to daily precipitation in the Mediterranean area. Journal of Geophysical Research: Atmospheres, 118: 1-14.

Hessami, M., Gachon, P., Ouarda, T.B.M.J., St-Hilaire, A., 2008. Automated regression-based statistical downscaling tool. Environ Modell Softw, 23(6): 813-834.

Hines, K.M., Bromwich, D.H., 2008. Development and Testing of Polar Weather Research and Forecasting (WRF) Model. Part I: Greenland Ice Sheet Meteorology*. Mon Weather Rev, 136(6): 1971-1989.

Hoerl, A.E., Kennard, R.W., 1970a. Ridge Regression: Applications to Nonorthogonal Problems. Technometrics, 12: 69-82.

Hoerl, A.E., Kennard, R.W., 1970b. Ridge Regression: Biased Estimation for Nonorthogonal Problems. Technometrics, 12: 55-67.

Hofer, M., Molg, T., Marzeion, B., Kaser, G., 2010. Empirical-statistical downscaling of reanalysis data to high-resolution air temperature and specific humidity above a glacier surface (Cordillera Blanca, Peru). J Geophys Res-Atmos, 115: -.

Hofstra, N., Haylock, M., New, M., Jones, P., Frei, C., 2008. Comparison of six methods for the interpolation of daily, European climate data. J Geophys Res-Atmos, 113(D21).

Hofstra, N., Haylock, M., New, M., Jones, P.D., 2009. Testing E-OBS European high-resolution gridded data set of daily precipitation and surface temperature. J Geophys Res-Atmos, 114.

Huebener, H., Kerschgens, M., 2007. Downscaling of current and future rainfall climatologies for southern Morocco. Part II: Climate change signals. Int J Climatol, 27(8): 1065-1073.

Huth, R., 2002. Statistical downscaling of daily temperature in Central Europe. J Climate, 15(13): 1731-1742.

Huth, R., 2004. Sensitivity of local daily temperature change estimates to the selection of downscaling models and predictors. J Climate, 17(3): 640-652.

Huth, R., Kliegrova, S., Metelka, L., 2008. Non-linearity in statistical downscaling: does it bring an improvement for daily temperature in Europe? Int J Climatol, 28(4): 465-477.

Im, E.S., Coppola, E., Giorgi, F., Bi, X., 2009. Validation of a High-Resolution Regional Climate Model for the Alpine Region and Effects of a Subgrid-Scale Topography and Land Use Representation. J Climate, 23(7): 1854-1873.

IPCC, 2007a. Climate Change 2007: Impacts, Adaptation and Vulnerability. IPCC AR4 WG2.

IPCC, 2007b. Climate Change 2007: Synthesis Report.

IPCC, 2007c. Climate Change 2007: The Physical Science Basis. IPCC AR4 WG1.

Ishida, T., Kawashima, S., 1993. Use of Cokriging to Estimate Surface Air-Temperature from Elevation. Theor Appl Climatol, 47(3): 147-157.

Kalnay, E., Cai, M., 2003. Impact of urbanization and land-use change on climate. Nature, 423(6939): 528-531.

Kalnay, E., Cai, M., Li, H., Tobin, J., 2006. Estimation of the impact of land-surface forcings on temperature trends in eastern United States. J Geophys Res-Atmos, 111(D6).

Kalnay, E. et al., 1996. The NCEP/NCAR 40-year reanalysis project. B Am Meteorol Soc, 77(3): 437-471.

Kanamitsu, M. et al., 2002. NCEP–DOE AMIP-II Reanalysis (R-2). B Am Meteorol Soc, 83(11): 1631-1643.

Klein Tank, A.M.G. et al., 2002. Daily dataset of 20th-century surface air temperature and precipitation series for the European Climate Assessment. Int J Climatol, 22(12): 1441-1453.

Kumar, D.N., Anandhi, A., Srinivas, V.V., Nanjundiah, R.S., 2008. Downscaling precipitation to river basin in India for IPCCSRES scenarios using support vector machine. Int J Climatol, 28(3): 401-420.

Kumar, D.N., Anandhi, A., Srinivas, V.V., Nanjundiah, R.S., 2009. Role of predictors in downscaling surface temperature to river basin in India for IPCC SRES scenarios using support vector machine. Int J Climatol, 29(4): 583-603.

Kunkel, E.K., 1989. Simple Procedures for Extrapolation of Humidity Variables in the Mountainous Western United States. J Climate, 2(7): 656-669.

Kysely, J., Plavcova, E., 2010. A critical remark on the applicability of E-OBS European gridded temperature data set for validating control climate simulations. J Geophys Res-Atmos, 115.

Lal, M., McGregor, J.L., Nguyen, K.C., 2008. Very high-resolution climate simulation over Fiji using a global variable-resolution model. Clim Dynam, 30(2-3): 293-305.

Lamptey, B.L., 2008. Comparison of Gridded Multisatellite Rainfall Estimates with Gridded Gauge Rainfall over West Africa. Journal of Applied Meteorology and Climatology 47(1): 185–205.

Laughlin, G.P., 1982. Minimum Temperature and Lapse-Rate in Complex Terrain - Influencing Factors and Prediction. Arch Meteor Geophy B, 30(1-2): 141-152.

Leander, R., Buishand, T., van den Hurk, B., de Wit, M., 2008. Estimated changes in flood quantiles of the river Meuse from resampling of regional climate model output. J Hydrol, 351(3-4): 331-343.

Lim, Y.K., Cai, M., Kalnay, E., Zhou, L., 2008. Impact of vegetation types on surface temperature change. J Appl Meteorol Clim, 47(2): 411-424.

Liston, G.E., Elder, K., 2006. A meteorological distribution system for high-resolution terrestrial modeling (MicroMet). J. Hydrometeorol., 7(2): 217-234.

Liston, G.E., Hiemstra, C.A., Elder, K., Cline, D.W., 2008. Mesocell Study Area Snow Distributions for the Cold Land Processes Experiment (CLPX). J. Hydrometeorol., 9(5): 957-976.

Lundquist, J.D., Cayan, D.R., 2007. Surface temperature patterns in complex terrain: Daily variations and long-term change in the central Sierra Nevada, California. J Geophys Res-Atmos, 112(D11).

Mahrt, L., 2006. Variation of surface air temperature in complex terrain. J Appl Meteorol Clim, 45(11): 1481-1493.

Mahrt, L. et al., 2001. Shallow drainage flows. Bound-Lay Meteorol, 101(2): 243-260.

Maraun, D. et al., 2010. Precipitation Downscaling under Climate Change: Recent Developments to Bridge the Gap between Dynamical Models and the End User. Rev Geophys, 48.

Marshall, S.J., Sharp, M.J., Burgess, D.O., Anslow, F.S., 2007. Near-surface-temperature lapse rates on the Prince of Wales Icefield, Ellesmere Island, Canada: implications for regional downscaling of temperature. Int J Climatol, 27(3): 385-398.

Maurer, E.P., Wood, A.W., Adam, J.C., Lettenmaier, D.P., Nijssen, B., 2002. A long-term hydrologically based dataset of land surface fluxes and states for the conterminous United States. J Climate, 15(22): 3237-3251.

Mauser, W., Bach, H., 2009. PROMET – Large scale distributed hydrological modelling to study the impact of climate change on the water flows of mountain watersheds. J Hydrol, 376(3–4): 362-377.

Mehrotra, R., Sharma, A., 2005. A nonparametric nonhomogeneous hidden Markov model for downscaling of multisite daily rainfall occurrences. J Geophys Res-Atmos, 110(D16).

Mernild, S.H. et al., 2009. Greenland Ice Sheet surface mass-balance modelling and freshwater flux for 2007, and in a 1995-2007 perspective. Hydrol Process, 23(17): 2470-2484.

MeteoSwiss, 2013. URL http://www.meteoswiss.admin.ch/web.

Meyer-Christoffer, A. et al., 2011. GPCC Climatology Version 2011 at 0.25°: Monthly Land-Surface Precipitation Climatology for Every Month and the Total Year from Rain-Gauges built on GTS-based and Historic Data.doi:10.5676/DWD_GPCC/CLIM_M_V2011_025.

Minder, J.R., Mote, P.W., Lundquist, J.D., 2010. Surface temperature lapse rates over complex terrain: Lessons from the Cascade Mountains. J Geophys Res-Atmos, 115.

Mokhov, I.I., Akperov, M.G., 2006. Tropospheric lapse rate and its relation to surface temperature from reanalysis data. Izv Atmos Ocean Phy+, 42(4): 430-438.

Mooney, P.A., Mulligan, F.J., Fealy, R., 2011. Comparison of ERA-40, ERA-Interim and NCEP/NCAR reanalysis data with observed surface air temperatures over Ireland. Int J Climatol, 31(4): 545-557.

Murphy, J., 1999. An evaluation of statistical and dynamical techniques for downscaling local climate. J Climate, 12(8): 2256-2284.

Nash, J.E., Sutcliffe, J.V., 1970. River flow forecasting through conceptual models part I — A discussion of principles. J Hydrol, 10(3): 282-290.

Nieto, H., Sandholt, I., Aguado, I., Chuvieco, E., Stisen, S., 2011. Air temperature estimation with MSG-SEVIRI data: Calibration and validation of the TVX algorithm for the Iberian Peninsula. Remote Sens Environ, 115(1): 107-116.

Onogi, K. et al., 2007. The JRA-25 Reanalysis. J Meteorol Soc Jpn, 85(3): 369-432

Pages, M., Miro, J.R., 2010. Determining temperature lapse rates over mountain slopes using vertically weighted regression: a case study from the Pyrenees. Meteorol Appl, 17(1):53-63.

Panofsky, H.W., Brier, G.W., 1968. Some Applications of Statistics to Meteorology. The Pennsylvania State University Press: Philadelphia.

Pappenberger, F., 2012. Personal comment.

Pendse, G.V., 2011. A tutorial on the LASSO and the shooting algorithm. URL http://www.gautampendse.com/software/lasso/webpage/lasso_shooting.html.

Pepin, N.C., Seidel, D.J., 2005. A global comparison of surface and free-air temperatures at high elevations. J Geophys Res-Atmos, 110(D3).

Piani, C. et al., 2010. Statistical bias correction of global simulated daily precipitation and temperature for the application of hydrological models. J Hydrol, 395(3-4): 199-215.

Poli, P., Healy, S.B., Dee, D.P., 2010. Assimilation of Global Positioning System radio occultation data in the ECMWF ERA-Interim reanalysis. Q J Roy Meteor Soc, 136(653): 1972-1990.

Prihodko, L., Goward, S.N., 1997. Estimation of air temperature from remotely sensed surface observations. Remote Sens Environ, 60: 335-346.

Prince, S.D., Goetz, S.J., Dubayah, R.O., Czajkowski, K.P., Thawley, M., 1998. Inference of surface and air temperature, atmospheric precipitable water and vapor pressure deficit using Advanced Very High-Resolution Radiometer satellite observations: comparison with field observations. J Hydrol, 213(1-4): 230-249.

Ramirez, M.C.V., Velho, H.F.D., Ferreira, N.J., 2005. Artificial neural network technique for rainfall forecasting applied to the Sao Paulo region. J Hydrol, 301(1-4): 146-162.

Regniere, J., 1996. Generalized approach to landscape-wide seasonal forecasting with temperature-driven simulation models. Environ Entomol, 25(5): 869-881.

Rienecker, M.M. et al., 2011. MERRA: NASA's Modern-Era Retrospective Analysis for Research and Applications. J Climate, 24(14): 3624-3648.

Rolland, C., 2003. Spatial and seasonal variations of air temperature lapse rates in Alpine regions. J Climate, 16(7): 1032-1046.

Rummukainen, M., 1997. Methods for statistical downscaling of GCM simulations. SMHI reports meteorology and climatology, no.80, Swedish Meteorological and Hydrological Institute, Norrköping, Sweden.

Rummukainen, M., 2010. State-of-the-art with regional climate models. Wires Clim Change, 1(1): 82-96.

Saha, S., Coauthors, 2010. The NCEP Climate Forecast System Reanalysis. Bulletin of the American Meteorological Society, 91(8): 1015-1057.

Schmidli, J., Frei, C., Schar, C., 2001. Reconstruction of mesoscale precipitation fields from sparse observations in complex terrain. J Climate, 14(15): 3289-3306.

Schmidli, J., Frei, C., Vidale, P.L., 2006. Downscaling from GC precipitation: A benchmark for dynamical and statistical downscaling methods. Int J Climatol, 26(5): 679-689.

Schmidli, J. et al., 2007. Statistical and dynamical downscaling of precipitation: An evaluation and comparison of scenarios for the European Alps. J Geophys Res-Atmos, 112(D4).

Schneider, U., Becker, A., Meyer-Christoffer, A., Ziese, M., Rudolf, B., 2011. Global precipitation analysis products of the GPCC. Global Precipitation Climatology Centre (GPCC), Deutscher Wetterdienst: 1-13.

Schoof, J.T., Pryor, S.C., 2001. Downscaling temperature and precipitation: A comparison of regression-based methods and artificial neural networks. Int J Climatol, 21(7): 773-790.

Simmons, A., Uppala, S., Dee, D., Kobayashi, S., 2006. ERA-Interim: New ECMWF reanalysis products from 1989 onwards. ECMWF Newsletter, No. 110: 25-35.

Simmons, A.J. et al., 2004. Comparison of trends and low-occurrence variability in CRU, ERA-40, and NCEP/NCAR analyses of surface air temperature. J Geophys Res-Atmos, 109(D24).

Simmons, A.J., Willett, K.M., Jones, P.D., Thorne, P.W., Dee, D.P., 2010. Low-occurrence variations in surface atmospheric humidity, temperature, and precipitation: Inferences from reanalyses and monthly gridded observational data sets. J Geophys Res-Atmos, 115.

Snell, S.E., Gopal, S., Kaufmann, R.K., 2000. Spatial interpolation of surface air temperatures using artificial neural networks: Evaluating their use for downscaling GCMs. J Climate, 13(5): 886-895.

Spak, S., Holloway, T., Lynn, B., Goldberg, R., 2007. A comparison of statistical and dynamical downscaling for surface temperature in North America. J Geophys Res-Atmos, 112(D8).

Stahl, K., Moore, R.D., Floyer, J.A., Asplin, M.G., McKendry, I.G., 2006. Comparison of approaches for spatial interpolation of daily air temperature in a large region with complex topography and highly variable station density. Agr Forest Meteorol, 139(3-4): 224-236.

Szczypta, C. et al., 2011. Verification of the new ECMWF ERA-Interim reanalysis over France. Hydrol Earth Syst Sc, 15(2): 647-666.

Tabony, R.C., 1985. The Variation of Surface-Temperature with Altitude. Meteorol Mag, 114(1351): 37-48.

Tatli, H., Dalfes, H.N., Mentes, S., 2004. A statistical downscaling method for monthly total precipitation over Turkey. Int J Climatol, 24(2): 161-180.

Taylor, K.E., 2001. Summarizing multiple aspects of model performance in a single diagram. Journal of Geophysical Research: Atmospheres, 106(D7): 7183-7192.

Themeßl, M.J., Gobiet, A., Heinrich, G., 2012. Empirical-statistical downscaling and error correction of regional climate models and its impact on the climate change signal. Climatic Change, 112: 449-468.

Themeßl, M.J., Gobiet, A., Leuprecht, A., 2011. Empirical-statistical downscaling and error correction of daily precipitation from regional climate models. Int J Climatol, 31(10): 1530–1544.

Tibshirani, R., 1996. Regression Shrinkage and Selection via the Lasso. Journal of Royal Statistical Society. Series B (Methodological), 58(1): 267-288.

Trenberth, K.E., Guillemot, C.J., 1998. Evaluation of the atmospheric moisture and hydrological cycle in the NCEP/NCAR reanalyses. Clim Dynam, 14(3): 213-231.

Trenberth, K.E., Koike, T., Onogi, K., 2008. Progress and Prospects for Reanalysis for Weather and Climate. Eos, Transactions American Geophysical Union, 89(26): 234-235.

Uppala, S., Dee, D., Kobayashi, S., Berrisford, P., Simmons, A., 2008. Towards a climate data assimilation system: status updata of ERA-Interim. ECMWF Newsletter, No. 115: 12-18.

Uppala, S.M. et al., 2005. The ERA-40 re-analysis. Q J Roy Meteor Soc, 131(612): 2961-3012.

Vicente-Serrano, S.M., Saz-Sanchez, M.A., Cuadrat, J.M., 2003. Comparative analysis of interpolation methods in the middle Ebro Valley (Spain): application to annual precipitation and temperature. Climate Res, 24(2): 161-180.

Viner, D., Hulme, M., 1997. The Climate Impacts LINK Project: Applying Results of the Hadley Centre's Climate Change Experiments for Climate Change Impacts Assessment Report Prepared for the UK Department of the Environment Transport and the Regions. Publ. Climatic Research Unit.

Vonstorch, H., Zorita, E., Cubasch, U., 1993. Downscaling of Global Climate-Change Estimates to Regional Scales - an Application to Iberian Rainfall in Wintertime. J Climate, 6(6): 1161-1171.

Vrac, M., Stein, M., Hayhoe, K., 2007. Statistical downscaling of precipitation through nonhomogeneous stochastic weather typing. Climate Res, 34(3): 169-184.

Weisberg, S., 2012. Variable Selection and Regularization. URL http://users.stat.umn.edu/.

Widmann, M., Bretherton, C.S., 2000. Validation of mesoscale precipitation in the NCEP reanalysis using a new gridcell dataset for the northwestern United States. J Climate, 13(11): 1936-1950.

Widmann, M., Bretherton, C.S., Salathe, E.P., 2003. Statistical precipitation downscaling over the Northwestern United States using numerically simulated precipitation as a predictor. J Climate, 16(5): 799-816.

Wilby, R.L. et al., 2004. Guidelines for use of climate scenarios developed from statistical downscaling methods. IPCC Task Group on Data and Scenario Support for Impact and Climate Analysis (TGICA). URL http://ipcc-ddc.cru.uea.ac.uk/.

Wilby, R.L., Dawson, C.W., Barrow, E.M., 2002. SDSM - a decision support tool for the assessment of regional climate change impacts. Environ Modell Softw, 17(2): 147-159.

Wilby, R.L., Tomlinson, O.J., Dawson, C.W., 2003. Multi-site simulation of precipitation by conditional resampling. Climate Res, 23(3): 183-194.

Wilby, R.L., Wigley, T.M.L., 1997. Downscaling general circulation model output: a review of methods and limitations. Prog Phys Geog, 21(4): 530-548.

Wilby, R.L., Wigley, T.M.L., 2000. Precipitation predictors for downscaling: Observed and general circulation model relationships. Int J Climatol, 20(6): 641-661.

Wood, A.W., Leung, L.R., Sridhar, V., Lettenmaier, D.P., 2004. Hydrologic implications of dynamical and statistical approaches to downscaling climate model outputs. Climatic Change, 62(1-3): 189-216.

Wörlen, C., Schulz, K., Huwe, B., Eiden, R., 1999. Spatial extrapolation of agrometeorological variables. Agr Forest Meteorol, 94: 233-242.

Xu, C.Y., 1999. From GCMs to river flow: a review of downscaling methods and hydrologic modelling approaches. Prog Phys Geog, 23(2): 229-249.

Yang, W., Bárdossy, A., Caspary, H.-J., 2010. Downscaling daily precipitation time series using a combined circulation- and regression-based approach. Theor Appl Climatol, 102(3-4): 439-454.

Yin, C.H., Li, Y.P., Ye, W., Bornman, J.F., Yan, X.D., 2011. Statistical downscaling of regional daily precipitation over southeast Australia based on self-organizing maps. Theor Appl Climatol, 105(1-2): 11-26.

Zorita, E., von Storch, H., 1999. The analog method as a simple statistical downscaling technique: Comparison with more complicated methods. J Climate, 12(8): 2474-2489.

Zou, L.W., Zhou, T.J., Li, L., Zhang, J., 2010. East China Summer Rainfall Variability of 1958-2000: Dynamical Downscaling with a Variable-Resolution AGCM. J Climate, 23(23): 6394-6408.

A

Appendix

A.1 Reduced Gaussian Grid N128

Gaussian grids are not regular by spacing of the lines of latitude symmetrically about the Equator. Different Gaussian grids are referred by the number "N", which is the number of latitude lines from Equator to Pole. The longitude points distribute even space along each line of latitude. For reduced Gaussian grid, the number of longitude is specified, although latitudes are differing number of points. Table A.1 shows the N128 Reduced Gaussian grid.

Table A.1: N128 Reduced Gaussian grid.

Latitude number	Reduced points	Regular points	Latitude	Latitude number	Reduced points	Regular points	Latitude
1	18	512	89.46282	129	512	512	-0.35087
2	25	512	88.76695	130	512	512	-1.05262
3	36	512	88.06697	131	512	512	-1.75438
4	40	512	87.36606	132	512	512	-2.45613
5	45	512	86.66480	133	512	512	-3.15788
6	50	512	85.96337	134	512	512	-3.85964
7	60	512	85.26184	135	512	512	-4.56139
8	64	512	84.56026	136	512	512	-5.26314
9	72	512	83.85863	137	512	512	-5.96490
10	72	512	83.15698	138	512	512	-6.66665
11	80	512	82.45531	139	512	512	-7.36840
12	90	512	81.75363	140	512	512	-8.07016
13	90	512	81.05194	141	512	512	-8.77191
14	100	512	80.35023	142	512	512	-9.47366
15	108	512	79.64852	143	512	512	-10.17541
16	120	512	78.94681	144	512	512	-10.87717
17	120	512	78.24509	145	512	512	-11.57892
18	125	512	77.54336	146	512	512	-12.28067
19	128	512	76.84163	147	512	512	-12.98243
20	144	512	76.13990	148	512	512	-13.68418
21	144	512	75.43817	149	512	512	-14.38593
22	150	512	74.73644	150	512	512	-15.08768
23	160	512	74.03470	151	512	512	-15.78944
24	160	512	73.33296	152	512	512	-16.49119
25	180	512	72.63123	153	512	512	-17.19294
26	180	512	71.92949	154	512	512	-17.89470
27	180	512	71.22774	155	500	512	-18.59645

28	192	512	70.52600	156	500	512	-19.29820
29	192	512	69.82426	157	500	512	-19.99996
30	200	512	69.12252	158	500	512	-20.70171
31	216	512	68.42077	159	500	512	-21.40346
32	216	512	67.71903	160	500	512	-22.10521
33	216	512	67.01728	161	500	512	-22.80697
34	225	512	66.31554	162	486	512	-23.50872
35	240	512	65.61379	163	486	512	-24.21047
36	240	512	64.91204	164	486	512	-24.91223
37	240	512	64.21030	165	480	512	-25.61398
38	250	512	63.50855	166	480	512	-26.31573
39	250	512	62.80680	167	480	512	-27.01748
40	256	512	62.10505	168	480	512	-27.71924
41	270	512	61.40330	169	480	512	-28.42099
42	270	512	60.70156	170	480	512	-29.12274
43	288	512	59.99981	171	480	512	-29.82449
44	288	512	59.29806	172	480	512	-30.52625
45	288	512	58.59631	173	480	512	-31.22800
46	300	512	57.89456	174	480	512	-31.92975
47	300	512	57.19281	175	450	512	-32.63150
48	320	512	56.49106	176	450	512	-33.33326
49	320	512	55.78931	177	450	512	-34.03501
50	320	512	55.08756	178	450	512	-34.73676
51	320	512	54.38581	179	450	512	-35.43851
52	324	512	53.68406	180	432	512	-36.14027
53	360	512	52.98231	181	432	512	-36.84202
54	360	512	52.28056	182	432	512	-37.54377
55	360	512	51.57881	183	432	512	-38.24552
56	360	512	50.87705	184	432	512	-38.94728
57	360	512	50.17530	185	432	512	-39.64903
58	360	512	49.47355	186	432	512	-40.35078
59	360	512	48.77180	187	405	512	-41.05253
60	375	512	48.07005	188	400	512	-41.75428
61	375	512	47.36830	189	400	512	-42.45604
62	375	512	46.66655	190	400	512	-43.15779
63	375	512	45.96479	191	400	512	-43.85954
64	384	512	45.26304	192	384	512	-44.56129
65	384	512	44.56129	193	384	512	-45.26304
66	400	512	43.85954	194	375	512	-45.96479
67	400	512	43.15779	195	375	512	-46.66655
68	400	512	42.45604	196	375	512	-47.36830
69	400	512	41.75428	197	375	512	-48.07005
70	405	512	41.05253	198	360	512	-48.77180
71	432	512	40.35078	199	360	512	-49.47355
72	432	512	39.64903	200	360	512	-50.17530
73	432	512	38.94728	201	360	512	-50.87705
74	432	512	38.24552	202	360	512	-51.57881
75	432	512	37.54377	203	360	512	-52.28056
76	432	512	36.84202	204	360	512	-52.98231
77	432	512	36.14027	205	324	512	-53.68406
78	450	512	35.43851	206	320	512	-54.38581

79	450	512	34.73676	207	320	512	-55.08756
80	450	512	34.03501	208	320	512	-55.78931
81	450	512	33.33326	209	320	512	-56.49106
82	450	512	32.63150	210	300	512	-57.19281
83	480	512	31.92975	211	300	512	-57.89456
84	480	512	31.22800	212	288	512	-58.59631
85	480	512	30.52625	213	288	512	-59.29806
86	480	512	29.82449	214	288	512	-59.99981
87	480	512	29.12274	215	270	512	-60.70156
88	480	512	28.42099	216	270	512	-61.40330
89	480	512	27.71924	217	256	512	-62.10505
90	480	512	27.01748	218	250	512	-62.80680
91	480	512	26.31573	219	250	512	-63.50855
92	480	512	25.61398	220	240	512	-64.21030
93	486	512	24.91223	221	240	512	-64.91204
94	486	512	24.21047	222	240	512	-65.61379
95	486	512	23.50872	223	225	512	-66.31554
96	500	512	22.80697	224	216	512	-67.01728
97	500	512	22.10521	225	216	512	-67.71903
98	500	512	21.40346	226	216	512	-68.42077
99	500	512	20.70171	227	200	512	-69.12252
100	500	512	19.99996	228	192	512	-69.82426
101	500	512	19.29820	229	192	512	-70.52600
102	500	512	18.59645	230	180	512	-71.22774
103	512	512	17.89470	231	180	512	-71.92949
104	512	512	17.19294	232	180	512	-72.63123
105	512	512	16.49119	233	160	512	-73.33296
106	512	512	15.78944	234	160	512	-74.03470
107	512	512	15.08768	235	150	512	-74.73644
108	512	512	14.38593	236	144	512	-75.43817
109	512	512	13.68418	237	144	512	-76.13990
110	512	512	12.98243	238	128	512	-76.84163
111	512	512	12.28067	239	125	512	-77.54336
112	512	512	11.57892	240	120	512	-78.24509
113	512	512	10.87717	241	120	512	-78.94681
114	512	512	10.17541	242	108	512	-79.64852
115	512	512	9.47366	243	100	512	-80.35023
116	512	512	8.77191	244	90	512	-81.05194
117	512	512	8.07016	245	90	512	-81.75363
118	512	512	7.36840	246	80	512	-82.45531
119	512	512	6.66665	247	72	512	-83.15698
120	512	512	5.96490	248	72	512	-83.85863
121	512	512	5.26314	249	64	512	-84.56026
122	512	512	4.56139	250	60	512	-85.26184
123	512	512	3.85964	251	50	512	-85.96337
124	512	512	3.15788	252	45	512	-86.66480
125	512	512	2.45613	253	40	512	-87.36606
126	512	512	1.75438	254	36	512	-88.06697
127	512	512	1.05262	255	25	512	-88.76695
128	512	512	0.35087	256	18	512	-89.46282

A.2 Lasso Algorithm MATLAB® codes

```matlab
%   ---------estimate Lasso Lambda function ----------------------------------------

function z = estimateLassoLambda(y, X, kfold, lambda_vec )
% Fu, W.J., 1998. Penalized Regressions: The Bridge versus the Lasso. Journal of Computational
and Graphical Statistics, 7(3): 397-416.


[n, p] = size(X);
CVO = cvpartition(n, 'kfold' , kfold );
MSEerror = zeros( length(lambda_vec), 1 );


for k = 1:length( lambda_vec )
  % vector to store MSE error for each fold
  err = zeros(CVO.NumTestSets,1);
  for i = 1:CVO.NumTestSets
     % get ith training set
     trIdx = CVO.training(i);
     % get ith test set
     teIdx = CVO.test(i);
     % train LASSO using training set
     sL = solveLasso( y(trIdx), X(trIdx,:), lambda_vec(k) );
     % test using testing set
     ypred = X(teIdx,:) * sL.beta;
     % calculate MSE error
     temp = y(teIdx) - ypred;
     % clear ypred
     clear ypred;
     % calculate average error for the ith test set
     err(i) = (temp'*temp)/length(temp);
  end
  % calculate the mean error over all test sets
  MSEerror(k) = mean(err);
```

```matlab
end
% where get the smallest MSE
min_index = find( MSEerror == min(MSEerror) );
min_index = min_index(1);
z.lambda = lambda_vec( min_index );
z.lambda_vec = lambda_vec;
z.MSEerror = MSEerror;
z.min_index = min_index;
z.CVO = CVO;
z.y = y;
z.X = X;
z.kfold = kfold;


%   --------solve Lasso function-------------------------------------------------------------------------------

function z = solveLasso( y, X, lambda )
[n1, p1] = size(y);
[n, p] = size(X);
beta = (X'*X + 2*lambda) \ (X'*y);
% convergence flag
found = 0;
% convergence tolerance
TOL = 1e-6;
while( found == 0 )
  % save current beta
  beta_old = beta;
  % optimize elements of beta one by one
  for i = 1:p
    xi = X(:,i);
    % get residual excluding ith col
    yi = (y - X*beta) + xi*beta(i);
    % calulate xi'*yi and see where it falls
    deltai = (xi'*yi); % 1 by 1 scalar
    if ( deltai < -lambda )
```

```matlab
            beta(i) = ( deltai + lambda )/(xi'*xi);
        elseif ( deltai > lambda )
            beta(i) = ( deltai - lambda )/(xi'*xi);
        else
            beta(i) = 0;
        end
    end
    % check difference between beta and beta_old
    if ( max(abs(beta - beta_old)) <= TOL )
        found = 1;
    end
end
z.X = X;
z.y = y;
z.lambda = lambda;
z.beta = beta;
```

A.3 Taylor diagrams for all 50 MeteoSwiss stations
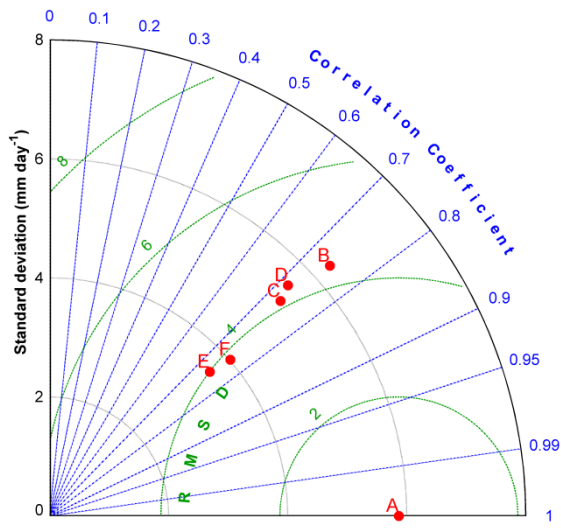
COV
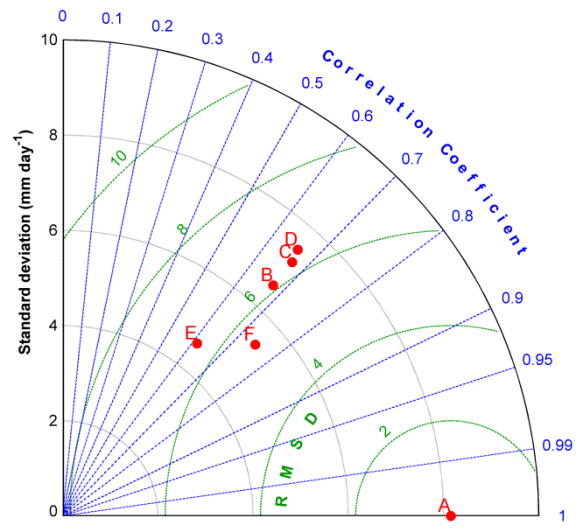
WFJ
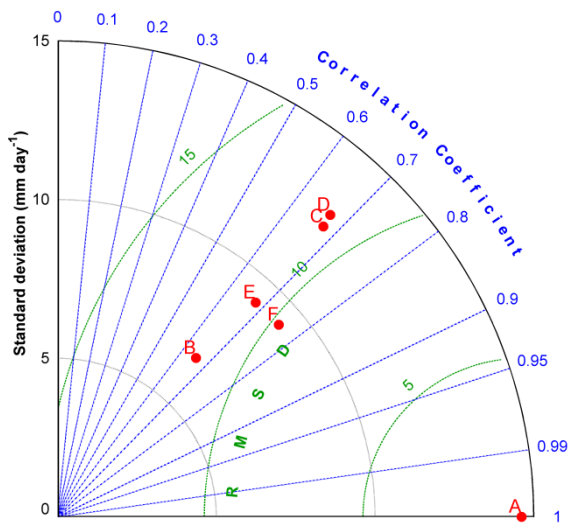
SAE
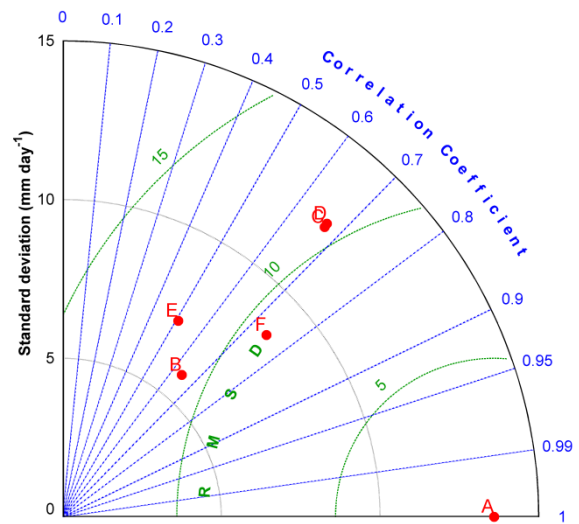
GSB
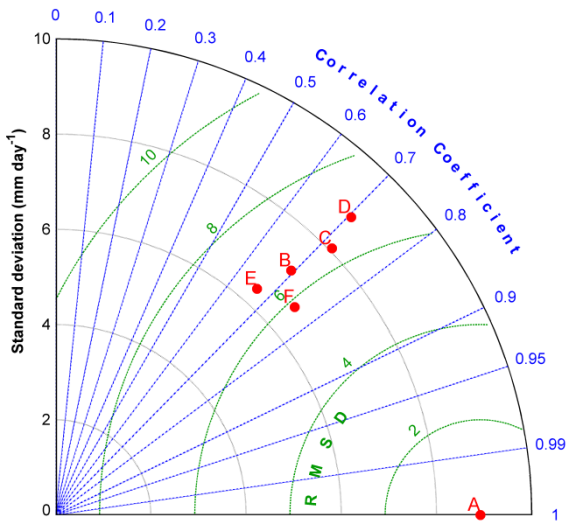
GUE
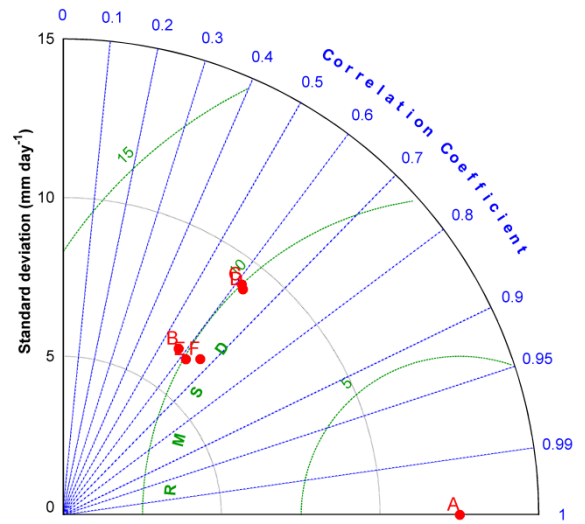
PIL
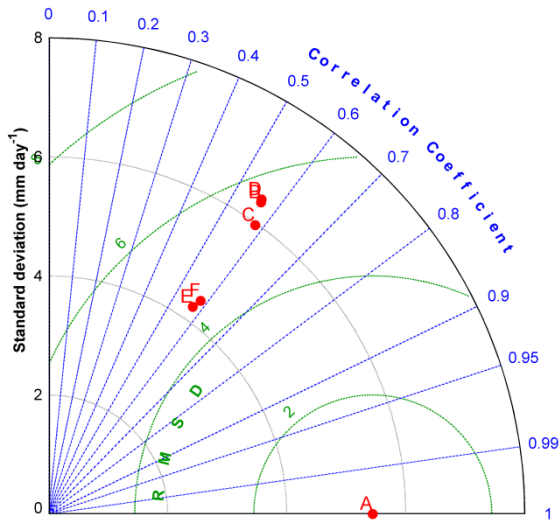
MLS
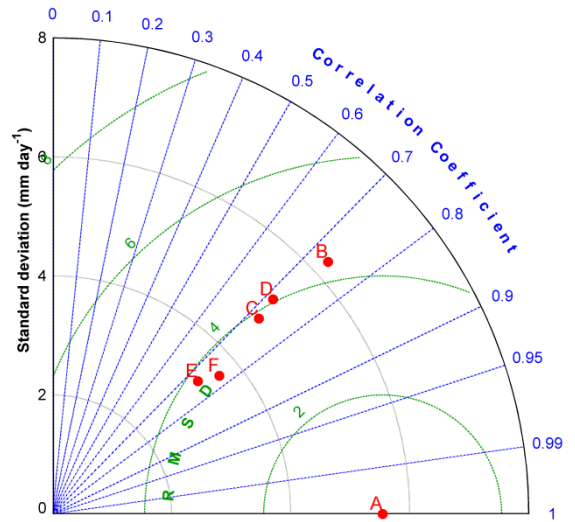
SAM
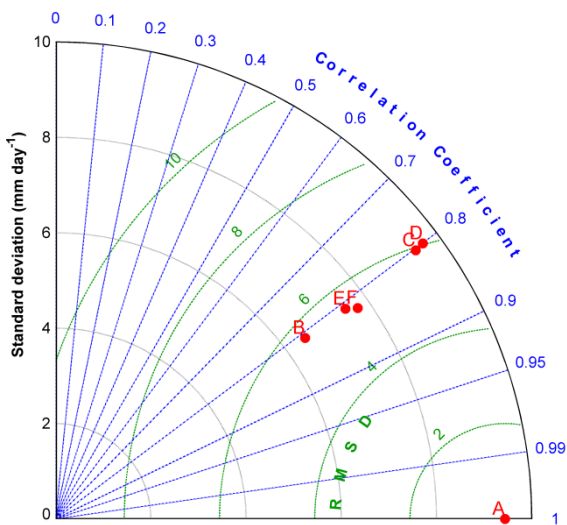
DOL
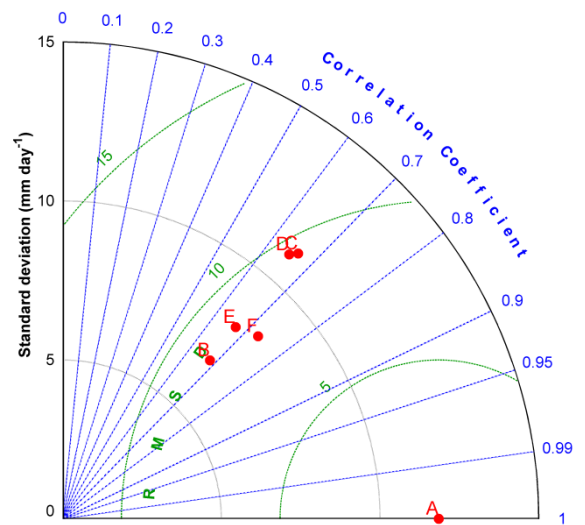
CIM
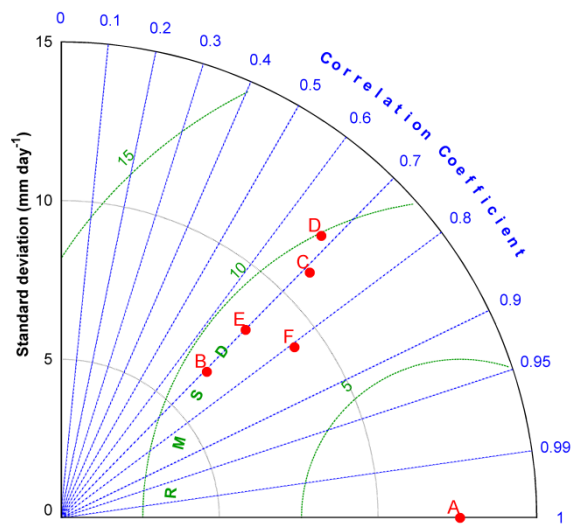
SBE
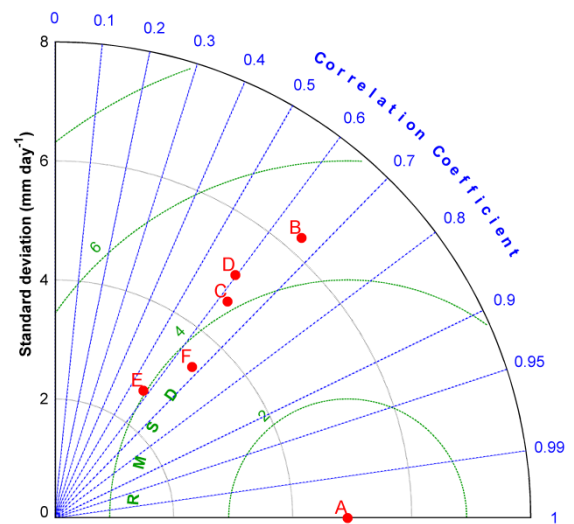
ZER
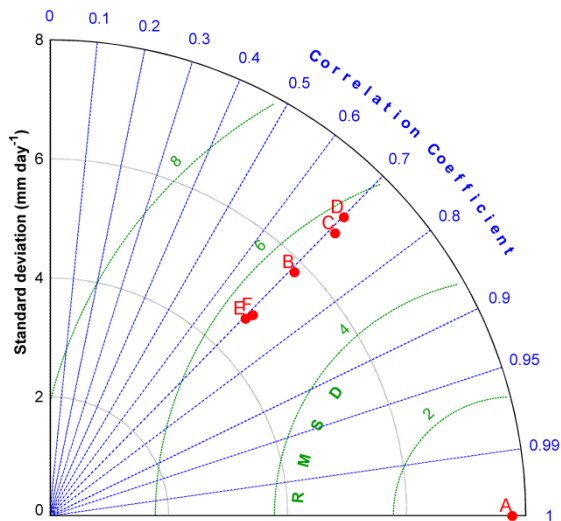
CHA
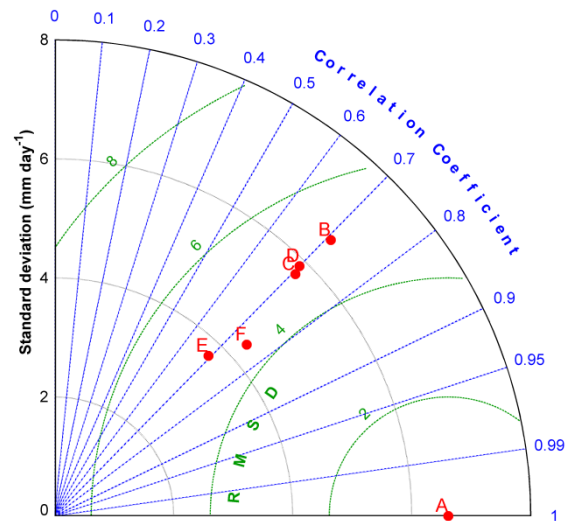
DAV
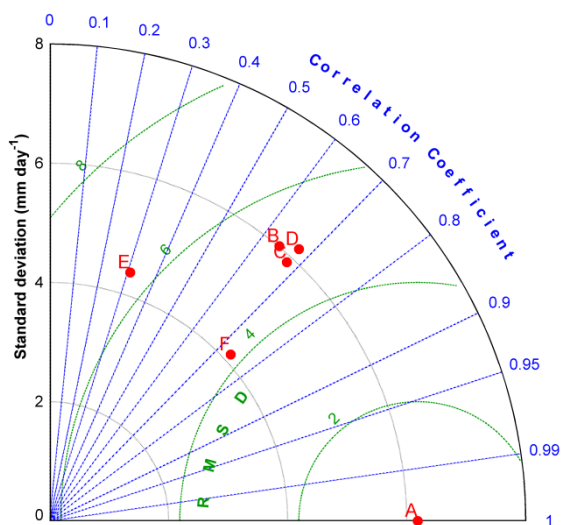
MVE
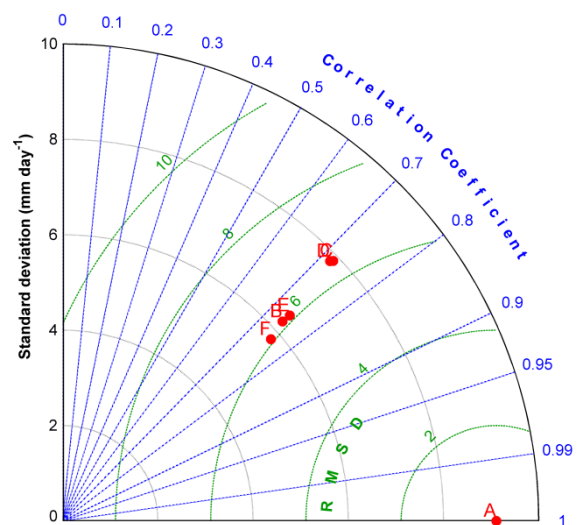
NAP
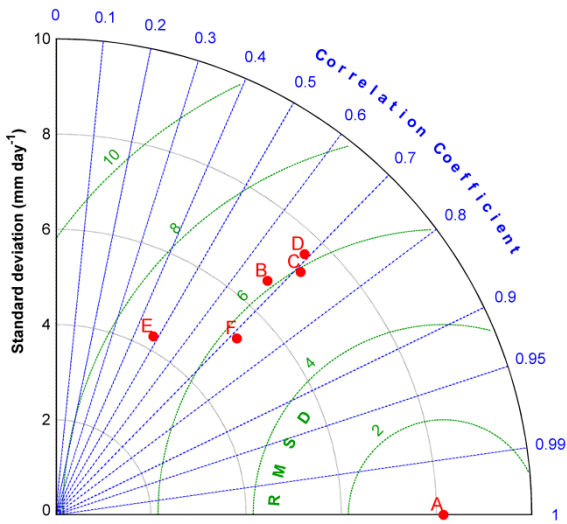
ULR
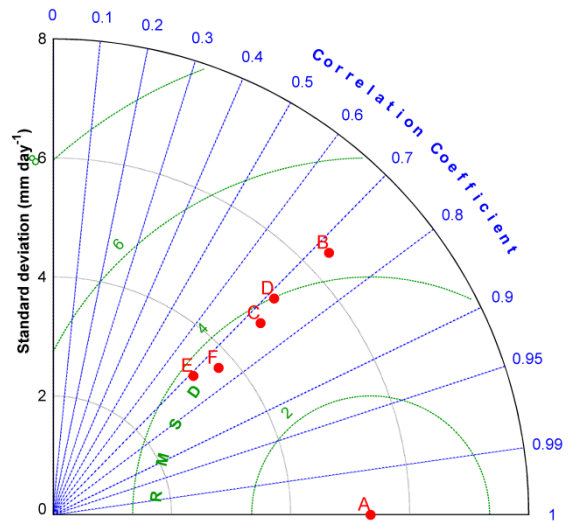
SCU
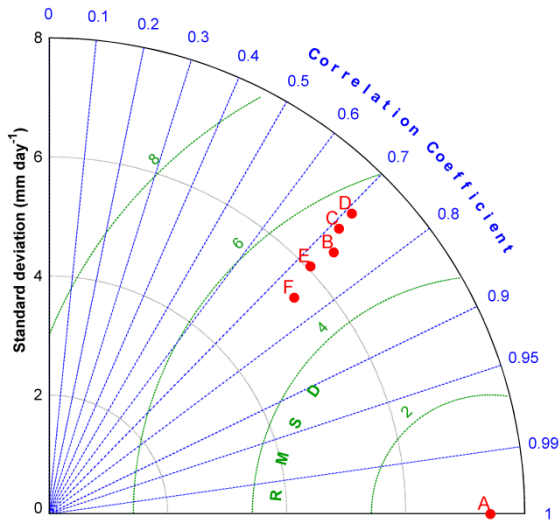
FRE
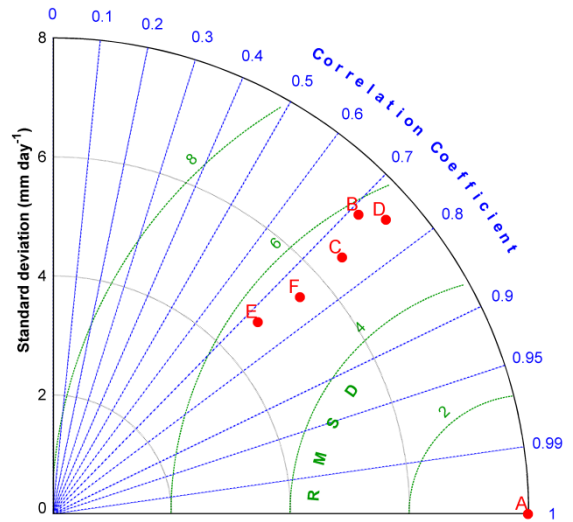
DIS
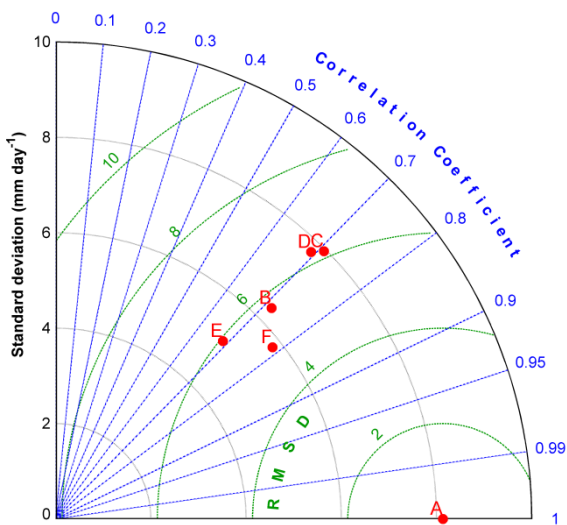
ROB
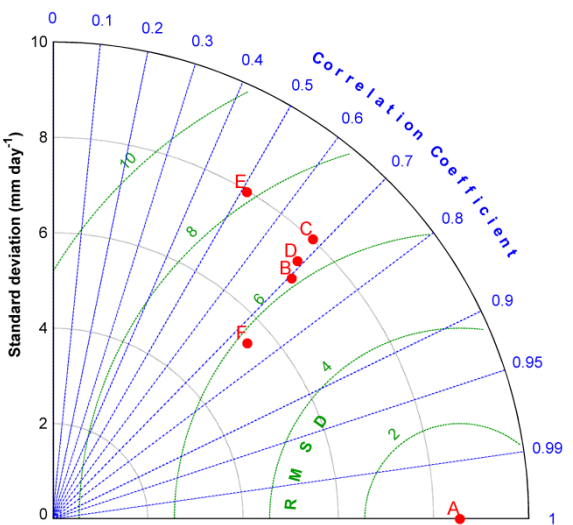
ENG
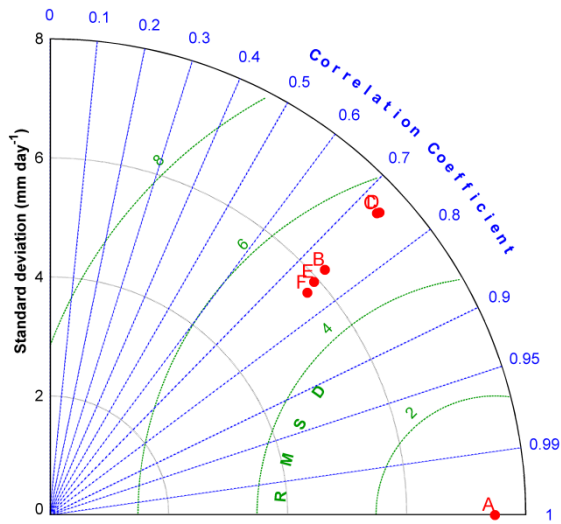
CDF
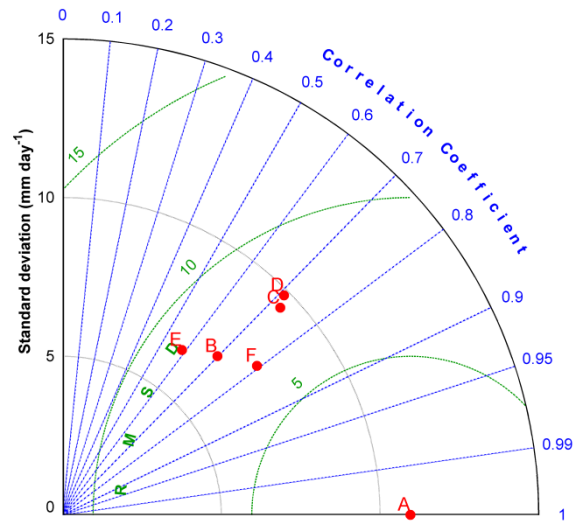
PIO
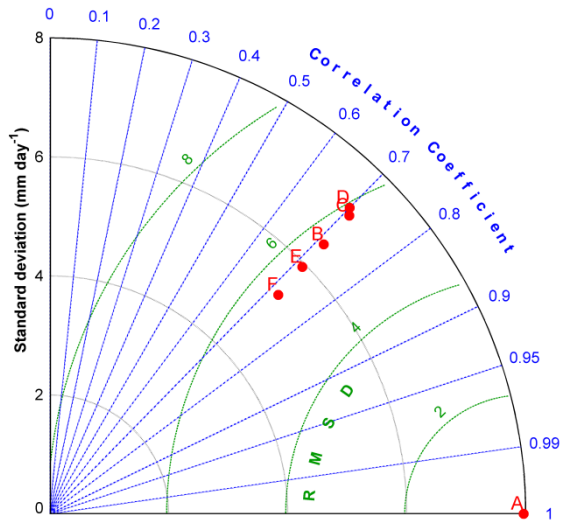
STG
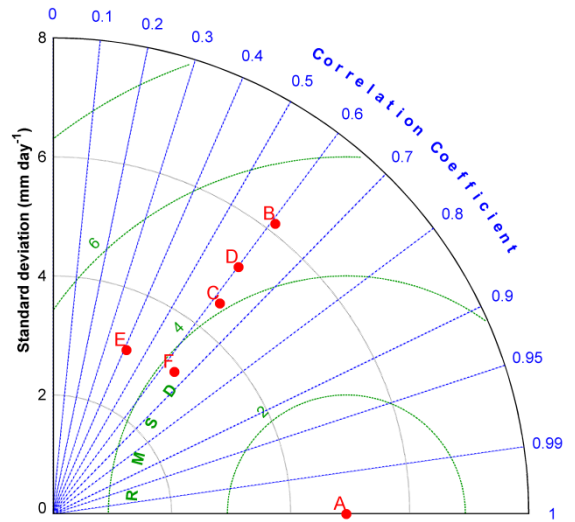
VIS
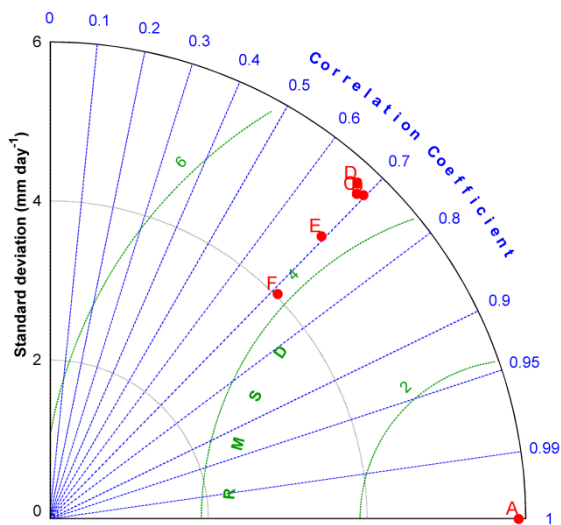
RUE
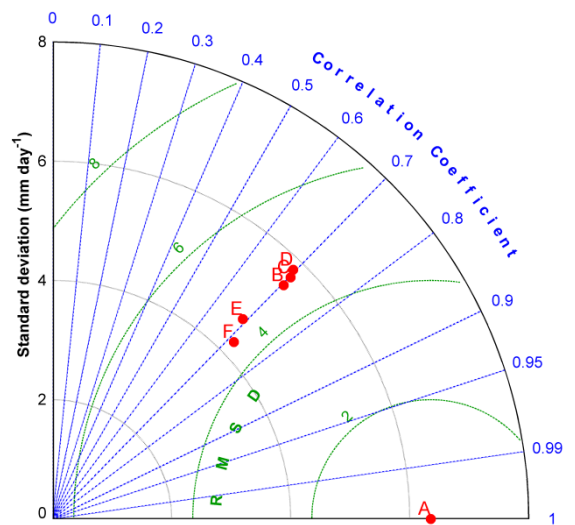
FAH
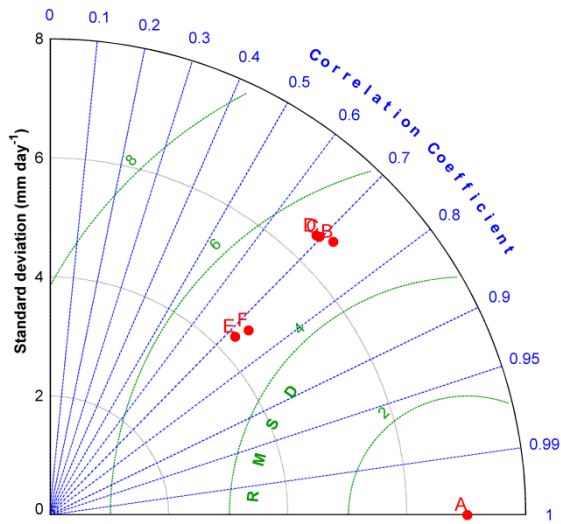
INT
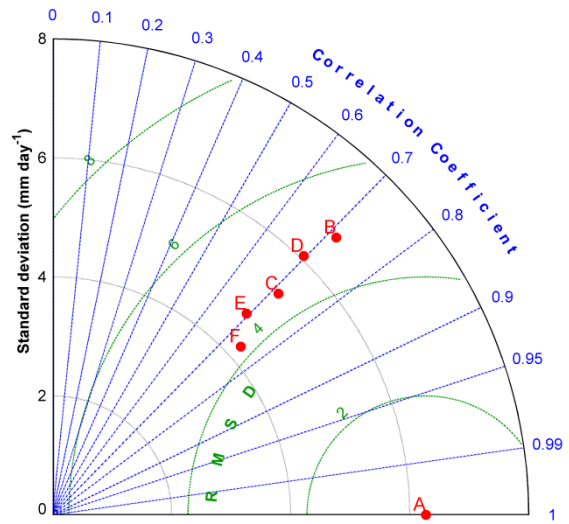
CHU
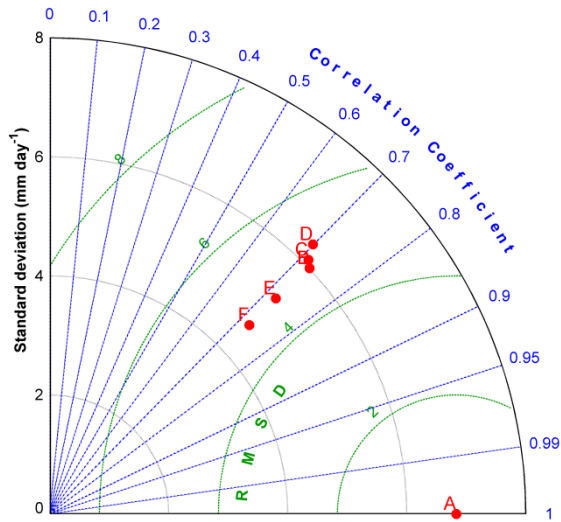
SMA
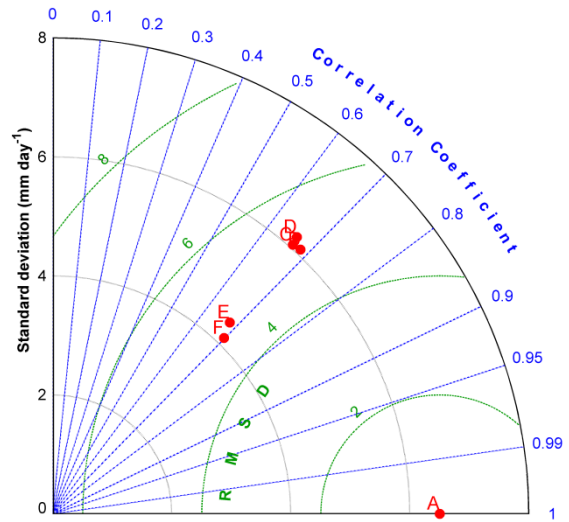
BER
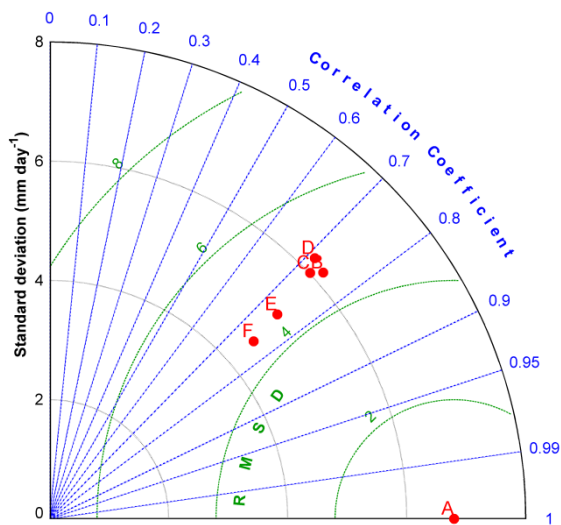
TAE
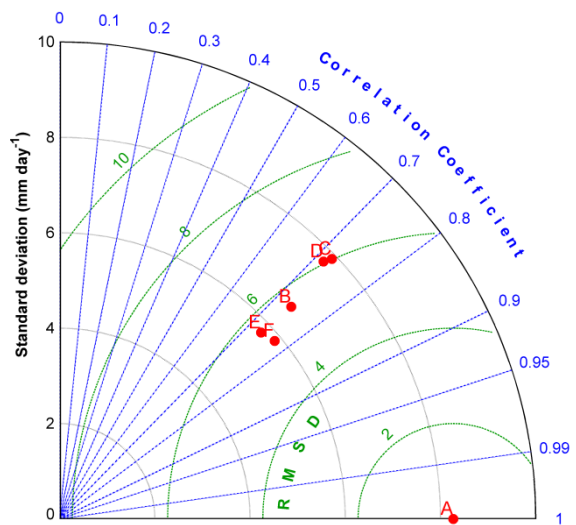
GLA
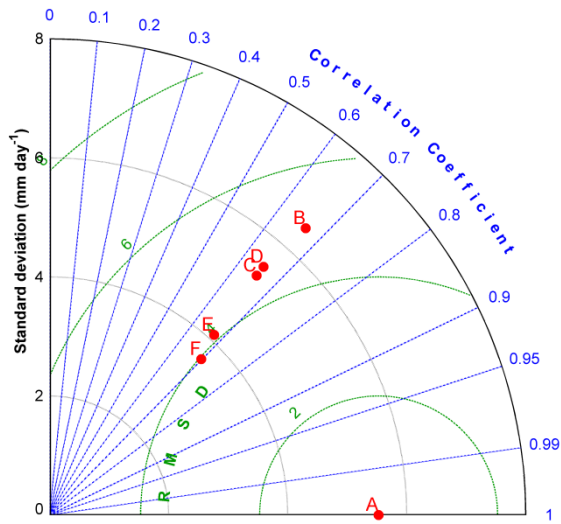
PAY
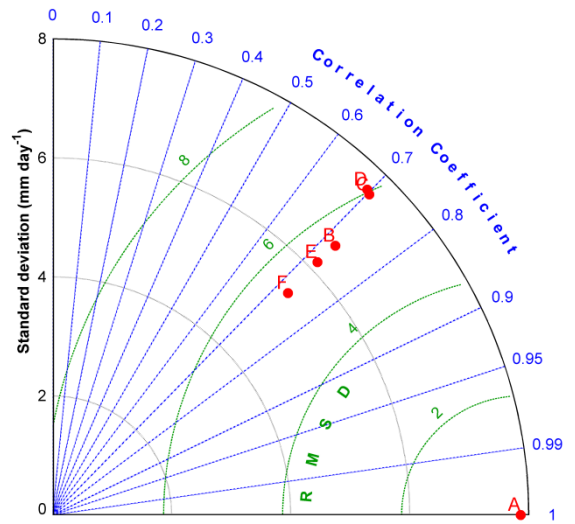
WAE
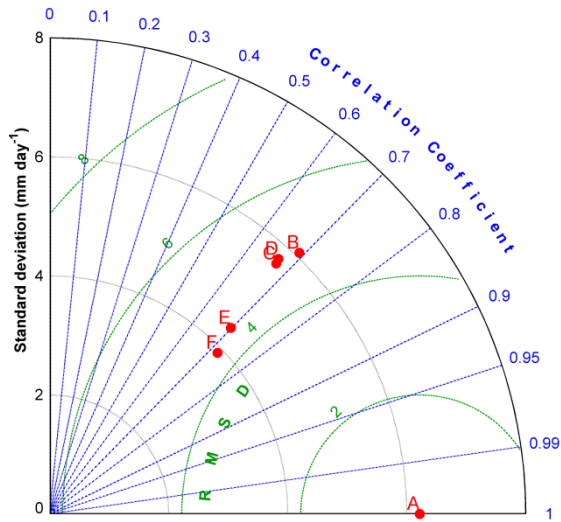
NEU
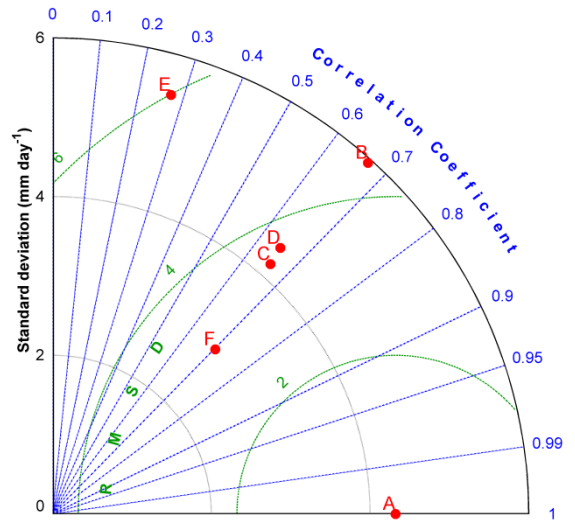
SIO
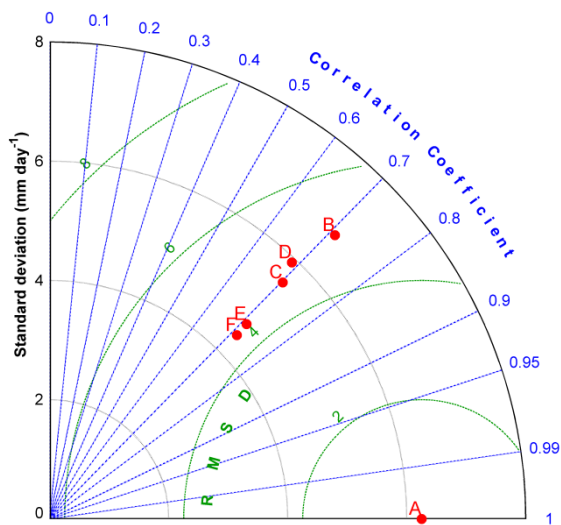
VAD
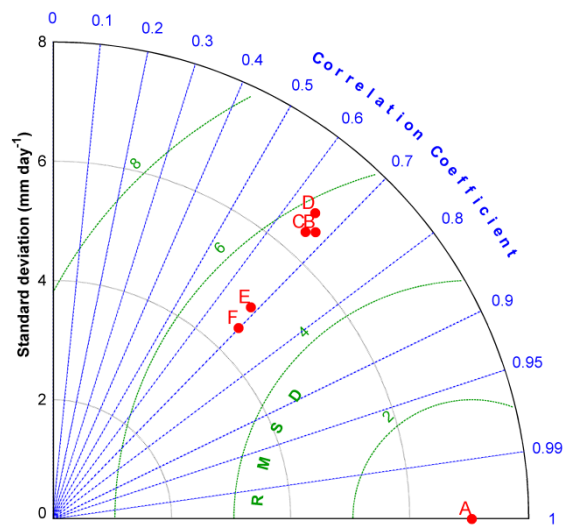
PUY
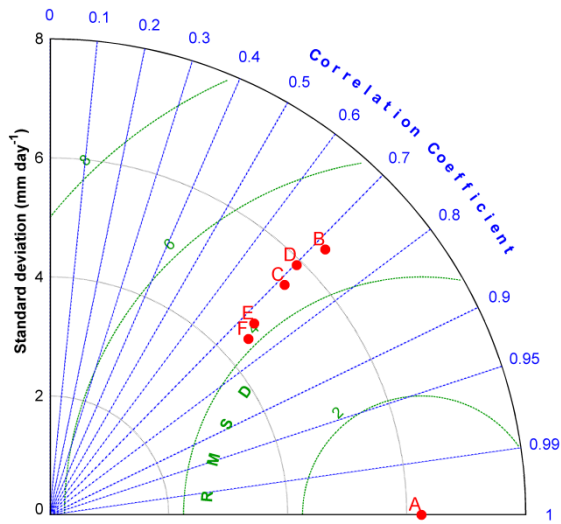
CGI
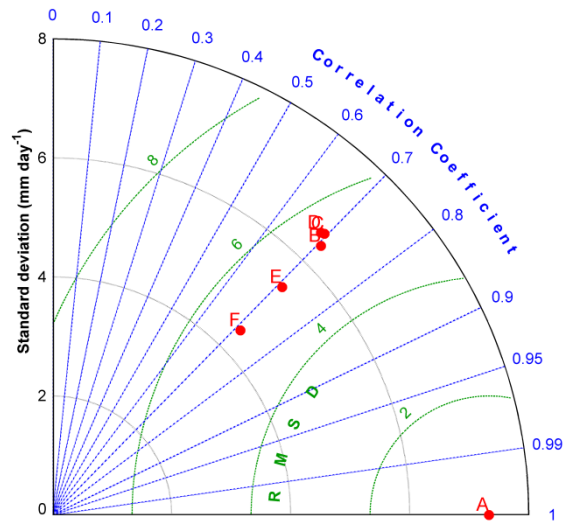
LUZ
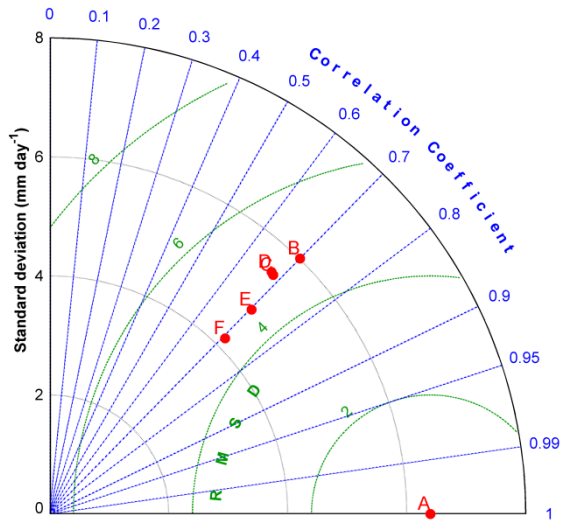
REH
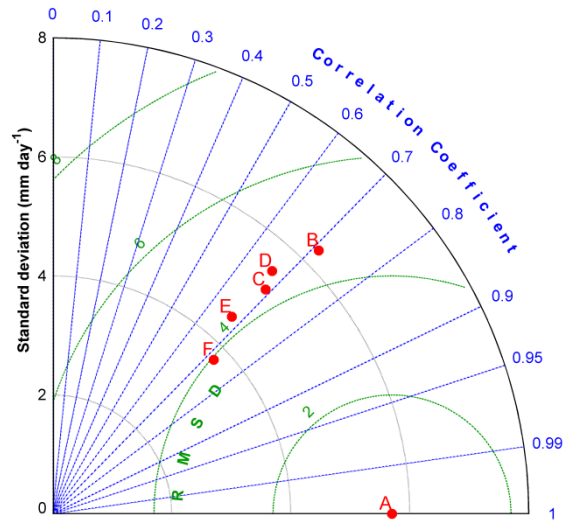
GUT
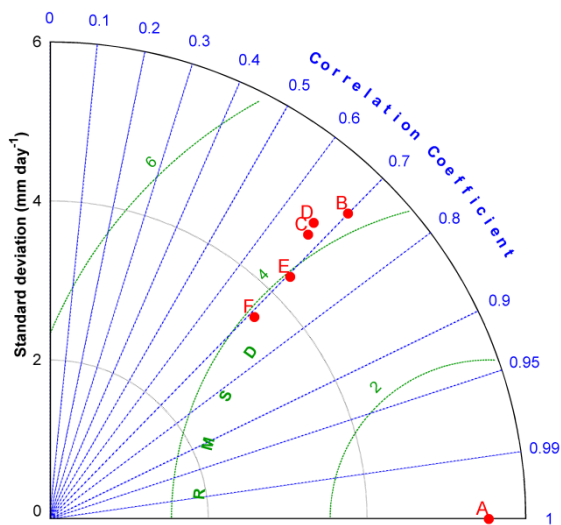
SHA
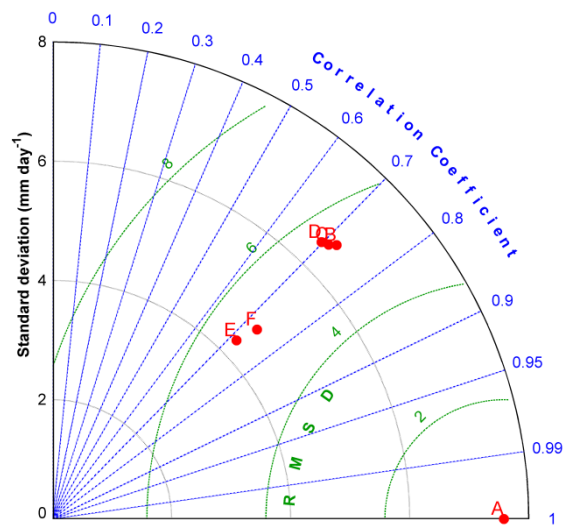
ALT
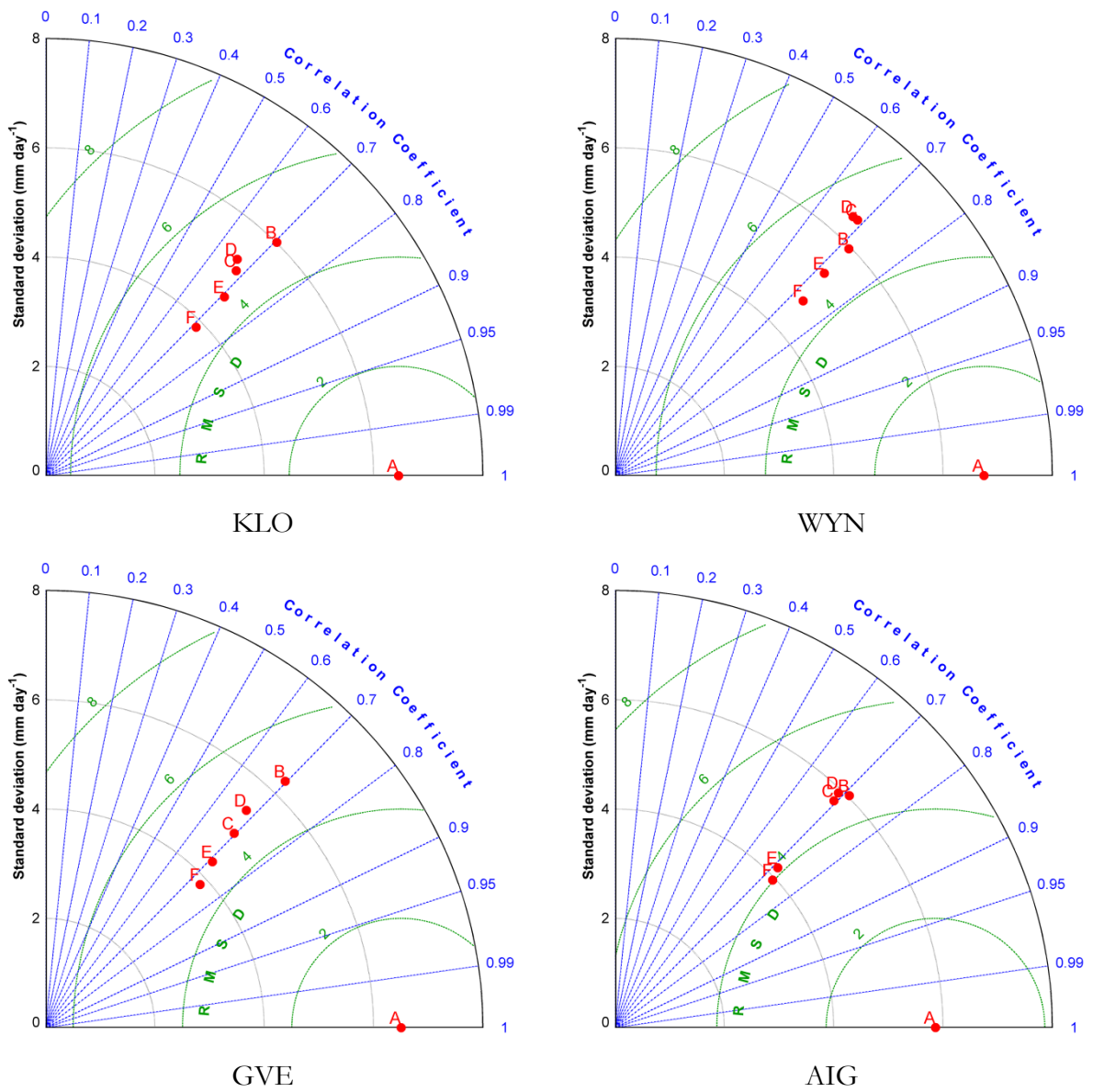
Figure A.1: Taylor diagrams of observations with downscaled daily precipitation for four downscaling methods, as well as the original ERA-Interim data for all 50 MeteoSwiss sites in the validation period 1999-2010. A= observation, B= original ERA-Interim, C= LOCI, D= QM, E= Stepwise and F= Lasso.

A.4 Quantile maps for the globe and southern Europe

Temperature - 0.1% quantile

3 hourly ERA-Interim data: Oct. 1989 - Dec. 2009, N=59176,
Temperature is lower than 0.1%-quantile for ≤ 9h/year (cumulated)

Temperature - 0.5% quantile

3 hourly ERA-Interim data: Oct. 1989 - Dec. 2009, N=59176,
Temperature is lower than 0.5%-quantile for ≤ 45h/year (cumulated)

Temperature - 1% quantile

3 hourly ERA-Interim data: Oct. 1989 - Dec. 2009, N=59176,
Temperature is lower than 1%-quantile for ≤ 90h/year (cumulated)

0   8,000 km

Legend / °C

< -50	-25 - -20	5 - 10	35 - 40
-50 - -45	-20 - -15	10 - 15	40 - 45
-45 - -40	-15 - -10	15 - 20	45 - 50
-40 - -35	-10 - -5	20 - 25	> 50
-35 - -30	-5 - 0	25 - 30	
-30 - -25	0 - 5	30 - 35	

Temperature - 5% quantile

3 hourly ERA-Interim data: Oct. 1989 - Dec. 2009, N=59176,
Temperature is lower than 5%-quantile for ≤ 450h/year (cumulated)

0   8,000 km

Legend / °C

< -50	-25 - -20	5 - 10	35 - 40
-50 - -45	-20 - -15	10 - 15	40 - 45
-45 - -40	-15 - -10	15 - 20	45 - 50
-40 - -35	-10 - -5	20 - 25	> 50
-35 - -30	-5 - 0	25 - 30	
-30 - -25	0 - 5	30 - 35	

Temperature - 95% quantile

3 hourly ERA-Interim data: Oct. 1989 - Dec. 2009, N=59176,
Temperature is higher than 95%-quantile for ≤ 450h/year (cumulated)

Legend / °C

< -50	-25 - -20	5 - 10	35 - 40
-50 - -45	-20 - -15	10 - 15	40 - 45
-45 - -40	-15 - -10	15 - 20	45 - 50
-40 - -35	-10 - -5	20 - 25	> 50
-35 - -30	-5 - 0	25 - 30	
-30 - -25	0 - 5	30 - 35	

0   8,000 km

Temperature - 99% quantile

3 hourly ERA-Interim data: Oct. 1989 - Dec. 2009, N=59176,
Temperature is higher than 99%-quantile for ≤ 90h/year (cumulated)

Legend / °C

< -50	-25 - -20	5 - 10	35 - 40
-50 - -45	-20 - -15	10 - 15	40 - 45
-45 - -40	-15 - -10	15 - 20	45 - 50
-40 - -35	-10 - -5	20 - 25	> 50
-35 - -30	-5 - 0	25 - 30	
-30 - -25	0 - 5	30 - 35	

0   8,000 km

Figure A.2: Global temperature distribution for 0.1 %, 0.5 %, 1 %, 5 %, 95 %, 99 %, 99.5 % and 99.9 % quantiles (Geographical Coordinate System: WGS 1984, Projection System: World Robinson, spatial resolution: 100 km, original ERA-Interim spatial resolution: ~79 km).

Temperature - 0.1% quantile

3 hourly ERA-Interim data: Oct. 1989 - Dec. 2009, N=59176,
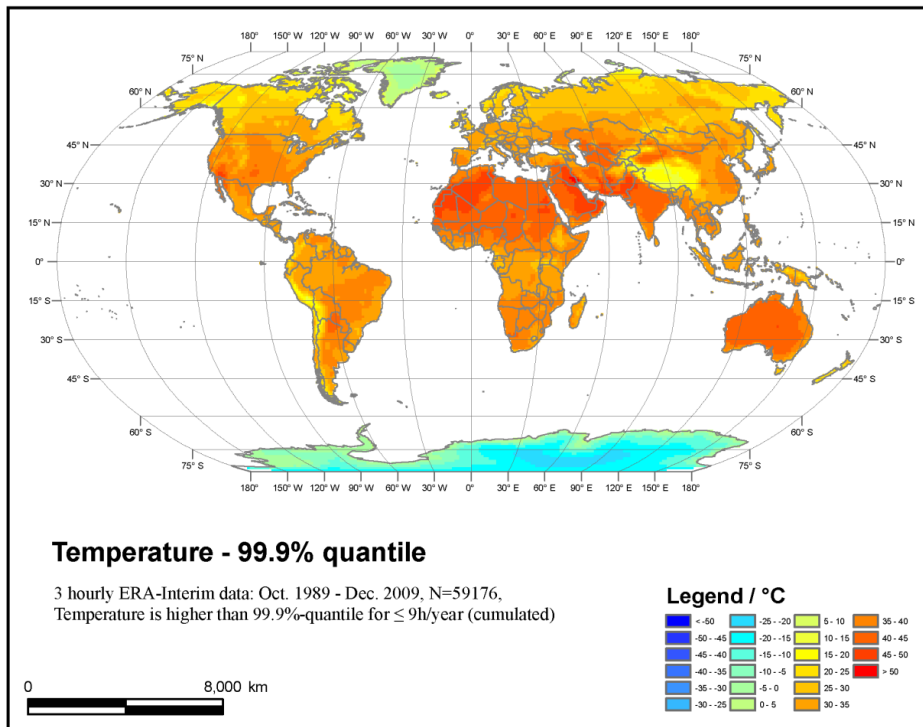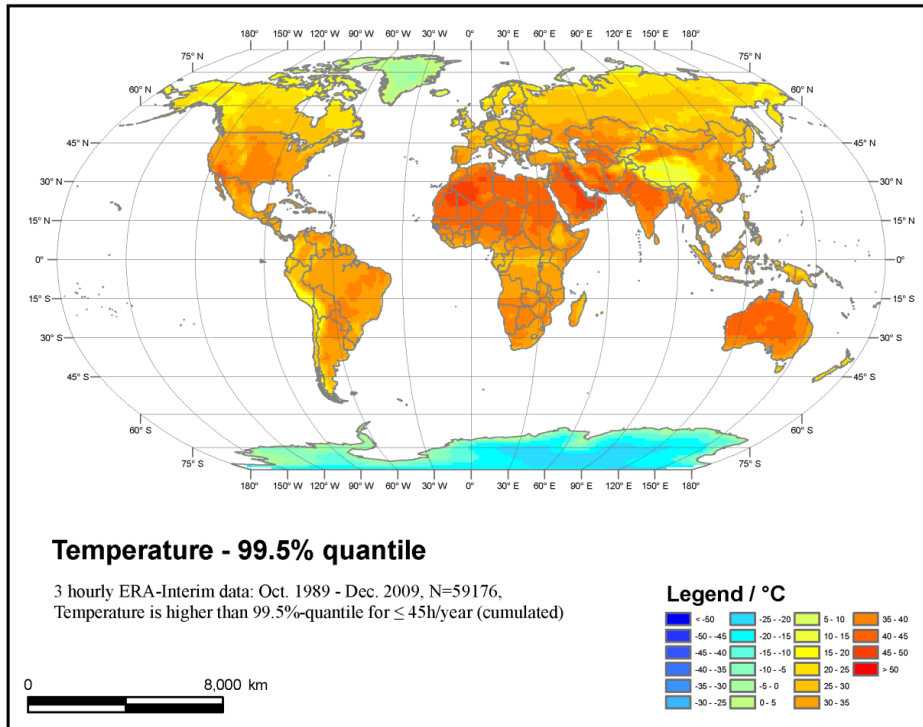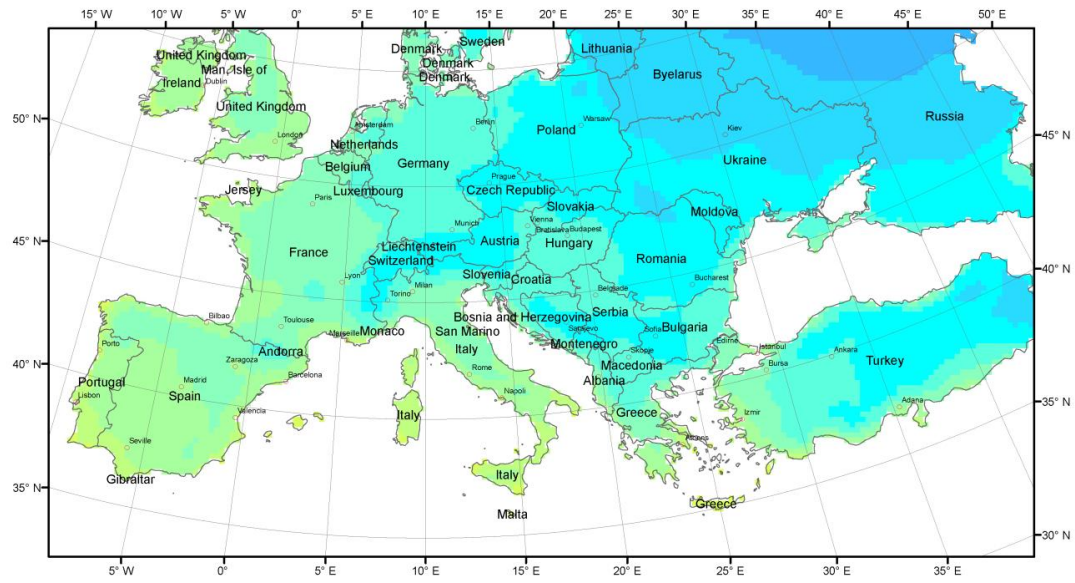Temperature is lower than 0.1%-quantile for ≤ 9h/year (cumulated)

0   1,000 km

Legend /°C

○ city	-30 - -25	0 - 5	30 - 35
< -50	-25 - -20	5 - 10	35 - 40
-50 - -45	-20 - -15	10 - 15	40 - 45
-45 - -40	-15 - -10	15 - 20	45 - 50
-40 - -35	-10 - -5	20 - 25	> 50
-35 - -30	-5 - 0	25 - 30	

Temperature - 0.5% quantile

3 hourly ERA-Interim data: Oct. 1989 - Dec. 2009, N=59176,
Temperature is lower than 0.5%-quantile for ≤ 45h/year (cumulated)

0   1,000 km

Legend /°C

○ city	-30 - -25	0 - 5	30 - 35
< -50	-25 - -20	5 - 10	35 - 40
-50 - -45	-20 - -15	10 - 15	40 - 45
-45 - -40	-15 - -10	15 - 20	45 - 50
-40 - -35	-10 - -5	20 - 25	> 50
-35 - -30	-5 - 0	25 - 30	

Temperature - 1% quantile

3 hourly ERA-Interim data: Oct. 1989 - Dec. 2009, N=59176,
Temperature is lower than 1%-quantile for ≤ 90h/year (cumulated)

0   1,000 km

Legend /°C

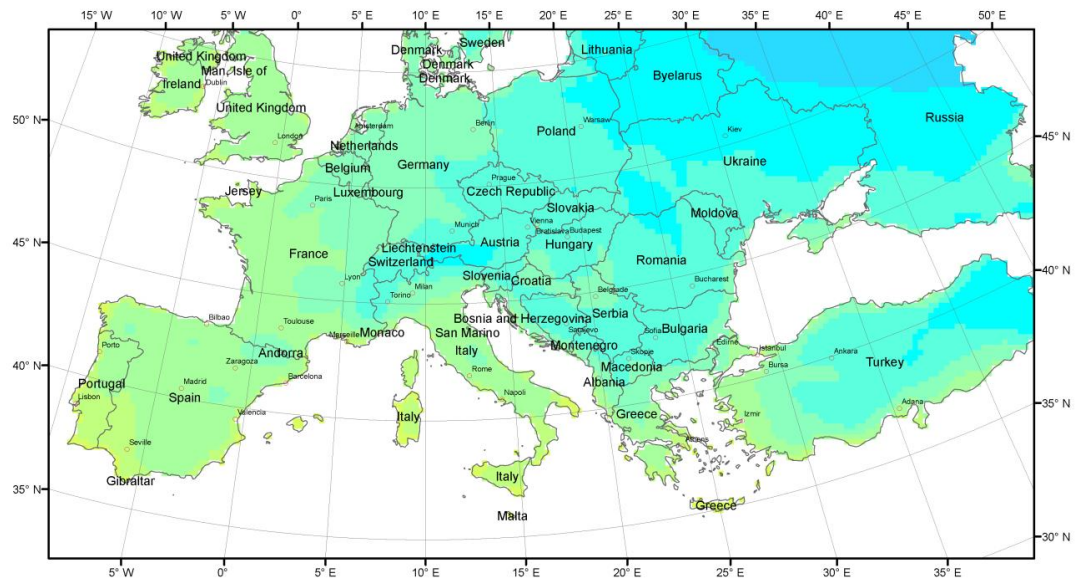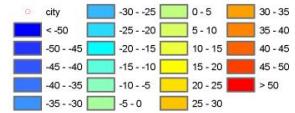|			
○ city	-30 - -25	0 - 5	30 - 35
< -50	-25 - -20	5 - 10	35 - 40
-50 - -45	-20 - -15	10 - 15	40 - 45
-45 - -40	-15 - -10	15 - 20	45 - 50
-40 - -35	-10 - -5	20 - 25	> 50
-35 - -30	-5 - 0	25 - 30	

Temperature - 5% quantile

3 hourly ERA-Interim data: Oct. 1989 - Dec. 2009, N=59176,
Temperature is lower than 5%-quantile for ≤ 450h/year (cumulated)

0   1,000 km

Legend /°C

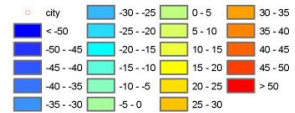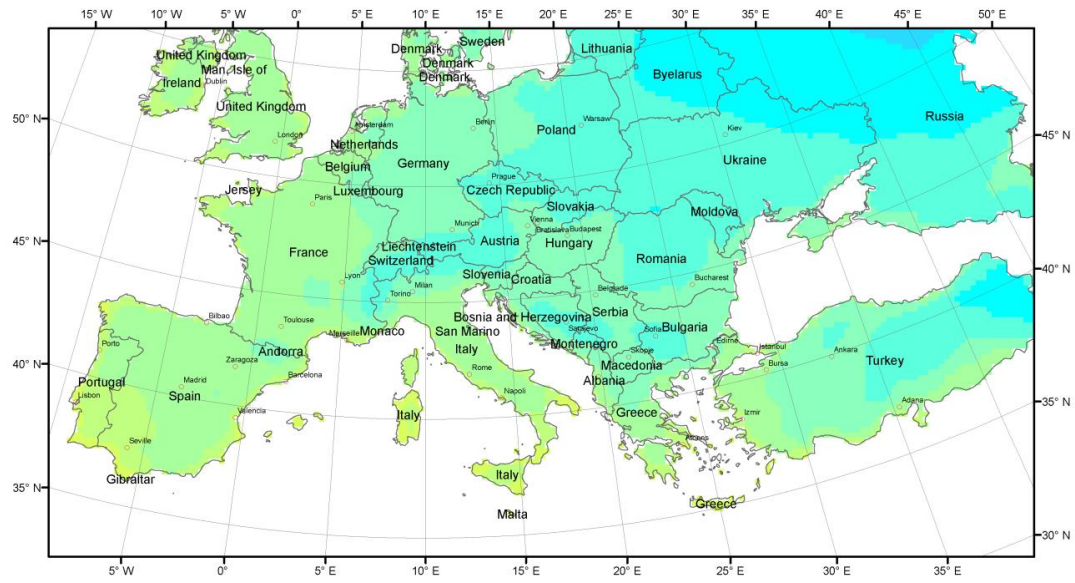|			
○ city	-30 - -25	0 - 5	30 - 35
< -50	-25 - -20	5 - 10	35 - 40
-50 - -45	-20 - -15	10 - 15	40 - 45
-45 - -40	-15 - -10	15 - 20	45 - 50
-40 - -35	-10 - -5	20 - 25	> 50
-35 - -30	-5 - 0	25 - 30	

Temperature - 95% quantile

3 hourly ERA-Interim data: Oct. 1989 - Dec. 2009, N=59176,
Temperature is higher than 95%-quantile for ≤ 450h/year (cumulated)

0   1,000 km

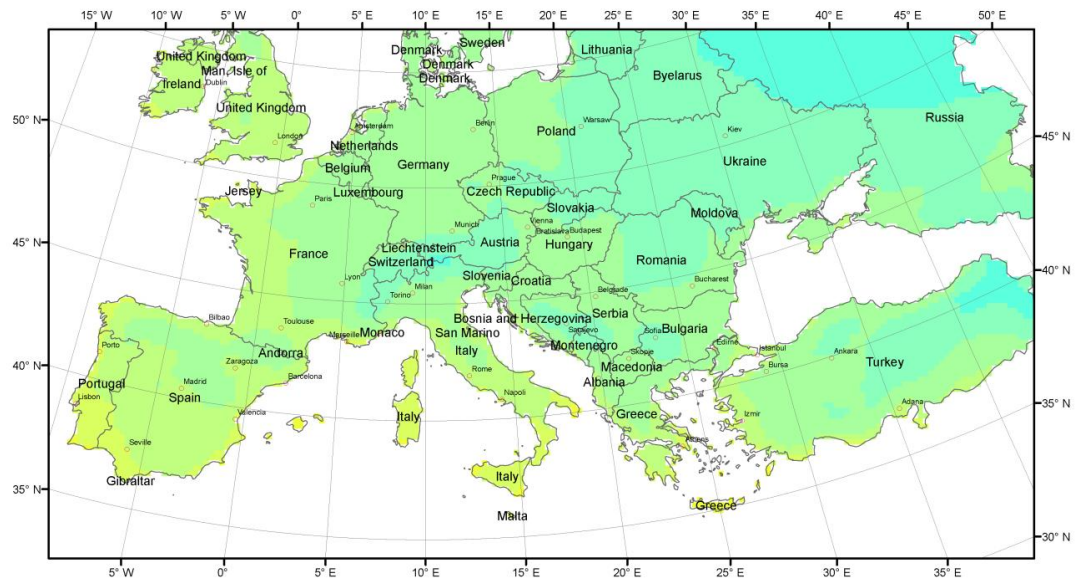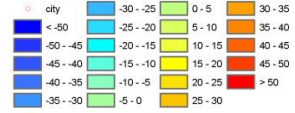| Legend /°C		
○ city	-30 - -25	0 - 5	30 - 35
< -50	-25 - -20	5 - 10	35 - 40
-50 - -45	-20 - -15	10 - 15	40 - 45
-45 - -40	-15 - -10	15 - 20	45 - 50
-40 - -35	-10 - -5	20 - 25	> 50
-35 - -30	-5 - 0	25 - 30	

Temperature - 99% quantile

3 hourly ERA-Interim data: Oct. 1989 - Dec. 2009, N=59176,
Temperature is higher than 99%-quantile for ≤ 90h/year (cumulated)

0   1,000 km

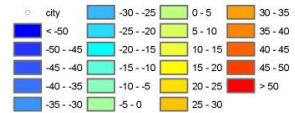| Legend /°C		
○ city	-30 - -25	0 - 5	30 - 35
< -50	-25 - -20	5 - 10	35 - 40
-50 - -45	-20 - -15	10 - 15	40 - 45
-45 - -40	-15 - -10	15 - 20	45 - 50
-40 - -35	-10 - -5	20 - 25	> 50
-35 - -30	-5 - 0	25 - 30	

Temperature - 99.5% quantile

3 hourly ERA-Interim data: Oct. 1989 - Dec. 2009, N=59176,
Temperature is higher than 99.5%-quantile for ≤ 45h/year (cumulated)

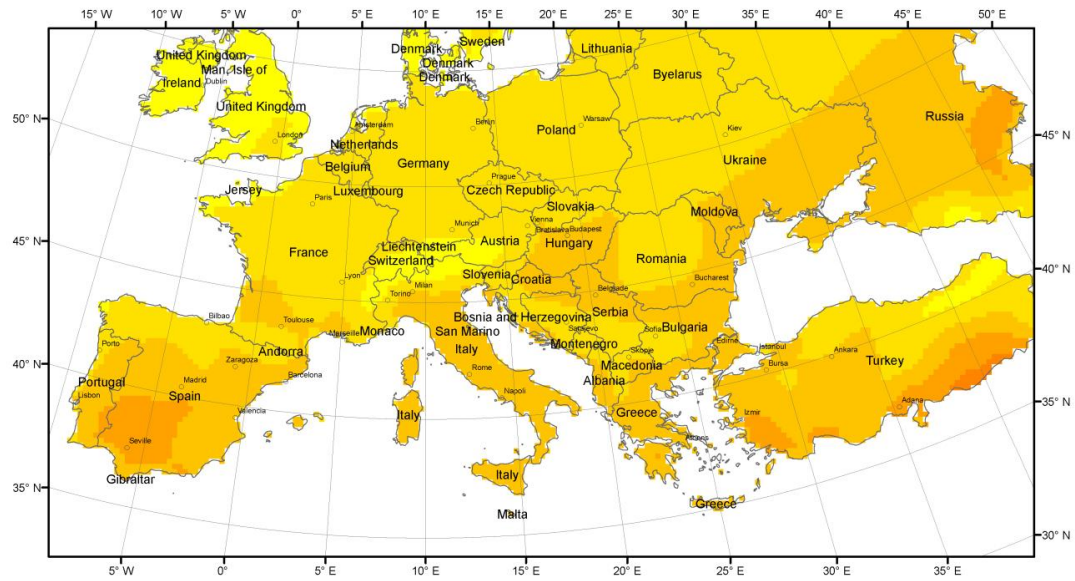0   1,000 km

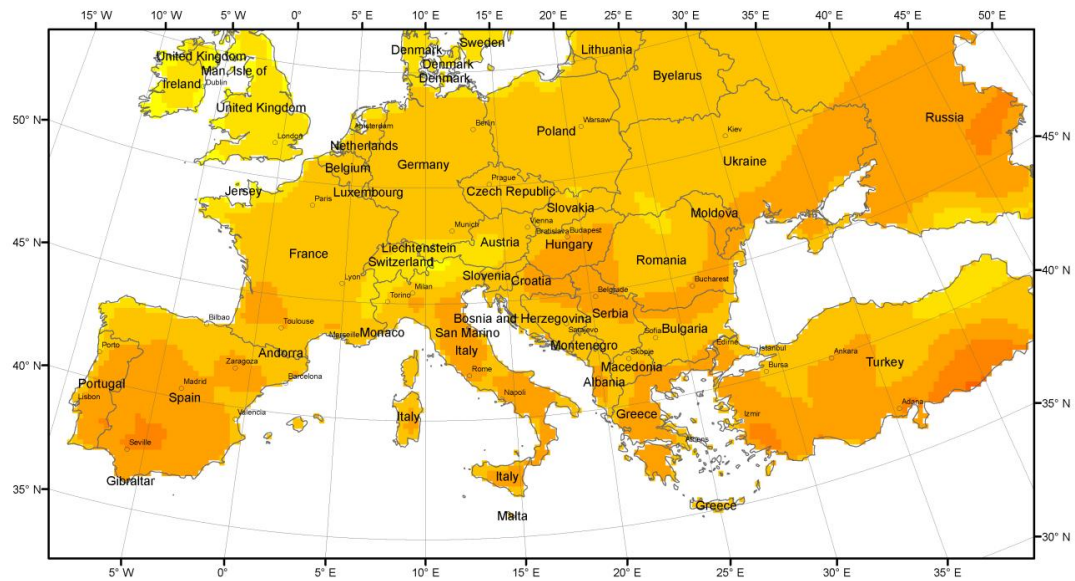**Temperature - 99.9% quantile**

3 hourly ERA-Interim data: Oct. 1989 - Dec. 2009, N=59176,
Temperature is higher than 99.9%-quantile for ≤ 9h/year (cumulated)

0   1,000 km

Figure A.3: Southern European temperature distribution for 0.1 %, 0.5 %, 1 %, 5 %, 95 %, 99 %, 99.5 % and 99.9 % quantiles (Geographical Coordinate System: European 1950, Projection System: Lambert Conformal Conic, spatial resolution: 25 km, original ERA-Interim spatial resolution: ~79 km).

A.5 Flux sites information

Table A.2: FLUXNET sites information. The vegetation type is based on MODIS International Geosphere-Biosphere Programme (IGBP) land cover classification. Climate type is based on Köppen climate classification.

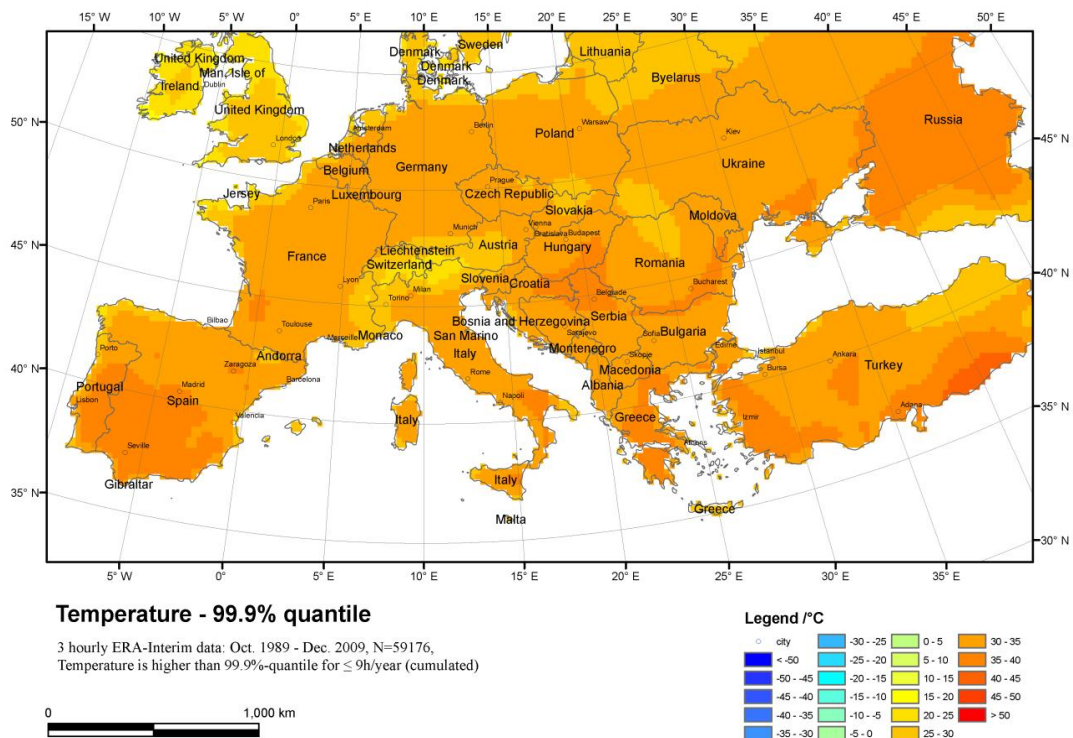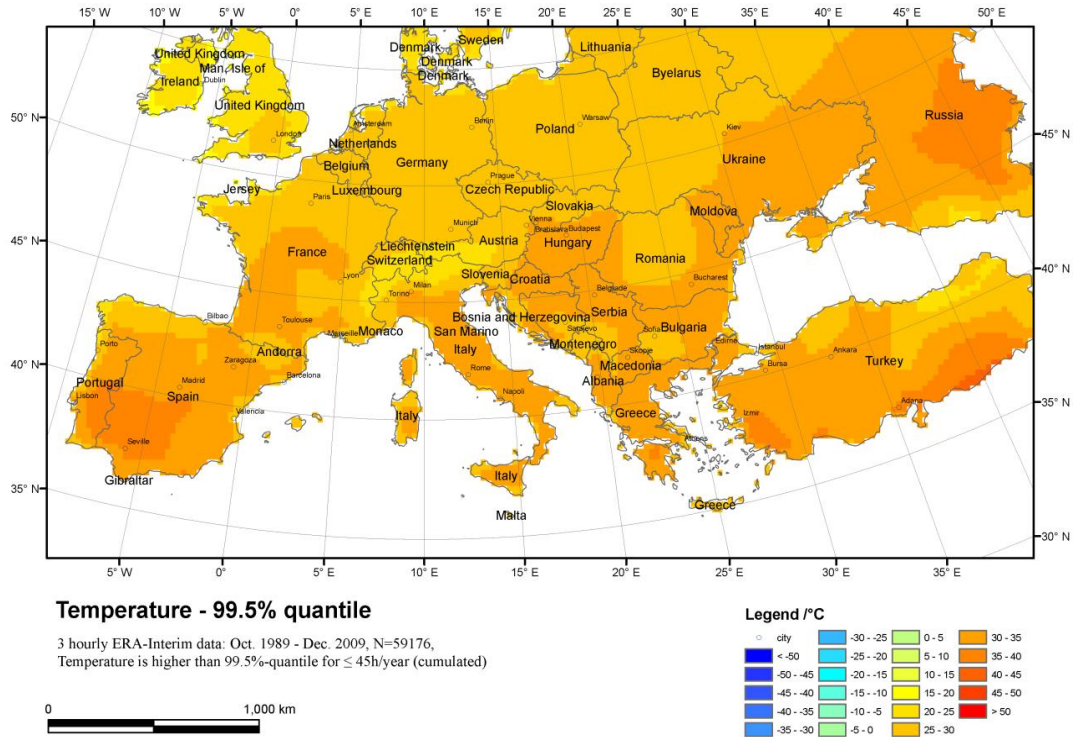| ID	Name	Country	IGBP	Climate type	Principal Investigator	E-mail
AT-Neu	Neustift	Austria	GRA	Cfb	Georg Wohlfahrt	Georg.Wohlfahrt@uibk.ac.at
BE-Bra	Brasschaat	Belgium	MF	Cfb	Ivan Janssens Reinhart Ceulemans	Ivan.Janssens@ua.ac.be Reinhart.Ceulemans@ua.ac.be
BE-Lon	Lonzee	Belgium	CRO	Cfb	Marc Aubinet	marc.aubinet@ulg.ac.be
BE-Vie	Vielsalm	Belgium	MF	Cfb	Marc Aubinet	marc.aubinet@ulg.ac.be
CH-Oe1	Oensingen1	Switzerland	GRA	Cfb	Ammann Christoph	christof.ammann@art.admin.ch
DE-Bay	Bayreuth	Germany	ENF	Cfb	Thomas Foken	thomas.foken@uni-bayreuth.de
DE-Geb	Gebesee	Germany	CRO	Cfb	Werner Kutsch Olaf Kolle	werner.kutsch@vti.bund.de olaf.kolle@bgc-jena.mpg.de
DE-Gri	Grillenburg	Germany	GRA	Cfb	Christian Bernhofer	christian.bernhofer@tu-dresden.de
DE-Hai	Hainich	Germany	DBF	Cfb	Alexander Knohl Olaf Kolle	aknohl@uni-goettingen.de olaf.kolle@bgc-jena.mpg.de
DE-Kli	Klingenberg	Germany	CRO	Cfb	Christian Bernhofer	christian.bernhofer@tu-dresden.de
DE-Meh	Mehrstedt1	Germany	MF	Cfb	Axel Don	axel.don@vti.bund.de
DE-Tha	Anchor Station	Germany	ENF	Cfb	Christian Bernhofer	christian.bernhofer@tu-dresden.de
DE-Wet	Wetzstein	Germany	ENF	Cfb	Corinna Rebmann Olaf Kolle	crebmann@bgc-jena.mpg.de olaf.kolle@bgc-jena.mpg.de
DK-Lva	Lille Valby	Denmark	GRA	Cfb	Kim Pilegaard	kipi@risoe.dtu.dk
DK-Ris	Risbyholm	Denmark	CRO	Cfb	Henrik Sogaard	hs@geogr.ku.dk
DK-Sor	Soroe- LilleBogeskov	Denmark	DBF	Cfb	Kim Pilegaard	kipi@risoe.dtu.dk
ES-ES1	El Saler	Spain	ENF	Csa	Maria Jose Sanz	miose@cceam.es
ES-ES2	El Saler_Sueca	Spain	CRO	Csa	Maria Jose Sanz	miose@cceam.es

Code	Site	Country	Veg	Climate	Name	Email
ES-LMa	Las Majadas	Spain	SAV	Csa	Maria Jose Sanz	mjose@ceam.es
ES-VDA	Vall d'Alinya	Spain	GRA	Cfb	Arnaud Carrara	arnaud@ceam.es
FR-Gri	Grignon	France	CRO	Cfb	Pierre Cellier	cellier@bcgn.grignon.inra.fr
FR-Hes	Hesse Forest	France	DBF	Cfb	André Granier Bernard Longdoz	Agranier@nancy.inra.fr bernard.longdoz@nancy.inra.fr
FR-LBr	Le Bray	France	ENF	Cfb	Denis Loustau	Loustau@pierroton.inra.fr
FR-Lq1	Laqueuille	France	GRA	Cfb	Katja Klumpp	kklumpp@clermont.inra.fr
FR-Pue	Puechabon	France	EBF	Csa	Serge Rambal	serge.rambal@cefe.cnrs.fr
HU-Bug	Bugacpuszta	Hungary	GRA	Cfb	Zoltan Nagy	Nagy.Zoltan@mkk.szie.hu
IE-Ca1	Carlow1	Ireland	CRO	-	Mike Jones Bruce Osborne	mike.jones@tcd.ie bruce.osborne@ucd.ie
IE-Dri	Dripsey	Ireland	GRA	Cfb	Gerard Kiely	g.kiely@ucc.ie
IT-Amp	Amplero	Italy	GRA	Cfa	Dario Papale	darpap@unitus.it
IT-BCi	Borgo Cioffi	Italy	CRO	Csa	Enzo Magliulo	Enzo.magliulo@cnr.it
IT-Col	Collelongo	Italy	DBF	Cfa	Dario Papale Giorgio Matteucci	darpap@unitus.it giorgio.matteucci@isafom.cs.cnr.it
IT-Cpz	Castelporziano	Italy	EBF	Csa	Dario Papale	darpap@unitus.it
IT-LMa	La Mandria	Italy	DBF	Cfb	Fabio petrella	petrella@ipla.org
IT-MBo	Monte Bondone	Italy	GRA	Cfb	Damiano Gianelle	damiano.gianelle@iasma.it
IT-Non	Nonantola	Italy	MF	Cfa	Franco Miglietta	f.miglietta@ibimet.cnr.it
IT-PT1	Zerbolo	Italy	DBF	Cfa	Günther Seufert	guenther.seufert@jrc.it
IT-Ren	Renon/Ritten	Italy	ENF	Dfb	Stefano Minerbi Leonardo Montagnani	stefano.minerbi@provincia.bz.it leonar@inwind.it
IT-Ro1	Roccarespampani1	Italy	DBF	Csa	Dario Papale	darpap@unitus.it
IT-Ro2	Roccarespampani2	Italy	DBF	Csa	Dario Papale	darpap@unitus.it
IT-SRo	San Rossore	Italy	ENF	Csa	Alessandro Cescatti	alessandro.cescatti@jrc.ec.europa.eu
NL-Ca1	Cabauw	Netherlands	GRA	Cfb	Eddy Moors	eddy.moors@wur.nl
NL-Hor	Horstermeer	Netherlands	GRA	Cfb	Han Dolman	han.dolman@falw.vu.nl
NL-Loo	Loobos	Netherlands	ENF	Cfb	Eddy Moors	eddy.moors@wur.nl
PT-Esp	Espirra	Portugal	EBF	Csa	Gabriel Pita	gabrielpita@ist.utl.pt

PT-Mi1	Mitra (Evora)	Portugal	EBF	Csa	Joao Santos Pereira	jspereira@isa.utl.pt
PT-Mi2	Mitra IV Tojal	Portugal	GRA	Csa	Casimiro Pio	casimiro@dao.ua.pt
SE-Deg	Degero	Sweden	GRA	Dfc	Mats Nilsson	Mats.B.Nilsson@sek.slu.se
UK-Gri	Griffin-Aberfeldy	UK	ENF	Cfb	John Moncrieff	j.moncrieff@ed.ac.uk

Curriculum Vitae

Personal

Name: Lu Gao

Date of birth: 16.06.1983

Place of birth: Yichang, Hubei, China

Nationalitiy: Chinese

Home Address: Schloß-Prunn-Str.1, 81375 München

Work Address: Luisenstraße 37, Department für Geographie, LMU, 80333 München, Deutschland

Telephone: +49 89 2180 6724

e-Mail: gaol2008@gmail.com

Education

09.2009-09.2013   PhD, funded by China Scholarship Council (CSC), Department of Geography, Ludig-Maximilians-Universtät München, Munich, Germany

09.2006-07.2009   Master of Science, School of Geography, Beijing Normal University, Beijing, China

09.2002-07.2006   Bachelor of Science, School of Gemology, China University of Geosciences (Beijing), Beijing, China

09.1999-07.2002   No.1 Senior High School of Dangyang, Hubei, China

09.1996-09.1999   Yuquan Middle School of Dangyang, Hubei, China

Publications

Journals:

1. **Gao, L**., Bernhardt, M., and Schulz, K.: Elevation correction of ERA-Interim temperature data in complex terrain, *Hydrology and Earth System Sciences*, 16, 4661-4673, doi: 10.5194/hess-16-4661-2012, 2012.

2. Zhou, H., Shi, P., Wang, J., Yu, D., and **Gao, L**. Rapid Urbanization and Implications for River Ecological Services Restoration: Case Study in Shenzhen, China. *Journal of Urban Planning and Development*, 137(2), 121–132. doi: 10.1061/(ASCE)UP.1943-5444.0000051, 2011.

3. **Lu Gao**, Si Chen, Hong-jian Zhou, Kui Luo, Jing-ai Wang, Jia Mao. Analysis of Drought Catastrophe in Chongqing in 2006 and Research on Post-Drought Resilience. *Journal of Natural Disasters (In Chinese)*, 2008, 17(1): 21-26.

4. Jing-ai Wang, Pei-jun Shi, Lu Hao, **Lu Gao**. Ecological Education Migration in Regional Sustainable Development. *Journal of Beijing Normal University(Social Sciences) (In Chinese)*, 2008, 4:139-145

5. Hong-jian Zhou, Pei-jun Shi, Jing-ai Wang, **Lu Gao**, Jing Zheng, De-yong Yu. River Network Change and Its Ecological Effects in Shenzhen Region in Recent 30 Years. *Acta Geographica Sinica(In Chinese)*, 2008, 63(9):969-980.

6. Lu Hao, Jing-ai Wang, **Lu Gao**, Dong-hua Pan. Trend and Jump Analysis on the Runoff in Recent 40 Years in Laohahe River Basin. *Journal of Beijing Normal University (Natural Sciences) (In Chinese)*, 2008, 44(6):16-21.

7. Hong-jian Zhou, Jing-ai Wang, Pei-jun Shi, Dong-hua Pan, **Lu Gao**, Hui-cong Jia. Influence of River Network Change in 1980-2005 on Flood Hazard in Shenzhen City, China. *Journal of Natural Disaster (In Chinese)*, 2008, 17(1): 97-103.

8. Jin-hong Wan, Jing-ai Wang, Zhen Liu, Hong-jian Zhou, **Lu Gao**, Li-long Gao, Feng Zhang. Drought resilience in view of income diversity of peasant household: a case study on Xinghe Country, Inner Mongolia. *Journal of Natural Disaster (In Chinese)*, 2008, 17(1):122-126.

Proceedings:

1. **L.Gao**, M. Berhardt, K. Schulz. Evaluation of ERA-Interim precipitation data in complex terrain. Geophysical Research Abstracts, Vol. 15, EGU2013-3330, EGU General Assembly 2013, Vienna, Austria, 07-12.04. 2013.

2. **L.Gao**, S. Härer ,M. Berhardt, K. Schulz. Skalierung von ERA-Interim Daten in komplexem Terrain. Tag der Hydrologie 2012, Freiburg, 22-23.03, 2012, Abstract.

3. **L.Gao**, M. Berhardt, S. Härer, K. Schulz. Downscaling ERA-Interim temperature data in complex terrain. Workshop zur Hydrologie Klimatologie von Gebirgsräumen, Umweltforschungsstation

Schneefernerhaus, 20-22.02, 2012, Abstract.

4. **L.Gao**, K. Schulz. Statistical temperature downscaling of ERA-Interim data using regression-based model. 14. Workshop zur Großskaligen Hydrologischen Modellierung, Tutzing, 03-05. 11, 2010, Abstract.

5. **Lu Gao**, Yao-jie Yue, Jing-ai Wang. Comparison of Error Analysis of TM Image Rough Registration from Three Different Methods [A]. The 5th International Symposium on Digital Earth Proposal Form, ISDE5, The University of California, Berkery, San Francisco, U.S.A, 2007.

6. **Lu Gao**, Si Chen, Hong-jian Zhou, Kui Luo, Jing-ai Wang, Jia Mao. Research on Tremendous Drought System Process and Resilience after Drought in Chongqing in 2006[A]. International Disaster Reduction Conference, IDRC 2007, *Strategy and Implementation of Integrated Risk Management*[C], Qunyan Press, 2007, 196-201.

7. Zhou, HJ; Wang, JA; Shi, PJ; Zheng, J; **Gao, L**; Su, XG; Yuan, Y. Impacts of rapid urbanization on river network and flood risk in Shenzhen Region, China [A]. International Disaster Reduction Conference, IDRC 2007, *Strategy and Implementation of Integrated Risk Management*[C], Qunyan Press, 2007, 34-39.

8. Yao-jie Yue, **Lu Gao**, Jing-ai Wang. Effectiveness of Survey Points' Density and Distribution on Vegetation Coverage Field Measurement [A]. The 16th International Conference on Geoinformatics and Joint Conference on GIS and Built Environment, Geoinformatics 2008. *Advanced Spatial Data Models and Analyses*[C], SPIE, 2009, Vol. 7146, doi: 10.1117/12.813167.

9. Lu Hao, Jing-ai Wang, **Lu Gao**. Assessing Drought Risk of Laohahe River Basin Using SWAT [A]. The International Conference on Risk Analysis and Crisis Response, Guangzhou, China, 2008. *Theory and Practice of Risk Analysis and Crisis Response*[C]**,** Atlantis Press, 2008, 586-591.